

12-2015

New visible light absorber for solar fuels : Ga(Sbx)N_{1-x} alloys.

Swathi Sunkara

Follow this and additional works at: <http://ir.library.louisville.edu/etd>



Part of the [Chemical Engineering Commons](#)

Recommended Citation

Sunkara, Swathi, "New visible light absorber for solar fuels : Ga(Sbx)N_{1-x} alloys." (2015). *Electronic Theses and Dissertations*. Paper 2288.

<https://doi.org/10.18297/etd/2288>

This Doctoral Dissertation is brought to you for free and open access by ThinkIR: The University of Louisville's Institutional Repository. It has been accepted for inclusion in Electronic Theses and Dissertations by an authorized administrator of ThinkIR: The University of Louisville's Institutional Repository. This title appears here courtesy of the author, who has retained all other copyrights. For more information, please contact thinkir@louisville.edu.

NEW VISIBLE LIGHT ABSORBER FOR SOLAR FUELS: Ga(Sb_x)N_{1-x} ALLOYS

By

Swathi Sunkara

Bachelor of Science, Jawaharlal Nehru Technological University, 2010

A Dissertation

Submitted to the Faculty of the
J.B. Speed School of Engineering
in Fulfillment of the Requirements
for the Degree of

Doctor of Philosophy

in Chemical Engineering

Department of Chemical Engineering
University of Louisville
Louisville, KY 40292

December 2015

NEW VISIBLE LIGHT ABSORBER FOR SOLAR FUELS: Ga(Sb_x)N_{1-x} ALLOYS

By

Swathi Sunkara

Bachelor of Science, Jawaharlal Nehru Technological University, 2010

A Dissertation Approved on

November 19 2015

By the Following Dissertation Committee

Dr. Mahendra Sunkara (Dissertation Director)

Dr. Thomas Starr

Dr. Xiao-an Fu

Dr. Jacek Jasinski

Dr. Shamus McNamara

DEDICATION

This Dissertation is dedicated to my Grandparents Subbarao Sunkara, Indira Devi, my parents Madhusudhana Rao, Aruna Sunkara and my dearest uncle.

ACKNOWLEDGEMENTS

I would like to thank Dr. Sunkara for giving me the opportunity to work on this excellent project and for his constant guidance and support throughout my PhD. I thoroughly enjoyed my work with the excellent synthesis and characterization facilities in the lab. I started Ph.D after my bachelors and didn't had any experience in research, Dr. Sunkara guided me through every step and helped me gain confidence.

I would also like to thank Dr. Starr, Dr. Jasinski, Dr. McNamara and Dr. Fu for serving on my thesis committee and for their valuable suggestions. I would also like to thank Dr. Menon for helping us with theoretical calculations. I would also like to thank the past and current members of my group. I had an enjoyable experience working with them. I would like to thank Alejandro for helping with my experiments. I learned a lot by working with my group, they were always very supportive and motivating.

ABSTRACT

NEW VISIBLE LIGHT ABSORBER FOR SOLAR FUELS: Ga(Sb_x)N_{1-x} ALLOYS

Swathi Sunkara

November 19, 2015

Solar energy conversion to fuels via photoelectrochemical water splitting is one of the most important technological directions toward meeting the global energy and environmental challenge. However, till date, there are no suitable semiconductor materials available that can absorb visible light, possess right kind of band edge energetics and are stable in aqueous environments. In this work, a new III-V alloy material Ga(Sb_x)N_{1-x} with dilute antimony concentration is proposed and developed for photoelectrochemical water splitting. Experimental studies were conducted first to synthesize the proposed alloy materials to understand structure-property relationships and compare them to those obtained using first principles computations. Finally, efforts were made to improve the quality of materials synthesized within the context of improving their photoactivity with water splitting reaction. In general, III-V nitrides have garnered immense interest as suitable materials for solar hydrogen generation due to their tunable band gaps with composition, high carrier mobilities and high absorption coefficients.

Computations using first principles density functional theory (DFT+U) revealed

that a small amount of Sb incorporation is sufficient to achieve a significant band gap reduction in GaN from 3.4eV to 2eV. Theoretical computations predicted that $\text{Ga}(\text{Sb})_x\text{N}_{1-x}$ alloys with 2 eV band gap straddle the electrochemical redox potentials. The synthesis of dilute $\text{GaSb}_x\text{N}_{1-x}$ alloys is conducted using a custom-built metalorganic chemical vapor deposition reactor. Extensive characterization of the resulting films suggests that there is a large band gap bowing even with small amounts (few percent \sim 2-3%) of antimony incorporation into GaN. In addition, photoelectrochemical characterization confirmed the band edges straddling redox potentials. All the experimental data regarding band gap bowing, lattice expansion and band edge straddling matched very well with the theoretical predictions. Moreover, the alloys with Sb incorporation $>7\%$ exhibited indirect band gap transition as predicted by DFT + U calculations.

The polycrystalline $\text{Ga}(\text{Sb})_x\text{N}_{1-x}$ thin films were shown to be capable of unassisted water splitting but with low efficiencies. So, two different approaches are investigated to improve the quality of resulting films: thick films with high texture and single crystal quality, $\text{Ga}(\text{Sb})_x\text{N}_{1-x}$ nanowires. The use of a pre-treatment step at 900°C , 40:1 ratio of antimony to gallium precursors and temperatures above 750°C allowed for good quality crystal growth while allowing for incorporation of antimony. Photoactivity of $1\text{mA}/\text{cm}^2$ was obtained. In addition, VLS approach has been demonstrated to obtain high crystalline quality films using copper as catalyst.

Vapor-liquid-solid growth experiments using copper particles allowed for tip led growth of $\text{GaSb}_x\text{N}_{1-x}$ nanowires at temperatures beyond 600°C . The antimony composition in the resulting nanowires increased with growth temperature up to 5 at%

while improving the quality. Also the photoactivity obtained from nanowires has been increased by two orders of magnitude when compared with polycrystalline films. In summary, a new class of III-V nitride alloys using dilute antimonides is demonstrated to have suitable properties for solar fuels applications but can find other applications.

TABLE OF CONTENTS

	PAGE
ACKNOWLEDGEMENTS.....	iv
ABSTRACT.....	v
LIST OF FIGURES.....	xii
CHAPTER	
1. INTRODUCTION.....	1
1.1 ENERGY AND ENVIRONMENTAL CHALLENGES.....	1
1.2 SOLAR FUELS: RENEWABLE HYDROGEN.....	2
1.3 PHOTOELECTROCHEMICAL WATER SPLITTING.....	4
1.4 PROPOSED APPROACH.....	7
1.5 OBJECTIVES OF THE STUDY.....	9
1.6 ORGANIZATION OF THESIS.....	10
2. BACKGROUND.....	12
2.1 INTRODUCTION.....	12
2.2 INTRODUCTION TO SEMICONDUCTOR-ELECTROLYTE INTERFACE.....	12
2.3 REVIEW ON DIFFERENT PEC CONFIGURATIONS.....	15
2.4 STATE OF THE ART ON MATERIALS FOR PEC WATER SPLITTING.....	17

2.4.1	Metal Oxides.....	21
2.4.2	Metal Chalcogenides.....	22
2.4.3	III-V semiconductor alloys.....	23
2.4.4	Nanowire architectures.....	28
2.4.5	Review on MOCVD of III-V alloys.....	31
2.5	PRIOR WORK ON GaSb _x N _{1-x}	34
2.5.1	Theoretical predictions.....	34
2.5.2	Band gap bowing in GaSb _x N _{1-x}	36
2.5.3	Prior experimental work on GaSb _x N _{1-x} alloy growth.....	39
3.	EXPERIMENTAL.....	41
3.1	INTRODUCTION.....	41
3.2	SYNTHESIS.....	41
3.2.1	Metal Organic Chemical Vapor Deposition.....	41
3.3	OPTICAL CHARACTERIZATION.....	46
3.3.1	UV-Vis Spectroscopy.....	46
3.3.2	Raman & Photoluminescence Spectroscopy.....	52
3.4	STRUCTURAL CHARACTERIZATION.....	55
3.4.1	X-ray Diffraction(XRD).....	55
3.4.2	Transmission Electron Microscopy(TEM).....	59
3.5	ELECTRICAL CHARACTERIZATION.....	60
3.6	ELECTROCHEMICAL AND PHOTOELECTROCHEMICAL CHARACTERIZATION.....	61
3.6.1	Electrode Fabrication.....	61

3.6.2	Photoelectrochemical Cell Setup.....	63
3.6.3	Open Circuit Potential.....	64
3.6.4	Photocurrent Measurements.....	64
3.6.5	Mott- Schottky Analysis.....	65
4.	METAL ORGANIC CHEMICAL VAPOR DEPOSITION OF GaSb_xN_{1-x}...	67
4.1	INTRODUCTION.....	67
4.2	COMPUTATIONAL CALCULATIONS.....	67
4.3	MOCVD of GaSb _x N _{1-x}	69
4.3.1	Synthesis.....	69
4.3.2	Morphology.....	71
4.3.3	Crystallinity.....	71
4.3.4	Bandgap Reduction in GaSb _x N _{1-x} Alloys.....	76
4.4	PHOTOELECTROCHEMICAL CHARACTERIZATION.....	82
4.4.1	Band Edge Determination.....	82
4.4.2	Illuminated Open Circuit Potential.....	86
4.4.3	Photocurrent Measurements.....	87
5.	VAPOR LIQUID SOLID (VLS) GROWTH OF GaSb_xN_{1-x} NANOWIRE...	91
5.1	INTRODUCTION.....	91
5.2	RATIONALE/MOTIVATION.....	91
5.3	EXPERIMENTAL DETAILS.....	95
5.3.1	Catalyst Deposition.....	95
5.3.2	MOCVD Growth.....	95
5.3.3	Characterization.....	96

5.4 RESULTS & DISCUSSION.....	97
5.5 SUMMARY.....	113
6. HIGHLY TEXTURED GaSb_xN_{1-x} FILMS.....	114
6.1 INTRODUCTION.....	114
6.2 RATIONALE.....	114
6.3 EXPERIMENTAL SECTION.....	117
6.4 RESULTS & DISCUSSION.....	117
6.4.1 Process Optimization for Textured and Oriented Film Growth.....	123
6.4.2 Photoelectrochemical Characterization.....	133
6.5 SUMMARY.....	138
7. CONCLUSIONS.....	139
8. FUTURE RECOMMENDATIONS.....	143
8.1 Growing Quality GaSb _x N _{1-x} Films.....	143
8.2 Photoelectrochemical Properties.....	143
8.3 Electrical Properties.....	145
REFERENCES.....	146
APPENDIX.....	154
CURRICULUM VITAE.....	186

LIST OF FIGURES

- Figure 1.1 A schematic illustrating coupled PV- water splitting versus direct PEC water splitting device for solar hydrogen production. 4
- Figure 1.2 A schematic showing the semiconductor-solution interface and the band edge positions with respect to hydrogen and oxygen evolution reaction potentials. 6
- Figure 1.3 A diagram showing the comparison of band edge positions with respect to vacuum for $\text{GaSb}_x\text{N}_{1-x}$ and $\text{In}_x\text{Ga}_{1-x}\text{N}$ alloys. 8
- Figure 2.1 Schematics of models for semiconductor/liquid interface showing before and after contact of semiconductor with electrolyte. 13
- Figure 2.2 Schematics illustrating band bending behavior in n-type and p-type materials. 14
- Figure 2.3 Schematics of different PEC configurations under illumination. 16
- Figure 2.4 Band edge positions of several semiconductor materials w.r.t. water oxidation and reduction potentials. 18
- Figure 2.5 Valence band (dark squares) and conduction band (open squares) positions of oxide semiconductors w.r.t the water redox potentials at $\text{pH} = 0$ showing the lack of

straddling by lower band gap materials and straddling by the large band gap materials. 19

Figure 2.6 Valence band (dark squares) and conduction band (open squares) positions of sulfide semiconductors w.r.t the water redox potentials at pH 0. 19

Figure 2.7 Relative abundances of elements in earth's crust per 10^6 atoms of silicon. 20

Figure 2.8 (a) Experimentally obtained photocurrent density with 0.5 V applied bias vs. theoretical maximum current density for III-V materials and commonly investigated metal oxides (b) band edge positions vs. maximum theoretical photocurrent density for III-V materials. The photocurrent onset potentials are indicated in open symbols. 25

Figure 2.9 Electronic band gap as a function of x in $\text{GaSb}_x\text{N}_{1-x}$ and $\text{GaN}_x\text{Sb}_{1-x}$ materials. 35

Figure 2.10 Band structure, density of states and optical transitions for $\text{GaSb}_x\text{N}_{1-x}$ alloys. 35

Figure 2.11 A schematic illustration for the VBAC model involving valence band splitting for Bi incorporation in GaAs. 37

Figure 2.12 A schematic illustration for formation of a defect state in GaN with antimony incorporation. 37

Figure 3.1 A schematic of the custom-built MOCVD reactor used for the growth of $\text{GaN}_x\text{Sb}_{1-x}$ alloys. 44

Figure 3.2 a) Picture of a reaction chamber with substrate stage covered with several samples b) Top view of the wafer with several samples c) Composition gradient across

the wafer.	45
Figure 3.3 A schematic of UV-Vis spectrometer setup.	48
Figure 3.4 A sample Tauc plot for a $\text{GaSb}_x\text{N}_{1-x}$ sample.	50
Figure 3.5 Tauc plots for direct transition and indirect transition for 2% Sb (a,b) and 8% Sb (c,d).	51
Figure 3.6 Optical absorption profile of a $\text{GaSb}_x\text{N}_{1-x}$ film.	52
Figure 3.7 A schematic showing photo-excitation processes in PL spectroscopy.	54
Figure 3.8 A schematic of the experimental setup used for X-ray diffraction in the Bragg-Bentano configuration.	56
Figure 3.9 Comparison of XRD patterns for $\text{GaSb}_x\text{N}_{1-x}$ and GaN.	58
Figure 3.10 A schematic showing the configuration used for EBIC measurements	61
Figure 3.11 Schematics showing electrical contacts with samples for testing with photoelectrochemical water splitting activity.	62
Figure 3.12 Photograph showing $\text{GaSb}_x\text{N}_{1-x}$ electrodes made for photoelectrochemical studies.	62
Figure 3.13 Photoelectrochemical setup used for water splitting studies.	63
Figure 3.14 A typical J-V curve for a $\text{GaSb}_x\text{N}_{1-x}$ sample.	65
Figure 4.1 Predicted band gap values for different Sb composition using 192 and 172	

atom supercells.	69
Figure 4.2 SEM images showing cross-sectional view for GaSb _x N _{1-x} films.	71
Figure 4.3 a) XRD pattern of GaSb _x N _{1-x} layers showing peak shift of (002) plane with various Sb concentrations b) Lattice expansion with Sb concentration of (002) plane c) GaSb _x N _{1-x} supercell with x= 5/96 optimized using DFT simulations. The Sb atoms are shown in red, Ga in green and N in blue.	72, 73
Figure 4.4 a) A schematic illustrating GaSb _x N _{1-x} growth on an array of GaN nanowires b) Low magnification TEM image and c) HRTEM image of typical MOCVD GaSb _x N _{1-x} layer grown on a-plane GaN nanowire.	75
Figure 4.5 Raman spectra of GaSb _x N _{1-x} samples containing different antimony concentrations.	76
Figure 4.6 a) UV-Vis absorption spectra of GaSb _x N _{1-x} samples b) Experimental and theoretical energy band gap of GaSb _x N _{1-x} alloys as a function of Sb concentrations.	77
Figure 4.7 a) Low temperature Photoluminescence spectra for GaSb _x N _{1-x} alloys with varying Sb composition.	78
Figure 4.7 b) Photoluminescence spectra for sample containing 1.5 ± 0.8 % Sb at 241 K.	79
Figure 4.8 a) Tauc analysis for direct transition and indirect transition for 2% Sb (a,b) and 8% Sb (c,d).	81
Figure 4.8 b) Photocurrent spectroscopy plots: a) and c) for indirect transition; and b) and	

d) for direct transition. The data is for GaSb _x N _{1-x} samples with Sb composition greater than 7%.	82
Figure 4.9 Mott- Schottky plots for various GaSb _x N _{1-x} samples with different Sb compositions.	84
Figure 4.10 Energy diagram showing the band edge positions for various GaSb _x N _{1-x} alloy samples. The band edge positions of GaSb and GaN are added for reference.	85
Figure 4.11 Two electrode chopped light linear sweep voltammogram for a GaSb _x N _{1-x} sample in a 0.5 M Na ₂ SO ₄ at pH = 9.	85
Figure 4.12 Chopped open circuit potential vs time for a GaSb _x N _{1-x} sample.	86
Figure 4.13 (a) Linear sweep voltammogram for a polycrystalline GaSb _x N _{1-x} thin film sample (x= 6%) under chopped AM 1.5 illumination at 1 Sun (b) Cross-section scanning electron microscopy image of thin film sample.	87
Figure 4.14 XRD patterns for a GaSb _x N _{1-x} sample and GaN showing peak at 34.5 °.	88
Figure 4.15 Chopped photocurrent density versus time for a GaSb _x N _{1-x} sample at an applied bias of 0.9 V vs Ag/AgCl using AM 1.5 illumination at 1 sun.	89
Figure 4.16 Photocurrent density vs light intensity for a GaSb _x N _{1-x} sample at 0.9 V vs Ag/AgCl.	90
Figure 5.1 Schematics illustrating differences with carrier diffusion and absorption length scales involved with polycrystalline film vs single crystalline films vs nanowire array samples when used for photoelectrochemical water splitting. .	92

Figure 5.2 SEM images of GaSb _x N _{1-x} nanowires grown using a) copper b) Gallium c) Tin d) Antimony.	97
Figure 5.3 Phase diagrams of Copper-Antimony and Copper-Gallium.	98
Figure 5.4 SEM image of GaSb _x N _{1-x} nanowire array sample synthesized at 700 °C using copper as a catalyst.	100
Figure 5.5 TEM-EDS line-scan compositional profile across a GaSb _x N _{1-x} nanowire.	101
Figure 5.6 SEM images of GaSb _x N _{1-x} nanowire growth using different catalyst thicknesses a) 2nm film b) 4nm film.	102
Figure 5.7 A Tauc plot obtained for a GaSb _x N _{1-x} nanowire array sample grown on GaN substrate at 700° C.	104
Figure 5.8 HRTEM images of GaSb _x N _{1-x} nanowires grown on GaN substrate.	104
Figure 5.9 HRTEM image and SAED pattern of GaSb _x N _{1-x} nanowire.	105
Figure 5.10 SEM images and Tauc plots of GaSb _x N _{1-x} nanowires at different temperatures.	106
Figure 5.11 Plot of antimony composition as a function of synthesis temperature used for growing GaSb _x N _{1-x} nanowires.	107
Figure 5.12 A schematic illustrating various stages of proposed growth mechanism for GaSb _x N _{1-x} nanowires.	109
Figure 5.13 Chopped photocurrent density – voltage plot of GaSb _x N _{1-x} NW array sample	

under AM 1.5 illumination.	110
Figure 5.14 Chopped open circuit potential of GaSb _x N _{1-x} nanowire array sample under AM 1.5 illumination.	111
Figure 5.15 Chopped photocurrent vs time plot of GaSb _x N _{1-x} electrodes under AM 1.5 illumination at a potential of – 0.6 V.	112
Figure 5.16 Photocurrent densities of GaSb _x N _{1-x} nanowires comparing at 700° C and 800° C.	113
Figure 6.1 A schematic illustrating cross-sectional view for textured thin film growth.	115
Figure 6.2 A schematic illustrating cross-sectional view for highly oriented film growth.	116
Figure 6.3 A schematic illustrating cross-sectional view for epitaxial growth.	116
Figure 6.4 Comparison of crystal quality and antimony incorporation at low and high temperatures.	118
Figure 6.5 Comparison of XRD peak for GaSb _x N _{1-x} polycrystalline film vs GaN substrate.	119
Figure 6.6 Adsorption processes of MOCVD precursors on substrate at elevated temperatures.	120
Figure 6.7 a) Reaction pathway showing adduct and decomposition routes for formation of GaN during metalorganic chemical vapor deposition.	121

Figure 6.7 (b) Chemical reaction pathway for formation of GaSb during metal organic chemical vapor deposition.	122
Figure 6.8 Evolution of epitaxial $\text{GaSb}_x\text{N}_{1-x}$ films by changing the growth temperature and TMSb:TMG flux ratio.	124
Figure 6.9 SEM images of $\text{GaSb}_x\text{N}_{1-x}$ layers grown at different temperatures on GaN substrates.	125
Figure 6.10 Comparison of XRD peaks for $\text{GaSb}_x\text{N}_{1-x}$ layers grown at different temperatures.	127
Figure 6.11 Tauc plots obtained for $\text{GaSb}_x\text{N}_{1-x}$ layers grown at different temperatures.	128
Figure 6.12 Comparison of XRD peaks for $\text{GaSb}_x\text{N}_{1-x}$ layers grown using H_2 and N_2 as carrier gas for metal organic precursors.	129
Figure 6.13 Photoluminescence spectra for $\text{GaSb}_x\text{N}_{1-x}$ layers grown at 775 °C and 800 °C using H_2 as carrier gas for metal organic precursors.	129
Figure 6.14 A schematic of formation of $\text{GaSb}_x\text{N}_{1-x}$ film using copper as catalyst.	131
Figure 6.15 a) SEM images showing top view of $\text{GaSb}_x\text{N}_{1-x}$ epitaxial films grown at 700 °C using catalyst layer (before etching)	131
Figure 6.15 b) Top view of $\text{GaSb}_x\text{N}_{1-x}$ epitaxial film via vapor-liquid-solid growth using copper as catalyst. Image is obtained after after etching in KOH.	132
Figure 6.15 c) Cross view showing $\text{GaSb}_x\text{N}_{1-x}$ coalesced into a epitaxial film (after	

etching in KOH).	132
Figure 6.16 Chopped I-V measurement of GaSb _x N _{1-x} film comparing photoactivity with and without using 450 nm filter for AM1.5 illumination.	134
Figure 6.17 Comparison of chopped I-V curves obtained for GaSb _x N _{1-x} polycrystalline thin film and textured thick film using AM 1.5 illumination.	135
Figure 6.18 Chopped I-V curves obtained for GaSb _x N _{1-x} films under illumination using sodium sulfite and sodium sulfate in electrolyte solution.	136
Figure 6.19 Band edge diagram showing the energetic requirements associated with the minimum thermodynamic energy to drive HER and OER reactions, catalytic overpotentials and photovoltage.	137
Figure 8 A schematic illustrating the charge carrier transport in compositionally graded GaSb _x N _{1-x} and conventional n-type electrode.	145

CHAPTER 1

INTRODUCTION

1.1 Energy and Environmental Challenge

Current energy consumption is 18TW¹ and it is predicted to rise by at least 50% by 2050. About 85% of the current energy demand is supplied by fossil fuels. The expected, unprecedented growth in energy demand using fossil sources will lead to unprecedented growth in atmospheric levels of CO₂. Currently, CO₂ levels in the atmosphere are already at 400 ppm and will increase at a rapid pace leading to environmental concerns from global warming. So, the advent of carbon free energy sources for meeting the anticipated energy demand is one of the grand challenges facing humanity.

Of all renewables (solar, biomass, hydro, geothermal etc.), solar energy has the advantages of being clean and abundant but has some serious disadvantages. The intermittent nature of sunlight and the fact that it is influenced by atmospheric conditions (clouds, rain) makes it imperative to develop suitable storage technologies or use some auxiliary source of energy during off hours. The main challenges with using solar cells for energy generation are high land area and the extra costs associated with transportation and energy storage.² Even though solar cells can be coupled with batteries, the slow charge/discharge rates of many state-of-the batteries available today creates a technical

barrier for implementing this approach. A prudent route would be to use an alternate high energy density fuel with minimal carbon footprint.

1.2 Solar Fuels – Renewable Hydrogen

Solar energy conversion to fuels represents as one of the best pathways for storing energy. The energy of a visible light which ranges from 1-3eV is sufficient enough to drive many chemical synthesis routes.³ Chemical fuels like hydrogen, methane, methanol, gasoline, diesel, etc. have advantages of high energy storage densities and ease of transportation. Out of all these, hydrogen is the only clean fuel whereas all other chemical fuels require a source of carbon. As the goal is to avoid a carbon source, hydrogen is the ideal chemical fuel. The next challenge would be to find an efficient route to convert solar energy into hydrogen. In 1874 Jules Verne made a comment that “water will be coal of the future” intimating the production of hydrogen from water.⁴ Also water is an abundant source of hydrogen

The solar water splitting reaction can be written as follows:



Hydrogen as a fuel contains 143 MJ/kg of energy density and has ten times more energy density compared to batteries and pumped hydro reservoirs etc. Moreover, hydrogen can drive an internal combustion engine and can also be used in fuel cells and electrolyzers. This offers the opportunity of having energy infrastructure based on sunlight, hydrogen, and electricity.³

Large scale production of hydrogen serves as a main solution to meet the world's clean energy demand. Conversion of solar energy to hydrogen by splitting water is the

most economical way as it uses water and sunlight which are abundant in nature. The US Department of Energy (DOE) has stated the cost goal for hydrogen at \$2-\$3 per kg including production, storage, and transportation.⁵ A scalable technology for hydrogen production with minimal carbon footprint is a challenge. Many technological routes are being considered and they include thermolysis, biomass conversion, photobiological methods, photovoltaic-electrolysis, photoelectrochemical water splitting, and photocatalytic water splitting. Out of all the above methods mentioned, direct photoelectrochemical water splitting is more appealing because it allows easy separation of gases and can be run at room temperatures.⁶ Also it is a single device which is entirely made up of inorganic materials which offers a chemical robustness that is not possible with organic or biological systems. Both photoelectrochemical (PEC) water splitting and coupled PV-electrolysis technologies using semiconductor electrodes have advantages like easy separation of hydrogen, and simple construction. Coupled PV- water splitting needs two systems: one to harvest solar energy and second one to split water whereas PEC combines these two steps into a single monolithic device as shown in Figure 1.1.⁷ The efficiency of coupled PV and electrolysis will depend on efficiencies of both photovoltaic (~15%) and electrolyzer (~70%) which can be estimated as around $0.15 \times 0.7 \sim 0.1$ (or ~10%). On the other hand, the efficiency of photoelectrochemical water splitting using a single semiconductor with appropriate band gap can be around 25%.⁸

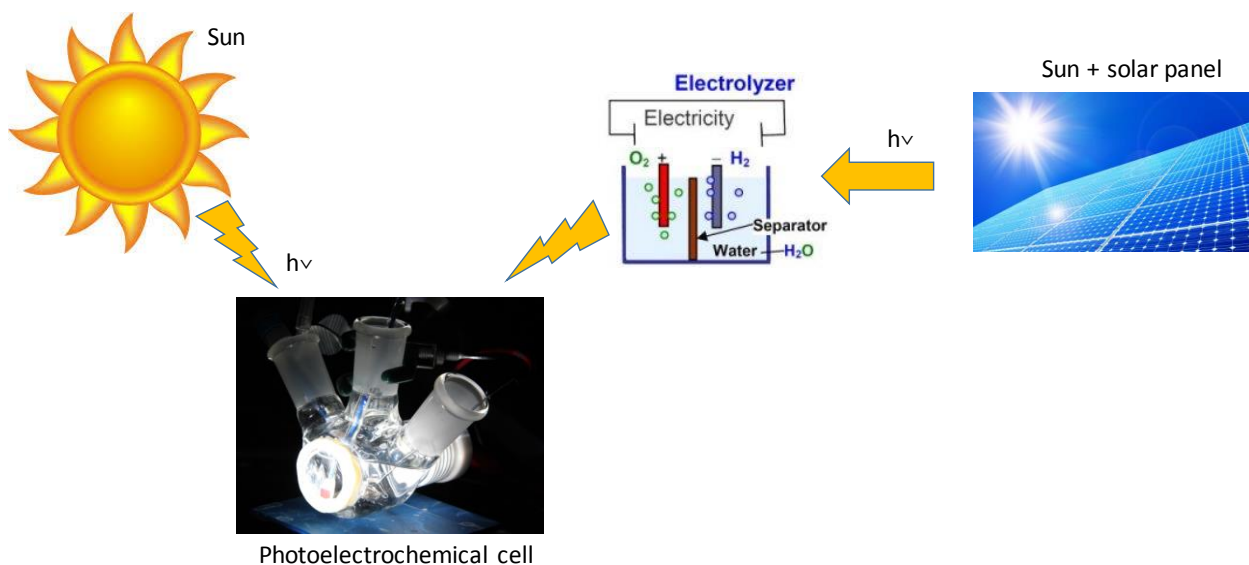


Figure 1.1 A schematic illustrating coupled PV- water splitting versus direct PEC water splitting device for solar hydrogen production.

1.3 Photoelectrochemical Water Splitting

Photoelectrochemical water splitting is carried out in a PEC cell that consists of a working electrode, which is a visible light absorbing semiconductor, and counter electrode immersed in an electrolyte solution. The main challenge with photoelectrochemical water splitting is the availability of a semiconductor that meets several necessary criteria for unassisted water splitting. The main requirements that need to be satisfied are (i) band gap between 1.7 to 2eV, (ii) band edges straddling the water oxidation and reduction potential, (iii) fast charge transfer kinetics at semiconductor-electrolyte interface and (iv) high stability in aqueous solution.⁹ The underlying reasons for these criteria are explained as follows.

Under standard condition the Gibbs free energy required to drive the water splitting reaction is +237KJ/mol which corresponds to electrochemical cell voltage of $E=1.23\text{V}$. The energy difference between generated electrons and holes upon illumination should be at least 1.23 eV in order to drive the reaction, but due to the losses at the interface, overpotential is required. Hence, energy difference of at least 1.7 eV is required. Also, the maximum energy of solar energy is concentrated around 1.7eV – 2eV and therefore it is important to use a semiconductor material with a band gap in the range 1.7eV -2 eV for efficient absorption of solar energy. The next important criterion is the energetic level of the band edge of the material straddling the water redox potentials as shown in Figure 1.2 which means the conduction band minimum of the material should be above hydrogen evolution potential and valence band maximum should be lower than oxygen evolution potential. If the band edges are too far away from the HER and OER potentials, extra energy is required to drive the reactions which results in higher external voltages being applied to split water. Another important criterion for a good PEC material to split water efficiently is to have excellent charge transport properties which help to transport generated carriers to electrolyte and counter electrode. If the charge transport is poor in the material charge carriers tend to recombine without separating which reduces the performance of the photoelectrochemical cell. The last requirement for long term PEC device application is stability of the semiconductor material in water.

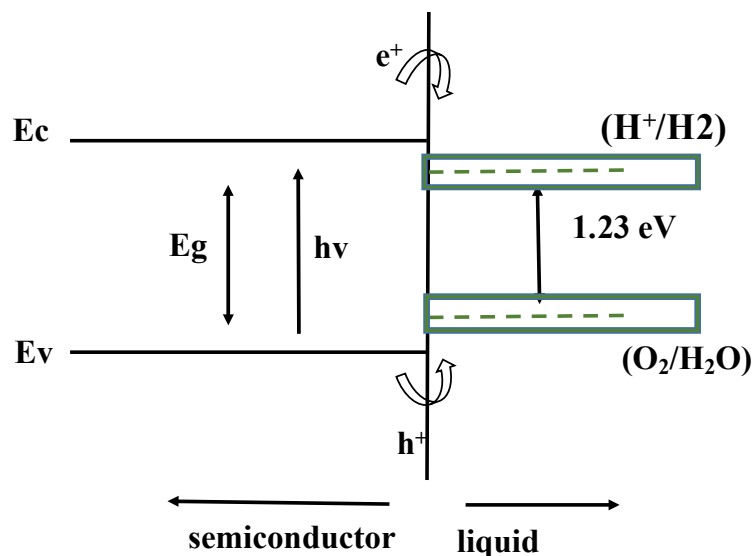


Figure 1.2 A schematic showing the semiconductor-solution interface and the band edge positions with respect to hydrogen and oxygen evolution reaction potentials.

Stability in aqueous solutions is a major shortcoming for many semiconductor materials. Metal oxides with wide band gap have excellent chemical stability but poor charge transport and light absorption is a major issue with many oxide materials.¹⁰ This occurs mostly in the metal oxide materials with indirect band gap where recombination is high due to the generation of carriers farther away from the surface. Another challenge observed in most of the materials is slow catalysis at the interface which create the necessity for co catalysts. The problem with some of the available catalysts like platinum is enhancing the back reaction of hydrogen and oxygen.⁸ One more challenge to be considered is the cost of the material. To date the highest efficiency was achieved using multijunction devices based on highly expensive materials and device configurations.¹¹

To date, very few materials or none satisfy all of the essential criteria described above. Hence it is very important for discovering and developing new semiconductor materials

that can satisfy all the criteria simultaneously or develop architectures that can improve the performance of the existing materials.

1.4 Proposed Approach

There are two well-known semiconductors whose band edges straddle water splitting reaction. They are titania and gallium nitride. Titania is an indirect semiconductor while Gallium Nitride (GaN) is a direct band gap semiconductor. Ternary alloys based on GaN have composition dependent band gaps and show good aqueous stability. Specifically, $\text{In}_x\text{Ga}_{1-x}\text{N}$ is the most widely studied material but huge Indium incorporation is required to get the band gap in visible region and reports showed phase segregation with such high indium content. *Synthesis of new ternary alloys of GaN that satisfy all the water splitting criteria offer a solution to selection of an appropriate material for scalable hydrogen production using PEC. Dilute $\text{Ga}(\text{Sb}_x)\text{N}_{1-x}$ alloy, formed by incorporating small amount of Sb into GaN, shows very high promise among ternary GaN alloys.* Density functional theory (DFT) calculations suggest that very low percentage of antimonide incorporation would be sufficient to bring down the GaN band gap from UV to visible region, where most of the solar spectrum is concentrated. Further, $\text{Ga}(\text{Sb}_x)\text{N}_{1-x}$ has right band edge energetics to drive the water oxidation and hydrogen evolution reactions. The applicability of the $\text{Ga}(\text{Sb}_x)\text{N}_{1-x}$ alloys for practical realization of direct PEC water splitting is illustrated in the band offset diagram in Figure 1.3. The band edges of GaN, GaSb and InN are also included for comparison.¹²

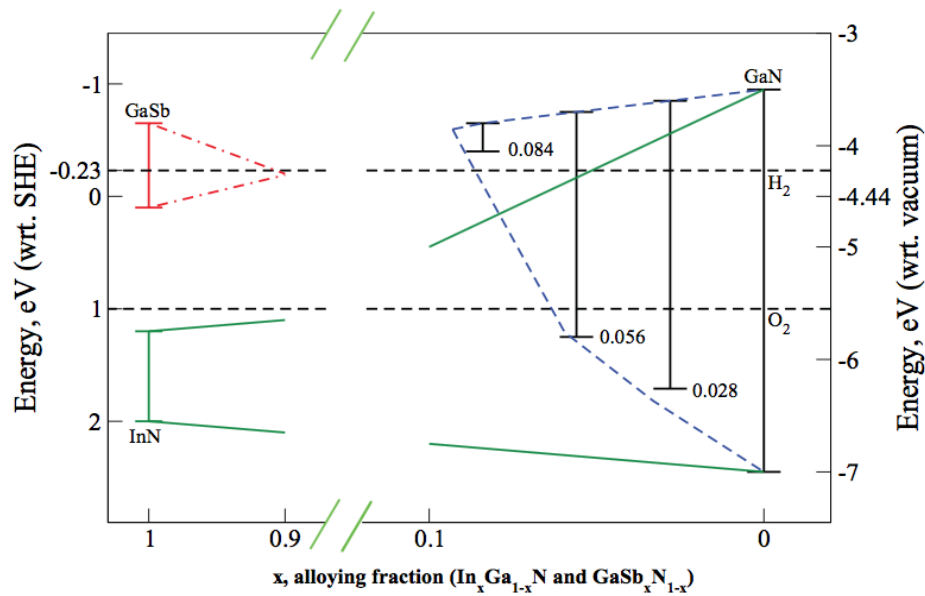


Figure 1.3 A diagram showing the comparison of band edge positions with respect to vacuum for $\text{GaSb}_x\text{N}_{1-x}$ and $\text{In}_x\text{Ga}_{1-x}\text{N}$ alloys

In the Figure 1.3, y-axis values are energy scales of SHE (standard hydrogen electrode) and vacuum scale. For $\text{In}_x\text{Ga}_{1-x}\text{N}$ alloys with 2.7 eV band gap, conduction band edge is positive of the H_2 potential which means it doesn't straddle $\text{H}_2/\text{H}_2\text{O}$ potential. Hence it is obvious that for 2 eV band gap the band edge will be too far from the H_2 potential making almost impossible for unassisted water splitting. X-axis is showing that alloying fraction in the dilute nitrogen (10%) and dilute antimony (10%) regions. For $\text{GaSb}_x\text{N}_{1-x}$ alloy, the vertical lines in the dilute antimony region indicate the band gaps of different alloy compositions. It can be observed that there is a huge shift in the valence band edge upward which is due to antimony incorporation while there is also small shift in the conduction band edge downward. Also in the band gap range of 1.7 eV to 2 eV the band edge positions of $\text{GaSb}_x\text{N}_{1-x}$ clearly straddle the water redox potentials. Antimony incorporation into nitrogen sites represents isovalent substitution and thus no charge

induced trap states are expected. Initial simulation results show that dilute antimonide $\text{Ga}(\text{Sb}_x)\text{N}_{1-x}$ alloys are promising materials for PEC water splitting applications.¹³ Hence, based on the preliminary theoretical predictions, antimony incorporation into GaN alloys is proposed as the way to create new III-V semiconductor alloys for visible light absorption toward solar hydrogen. However, antimony incorporation into GaN materials during growth has not been achieved to-date because of the differences with synthesis temperatures. Antimony species exhibit high vapor pressures and typical temperatures for GaSb growth is around 575 °C. However, GaN is typically grown at temperatures in excess of 950 °C. In addition to studying the use of traditional metal organic chemical vapor deposition, the use of liquid phase epitaxy and/or vapor-liquid-solid method involving catalyst metals is also proposed to obtain good quality $\text{GaSb}_x\text{N}_{1-x}$ alloy materials.

1.5 Objectives of the Study

The first step is to synthesize $\text{Ga}(\text{Sb}_x)\text{N}_{1-x}$ thin films and study the fundamental optical and photoelectrochemical properties of the material. In addition to synthesizing the right material, it is also equally important to grow good crystal quality films or 1-D nanostructures such as nanowires to improve light absorption and collect charge carriers efficiently. In this dissertation, we also proposed growth of $\text{Ga}(\text{Sb}_x)\text{N}_{1-x}$ nanowires and epitaxy films using VLS mechanism which allows for high antimony incorporation at high temperatures. Fundamental knowledge of the growth mechanisms of $\text{Ga}(\text{Sb}_x)\text{N}_{1-x}$ single crystalline nanowires and films will be obtained for realizing the full potential of this material towards solar hydrogen production. The overall objectives for this

dissertation include the following:

- Compare the electronic and optical properties of ternary alloys of GaN with dilute incorporation of antimony using density functional theory
- Investigate the synthesis of dilute $\text{Ga}(\text{Sb}_x)\text{N}_{1-x}$ ternary alloys using metalorganic chemical vapor deposition approach and establish optical and structural properties of $\text{Ga}(\text{Sb}_x)\text{N}_{1-x}$ alloys.
- Investigate vapor-liquid-solid growth method for increasing the antimony incorporation to produce $\text{Ga}(\text{Sb}_x)\text{N}_{1-x}$ alloys with a range of compositions.
- Improve the quality of synthesized materials through epi-growth and single crystal quality nanowire arrays for $\text{Ga}(\text{Sb}_x)\text{N}_{1-x}$ alloys.
- Investigate the charge transport, recombination and charge-transfer kinetics using n-type $\text{Ga}(\text{Sb}_x)\text{N}_{1-x}$ alloy nanowire arrays grown on GaN substrates.

1.6 Organization of Thesis

The thesis is divided into eight chapters. Chapter 1 introduces the basic PEC concepts, materials challenges associated with PEC water splitting. The objectives of the work, rationale for using $\text{Ga}(\text{Sb}_x)\text{N}_{1-x}$ and the impact of the work are also detailed. Chapter 2 reviews the state-of-the art materials for PEC water splitting testing and introduction to the $\text{Ga}(\text{Sb}_x)\text{N}_{1-x}$ system. Chapter 3 contains details of all experimental techniques used for synthesis, materials characterization and photoelectrochemical characterization. Chapter 4 describes theoretical and experimental studies on $\text{Ga}(\text{Sb}_x)\text{N}_{1-x}$ thin films and related photoactivity measurements. Chapter 5 talks about the Vapor-Liquid-Solid (VLS) growth of $\text{Ga}(\text{Sb}_x)\text{N}_{1-x}$ nanowires and the structural and fundamental

PEC characterization of the nanowires. Chapter 6 discusses the growth of highly textured Ga(Sb_x)N_{1-x} films growth and photoactivity measurements with these films. Chapter 7 summarizes the conclusions of this work and Chapter 8 lists the directions for future studies.

CHAPTER 2

BACKGROUND

2.1 Introduction

This chapter reviews the status of materials for photoelectrochemical water splitting. Specifically, different configurations used for photoelectrochemical cells for PEC water splitting and the performance of various materials systems such as metal oxides, sulfides and III-V alloys with water splitting reaction are summarized. In particular, the drawbacks of all of the materials systems studied to date are highlighted. Specific attention is given to III-V materials system and synthesis techniques used for making III-V semiconductor alloys.

2.2 Introduction to Semiconductor-Electrolyte Interface

The grand challenge in energy research is to develop a way to generate sustainable energy while simultaneously reducing carbon dioxide emissions. Among several technologies considered, the production of hydrogen by photo-electrochemical (PEC) water splitting seems to be one of the most promising techniques that can offer a route towards hydrogen production costs of \$3-\$5 per Kg which is competitive with existing energy sources.¹⁴ Direct two electrode setup where a semiconductor absorbs sunlight to generate electron hole pairs that are separated and then drive the water splitting reaction is the ideal setup to solve the problem. When semiconductor is not in contact with

electrolyte, bands of the semiconductor are flat. When the semiconductor comes in contact with the electrolyte, fermi levels of semiconductor and electrolyte try to equilibrate due to the difference in electrochemical potentials by transferring charges between them until an equilibrium is established and this results in bending of the bands. The band bending results in a built in electric field at the interface which is also called depletion layer or space charge layer. This depletion layer is mainly responsible for the separation of electron hole pairs. The schematic of the structure of semiconductor/electrolyte interface is shown in Figure 2.1

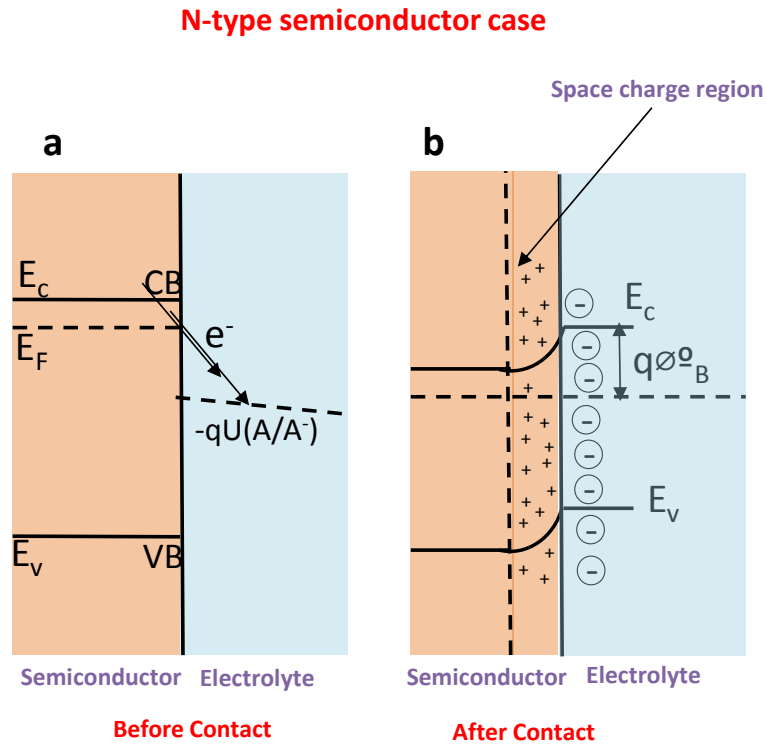


Figure 2.1 Schematics of models for semiconductor/liquid interface showing before and after contact of semiconductor with electrolyte.

In an n-type semiconductor, bands bend upwards as the fermi level moves downward

upon equilibration. This causes majority carriers which are electrons in n-type, to move into the electrolyte and minority carriers, which are holes, to move toward counter electrode. A similar process occurs in p-type semiconductors where the fermi level moves upward and bands bend downward. The band bending behavior of n-type and p-type materials is shown in Figure 2.2

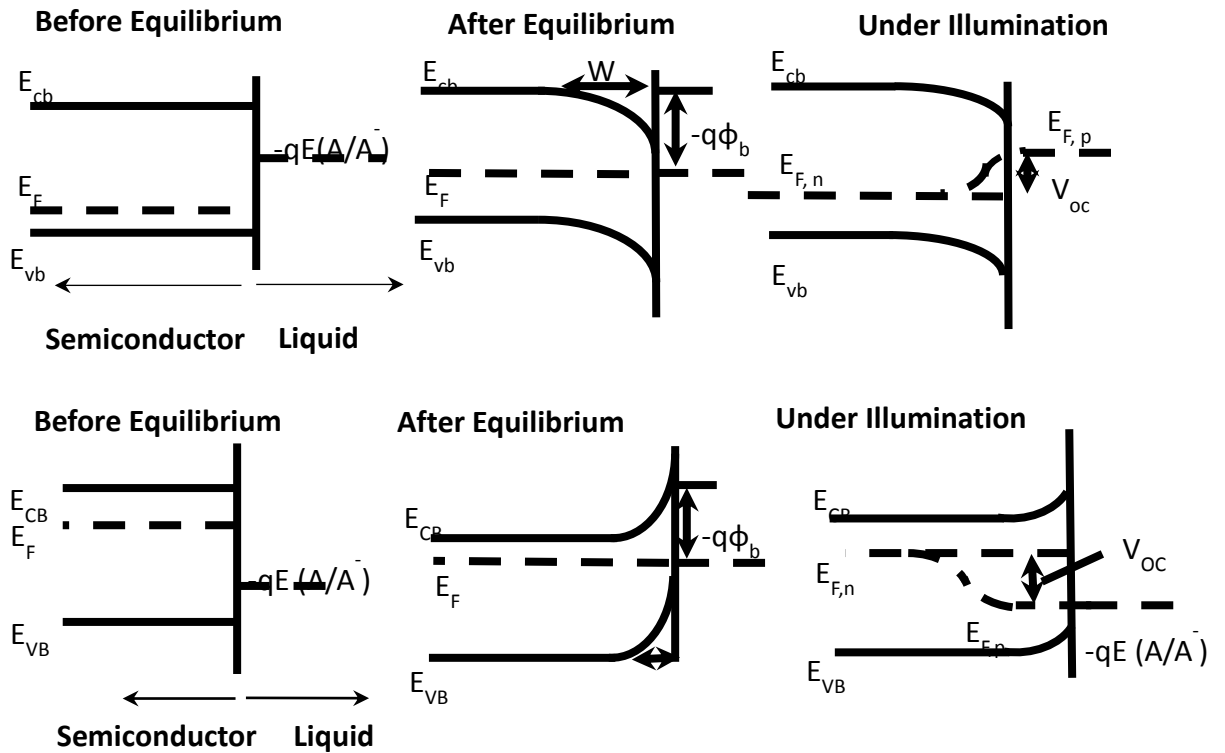


Figure 2.2 Schematics illustrating band bending behavior in n-type and p-type materials.

For n-type semiconductor, electrons reduce water at metal counter electrode (Equation 1.1) whereas photogenerated holes move toward the semiconductor/electrolyte interface where they undergo water oxidation (Equation 1.2). The two half reactions involved in the water splitting reaction mechanism are as follows.





The two reactions have to be driven simultaneously on separate electrodes to evolve hydrogen and oxygen depending on the conductivity type of the semiconductor. In order for efficient photoelectrochemical water splitting, semiconductor materials need to satisfy several criteria and this imposes severe materials challenge. Most of the materials being investigated fall short in one or the other criteria.

2.3 Review on different PEC configurations

PEC water splitting is performed using a photoelectrochemical cell that is comprised of electrodes immersed in water. The ultimate goal in solar hydrogen production using photoelectrochemical cell is to have unassisted water splitting. In order to achieve water splitting using various materials available, different cell configurations were researched. A photoelectrochemical cell consists of different schemes like (i) Schottky type device, (ii) Tandem cell and (iii) Z-scheme.⁹ Schottky type device contains a photoanode and metal counter electrode in which semiconductor is the main component that converts incident photons to electron hole pairs. One main challenge in using a single semiconductor to perform water splitting is the band edge mismatch with the hydrogen and oxygen evolution reactions which could require high overpotentials. So, a combination of two or more semiconductors may offer a solution. In such a device, one semiconductor acts as a regular photoanode or photocathode. The other semiconductors function as either as a complementary photoelectrode, or as an integrated photovoltaic device that provides a bias voltage. Figure 2.3 shows some examples of possible configurations. Configurations A and B use single photoanode and photocathode vs. metal counter electrode. Hematite (Fe_2O_3) and Strontium titanate (SrTiO_3) are widely

used photoanodes in this configuration and cuprous oxide (Cu_2O) and Silicon Carbide (SiC) were broadly tested photocathodes in this configuration.^{3, 15-17} Configurations C and D were the ones which reported high efficiency till date. In this configuration, bias voltage is applied through an integrated p-n junction.

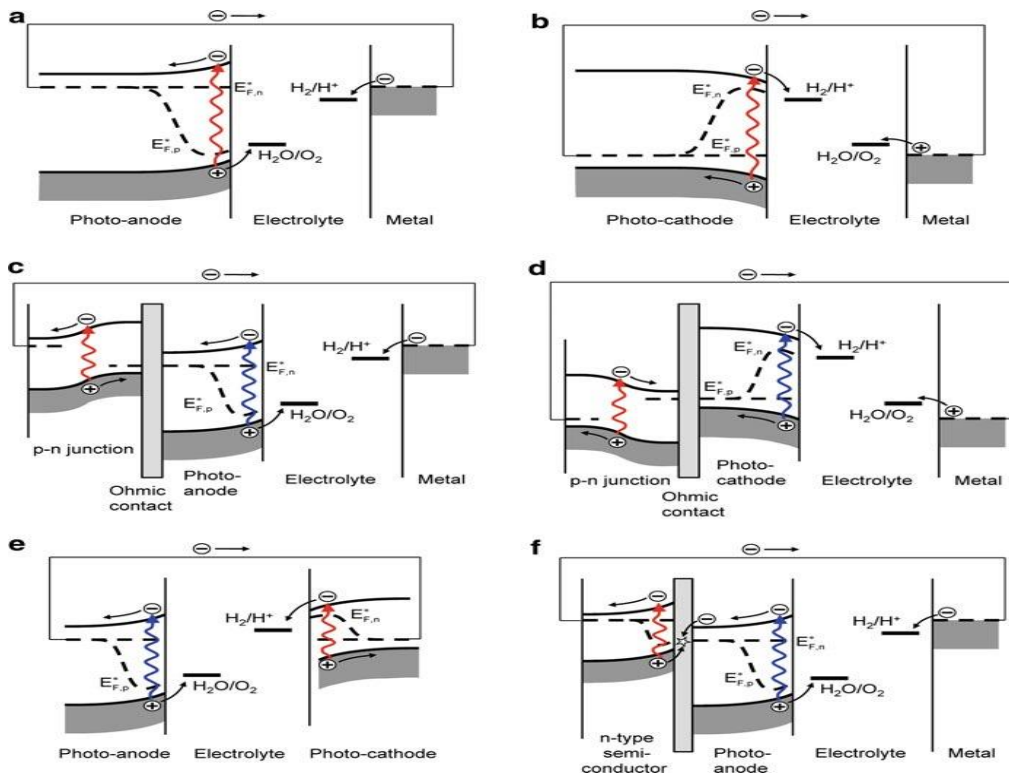


Figure 2.3 Schematics of different PEC configurations under illumination.³

Bias voltage was applied in different ways. For example, Turner et al developed a tandem device based on p-type GaInP_2 in combination with GaAs p-n junction that resulted in 12.4% solar to hydrogen efficiency which is the highest efficiency till date using PEC water splitting.⁷ Another approach with same configuration was developed by Gratzel et al where dye sensitized solar cell was used to bias a Fe_2O_3 photoanode which was similar to the above approach except that tandem junction was replaced by a dye sensitized solar

cell. In configurations (E) and (F), two absorbers are used where bias potential is generated by an additional absorber. Even though different configurations are available, single material device configuration is of most interest. Even with dual semiconductor configuration, there is a need for semiconductors with band gaps around 1.8 eV and 1.3 eV for efficient photoelectrochemical cell.¹⁸ Nevertheless, there is a need for semiconductors with band gaps ranging from 1.3 – 1.8 eV with band edges straddling either hydrogen or oxygen evolution reactions or both. The remainder of the chapter in this dissertation is focused on various materials systems and their performance in a single material device configuration.

2.4 State of the art on materials for PEC water splitting

As mentioned above, the requirements for suitable semiconductors are as follows: the semiconductor materials should have appropriate band gaps from 1.6 – 2.2 eV; band edges should straddle water splitting reactions; stable in aqueous environments; and made of earth abundant elements. Although, there are numerous materials available for PEC water splitting, none of these straddle both the water oxidation and reduction potentials. The binary oxides that have the band gap in the 1.7 – 2.2 eV range are CuO (1.7 eV), HgO (1.9 eV), CdO (2.2 eV) and Fe₂O₃ (2.2 eV). Out of the numerous materials, only a very few have the right band gap.¹⁹ The binary sulfides with band gap in the desired range¹⁹ are Sb₂S₃ (1.72 eV), ZnS₂ (1.82 eV), In₂S₃ (2 eV), SnS₂ (2.1 eV) and Ce₂S₃ (2.1 eV)

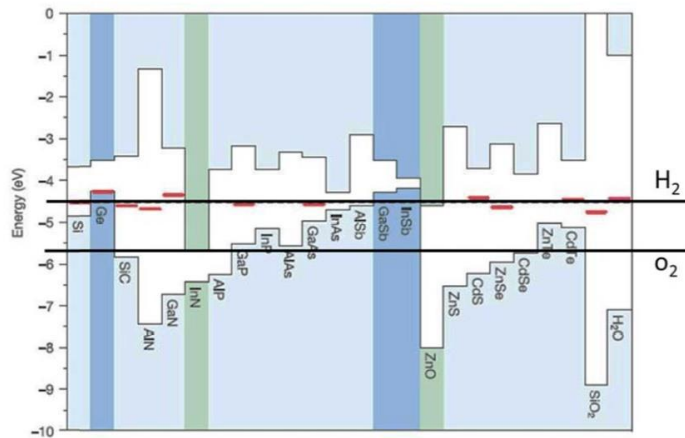


Figure 2.4 Band edge positions of several semiconductor materials w.r.t. water oxidation and reduction potentials. ¹²

It is evident that most of the materials do not straddle the potentials, and hence require additional bias when used for PEC water splitting. ¹²

Figures 2.5 and 2.6 show the valence and conduction band edge positions of the various oxides and sulfide materials w.r.t. the water redox potentials and it shows that only large band gap materials have band edges straddling the water redox potentials. Almost, all of the materials with the right band gap do not straddle the redox potentials

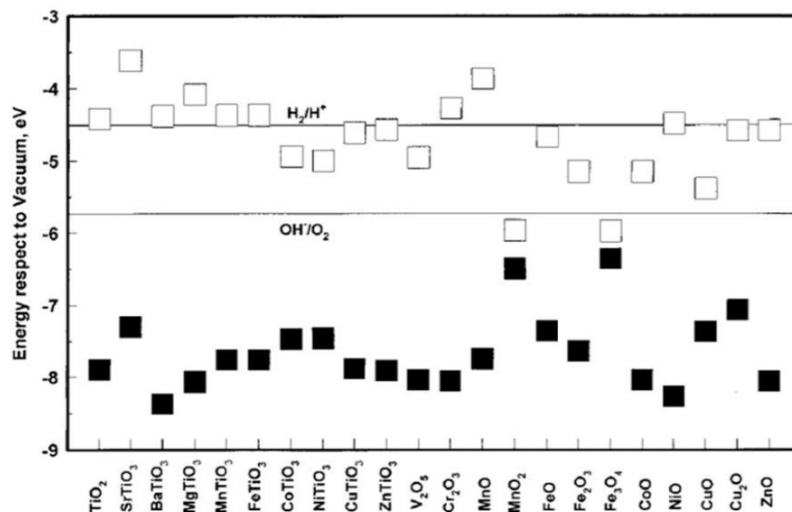


Figure 2.5 Valence band (dark squares) and conduction band (open squares) positions of oxide semiconductors w.r.t the water redox potentials at pH = 0 showing the lack of straddling by lower band gap materials and straddling by the large band gap materials.¹⁹

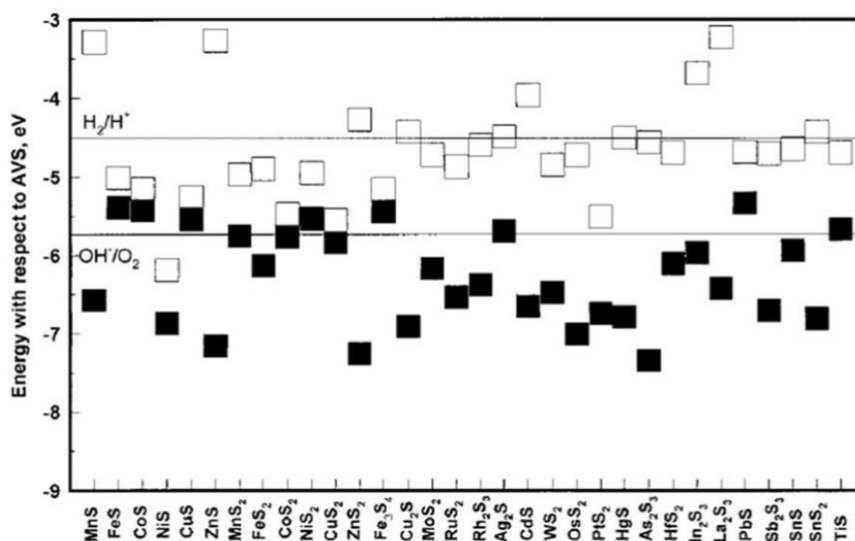


Figure 2.6 Valence band (dark squares) and conduction band (open squares) positions of sulfide semiconductors w.r.t the water redox potentials at pH 0.¹⁹

The lack of straddling by lower band gap materials and straddling by the large band gap materials is clearly evident.¹⁹

Figure 2.4 is a compilation of some of the semiconductors with their band edges matched to water splitting potentials. It is evident that most of them do not straddle the potentials. Also, none of the oxides with the right band gap barring Fe_2O_3 which straddles the redox potentials as shown in Figure 2.4. This is the case with the sulfides as well where the band edge straddling is the criterion that eliminates a lot of the materials.

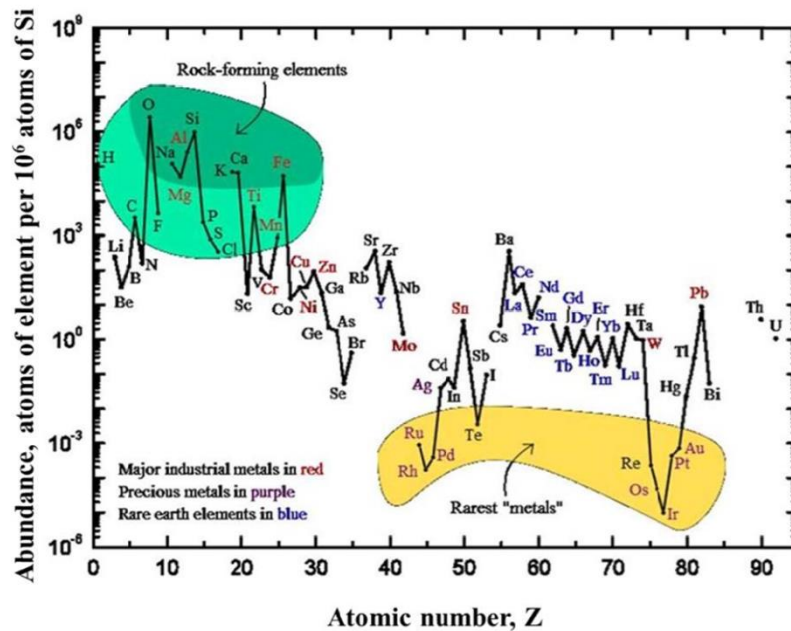


Figure 2.7 Relative abundance of elements in earth's crust per 10^6 atoms of silicon.²⁰

Figure 2.7 shows the relative abundance of the elements in earth's crust.²⁰ It is startling to note that most of the oxide and sulfide materials with the right band gap are not earth abundant. Hence, the challenge is to find ways to get the right properties with the materials that are reasonably abundant. The alternative solution to this issue is to find

ternary compositions that straddle the band edges or devise new PEC cell designs to circumvent the problem. While the search for ternary compositions is an ongoing research thrust driven mostly by combinatorial methods and computational guidance.²¹ Good performance has also been shown for water oxidation catalysts²² and photocatalytic water splitting is an interesting avenue.²³ The current bottleneck of the practical implementation of this technology is finding a semiconductor that will satisfy the major criteria needed to efficiently split water using solar radiation. A wide range of materials ranging from metal oxides, metal sulfides, III-V compound semiconductors and metal nitrides have been extensively investigated for their suitability towards solar water splitting. Binary materials have little promise but researchers have tried interesting approaches to forward the process. Ternary materials are interesting due to the possibility of band gap tuning with composition.

2.4.1 Metal oxides

The first report on the electrolysis of water into oxygen and hydrogen using a photoelectrochemical cell by Fujishima and Honda²⁴ used TiO₂ as the semiconductor. This work has prompted the research on several metal oxides for photoelectrochemical water splitting. The high stability of many of the metal oxide in water, especially for water oxidation motivated the investigation of different metal oxides. Among the several metal oxides that have been investigated, Hematite (Fe₂O₃),^{25, 26} Tungsten oxide (WO₃),²⁷ Cuprous oxide (Cu₂O),²⁸⁻³⁰ Bismuth vanadate (BiVO₄)^{25, 31} have been widely investigated as promising materials for PEC water splitting. Despite having very good capability for the application of solar water splitting, metal oxides endure few challenges such as poor light absorption, mismatch in band edge energetics, poor charge transport, all of which

need to be overcome. Most of the metal oxides have poor light absorption in the visible region of the solar spectrum due to their wide band gap. Approaches to address the above challenges with metal oxides have looked at (i) doping foreign elements to improve light absorption as in the case of WO_3 ³² (ii) using multijunction devices that provide external bias to overcome the limitation of band edges not straddling the water redox potentials. For example, hematite ($\alpha\text{-Fe}_2\text{O}_3$) has the desired 2 eV band gap and excellent chemical stability in broad pH range. However, the conduction band of hematite is 0.2-0.4eV positive to the hydrogen evolution reaction. John Turner and E. L. Miller groups attempted to overcome this problem by enabling a multijunction device that combines thin film solid state and PEC junctions which provide required voltage, current and stability³³⁻³⁵ (iii) doping to improve the diffusion lengths and photocurrent onsets as in case of hematite and employing graded architecture for bismuth vanadate to improve electron transport³⁶ (iv) using protective coatings to improve stability as in the case of copper oxide.²⁸ Strontium titanate, SrTiO_3 , is one of very few materials that have been observed to split water in this configuration.¹⁵ However, the efficiency is less than 1% due to its large band gap (3.2 eV).

2.4.2 Metal chalcogenides

Metal chalcogenides also have been in focus for PEC water splitting for several years. The mostly elaborated materials in this section are molybdenum sulfide (MoS_2), cadmium sulfide (CS_2), cadmium selenide, Zinc sulfide, molybdenum sulfide. Many of the metal chalcogenides have a low band gap and hence cannot generate sufficient built-in voltage to drive the water splitting reactions. The aqueous stability of these metal

chalcogenides is another challenge. Attempts to improve the stability of these materials have focused on modifying the semiconductor surface with electrocatalysts.^{37,38}

2.4.3 III-V semiconductor alloys

III-V semiconductor materials are gaining interest mainly due to their direct transition optical band gaps, high thermal stability, ability to grow high quality epitaxial films with low defects, high carrier concentrations and mobilities. Another important property they possess is the ability to form alloys whose band gap can be tuned with composition. The above mentioned properties make these III-V alloys highly studied materials for solar water splitting. III-V materials have set records of 12.4% PEC efficiency and 43.5% PV efficiency to date. However, these materials have technical challenges such as stability, band edge mismatch and not being cost effective that need to be addressed. The main challenges with many of III-V alloys reported in literature were their stability, band edge locations not straddling the water redox potentials and short diffusion lengths.

Binary Compounds: Some of the popular binary III-V compounds that were tested for PEC water splitting were Gallium Nitride (GaN), Gallium phosphide (GaP), Gallium Arsenide (GaAs). The main issue with most of the binary alloys is their band gap which is either too small or too wide. S.H. Kim et al. tested GaN as photoanode using NiO as cocatalyst and reported photocurrent densities of $3\text{mA}/\text{cm}^2$ which were relatively higher when compared with GaN without catalyst but the problem with GaN is band gap is 3.4 eV which cannot absorb enough light in visible region. Lee et al. reported high photocurrent densities of $34\text{mA}/\text{cm}^2$ using Indium Phosphide (InP) nanopillars as

photocathode with Ru as co-catalyst and stability has been improved by passivating layers with TiO. The issue with InP is high band edge mismatch which needs huge applied bias for efficient solar hydrogen generation. Out of available III-V binary alloys GaP and GaAs have band gaps required for PEC water splitting but they lack corrosion stability in aqueous solutions. To overcome this issue Lewis et al. deposited an amorphous titania layers of around 4-143 nm thick which exhibited huge improvement in the stability of both materials.³⁹ However the band edges of these two materials does not straddle water redox potentials. Some other binary alloys that were tested for PEC water splitting are reported elsewhere.⁴⁰ From all the reports, it was observed that even though some binary alloys showed decent photocurrent densities they undergo problems like unsuitable band gap, band edge mismatch and chemical stability. However, as we discussed earlier the advantage of III-V alloys is the ability to tune the properties by alloying with foreign elements which shows ternary alloys potential for solar water splitting. Some attempts have been made to address the above discussed challenges.

Methods to improve durability: Many III-V materials undergo photocorrosion due to the oxidation of semiconductor and usually there is a loss of photoactivity with time. For example, tandem GaInP₂ is the champion material which gave 12.4% PEC efficiency but after a few hours of operation it loses its photoactivity from 120 mA/cm² to 105 mA/cm² which makes loss in efficiency from 12.4% to 10.8%. To overcome this problem, Turner's group tried two approaches: (i) incorporating nitrogen into GaP and (ii) incorporating nitrogen into GaInP₂.⁷ The first approach reduced the corrosion to some extent but reduced the photoconversion efficiency whereas the second approach improved the stability of GaInP₂ without any loss in photocurrents. To date this is the

only material which has produced efficiency near to the benchmark efficiency (20%) set by DOE. However, this material needs to be of single crystalline quality material, utilizes expensive molecular beam epitaxy (MBE) technique and also the tandem cell approach. Recent interest has been turned to GaN alloys as GaN is a direct band gap semiconductor with the right band edge energetics and shows high stability under visible photolysis.⁴¹ The main problem with it is, however, its wide band gap of 3.45 eV,⁴² which restricts most of the solar spectrum from being absorbed. One way to overcome this obstacle is the band gap engineering by means of producing GaN-based ternary or quaternary compounds which possess a composition dependent band gap. Lewis group proposed the use of defective titania layers grown by atomic layer deposition as a way to protect photoelectrodes such as silicon and other III-V materials.³⁹

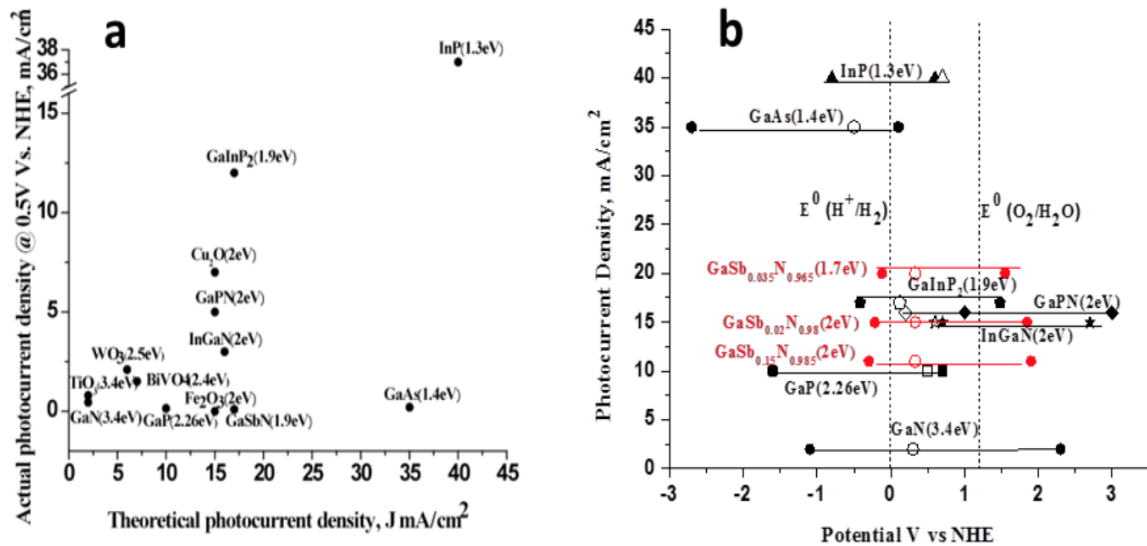


Figure 2.8 (a) Experimentally obtained photocurrent density with 0.5 V applied bias vs. theoretical maximum current density for III-V materials and commonly investigated metal oxides (b) band edge positions vs. maximum theoretical photocurrent density for

III-V materials. The photocurrent onset potentials are indicated in open symbols. The data is obtained from Refs^{24, 25, 32-37, 41-49}

Figure 2.8 shows the status of some of the best performing materials for PEC water splitting. In 2.3 a) experimental photocurrent densities vs. theoretical photocurrent densities of some materials were plotted. Experimental photocurrent densities values @ 0.5 V vs NHE of some of the so far best performing materials were taken from the literature. From this plot it can be inferred that no material exhibited photocurrent densities as predicted by theory except InP and GaInP₂. But GaInP₂ needs a tandem cell with GaAs which is very expensive and also band edges of GaInP₂ and InP does not straddle water redox potentials which is shown in plot b). Moreover, from plot a) we can learn that III-V materials have room for improvement in experimental as well as theoretical efficiencies due to their ability to tune the band gap whereas metal oxides are limited by their theoretical efficiencies itself. Therefore, there is huge parametric space for improvement for III-V alloys in terms of exhibiting high efficiencies. As discussed before, GaN has all the required properties for water splitting except the right band gap and attempts have been made to reduce the band gap of GaN to visible region and these are discussed in the next section. Plot b) is the compilation of values of band edges and onset potentials for few III-V binary and ternary alloys. In the plot, closed pointers are band edge values and open pointers are onset potentials and it clearly indicates except GaSb_xN_{1-x} no material is straddling the HER and OER reactions indicating the potential of GaSb_xN_{1-x} in unassisted water splitting.

Band gap engineering with GaN alloys: Recently a solid solution of ZnO and GaN, (Ga_{1-x}Zn_x)(N_{1-x}O_x) with 0.05 < x < 0.22, has been shown to be a promising photocatalyst

for direct water splitting under visible light illumination.⁵⁰ However, in the case of $(\text{Ga}_{1-x}\text{Zn}_x)(\text{N}_{1-x}\text{O}_x)$ solid solution, the band gap reduction is relatively small, mainly due to close similarities of lattice parameters and band gaps between GaN and ZnO and thereby limits PEC efficiency of this material.⁴⁹ $\text{In}_x\text{Ga}_{1-x}\text{N}$ ternary alloys offer much more flexibility and have been widely studied.⁵¹⁻⁵³ However, for the desired band gap reduction and efficient direct solar water splitting, high In incorporation of about 40-50 % is required, which can lead to In phase segregation and the material degradation. In a prior work, it was shown that thick epilayers of $\text{In}_x\text{Ga}_{1-x}\text{N}$ with high indium contents can be synthesized using GaN as strain relaxing substrates.⁴³ The band edges of the $\text{In}_x\text{Ga}_{1-x}\text{N}$ alloys do not straddle both water oxidation and reduction potential at $\sim 2\text{eV}$ band gap required for water splitting. Deutsch and co-workers synthesized epilayers of GaAsPN and GaPN and found that the band edges are too negative to efficiently drive the water splitting reaction without applying a considerable external bias.⁵⁴ Also recently there were reports studying band gap reduction in GaN by incorporating Arsenic (As)⁵⁵ and bismuth (Bi)⁵⁶ The problem with $\text{GaAs}_x\text{N}_{1-x}$ is that with very small amounts of As that is as low as 0-0.8%, the band gap has been reduced to less than 1 eV which is too low for water splitting whereas in $\text{GaBi}_x\text{N}_{1-x}$ the band gap has been reduced from 3.4 eV to 2.6 eV with very small amounts of bismuth composition ($\sim 0.01\%$). However, there were no reports testing the material for PEC water splitting. While $\text{In}_x\text{Ga}_{1-x}\text{N}$ and other GaN based alloys attracted a lot of research, very little attention has been given to nitride antimonides, such as $\text{GaN}_{1-x}\text{Sb}_x$. There are only a very few experimental reports on such materials in the low nitrogen composition range.^{57, 58} They indicate that for even a very small x value, the material shows electronic band gap bowing that has been extended to

negative band gaps for composition in excess of about 8% N.⁵⁹ First principle computations confirmed a drastic band gap reduction in these materials for low nitrogen compositions.¹³ In addition, these calculations provided evidence for an anomalous decrease in the band gap of GaN_{1-x}Sb_x alloys in the low antimony composition range, where even less attention has been paid. Most importantly, the band edges of the Ga(Sb_x)N_{1-x} alloys straddle the water oxidation and reduction potentials at the optimal 2 eV band gap as predicted by DFT calculations. Also, Figure 2.3 b) shows the plot of band edge positions vs applied potential for few III-V materials. It can be clearly observed that out of all materials GaSb_xN_{1-x} is the only material that has right band edges that can straddle water redox potentials with band gap in visible region. This shows that Ga(Sb_x)N_{1-x} material has huge potential towards efficient unassisted water splitting.

2.4.4 Nanowire Architectures

An ideal architecture for water splitting should allow for both sufficient light absorption and efficient transport of charge carriers. Single crystal films have higher absorption depths leading to thicker films to absorb incident light and hence, charge carriers have to move longer distances before they can drive the water splitting reactions. Diffusion length is the distance of the carrier to travel before recombining. If the carrier needs to travel a distance larger than diffusion length, it tends to recombine before reaching the semiconductor-electrolyte interface or counter electrode. The most recognized advantage of nanowires is their higher surface area which enables sufficient light absorption and shorter charge transport pathways resulting in faster charge transfer kinetics at the semiconductor/electrolyte. Nanowires have lengths ideal for light absorption and smaller diameters allow the carriers to reach the interface and counter

electrode to drive the HER and OER reactions efficiently.⁶⁰ Another advantage of nanowires over single crystal films is the ease of synthesis. Synthesis of single crystal films is very difficult due to several reasons. The first reason is the lattice mismatch with the substrate as for most of the semiconductor materials availability of the lattice matched substrates is quite low. Another reason is that films need to be made very thick due to the need for high absorption depth which is usually in microns. The main problem with growing thick films in most of the materials is phase segregation or formation of dislocations. Hence, nanowire based device architectures offer significant advantages over thin films for efficient PEC water splitting. Improvement in the photoactivity by employing nanowires has been reported with many materials. For example, tungsten oxide (WO_3) films exhibited low photocurrents of 0.2 mA/cm^2 .⁶¹ But by employing nanowires of same material (WO_3), Sunkara and coworkers reported photocurrent densities of 1.6 mA/cm^2 .⁶² PEC water oxidation with hematite (Fe_2O_3) was reported by several studies⁶³⁻⁶⁵ but all these reports showed low photocurrents from this material and the underlying reasons were reported as combination of poor absorption depth, charge carrier mobility and short exciton lifetime.⁶⁶ And improvement in charge transport, light absorption and charge separation has been observed by using nanorod arrays.⁶⁷ Similar observations have been observed with our prior work with cuprous oxide where using cuprous oxide nanowires were shown to perform better compared to thin films.³⁰ The work is presented in the appendix of this thesis. Also depositing tungsten oxide on cuprous oxide nanowires led to high phase purity thereby increasing photocurrents.²⁹ Similar observations have been reported on other materials which are reviewed elsewhere.⁶⁶ However, the efficiency and the applicability of materials vary drastically

with the system employed. There has been a good amount of work done on the alternate configurations but the current work is primarily geared towards development of materials for direct single band gap cell.

1-D crystal growth was first developed for Si about 50 years ago in 1964 by Wagner and Lewis using a mechanism called vapor-liquid-solid (VLS).⁶⁸ Vapor liquid solid (VLS) mechanism) results in rods, wires and whiskers through crystal growth in 1-D and is the most common method employed for growth of nanowires. In this mechanism, a metal catalyst is employed that absorbs vapor components and forms liquid alloy droplets at a higher temperature. This mechanism involves supersaturation of the metal alloy solution, in which the actual concentration of the component is higher than the equilibrium concentration thereby precipitating as 1D crystal growth by achieving minimum free energy of the alloy system.⁶⁹ The growth continues until the vapor species are being supplied. So from the mechanism it shows that it involves vapor phase to carry solid components, liquid phase as catalyst alloy and solid as precipitated 1-D structures which is why it is called Vapor Liquid Solid (VLS) mechanism. As the 1-D structure precipitates from the catalyst alloy, the diameter of the 1-D structures depends on the size of the catalyst. In 1970's the mechanism was widely used for the growth of whiskers and SiC whiskers were the mostly studied ones due to their high strength, high toughness ceramic or metal composites. From the study, it was found that the diameter of the whiskers was highly dependent on size of the catalyst.⁷⁰ There was a tremendous focus on this mechanism especially for the growth of semiconductor nanowires. Regarding this, Wu et al reported the growth of Ge nanowires by using an in situ high-temperature transmission electron microscope.⁷¹ The findings of Wu's study showed that there are

three well-defined stages in the VLS mechanism: alloying, precipitation of Ge, and axial growth.

Solution-Liquid-Solid (SLS)^{72, 73} and Supercritical-Fluid-Liquid-Solid (SFLS)^{74, 75} techniques are similar to VLS for the growth of single crystalline 1-D nanostructures. The only difference is those methods is they use liquid to transport the precursor materials whereas VLS uses vapor phase. Also, techniques using anodic aluminum oxide⁷⁶ or block copolymers⁷⁷ as template materials have also been used to produce nanowire and nanorod structures. In this class of techniques, high aspect ratio nanopores in the template material are filled with a metal or semiconductor creating nanowires.

2.4.5 Review on MOCVD of III-V alloys

Several routes have been studied for the thin film growth of III-V alloys. These are divided into three main categories that are a) Molecular beam epitaxy (MBE) b) Liquid phase epitaxy and c) Vapor phase epitaxy. MBE growth uses molecular atomic beams as a source material for controlled supply of material flux which requires ultrahigh vacuum during growth. Due to the very small growth rates in this method the deposited film is of single crystal quality. However, this technique is usually very expensive due to the MBE instrumentation and low growth rates. Liquid phase epitaxy (LPE) utilizes heated liquid metal solutions as precursors for the deposition. Growth is achieved by cooling the liquid solution to a supersaturation point and bringing the substrate in contact with the liquid melt which will result in thin film growth. The advantage of using LPE is high growth rates and low growth temperatures but the drawback of this method is the difficulty in control of liquid melt which majorly influence the epitaxial growth. The last one is the

vapor phase technique which utilizes vapors of metal compounds that needs to be deposited. Metal organic chemical vapor deposition (MOCVD) is one particular technique in this category. MOCVD uses metal organic precursors that are supplied in vapor phase. This allows for a good control on the material flux which plays a huge role in thin film growth. Growth rates in MOCVD are high when compared to MBE. This method allows for a large area growth which makes this method very scalable and the only problem with MOCVD is that precursors are pyrophoric which requires high safety measures and carbon contamination from the precursors. However out of all the available techniques MOCVD received the most attention due to its precise control on material flux, uniformity and scalability. Several binary and ternary III-V alloys have been synthesized by MOCVD. Metal organic chemical vapor deposition was first demonstrated by Robert Bunsen⁷⁸ and since then MOCVD became a crucial technique for the applications of transistors, LED's, laser diodes etc. The first epitaxial growth by MOCVD was reported in 1967 on GaAs using trimethyl gallium and AsH₃ as precursors.⁷⁹ In this study we are only interested in growth of GaN based alloys by MOCVD. Nakumara and coworkers reported epitaxial GaN growth by using two flow atmospheric pressure MOCVD reactor and until today the high quality films required for devices have been produced using two flow reactors.⁸⁰ Trimethyl gallium and ammonia were the commonly used precursors for the growth of GaN. It was found that growth of GaN occurs by two pathways that are pyrolysis and adduct pathways. In pyrolysis pathway, trimethyl gallium decomposes to dimethyl gallium (DMG) which in turn decomposes to monomethyl gallium (MMG) and ammonia decomposes to NH₂, NH and lastly N. These decomposed species adsorb onto the substrate and reacts on the surface

leading to the GaN film growth.⁸¹ In adduct pathway TMG reacts with ammonia and forms intermediate species which take part in the final film growth. These pathways strongly depend on growth temperature, reactor configuration and III/V ratio.⁸² In the device applications uniformity of the films is very important and in order to achieve uniformity, shower head reactors^{83, 84} and rotation of the substrate⁸⁵ were employed. Some of the widely explored ternary GaN alloys grown using MOCVD are AlGa_N,⁸⁶⁻⁸⁸ InGa_N^{89, 90} and GaAs_N.⁹¹ The main concern with growing ternary alloys by MOCVD was the selection of the substrate with lattice matching and low cracking efficiency of ammonia which require high pressures of ammonia for good crystal quality growth of GaN alloys. Also it has been observed that III/V ratio and growth temperature plays a huge role in achieving a high quality growth of films. For example in the case of InGa_N, incorporation of In was observed to be strongly dependent on growth temperature and growth rates.⁹² In the case of AlGa_N, Al incorporation and film quality was strongly dependent on III/V ratio. From the study it was observed that at high ammonia / trimethyl aluminum flow rates growth rates were low due to the parasitic reactions between metal organic precursors and ammonia.⁹³ Also it was observed from some studies that carrier gas effects the crystal quality of the film. In the case of InGa_N it was shown that using hydrogen as a carrier gas has better In incorporation and film quality for InGa_N when compared to using nitrogen as carrier gas.^{94, 95} The above reports indicate that the quality of the growth of GaN alloys strongly depends on growth temperature, III/V ratio and carrier gas. Some of the ternary and quaternary alloys synthesized by MOCVD have been reviewed elsewhere.⁹⁶

2.5 Prior work on $\text{GaSb}_x\text{N}_{1-x}$

2.5.1 Theoretical Predictions

Electronic structure analysis has been performed on both $\text{Ga}(\text{Sb}_x)\text{N}_{1-x}$ and $\text{Ga}(\text{N}_x)\text{Sb}_{1-x}$ structures. Due to the difference in electronegativity between Sb and N, local distortions appear due to structural optimizations. From the theoretical observations large band gap bowing was seen with incorporation of antimony in GaN. With increase in the Sb concentration band gap has been observed to decrease in $\text{GaSb}_x\text{N}_{1-x}$. Figure 2.9 shows the electronic band gap as a function of the fraction, x , for $\text{Ga}(\text{Sb}_x)\text{N}_{1-x}$ and $\text{Ga}(\text{N}_x)\text{Sb}_{1-x}$ alloys. In all $\text{Ga}(\text{Sb}_x)\text{N}_{1-x}$ cases considered, the gaps are direct. The figure also lists the experimental band gaps of $\text{Ga}(\text{N}_x)\text{Sb}_{1-x}$ for $x = 0.015^{97}$ and $x = 0.017^{97}$ for comparison. In the case of the $\text{Ga}(\text{Sb}_x)\text{N}_{1-x}$ alloy the rapid closing of the gap for $x > 0.06$ is worth noting. The band-gap value of 2 eV found for $0.05 < x < 0.06$ is ideal for PEC water splitting. Another interesting observation from the DFT calculations was monotonic increase in the lattice parameters with an increase in Sb composition in $\text{GaSb}_x\text{N}_{1-x}$ whereas there was a monotonic decrease in the lattice parameters with an increase in the N incorporation.

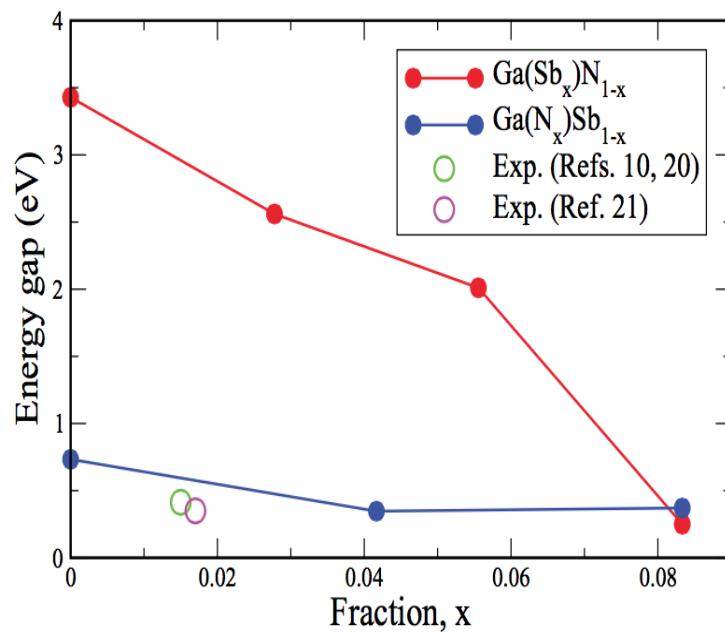


Figure 2.9 Electronic band gap as a function of x in $\text{GaSb}_x\text{N}_{1-x}$ and $\text{GaN}_x\text{Sb}_{1-x}$ materials.¹³

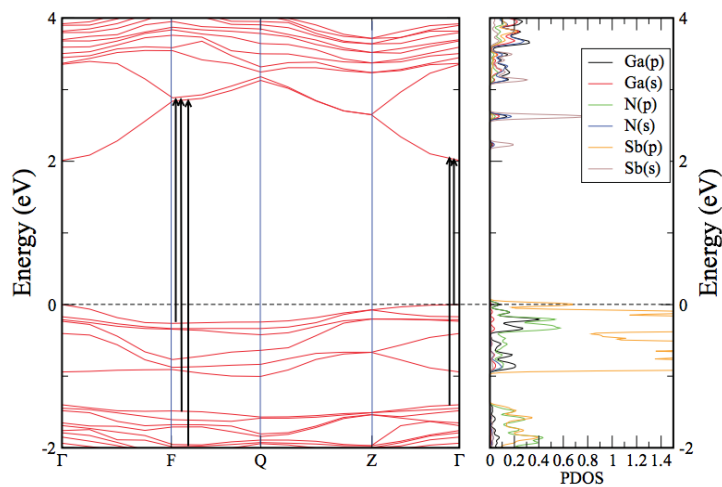


Figure 2.10 Band structure, density of states and optical transitions for $\text{GaSb}_x\text{N}_{1-x}$ alloys.¹³

As $\text{Ga}(\text{Sb}_x)\text{N}_{1-x}$ possess the essential 2eV band gap for PEC water splitting, and straddles the water redox potentials. On the other hand, $\text{GaN}_x\text{Sb}_{1-x}$, which does not have the right band, edge energetics. Hence $\text{Ga}(\text{Sb}_x)\text{N}_{1-x}$ is more suitable for solar water splitting than $\text{Ga}(\text{Sb}_x)\text{N}_{1-x}$.

2.5.2 Band gap bowing in $\text{GaSb}_x\text{N}_{1-x}$

The large band gap bowing with very little amount of incorporation is a very important feature which is why is very essential to understand the reason behind the band gap reduction. A number of models have been proposed to explain the band-gap reduction in these materials. Band anticrossing model (BAC) has been the popular model until today to explain the band gap reduction. The BAC model takes into account an anticrossing interaction between localized states of the substitutional isovalent anion atoms and the extended states of the host III-V semiconductor matrix. Depending on whether the impurity level is coupled to the host conduction band or to the host valence band, the BAC model will be referred to as a conduction-BAC (CBAC) or a valence-BAC (VBAC) model, respectively. In particular, the VBAC model has been used to explain band-gap reduction in a number of HMA's. This model was developed by Berkeley national lab where they explain the band gap reduction by alloying with foreign element.⁹⁸ They developed this model for GaBiAs and from their observations when large metallic isovalent impurity is substituted into lattice of a semiconductor, it introduces a localized defect state and when this impurity atom has low electronegativity and ionization energy than host material it forms a defect state near valence band of the host semiconductor.

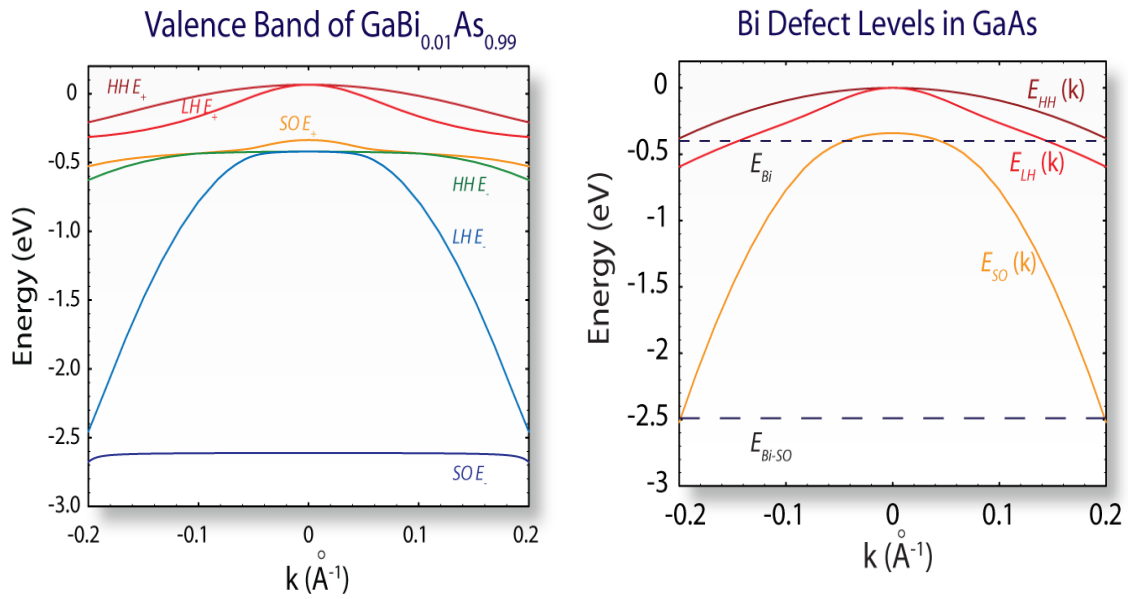


Figure 2.11 A schematic illustration for the VBAC model involving valence band splitting for Bi incorporation in GaAs.^{98, 99}

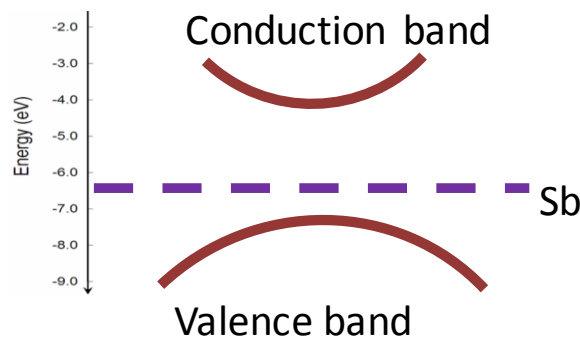


Figure 2.12 A schematic illustration for formation of a defect state in GaN with antimony incorporation.

The strong interaction between the host valence band states and impurity atom defect states which in their case Bi splits the VB into E+ and E- sub bands which cause an upward shift in the valence band with increase in Bi concentration thereby reducing the

band gap of GaBiAs as shown in Figure 2.11. Similarly, in our case by applying this model, we can explain that as ionization energy of Sb is near or below the valence band maximum of GaN it forms a defect state near VB of GaN as shown in Figure 2.12 and as explained by the model above the anticrossing interaction results in band splitting and shift of VB upwards reducing the energy gap. The strong anticrossing interaction between these bands and antimony defect state results in rapid upward shift of VB and CB shift to downward at a slower pace. The non-linear movement in energy of these band edges is the primary cause for band gap bowing in $\text{Ga}(\text{Sb}_x)\text{N}_{1-x}$. In Figure 2.9 the electronic band structure and density of states for the geometry for $0.05 < x < 0.06$ is shown. From the figure, it is clearly evident that band gap reduction in $\text{Ga}(\text{Sb}_x)\text{N}_{1-x}$ is occurring mainly due to valence band splitting. The band gap of 2 eV obtained for very small amounts of antimony incorporation opens up the exciting possibility of efficient visible absorption for $\text{Ga}(\text{Sb}_x)\text{N}_{1-x}$ alloys. Further investigation by way of rigorous simulations supported by experimental data is needed to explore and understand this material system. The $\text{Ga}(\text{Sb}_x)\text{N}_{1-x}$ system could also be an alternative to the $(\text{ZnO})_{1-x}(\text{GaN})_x$ solution, which has shown some promise for overall water splitting since the latter could suffer from charge imbalance resulting from non isovalent substitutions of Ga with Zn and N with O.⁴⁹ In particular, if the N atom is in a position far away from the Ga atom in the ZnO matrix, local defect centers would be created, resulting in charge recombination centers which could adversely affect the efficiency of PEC water splitting.

2.5.3 Prior experimental work on GaSb_xN_{1-x} alloy growth

As discussed in the earlier section, most of the reports show growth of GaN_xSb_{1-x} alloys in the low nitrogen composition region. Veal et al. reported the growth of GaN_xSb_{1-x} alloys using MBE and show a huge band gap reduction with little amount of nitrogen.⁵⁸ They explain the band gap reduction based on the BAC model where they say that band gap reduction in GaSb alloys with nitrogen incorporation is higher compared to other III-V alloys due to the large anion mismatch between antimony and nitrogen compared to other elements. Belabbes et al. also reported a huge band gap bowing in GaN_xSb_{1-x} with less than 0.2% nitrogen incorporation.⁵⁹ Also, there are several other reports on band gap bowing in GaN with nitrogen incorporation. However, there are very few or no reports on incorporation of antimony in GaN alloys. Yu et al. attempted to synthesize the amorphous GaSb_xN_{1-x} films using a low temperature molecular beam epitaxy.¹⁰⁰ A continuous reduction of band gap in the 0 to 1% Sb composition was reported. This is in disagreement with both the theoretical calculations and the photoluminescence results shown for 1 % Sb presented in this work. In addition, the band gap transition is shown to be direct for Sb compositions ranging from 0 to 30 %. The XRD patterns did not show any peak shift with increasing antimonide (Sb) concentration indicating no monotonic increase in lattice expansion. Hence, it is not clear about the validity of the type of material created. It is absolutely sure that a GaSb_xN_{1-x} alloy had not been synthesized. The films reported in their work were of highly amorphous nature and the attempts to increase the crystallinity by annealing has resulted in phase segregation. This shows that their attempt in growing GaSb_xN_{1-x} alloys was not successful. Hence, the work presented in this dissertation is the first successful report on growth of GaN alloys

in the low antimonide region. Further, a huge band gap bowing in GaN with antimony incorporation is observed and this further corroborates the theoretical predictions.

CHAPTER 3

EXPERIMENTAL

3.1 Introduction

This chapter describes the details on synthesis and characterization methods used for $\text{GaSb}_x\text{N}_{1-x}$ ternary alloy. Metal organic chemical vapor deposition was used as the synthesis method for growth of $\text{GaSb}_x\text{N}_{1-x}$ and several materials, optical, electrical and photoelectrochemical characterization techniques were performed to understand the properties of the material.

3.2 Synthesis

3.2.1 Metal Organic Chemical Vapor Deposition

Synthesis experiments were performed using a custom-built metal organic chemical vapor deposition (MOCVD) reactor. There are two major parts for the MOCVD reactor: one is a precursor delivery system and another one is the reaction chamber that includes a substrate heater and showerhead.

Precursor delivery system: The precursor delivery system is equipped to deliver four different precursors using nitrogen as a carrier gas. The carrier gas which is used to transport these precursors to the reaction chamber is delivered independently to the inlet of all the precursor cylinders via mass flow controllers. Upstream of the bubbler, a bypass line is available on which can be used for purging the lines using nitrogen. Downstream

to the bubbler outlet, a control valve is configured which allows for the precise composition control by controlling the pressure which is measured by capacitance manometer attached near control valve. The metal organic precursors that are available in the system are Trimethyl Gallium (TMGa), Trimethyl Indium (TMIn), Trimethyl antimony (TMSb) and Biscyclopentadienyl Magnesium. Each precursor has a temperature dependent vapor pressure that can be set to the desired point using thermal baths. These bubblers are inserted into these chillers to maintain at a certain temperature in order to have the desired vapor pressures that in turn can be controlled to achieve the desired flux. The vapor pressure of each precursor can be calculated using following equations

$$\text{TMGa} = \text{Log}_{10}P \text{ (mm Hg)} = 8.07 - 1703/T \text{ (K)} \quad 3.1$$

$$\text{TMIn} = \text{Log}_{10}P \text{ (mmHg)} = 10.52 - 3014/T \text{ (K)} \quad 3.2$$

$$\text{TMSb} = \text{Log}_{10}P \text{ (mm Hg)} = 7.73 - 1709/T \text{ (K)} \quad 3.3$$

$$\text{Cp}_2\text{Mg} = \text{Log}_{10}P \text{ (mm Hg)} = 10.00 - 3372/T \text{ (K)} \quad 3.4$$

The mole fraction of the precursor in the bubbler is calculated using $X_{\text{vap}} = (P_{\text{vap}}/P)$.

This can be converted to molar flow rate by using the flow rate of the carrier gas using

$$M_{\text{vap}} \text{ (moVmin)} = X_{\text{vap}} * M/22400 \quad 3.5$$

Once the precursors are at their desired values they are transported to the reaction chamber via carrier gas. Safety measures are very important in operating the precursors as they are pyrophoric in nature. Precursor cylinder valves should be always closed when not in use. The gas lines that are used to transport precursors are always heated by wrapping with heating tape in order to avoid condensation of the precursor on the lines. Also the chillers that are used to cool the precursors should be sealed properly to avoid

the moisture entering into the chillers as it leads to condensation and ice formation which disturbs the cooling thereby affecting the temperature control. Commercial thermal baths Julabo F12 and polydimethylsiloxane is the fluent used in chillers.

Reaction Chamber: It is a vertical chamber with a water cooled stainless steel vessel and a shower head for the uniform distribution of the gases. It consists of a top plate that is a quick access door with water cooling and a perforated stainless steel plate to act as the showerhead. The chamber enclosure is a stainless steel cylinder 8 inch in diameter and 12 inches length with cooling jacket around the walls. The bottom plate is a stainless steel 8 inches conflat blank plate that is equipped with 2 inch resistive susceptor through centering rod. The bottom plate of the chamber is connected to rotary vane pump which is connected to the exhaust of the pump. Between the reaction chamber and the rotary vane pump, a vacuum trap was added to avoid any unreacted precursors entering the pump or back streaming of pump oil into the chamber. Commercial multi trap from MV company is used which traps the unreacted precursors in two stages. In the first stage the particles are dispersed by using a metal gauge which is copper that provides a large surface area for vapors to condense and for trapping larger particles and in the second stage it consists of five or six filter elements that is activated charcoal which removes organic vapors. Substrate heating is achieved using a resistive heater with a coating of aluminum nitride. The distance from the susceptor and showerhead is varied with a switch that moves the entire heater assembly up and down. The gas inlet connector is welded on the top plate which is connected to the gas manifold where all the gases desired for the reaction meet and enter at the inlet. Since there are four precursors and an

ammonia line, a manifold is necessary. The gas manifold line connects the precursor delivery system and the reaction chamber.

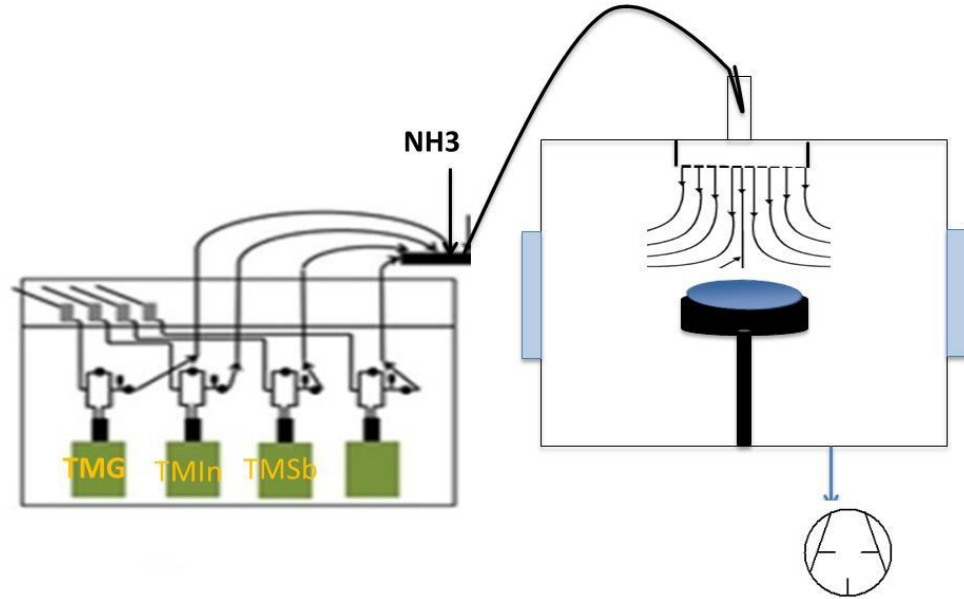


Figure 3.1 A schematic of the custom-built MOCVD reactor used for the growth of $\text{GaN}_x\text{Sb}_{1-x}$ alloys.

Synthesis of $\text{GaSb}_x\text{N}_{1-x}$ alloys was divided into thin polycrystalline films, highly textured films and nanowires. Precursors used for the growth of all three different structures were trimethyl gallium, trimethyl antimony and ammonia. Several substrates like epi-GaN on sapphire, stainless steel and quartz were used for the growth. As shown in Figure 3.2 b several samples were placed on the susceptor for each experiment and there was composition gradient across the samples caused by the vertical stagnation flow. Growth conditions like temperature, pressure and precursor flux has been varied in order to vary the properties and crystal structure of $\text{GaSb}_x\text{N}_{1-x}$ alloys.

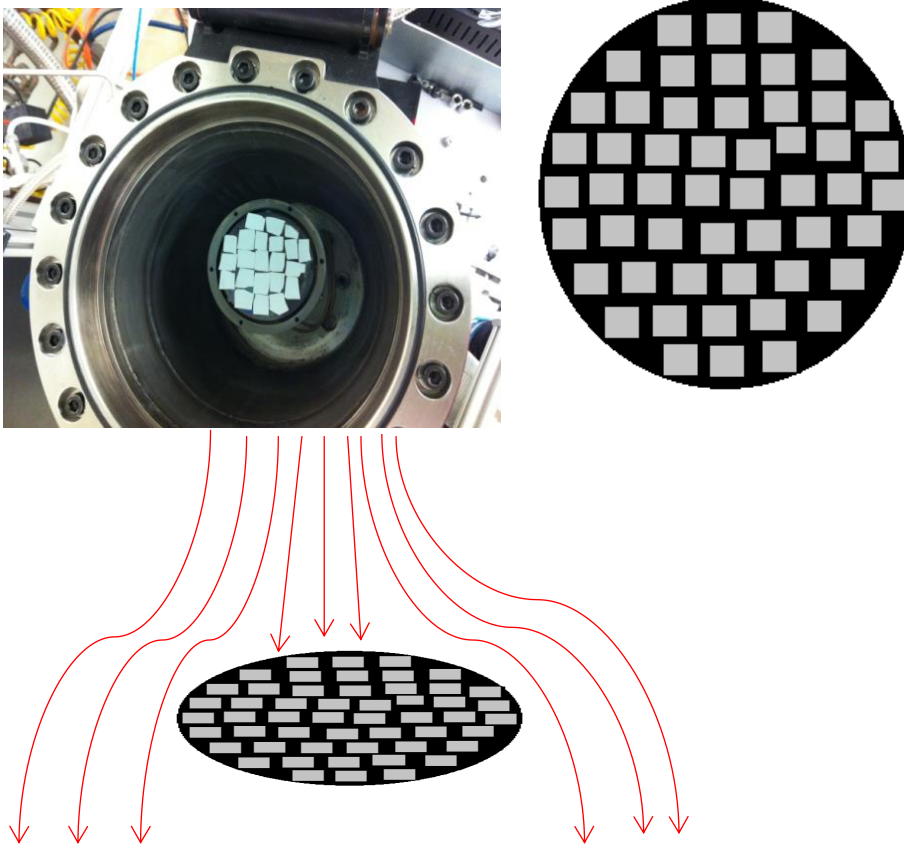


Figure 3.2 a) Picture of a reaction chamber with substrate stage covered with several samples b) Top view of the wafer with several samples c) Composition gradient across the wafer.

Residence time plays important role in the formation of films during MOCVD growth. It is defined as time of the precursor species spent in the reactor before being consumed and can be calculated using $\tau = V/v_0$ where V is volume of the chamber and v_0 is volumetric flow rate of the precursor. For each precursor residence time will change as they enter separately with different flow rates. So, residence times have been calculated for both precursors TMGa and TMSb and made sure that both precursors enter at the same time.

3.3 Optical Characterization

Thin films and nanowire samples are characterized for understanding structural, optical and electronic properties. This section will provide details for all of the techniques and the analysis methods used.

3.3.1 UV-Vis Spectroscopy

The UV-Vis absorption spectroscopy is performed using PerkinElmer Lambda UV/Vis/NIR spectrometer. In this technique, light is incident on the sample and the absorption is measured as a function of wavelength of incident light. The fraction of light absorbed is described by the Beer-Lambert law, which states that absorbance is dependent on the path length of light through the sample (l), the absorption cross section (σ) of the transition, and the difference in the population of the initial state (N_1) and final state (N_2) of the initial (E_1) and final (E_2) electronic energy levels.

$$\frac{I}{I_0} = e^{-\sigma(N_1-N_2)l} \quad 3.6$$

Which can also be written as?

$$A = \epsilon cl = -\log\left(\frac{I}{I_0}\right) \quad 3.7$$

where A is the absorbance, ϵ is the molar absorptivity coefficient of the material, c is the concentration of the absorbing species, and l is the path length of light through the sample. The electronic transitions in the material could be direct or indirect where the indirect transition involves phonon interaction addition to photon and electron when compared with direct transition.

For the measurement, two different techniques were used – (i) diffuse reflectance and (ii) transmittance. For both configurations, the experimental procedure was the same which is described below.

- Before starting the measurement, lamp source is turned on at least 30 minutes early in order to warm up the lamp.
- All the parameters like wavelength range, scan speed, type of the scan are specified before taking the measurement
- Reference sample is placed into the path of the beam and an autozero scan is taken which collects the baseline of the reference sample and subtracts the background w.r.t the reference scan.
- After the autozero scan, sample to be measured is placed in the path of the beam and transmission/reflectance/absorption spectrums are collected.
- The collected raw data is converted to Tauc plots for band gap analysis.

The scan mode is determined based on the samples. Usually samples that have some degree of transparency is used for transmittance measurement. For opaque samples, diffuse reflectance spectroscopy is used. Commercial dual beam UV-Vis-NIR spectrometer has been used for the measurements. The spectrometer is equipped with a wide wavelength window to measure from UV to IR radiation. The instrumentation of the UV-Vis spectrometer consists of light source (tungsten halogen for UV and deuterium lamps for visible radiation) monochromator, filters, Integrating sphere, beam splitter and detector. Integrating spheres were used especially for diffuse reflectance measurements to

avoid any transmitted light being detected. In transmission configuration, a transparent sample is placed in the path of the collimated beam of light. This configuration was used for the thin film samples used this work. In this configuration, first the reference measurement was taken which corresponds to 100% transmittance and then transmitted light of the working sample is collected.

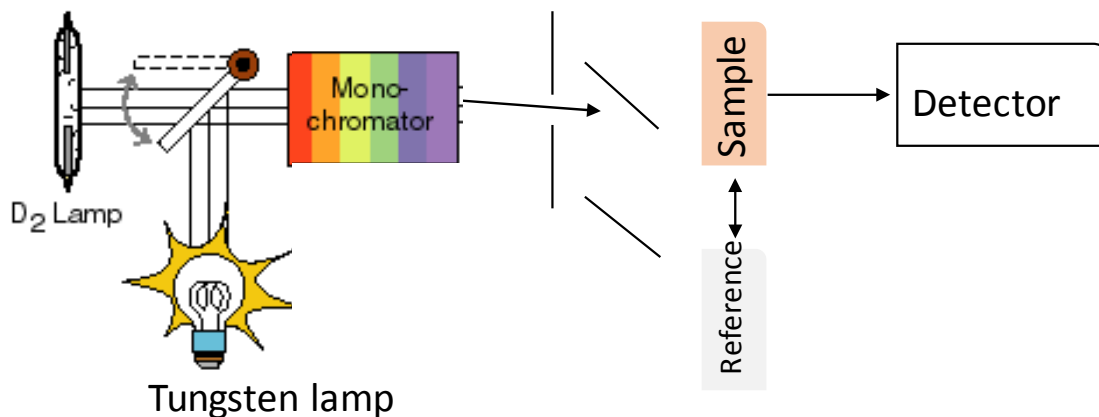


Figure 3.3 A schematic of UV-Vis spectrometer setup.

In a diffuse reflectance configuration, the spectrometer measures the diffusely reflected light from a sample rather than the transmitted light. Samples used for this configuration were either opaque or semitransparent.

Similar to transmittance measurement, a diffuse reflectance measurement starts by taking a reference scan and uses integrating sphere to capture all the photons reflected from the sample in all directions. After the reference scan the working sample is placed and amount of light reflected by the sample is collected. Depending on the scanning mode, the raw data collected for are reported in % reflectance or % transmittance vs wavelength (nm). The band gap values are estimated by converting this data into Tauc plots. Firstly, data is converted from wavelength (nm) to energy units eV by using equation

$$E \text{ (eV)} = \frac{1240 \text{ (eV} \times \text{nm)}}{\lambda \text{ (nm)}} \quad 3.8$$

Different equations are used for different configurations to convert the raw data into Tauc plots

In a transmission experiment, the measured absorbance A is converted to absorption coefficient α .

$$\alpha \text{ (cm}^{-1}\text{)} = \frac{A}{t \text{ (cm)}} \quad 3.9$$

In the case of a diffuse reflectance measurement, in which the reflectance R is measured rather than absorbance, the Kubelka-Munk radiative transfer model must be employed to determine α

$$f(R) = \frac{(1-R)^2}{2R} = \frac{\alpha}{s} \quad 3.10$$

Where $f(R)$ the Kubelka-Munk function and s is the scattering coefficient. If the scattering coefficient is assumed to be wavelength independent, then $f(R)$ is proportional to α and the Tauc plots can be made using $f(R)$ in place of α . For a direct band-band transition, α is proportional the square root of the difference in energy between the photon (E_{hv}) and the band gap (E_g), i.e.

$$\alpha \propto \frac{(E_{hv} - E_g)^{1/2}}{E_{hv}} \quad 3.11$$

where E_g can be found from a $(\alpha E_{hv})^2$ versus E_{hv} plot. For indirect band gap transitions, α is proportional to the square of the difference between the photon energy and the band gap.

$$\alpha \propto \frac{(E_{hv} - E_g)^2}{E_{hv}} \quad 3.12$$

Similarly, a plot of $(\alpha E_{hv})^{1/2}$ versus E_{hv} will determine the E_g in the case of an indirect band gap semiconductor. From the above plots as shown in Figure, the band gap value is extrapolated by simply drawing a tangent to the slope of the curve and the point at which this line intersects on x-axis is the value of the band gap. From the Figure 3.4 it can be observed that tangent is extrapolated to 2.2 eV band gap value.

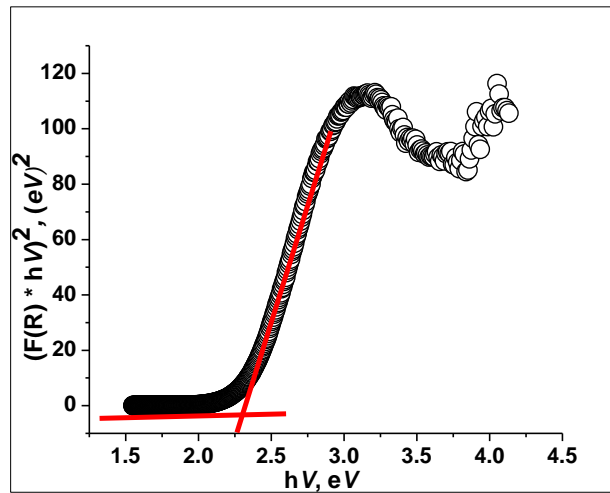


Figure 3.4 A sample Tauc plot for a $\text{GaSb}_x\text{N}_{1-x}$ sample.

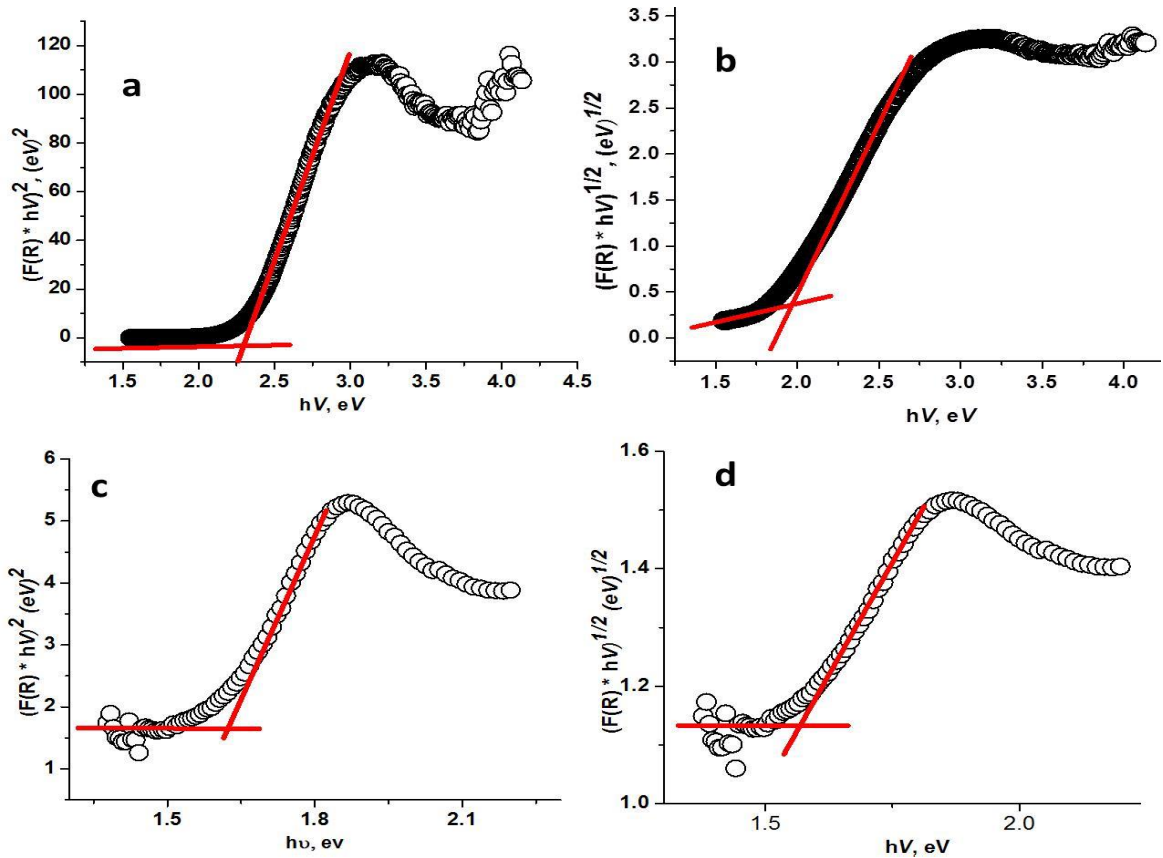


Figure 3.5 Tauc plots for direct transition and indirect transition for 2% Sb (a,b) and 8% Sb (c,d).

Figure 3.5 is showing the comparison between direct and indirect band gap transition for $\text{GaSb}_x\text{N}_{1-x}$ sample. From plots a and b it can be observed that the curve is more sharp and fits better for $(\alpha E_{in})^2$ versus E_{in} than $(\alpha E_{in})^{1/2}$ versus E_{in} which shows that material is exhibiting direct band gap transition. However, in plots c and d it is reverse it fits better to the indirect transition. Absorption coefficient and absorption depth of the material can be determined using transmittance spectroscopy. The % transmittance is converted to absorption coefficient using below equation

$$\text{Fraction transmitted} = T = (I/I_0) = \exp(-\alpha \cdot d) \quad 3.13$$

Fraction absorbed = 1-T

3.14

From the plot of fraction absorbed vs thickness, absorption depth of the material can be calculated that is of around 2 microns in the case of $\text{GaSb}_x\text{N}_{1-x}$ as shown in the Figure 3.6. Reciprocal of the absorption depth is the absorption coefficient $\alpha = 1/d$.

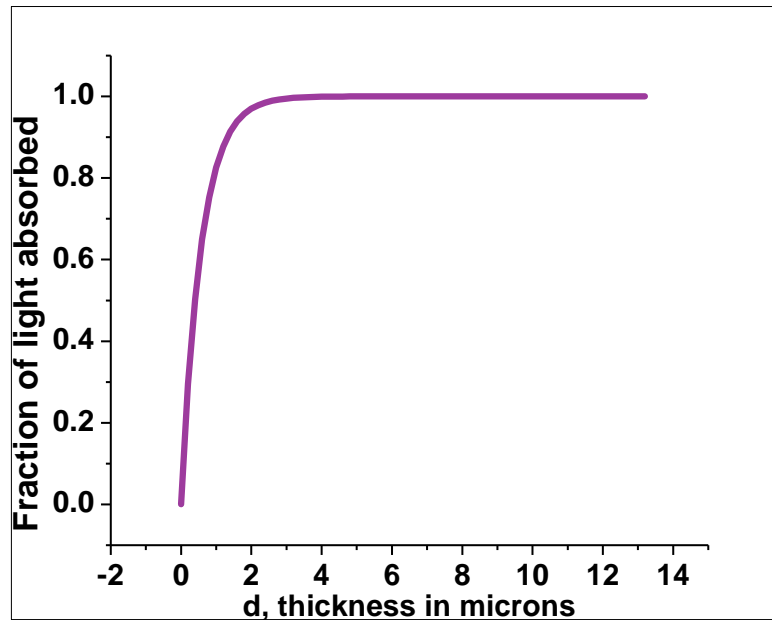


Figure 3.6 Optical absorption profile of a $\text{GaSb}_x\text{N}_{1-x}$ film.

3.3.2 Raman and Photoluminescence Spectroscopy

Raman and photoluminescence spectroscopy use similar instrumentation but each technique gives different information. The instrumentation of both techniques include

- Lasers (light source containing UV to IR)
- lenses (both to focus the light onto the sample and to collect the scattered light)
- Notch & edge filters (to purify the reflected and scattered light so that only the Raman light is collected)

- Diffraction grating
- CCD detector & NIR detector (for different wavelength ranges)
- Electronics

The measurement is performed by impinging a laser beam onto the sample. Both Raman and PL signals are emitted from the sample. Raman signal gives the information on molecular vibrational and rotational motions whereas PL gives information of optical properties of the material like band gap. In order for the Raman signal to be detected molecule should cause a change in polarizability. When photons hit the sample at a certain frequency the molecules excite from ground state to virtual states and fall back to the ground state or lower level states emitting a photon. Information is gathered depending upon the frequency of the emitted photon. If the frequency of the emitted photon is same as the incident photon, this phenomenon is called Rayleigh scattering and does not give any information in identifying the compound. However, when the frequency of the emitted photon is different, the change in the frequency is identified as Raman shift and is characteristic for a given compound.

In photoluminescence spectroscopy, when a photon is incident on a sample it is absorbed and excites an electron to higher state that is from valence band to the conduction band and upon excitation it falls back to the valence band releasing a photon which corresponds to band gap energy of the material. This process of photon excitation followed by photon emission is called photoluminescence.

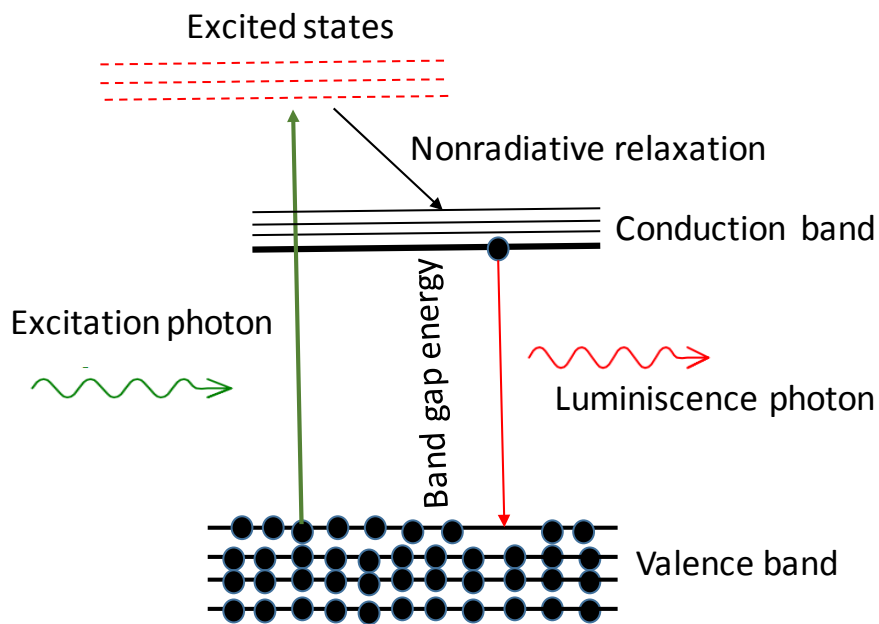


Figure 3.7 A schematic showing photoexcitation processes in PL spectroscopy.

PL can also be used in studying defects in semiconductors, when excited electrons relax into the defect states. For some compounds Raman and PL signal can be overlapped, different laser sources can be used to avoid that. For PL, analysis has been done at both room temperature and cold temperature using 325 nm laser excitation source. It is important to do analysis at both temperatures because sometimes depending upon the material at room temperature carriers can escape thermally to higher energy levels which might cause other peaks. This causes non-radiative recombination centers, which reduces the intensity of the PL signal whereas at low temperature carriers are effectively frozen which allow lowest energy states to appear more clearly. In general, it is easy to get PL signal at low temperature (LT) than room temperature. Also the deep impurity levels are revealed in LT PL. In our case especially with polycrystalline films we did not observe any signal at RT whereas LT PL revealed peaks in the range of 1.7 eV to 2.1 eV

depending upon the antimony composition in $\text{GaSb}_x\text{N}_{1-x}$ layers.

In this study, Raman analysis has been done using 632 nm laser excitation source. This is majorly used to check if the synthesized layers were $\text{GaSb}_x\text{N}_{1-x}$. There was no Raman data available on $\text{GaSb}_x\text{N}_{1-x}$ in literature. So we did analysis on $\text{GaSb}_x\text{N}_{1-x}$ and GaN to see the difference between them. Even though all the peaks appeared for GaN appeared for $\text{GaSb}_x\text{N}_{1-x}$, there was an additional peak in $\text{GaSb}_x\text{N}_{1-x}$ layers and the intensity of the peak has been increased with increase in antimony composition. This is explained in detail in chapter 4.

3.4. Structural characterization

The morphology of synthesized $\text{GaSb}_x\text{N}_{1-x}$ samples has been studied using JEOL JSM-5310 scanning electron microscope (SEM) operating at 20 keV. Samples after deposition were cut into half to analyze the interface between GaN and $\text{GaSb}_x\text{N}_{1-x}$ from SEM which gives information on the quality of the crystal. SEM-EDS analysis has been performed on the sample to determine the composition of antimony in $\text{GaSb}_x\text{N}_{1-x}$ layers.

3.4.1 X-ray Diffraction (XRD)

To obtain crystallographic information of the material Bruker Discovery D8 XRD system has been used.¹⁰¹ X-rays are generated using an X-ray tube comprising of heated tungsten filament enclosed in an evacuated ceramic vessel. The tungsten filament emits electrons by thermionic emission and acts as a cathode. The electrons are accelerated towards a water cooled metal (typically copper) which acts as the anode. The electrons reaching the Cu anode lose their energy by two mechanisms. Firstly, the electrons can decelerate as they approach the nuclear cores of the atoms in the anode due to opposing

electric field from the nucleus towards the valence electrons. This type of deceleration produces Bremsstrahlung X-rays.¹⁰² Secondly, the electrons can knock out the electrons in the inner shells of the Cu atoms. Electrons in the valence shells relax to the inner shells and the difference in energy is emitted in the form of continuous X-rays. In case of Cu, characteristic X-rays of two wavelengths namely Cu K_{α} ($\lambda = 0.154$ nm) and Cu K_{β} ($\lambda = 0.139$ nm) are produced. The continuous X-rays and the Cu K_{β} radiation are absorbed by a Ni filter in a monochromator. X-ray radiation passes through the Soller slits and divergence slits to reduce the axial divergence and height divergence respectively, and strikes the samples causing the diffraction of X-rays. (Figure 3.8)

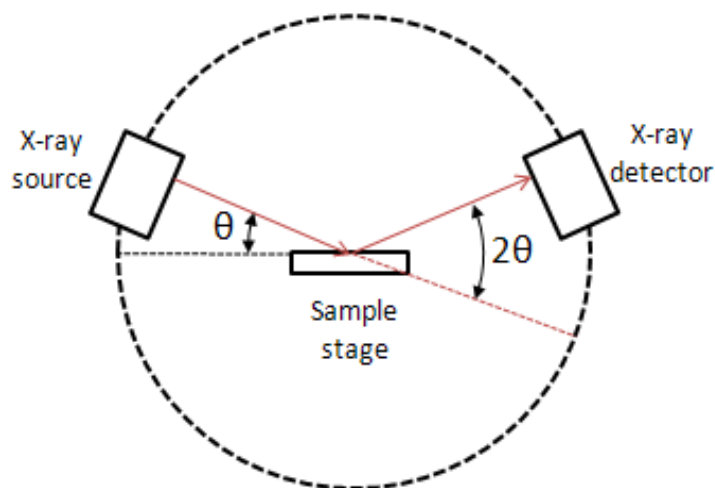


Figure 3.8 A schematic of the experimental setup used for X-ray diffraction in the Bragg-Brentano configuration. Image Source

http://chemwiki.ucdavis.edu/Analytical_Chemistry/Instrumental_Analysis/Diffraction/Powder_X-ray_Diffraction)

The diffracted X-rays then pass through the anti-scatter slit, soller slit, followed by the receiving slit and an X-ray detector. The detector is usually a scintillation counter, which measures the intensity of the diffracted X-rays in counts. The scintillator comprises of a fluorescent material that emits photons when hit with X-rays, the photons are then converted to electrons using a photomultiplier tube. The processing electronics measures the number of electrons and calculate the intensity of the diffracted X-ray beam. The peaks observed in a diffraction pattern correspond to the particular angles at which the diffracted X-rays from the sample interfere constructively. This is described the Bragg's law of diffraction as follows

$$n\lambda = 2d\sin\Theta \quad 3.15$$

where n is an integer, d is the interplanar spacing, 2Θ 'ls the angle between the incident X-ray beam and the diffracted X-ray beam.

X-ray diffraction was also used to estimate the crystallite size of $\text{GaSb}_x\text{N}_{1-x}$ films. The crystallite size was calculated using Scherrer equation

$$B \times 2\theta = (k\lambda)/l \cos \theta \quad 3.16$$

where B is full width half maxima (FWHM) of XRD peak, l is the crystallite size, λ is wavelength copper k- alpha radiation (1.45 \AA), k is Scherrer constant and Θ is the Bragg angle. XRD analysis is also useful to determine lattice parameters. From the peak shift and using the equations shown below lattice spacing and lattice expansion at different antimony compositions has been determined.

Hexagonal:

$$\frac{1}{d^2} = \frac{4}{3} \left(\frac{h^2 + hk + k^2}{a^2} \right) + \frac{l^2}{c^2} \quad 3.17$$

$$\sin^2 \theta = \frac{\lambda^2}{4d^2} \quad \sin^2 \theta = \left(\frac{\lambda^2}{4} \right) = \left[\frac{4}{3} \left(\frac{h^2 + hk + k^2}{a^2} \right) + \frac{l^2}{c^2} \right] \quad 3.18$$

Moreover, important parameters need to be considered in XRD are peak width, peak position and peak intensity. A full width half maximum of the peak determines the grain size and lattice strain. Strain caused in the crystal effects the position and shape of the XRD peak. For example, if there is a uniform strain in the material, peak moves to the lower angles and if the strain is caused by small grains peak broadening occurs. The smaller the grains and more non uniform the strain in the lattice is, the more the peak broadening will be. Figure 3.9 is showing the difference in FWHM of polycrystalline vs single crystalline film of the sample $\text{GaSb}_x\text{N}_{1-x}$ and GaN films and the peak shift in the figure is due to the large strain caused in the lattice due to incorporation of antimony.

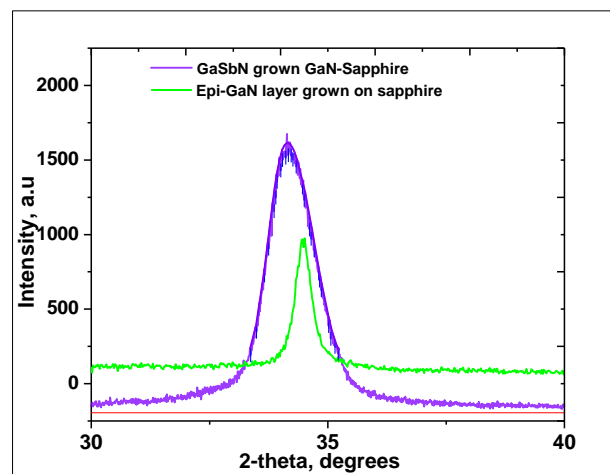


Figure 3.9 Comparison of XRD patterns for $\text{GaSb}_x\text{N}_{1-x}$ and GaN.

3.4.2 Transmission Electron Microscopy (TEM)

TEM is similar to SEM but gives detailed information on crystal orientation. The components in the electron gun column of TEM are similar to that of SEM. However, unlike the SEM where secondary electrons and back scattered electrons are detected, TEM detects the elastically scattered electrons that are transmitted through the specimen. For a crystalline sample, the electrons diffract through the crystal planes of the sample and can interfere to form a diffraction pattern. Electrons scattered from the sample located in the object plane are focused by an object lens. Images in the TEM can be obtained either in the bright field (BF) mode or dark field mode.¹⁰³ In the bright field mode, an aperture is placed in the back focal plane and only the direct beam of electrons that have interacted with the sample are used for image formation and the diffracted electron beam are blocked. As a result of this, the electrons interacting with atoms of higher atomic mass and thicker regions produced a darker contrast which means the BF images give information of the thickness of the sample. In dark field (DF) image the direct beam is blocked by an aperture in the back focal plane and the diffracted beam of electrons that have strongly interacted with the sample are used for image formation. Hence, the DF images give information about the defects in the sample. High Resolution TEM (HRTEM) mode in the TEM is used for high resolution imaging of crystalline material and can provide resolution up to 0.8 \AA .¹⁰⁴ In this technique several diffracted beams are used to form the image. Indeed, in general, the most common way to analyze NWs is to take advantage of the easy detachment of the NWs from the substrate for their observation by TEM. In that case, the NWs are removed from the native substrate after sonication in an isopropanol bath or directly after scratching from the sample surface and

then dispersed on a TEM carbon grid. This preparation method has the advantage that the NWs are free of the artifacts introduced during the conventional TEM preparation process, where the final Ar-ion milling sometimes results in an undesired amorphous coating on the sample surface. Selected area diffraction (SAED) analysis has been performed on nanowire sample to understand the crystallinity of the nanowires. This can selectively perform analysis on very small parts of the sample independently under the electron beam by using an aperture which sends only small part of the beam. Crystal quality can be determined from the obtained diffraction pattern. For example if the sample is polycrystalline it gives rise to a series of spot patterns forming like rings whereas for single crystalline it will give straight lines.

3.5 Electrical Characterization

An important parameter that determines the photoelectrochemical performance of the semiconductors is the minority carrier diffusion length.¹⁰⁵ The minority carrier diffusion lengths have been measured using electron beam induced spectroscopy.¹⁰⁶⁻¹⁰⁸ The electron beam from a scanning electron microscope (FEI-NOVA SEM) was used to irradiate the samples. Samples were prepared into metal-semiconductor-schottky configuration and scanning was carried out by moving the electron beam starting at the edge of the schottky contact. When electrons are injected from the electron beam into the semiconductor near a schottky contact, electron-hole pairs are generated. Due to the large concentration of electrons in n-type sample than the generated electron-hole pair concentration, only holes are effectively generated assuming low electron beam currents. When the circuit is closed with ohmic contact on the other end of the semiconductor

surface holes which diffuse close to the Schottky contact will generate an induced current which follows the law

$$I = I_{max} \exp\left(-\frac{x}{L}\right) \quad 3.19$$

where L is minority carrier diffusion length, I is collected total current and x is electron beam scanning distance between the schottky diode and the injected spot. The irradiation volume is calculated based on the beam penetration depth and the distance covered during the line scan. The total charge is determined as the product of multiple line scan and absorbed electron beam current that is measured by ammeter. The minority carrier diffusion length will then estimated by fitting the theoretical equation 3.19 to the profile of current vs. distance.

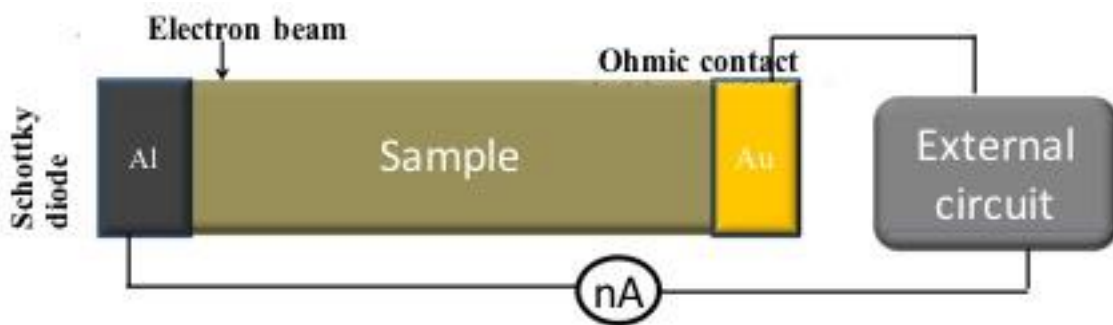


Figure 3.10 A schematic showing the configuration used for EBIC measurements

3.6 Electrochemical and Photoelectrochemical characterization

3.6.1 Electrode Fabrication

For the photoelectrochemical measurements, samples are made into electrodes to form an electrical contact. Copper wire has been used for the electrical connection; first copper wire is twisted into a spiral form with the head being approximately same size as sample which is shown in the Figure 3.11

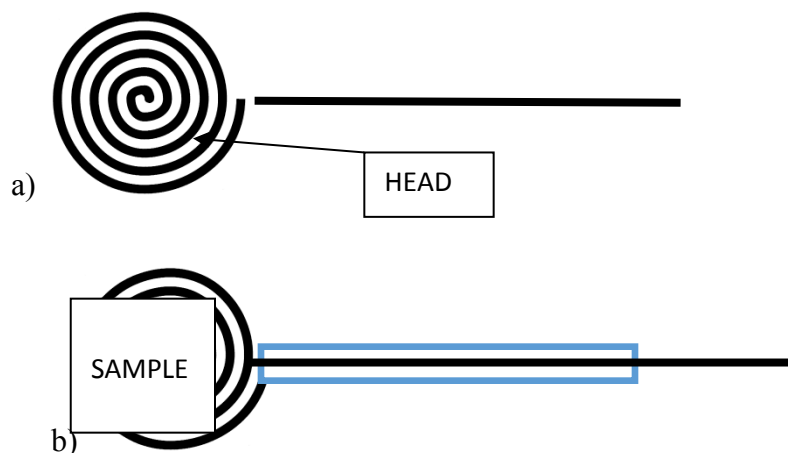


Figure 3.11 Schematics showing electrical contacts with samples for testing with photoelectrochemical water splitting activity.

Indium-Gallium eutectic alloy was used for ohmic contact

And silver paste was used to glue the copper wire to the sample. Once the silver epoxy is cured it is inserted into the glass tube. Loctite 9464 Hysol Epoxy was used to cover the silver epoxy and the metal surface to avoid contact with electrolyte. The epoxy is allowed to dry overnight, once the epoxy is completely dry the electrodes are ready for testing as shown in the Figure 3.12



Figure 3.12 Photograph showing $\text{GaSb}_x\text{N}_{1-x}$ electrodes made for photoelectrochemical studies.

3.6.2 Photoelectrochemical Cell Setup

The PEC cell setup consists of PEC cell, light source, power meter and potentiostat. Three electrode PEC cell has been used for all the photoelectrochemical measurements performed on $\text{GaSb}_x\text{N}_{1-x}$ samples. Cell consists of three separate windows to insert working electrode (WE), counter electrode (CE) and reference electrode (RE) immersed in an electrolyte. Cell is also equipped with a quartz window as shown in the Figure 3.13. Solar simulator has been used for the light source which is shown left of the figure. The light source contains Xenon lamp adjusted to AM 1.5 spectrum. Light coming out from the solar simulator is measured using power meter which is simply a silicon photodiode that measures that light intensity upon light hitting on it. Once the light intensity was measured, light is allowed to shine onto the sample through quartz window. Working electrode is the sample to be tested, platinum mesh was used as counter electrode and Ag/AgCl in saturated KCl was used as reference electrode. All the three electrodes were connected into a circuit to a potentiostat where all the measurements were recorded.

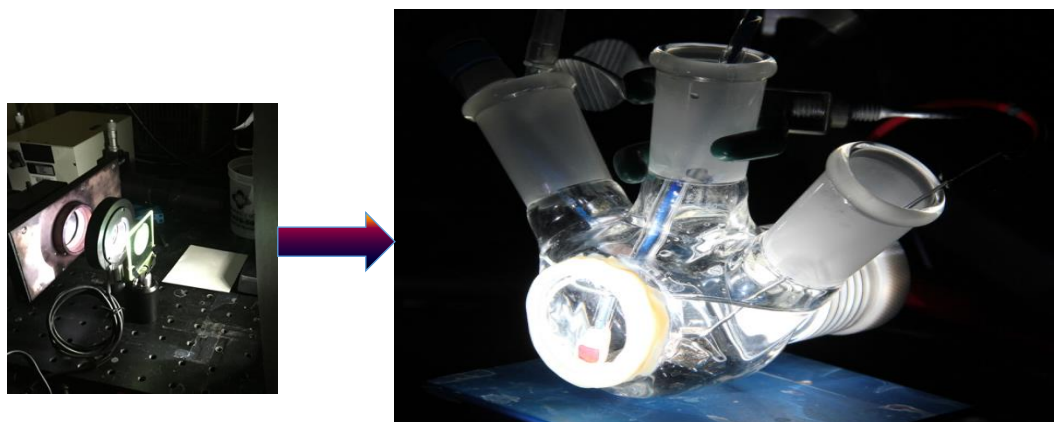


Figure 3.13 Photoelectrochemical setup used for water splitting studies.

3.6.3 Open Circuit Potential

To determine the conductivity type of the material illuminated open circuit potential technique has been used. A three electrode setup as explained in the previous was used for the experiment. Firstly, OCP was measured under dark by covering the whole setup with a black box. Open circuit potential is the difference between Fermi level in the semiconductor and the electrolyte redox potential. OCP of semiconductor is measured under chopped illumination. Conductivity type is determined by observing the direction of potential shift under illumination. The material is n-type if OCP moves towards more cathodic potentials (negative) and it is p-type if OCP moves towards more anodic potentials (positive).

3.6.4 Photocurrent measurements

Photocurrent measurement is an important measurement in order to check if material can split water efficiently. Measurement was performed in the same setup as explained above. The photocurrent onset can be used to estimate the E_{fb} , and can be determined by measuring the photocurrent density (j_{ph}) as a function of the potential versus a reference electrode (E_{ref}) and then comparing the dark and illuminated scans. As the potential moves towards greater reverse bias, the electric field generated across the space charge layer increases and drives charge separation and charge transfer to the electrolyte, thereby enhancing the photocurrent. Under ideal circumstances, the potential at which the semiconductor changes from accumulation to depletion coincides with the onset of photocurrent and this potential is taken as the E_{fb} , although this is often offset by the required kinetic overpotential to drive the reaction. The sample J-V curve of $GaSb_xN_{1-x}$

sample is shown in the Figure 3.14

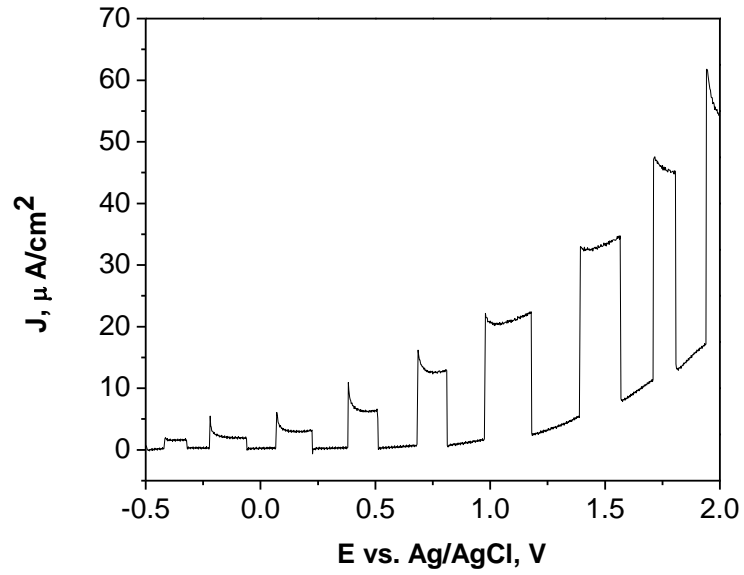


Figure 3.14 A typical J-V curve for a $\text{GaSb}_x\text{N}_{1-x}$ sample.

3.6.5 Mott-Schottky Analysis

To determine the band edges and flat band potential of $\text{GaSb}_x\text{N}_{1-x}$ samples Mott-Schottky technique has been used. This technique measures the capacitance of the space charge layer of semiconductor material as a function of applied potential (E) according to the relation⁸

$$\frac{1}{C_{sc}^2} = \frac{2}{e\epsilon\epsilon_0N} \left(E - E_{FB} - \frac{kT}{e} \right) \quad 3.18$$

where ϵ_r is the relative permittivity of the semiconductor), ϵ_0 is permittivity in vacuum, A is the surface area, e is the charge of an electron, N is the free carrier density, k is Boltzmann constant, T is the temperature, and E is the applied potential. The Mott-

Schottky technique also provides information on charge carrier density, conductivity type of the material which is estimated from the slope of the Mott-Schottky plot. A negative slope means material is p-type and positive slope means material is n-type. The direction of the potential scan depends on the conductivity of the material. For n-type materials, the scan should be performed at potentials positive of OCP and vice versa for p-type materials. The Mott-Schottky measurements described in this dissertation were made using 3-electrode cell equipped with a quartz window. A three electrode configuration comprising of GaSb_xN_{1-x} working electrode, Ag/AgCl (with a 3M KCl filling solution) was used as the reference electrode and Pt was used as the counter electrode. The electrolyte used for the Mott-Schottky characterization comprised of an aqueous solution of 200 mM K₄Fe(CN)₆, 20 mM K₃Fe(CN)₆, 200mM KCl. The AC signal amplitude was 10 mv rms and a frequency of 10 kHz was used. A simple R-C circuit was used to extract the value of capacitance (C). A linear extrapolation of the linear region in the Mott-Schottky plot ($1/C^2$ vs. E) was used to determine the intercept which gives the value of flat band potential.

CHAPTER 4

METAL ORGANIC CHEMICAL VAPOR DEPOSITION OF GaSb_xN_{1-x}

4.1 Introduction

In this chapter, theoretical calculations on Ga(Sb_x)N_{1-x}, and experimental results on the synthesis of Ga(Sb_x)N_{1-x} ternary layers in the low antimonide composition regime, will be discussed. Specifically, anomalous band gap reduction and unit cell expansion predicted theoretically for small antimonide composition are confirmed by experimental data. In addition, quantitative comparisons are made with experimentally observed values for band gap and optical properties. Photoelectrochemical measurements to determine band edge positions and photoactivity will also be discussed.

4.2 Computational Calculations

Computations that were performed using DFT to understand the properties of antimony incorporation into GaN will be discussed in this section

For this, the structural optimizations and electronic structure analysis for all Sb doped GaN structures were performed using first principles density functional theory (DFT). The DFT calculations were performed in the generalized gradient approximation (GGA) of Perdew-Burke-Ernzerhof (PBE)¹⁰⁹ for exchange and correlation as implemented in the Vienna Ab-initio Simulation Package (VASP)¹¹⁰⁻¹¹² The projected augmented wave (PAW) potential^{113, 114} was used to describe the core electrons. To circumvent the well-

known "gap problem" in the LDA/GGA formalism, we incorporate the Hubbard parameter, U , in the formalism (LDA/GGA+ U method).^{114, 115} The U parameter is an on-site Coulomb repulsion parameter that incorporates part of the electron correlation absent in LDA/GGA. The U values used in the GGA+ U formalism are: $U_{d,Ga} = 6.5$ eV and $U_{p,N} = U_{p,Sb} = -4.2$ eV. All other U values are set to zero. These values of U for Ga and N reproduce the experimental band gaps of bulk GaN (3.43 eV)¹¹⁶ and GaSb (0.73 eV).¹¹⁷ The bulk GaN in the wurtzite structure was simulated using a 192 atom supercell with periodic boundary conditions. Ga(Sb_x)N_{1-x} structures are obtained by substituting up to 8 N atoms with Sb. In Fig. 1c we show the optimized atomic configuration for GaN supercell with 5 substitutional Sb. After testing for convergence we settled for a 3x6x2 Γ -centered pack for \mathbf{k} -vectors sampling. A kinetic energy cutoff of 550 eV was found to be sufficient to achieve a total energy convergence of the energies of the systems to within 1 meV. Gaussian smearing of 0.05 eV was chosen to accelerate the electronic convergence. The optimization of atomic positions (including full cell optimization) was allowed to proceed without any symmetry constraints until the force on each atom is less than 5 meV/Å. In each case considered, both the cell volume as well as individual atomic positions have been fully optimized without any symmetry constraints. In Figure 4.2, previously published theoretical results¹³ are presented for a smaller supercell (72 atoms) using the GGA+ U formalism within the Perdew-Wang (PW91)¹¹⁸ scheme for exchange-correlation as implemented in the Cambridge Serial Total Energy Package (CASTEP) and compare with our present results using a 192 atom supercell. The U values used in these calculations were: $U_{d,Ga} = 0$ eV, $U_{s,N} = 19.25$ eV and $U_{s,Sb} = 0.40$ eV. These values of U also reproduced the experimental bandgaps of bulk GaN (3.43 eV)¹¹⁶ and GaSb (0.73

eV).¹¹⁷ The experimental values are in better agreement with the present computations using the PBE scheme implemented in VASP for the larger (192 atom) cell. It should be noted that the PBE functional has been designed to give essentially the same results as the PW91 functional but it is more robust in systems with rapidly varying electron density.

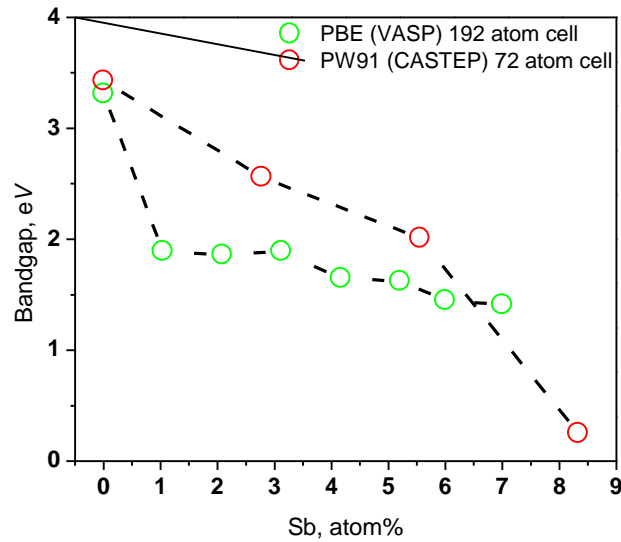


Figure 4.1 Predicted band gap values for different Sb composition using 192 and 172 atom supercells.

4.3 MOCVD of $\text{GaSb}_x\text{N}_{1-x}$

4.3.1 Synthesis

The experimental procedure of $\text{GaSb}_x\text{N}_{1-x}$ thin films by MOCVD is as follows:

1. Firstly, substrates were cleaned properly to remove any native oxide before placed in the chamber and the chamber was pumped to its base pressure.

2. Once the chamber reached its base pressure, it was purged with nitrogen for at least two cycles using a bypass valve and isolating bubbler valves.
3. The metal organic precursors were maintained at desired vapor pressures which were controlled by maintaining the precursors at certain temperatures with thermal baths.
4. After the purging cycles and making sure chamber was leak tight by rate of rise method, which involved closing all the valves connected to the chamber and monitoring rise in pressure.
5. The chamber was pressurized with ammonia to the desired value and stabilized for at least 15 minutes before heating the chamber to the desired temperature.
6. Heating was done with resistive heater that was controlled by a temperature controller which was used to set the desired temperature value. Heating rate, duration of heating and cooling rate was controlled using the temperature controller.
7. Precursors were then allowed to flow into the chamber with a known flow rate of carrier gas.
8. Reaction was performed for 30-60 minutes depending upon the required sample thickness. After the desired reaction time, precursor flow was shut down followed by ammonia flow and chamber was pumped down to its base pressure and then lastly heater was turned off.
9. The reaction chamber was vented to atmosphere under nitrogen environment and the samples were retrieved

4.3.2 Morphology

Morphology of as synthesized $\text{GaSb}_x\text{N}_{1-x}$ thin films was analyzed using SEM. The samples turned out to be polycrystalline as shown in the figure. The interface between $\text{GaSb}_x\text{N}_{1-x}$ and GaN has been shown in the Figure 4.2 with small grains all over the surface.

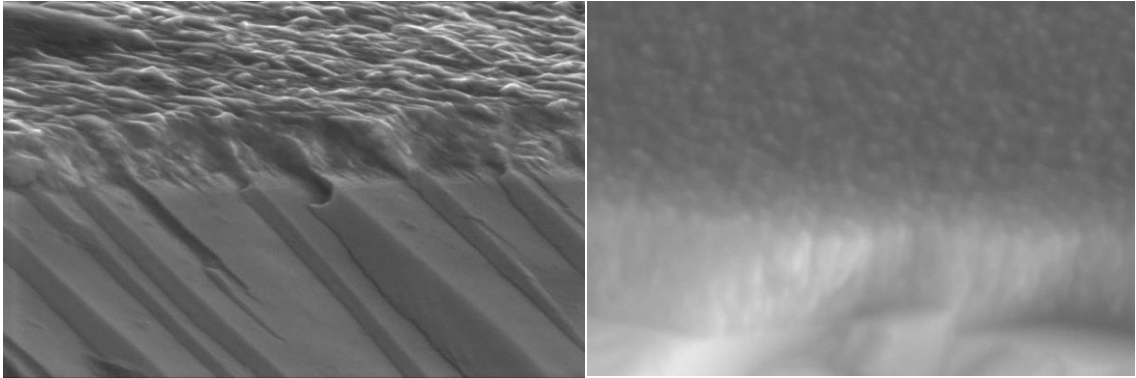


Figure 4.2 SEM images showing cross-sectional view for $\text{GaSb}_x\text{N}_{1-x}$ films.

4.3.3 Crystallinity

To confirm alloys made were $\text{GaSb}_x\text{N}_{1-x}$ crystallinity and lattice expansion has been measured using X-ray diffraction. Figure 4.3 (a) shows the X-ray diffraction (XRD) patterns for several MOCVD-grown samples. The peaks observed in GaN sample appear for $\text{Ga}(\text{Sb}_x)\text{N}_{1-x}$ samples, the (0002) peak at around 35° is present in all samples and is the most dominant peak. Interestingly, the 35° peak position shifts monotonically to lower angles with the increase of Sb concentration. Substitution of a nitrogen with an anion of larger covalent radius causes large initial strain and the lattice expands to relax this strain that corresponds to the monotonic increase of the unit cell and confirms the prediction of our first principle calculations $\text{Ga}(\text{Sb}_x)\text{N}_{1-x}$ films with different amounts of Sb. Although,

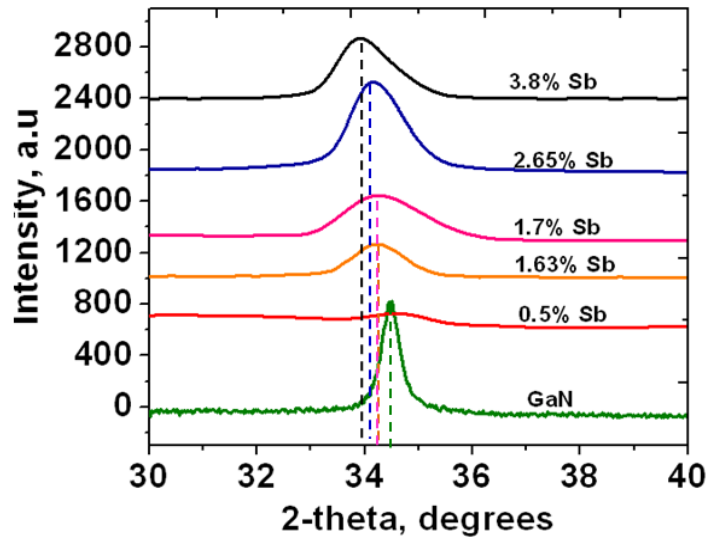
not all of the typical wurtzite XRD for $\text{Ga}(\text{Sb}_x)\text{N}_{1-x}$ structures which reveal a monotonic increase in the lattice parameters with an increase in x on relaxation as shown in Figure 4.3 (b). The lattice parameters were calculated using equations

$$\frac{1}{d^2} = 4/3((h^2 + hk + k^2)/a^2) + l^2/c^2$$

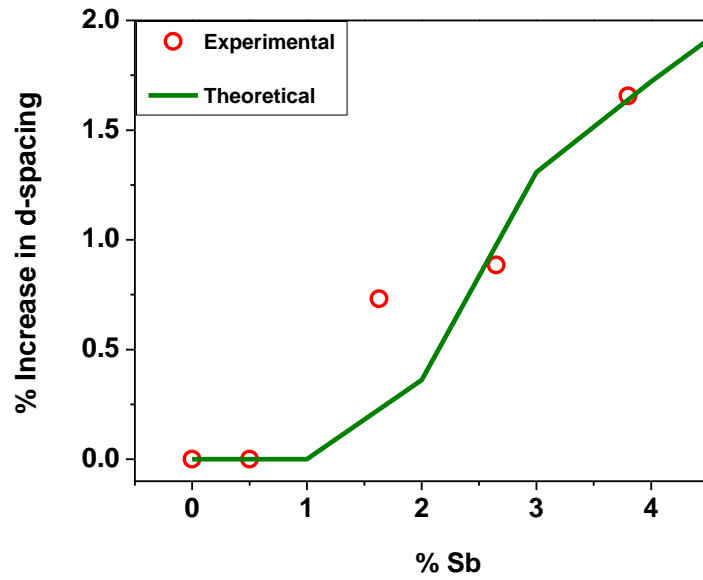
$$\boxed{\sin^2 \theta = \frac{\lambda^2}{4d^2}} \quad \sin^2 \theta = \left(\frac{\lambda^2}{4} \right) = \left[\frac{4}{3} \left(\frac{h^2 + hk + k^2}{a^2} \right) + \frac{l^2}{c^2} \right]$$

Figure 4.3 (c) shows the ball and stick model of the 192 atom super cell used in our density functional theory (DFT) studies. The structural optimizations result in considerable local distortions in $\text{Ga}(\text{Sb}_x)\text{N}_{1-x}$ structures due to the size and electronegativity mismatch between N and Sb.

a)



b)



c)

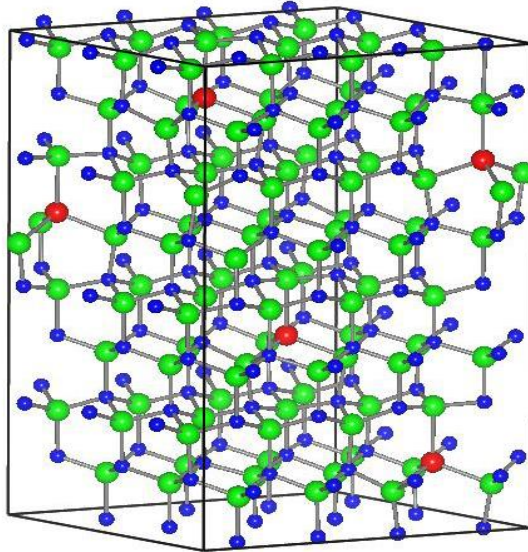


Figure 4.3 a) XRD pattern of GaSb_xN_{1-x} layers showing peak shift of (002) plane with various Sb concentrations b) Lattice expansion with Sb concentration of (002) plane c) GaSb_xN_{1-x} supercell with x= 5/96 optimized using DFT simulations. The Sb atoms are shown in red, Ga in green and N in blue.

Also GaN nanowire substrates were used for the growth of $\text{GaSb}_x\text{N}_{1-x}$ films. High level of crystallinity of the $\text{Ga}(\text{Sb}_x)\text{N}_{1-x}$ layers indicated by the XRD measurements was also confirmed by high-resolution transmission electron microscopy (HRTEM). Figure 4.4 shows HRTEM image of a typical $\text{Ga}(\text{Sb}_x)\text{N}_{1-x}$ layer grown on a-plane GaN nanowire substrate. The $\text{Ga}(\text{Sb}_x)\text{N}_{1-x}$ layer grows epitaxially on the GaN nanowire and maintains the orientation relationship with the nanowire substrate as its basal c-planes are parallel to those of the GaN nanowire substrate. High density of basal stacking faults observed in these $\text{Ga}(\text{Sb}_x)\text{N}_{1-x}$ layers is most likely due to lower growth temperature used compared to typical growth temperatures of 850°C or above for GaN. The most striking result is that epitaxial growth on nanowire along the entire length is observed at the low growth temperatures used. At these temperatures, the growth on planar substrates yielded nucleation of islands. These observations suggest that the epitaxial growth over entire nanowire length (over several microns) is possible due to faster surface diffusion of adatoms on nanowire substrates. High level of crystallinity and the epitaxial growth on nanowire substrates is necessary for fast transport of charge carriers and reduced recombination losses in the material, which is an important factor for water splitting.

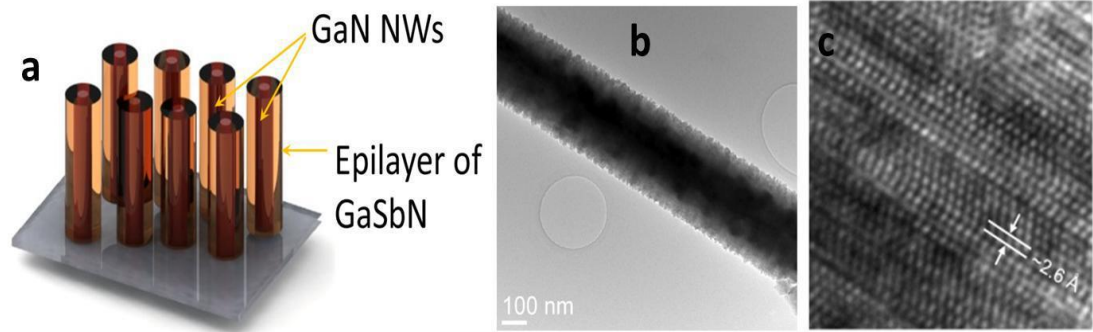


Figure 4.4 a) A schematic illustrating $\text{GaSb}_x\text{N}_{1-x}$ growth on an array of GaN nanowires b) Low magnification TEM image c) HRTEM image of typical MOCVD $\text{GaSb}_x\text{N}_{1-x}$ layer grown on a-plane GaN nanowire.

Also Raman studies were performed on the $\text{GaSb}_x\text{N}_{1-x}$ alloys. Figure 4.5 shows the Raman spectra for $\text{GaSb}_x\text{N}_{1-x}$ samples with different antimonide (Sb) concentrations. The spectrum of a GaN substrate, shown for comparison, contains a strong peak at around 575 cm^{-1} consisting of the E1(TO) mode at 572 cm^{-1} and the E2H mode at 581 cm^{-1} as well as the A1(LO) line at 751 cm^{-1} . In addition, there is also a weak peak at around 420 cm^{-1} which corresponds to overtones of transverse acoustic.¹¹⁹ In samples with Sb incorporation, the GaN peaks are still observed, but the relative intensity of the forbidden A1(LO) increases and an additional peak at around 650 cm^{-1} is observed. No prior data using Raman spectroscopy for $\text{Ga(Sb}_x\text{)N}_{1-x}$ alloys exist in the literature.

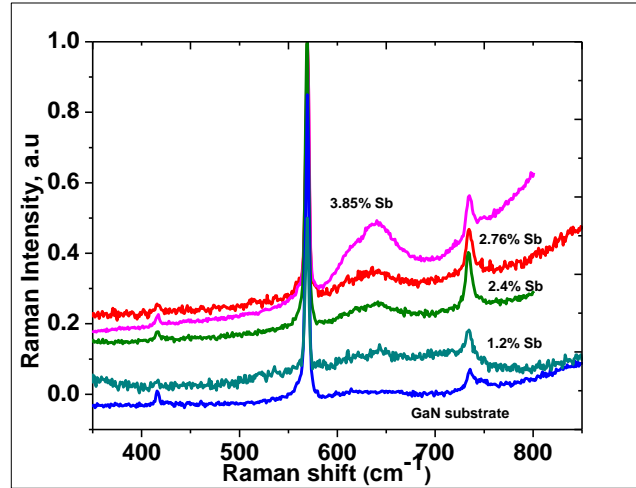


Figure 4.5 Raman spectra of $\text{Ga}(\text{Sb}_x)\text{N}_{1-x}$ samples containing different antimony concentrations.

4.3.4 Band gap Reduction in $\text{GaSb}_x\text{N}_{1-x}$ alloys

Band gap measurement is an important observation to confirm alloys were $\text{Ga}(\text{Sb}_x)\text{N}_{1-x}$ which has been measured for different antimony concentrations. The optical spectra for several $\text{Ga}(\text{Sb}_x)\text{N}_{1-x}$ layers with different Sb concentration are shown in **Figure 4.6 (a)** in the form of Tauc plots. The data suggests a direct band gap transition based on the UV-Vis reflectance data and Tauc plots for samples with Sb compositions up to 5%. Figure 3b shows the band gap data as a function of Sb concentration determined from the energy dispersive x-ray spectroscopy (EDS) analysis conducted using a scanning electron microscope (SEM). The x-axis error bars indicate the standard deviation of the Sb composition at different points on a sample. The transmission and the diffuse reflectance spectroscopy give the average band gap values over samples with 1 cm^2 area for the samples. Hence the y-axis error bars are not shown. Both experimental

and computational results suggest a rapid initial decrease in the band gap with an increase in the antimonide concentration for the $\text{Ga}(\text{Sb}_x)\text{N}_{1-x}$ system. These results indicate that an antimonide (Sb) concentration as low as 2% is sufficient to bring down the band gap of GaN from 3.45 eV to the visible range (~ 2 eV). After the initial decrease, the band gap seems to decrease at a slower pace with Sb concentration to about 1.5 eV with antimony

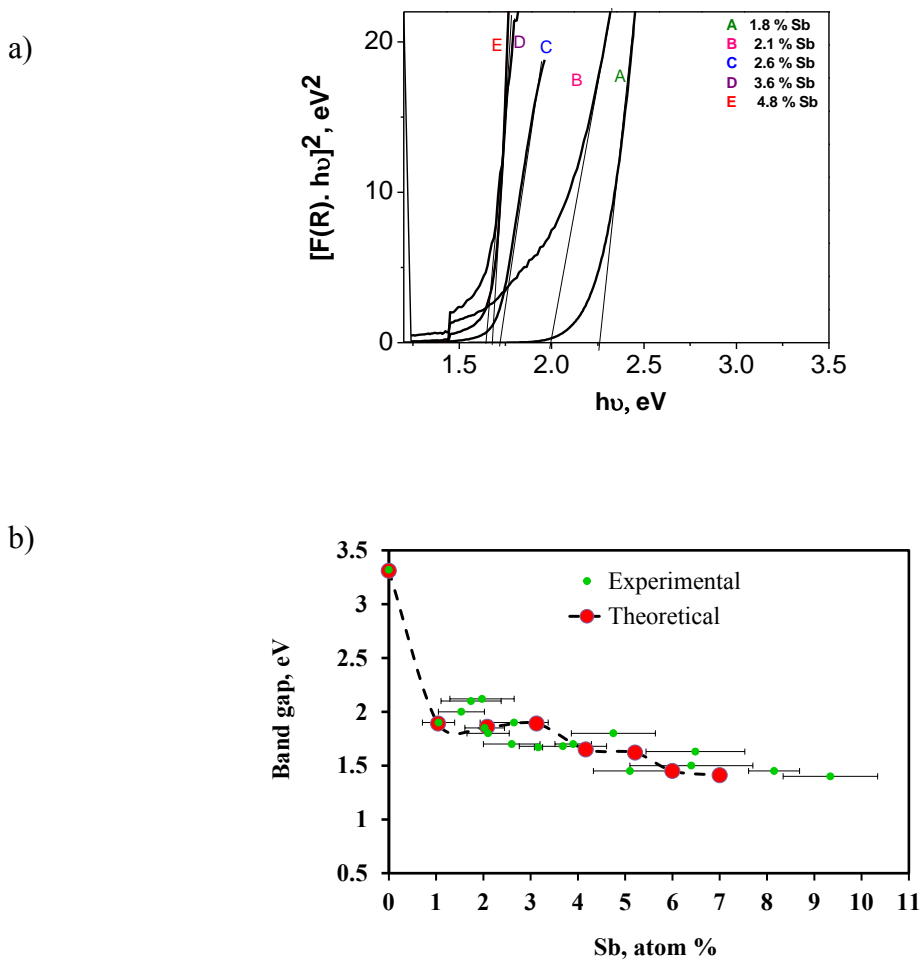


Figure 4.6 (a) UV-Vis absorption spectra of $\text{GaSb}_x\text{N}_{1-x}$ samples (b) Experimental and theoretical energy band gap of $\text{Ga}(\text{Sb}_x)\text{N}_{1-x}$ alloys as a function of Sb concentration.

concentrations as high as 8%. Introduction of the first substitutional Sb produces a localized state just above the valence band maximum (VBM) of GaN. Addition of more substitutional Sb atoms broadens and delocalizes this state. This explains the rapid initial decrease and subsequent slow variation of the band gap seen in Figure 4.6 b. Both UV-Vis data and photoluminescence analysis as shown in suggest that the optical band gap values reported for alloys with Sb compositions up to 6% or below are due to direct electronic transitions.

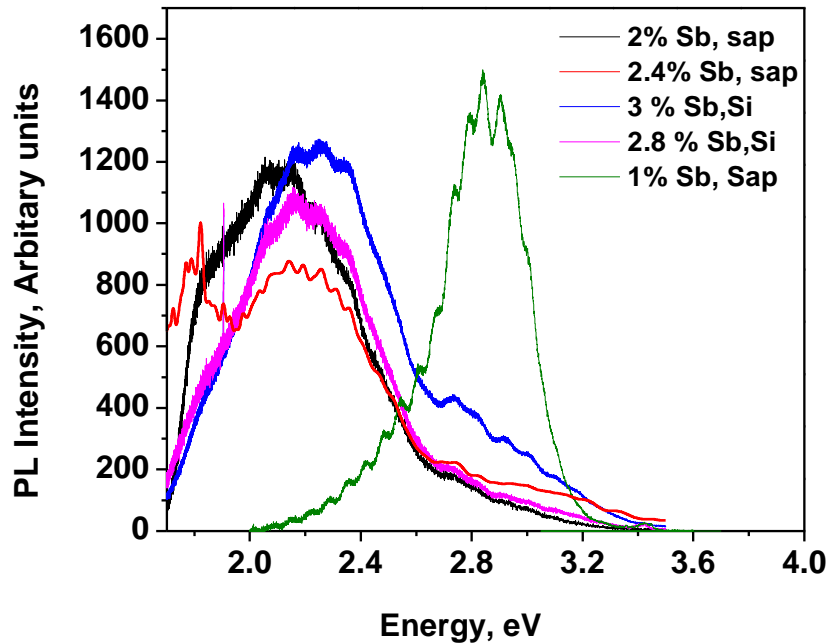


Figure 4.7 a) Low temperature Photoluminescence spectra for $\text{GaSb}_x\text{N}_{1-x}$ alloys with varying Sb composition.

Figure 4.7 a) shows the photoluminescence spectra of $\text{GaSb}_x\text{N}_{1-x}$ samples for different antimony (Sb) concentrations. A broad peak around visible range is seen. Even though, the peaks are broad their actual peaks range from 1.7 – 2.8 eV. Tauc plot analysis for these samples confirms the bandgaps of the same samples are shown in Figure 4. The

variation of the peak position with Sb concentration and the absence of 3.4 eV peak (corresponding to band edge emission of GaN) showed that the PL signal was from the band edge emission of $\text{GaSb}_x\text{N}_{1-x}$. The broadening of the peak could be related to the formation of deep level point defects such as native defects, impurities and complexes during the synthesis which could cause electron-phonon coupling.¹²⁰ No PL signal is observed at room temperature. This could be attributed to the thermal quenching of PL at elevated temperatures, where carriers return from the excited state to the ground states via non-radiative recombination pathways.

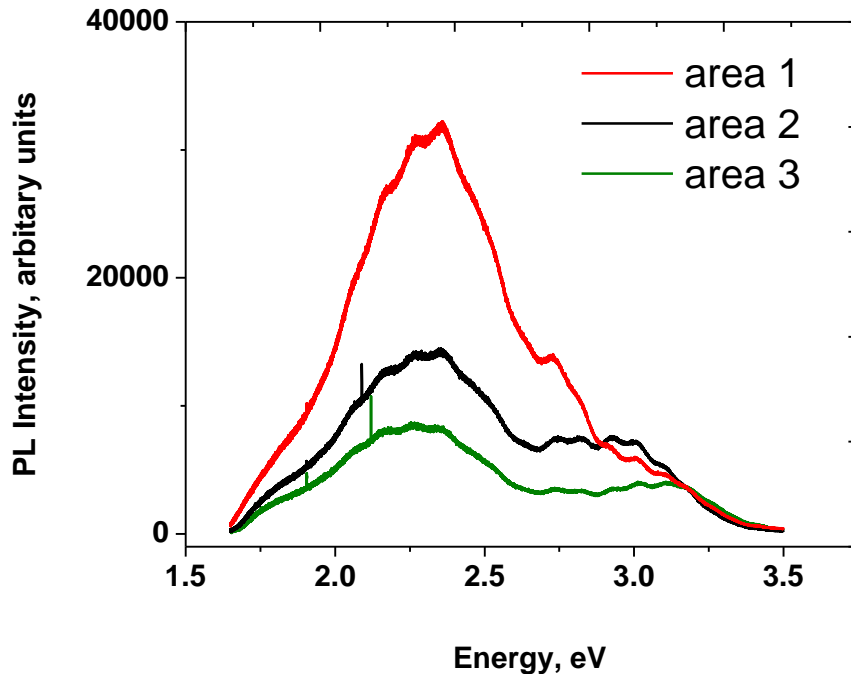


Figure 4.7 b) Photoluminescence spectra for sample containing 1.5 ± 0.8 % Sb at 241 K.

Prior reports on growth of ternary alloys of GaN have also reported a loss in the PL intensity with increased temperature due to thermal quenching.¹²¹ DFT calculations indicate that in the composition range from 0 to 1 %, Sb forms discrete energy states rather than a band. Moreover, there is no reduction in the electronic band in this

composition range. Low temperature PL measurements on samples with close to 1% Sb also show some evidence that a discrete energy level is formed in this range of composition. Photoluminescence spectra on different regions of a sample with about 1% Sb is shown in Figure 4.7 (b). The peaks in the 2.6 to 3.2 eV energy range in addition to the dominant peak seen at around 2.2 eV, these peaks could be due to the transitions from states close to the conduction band of GaN. These peaks are absent in the PL spectra of samples with high Sb content ($> 2\%$) as shown in Figure 4.7 (a). The peak at 2.2 eV could be attributed to transition from the conduction band edge of GaN to the Sb discrete energy level. The variations in the PL spectra are due to a gradient in the Sb composition in the sample. These variations coupled with error associated with measuring Sb composition using energy dispersive spectroscopy in a SEM make it challenging to obtain samples precisely in the 0 to 1% Sb composition.

Tauc plot analysis on $\text{Ga}(\text{Sb}_x)\text{N}_{1-x}$ samples with different Sb composition shows that the nature of the band gap was found to change from direct to indirect for Sb composition higher than 7% as shown in Figure 4.8 (a) which was also confirmed by photocurrent spectroscopy for high Sb concentrations. DFT calculations also predict direct to indirect band electronic transition for optical band gaps for alloys with Sb compositions greater than 7%. However, for alloys with Sb compositions near 1% or below, the data is insufficient to prove a continuous band gap reduction from 3.45 eV to ~ 2 eV. Instead, both DFT band structure and experimental data using photoluminescence (Figure 4.7 b) suggest localized density of states near a discrete energy state.

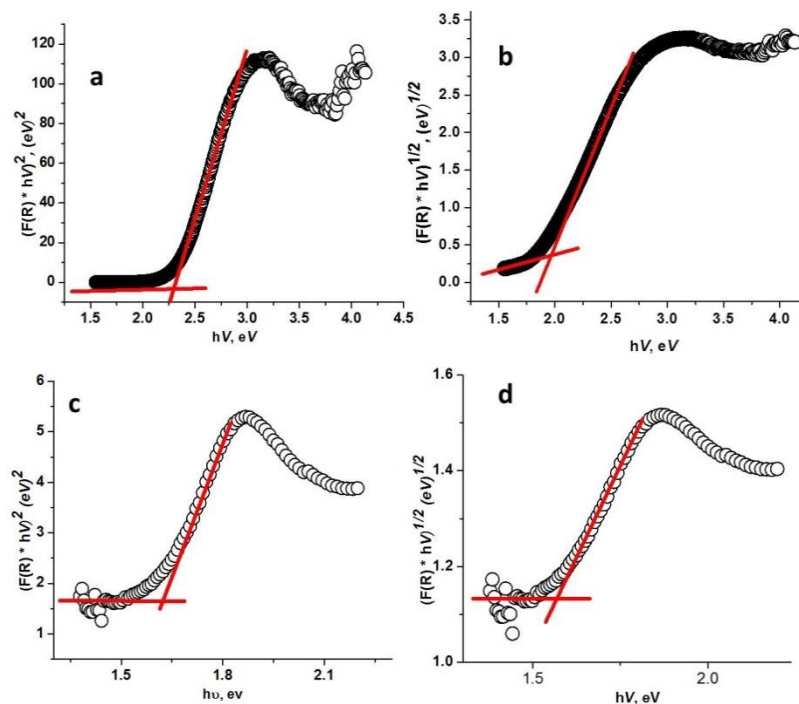


Figure 4.8 a) Tauc analysis for direct transition and indirect transition for 2% Sb (a,b) and 8% Sb (c,d).

The nature of the band gap was found to change from direct to indirect as the Sb composition increased above 7%. Tauc plots in the Figure 4.8 (a) show that at low Sb compositions ($< 7\%$) the Tauc plots for direct band transition provide a better linear fit and that for high Sb compositions ($> 7\%$) Tauc plots for the indirect band transition exhibit a better linear fit.

Photocurrent spectroscopy was also used to verify the nature of the band gap (direct/indirect) for samples with high Sb composition. The chopping frequency was 71 Hz and a bias of 1.4 V vs. Ag/AgCl was used. The electrolyte was a 0.5 M Na_2SO_4 solution adjusted to pH=9 using a 1 M sodium hydroxide. The experimental setup used to characterization is described elsewhere.⁵⁴ Figure 4.8 (b) shows the plots for two different

samples with high Sb composition ($> 6\%$) and it is seen that band gap becomes indirect at higher Sb compositions.

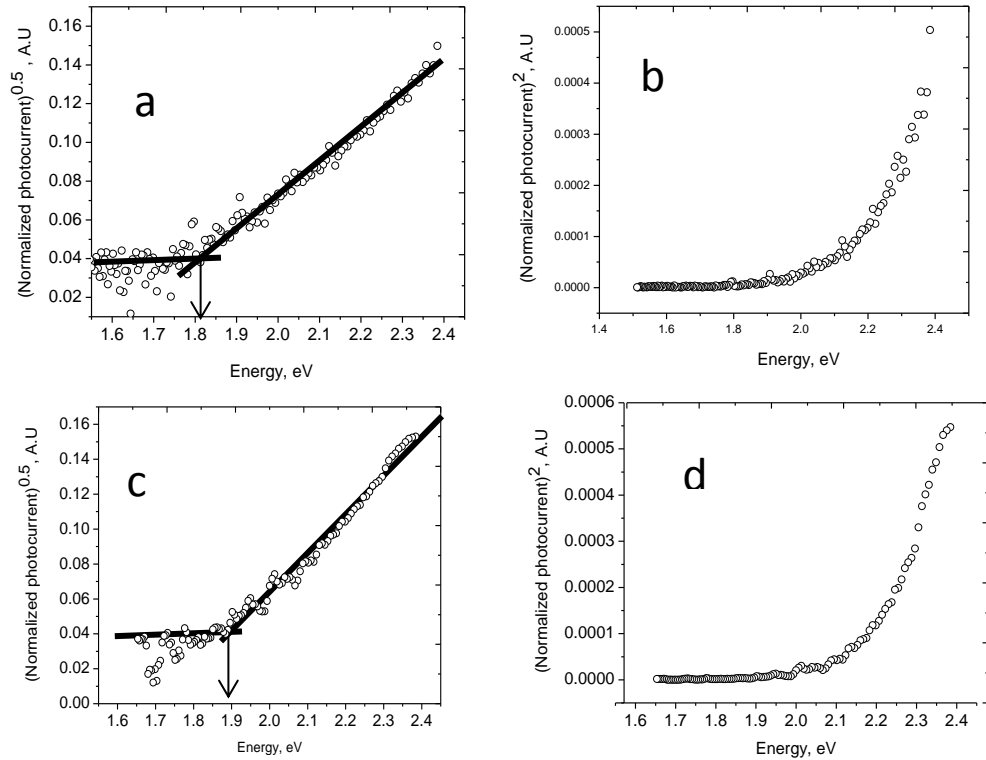


Figure 4.8 b) Photocurrent spectroscopy plots: a) and c) for indirect transition; and b) and d) for direct transition. The data is for $\text{GaSb}_x\text{N}_{1-x}$ samples with Sb composition greater than 7%.

4.4 Photoelectrochemical Characterization

4.4.1 Band edge determination

Band edges have been determined using Mott-Schottky analysis at different antimony concentrations. The band edge positions of $\text{Ga}(\text{Sb}_x)\text{N}_{1-x}$ alloys were determined using Mott-Schottky analysis as shown in Figure 4.10 for location of Fermi-energy level (very close to the conduction band edge position for these n-type semiconductors) and the

band gap values. The positive slope in the Mott-Schottky plots (Figure 4.9) shows that the $\text{Ga}(\text{Sb}_x)\text{N}_{1-x}$ alloys have an n-type conductivity. The band edge diagram (Figure 4.10) shows that the band gap reduction occurs mainly due to valence band shifting upwards. The band edge diagram also illustrates that the band edges of the $\text{Ga}(\text{Sb}_x)\text{N}_{1-x}$ alloys straddle the water oxidation and reduction potentials even at Sb concentrations around 8 at%. If the band edges of semiconductor straddle the water oxidation and reduction potentials, the inbuilt voltage generated in the semiconductor under illumination is sufficient to observe photocurrents at zero bias. To further validate that the $\text{Ga}(\text{Sb}_x)\text{N}_{1-x}$ band edges straddle the water redox potentials, linear sweep voltammogram was obtained under intense chopped light illumination using a two electrode configuration with a $\text{Ga}(\text{Sb}_x)\text{N}_{1-x}$ working electrode and Pt mesh counter electrode. Mott-Schottky analysis was used to determine the flat band potential of the $\text{GaSb}_x\text{N}_{1-x}$ alloys. The flat band potential becomes less negative with increasing Sb concentration as shown in Figure 4.9. The small change in the flat band potential indicates that the band gap reduction occurs mainly due to the valence band edge moving upwards. The flat band potential along with band gaps are used for determining the band edge positions shown in Figure 4.10. Band edge positions of $\text{GaSb}_x\text{N}_{1-x}$ alloys calculated from the Mott-Schottky plots and the band gap straddle the water oxidation and reduction potential. A semiconductor straddling the oxidation and reduction potentials should split water without any external bias. To verify this, a chopped J-V curve is obtained with a two electrode setup comprising of a $\text{GaSb}_x\text{N}_{1-x}$ working electrode and Pt counter electrode. The $\text{GaSb}_x\text{N}_{1-x}$ sample used for this test was synthesized on FTO substrate and a back contact was made to FTO during the preparation of the working electrode. The electrolyte was nitrogen purged 0.5 M

sodium sulfate, adjusted to pH=9. A light intensity of 500 mW/cm² was used. The photocurrent at zero applied bias (Figure 4.11) also validate that the band edges straddle the water oxidation and reduction potentials.

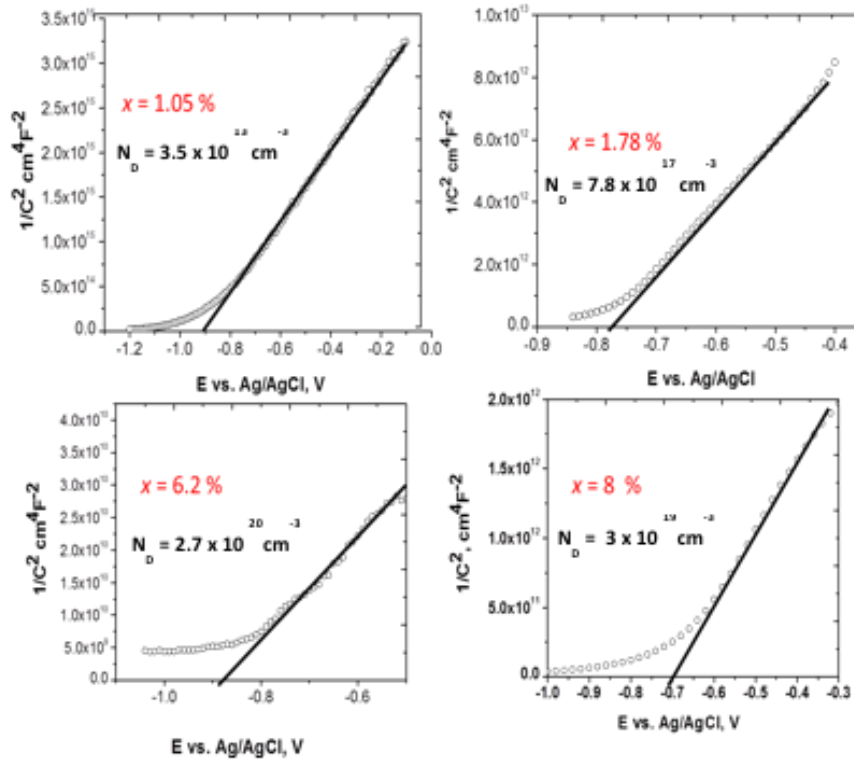


Figure 4.9 Mott- Schottky plots for various GaSb_xN_{1-x} samples with different Sb compositions.

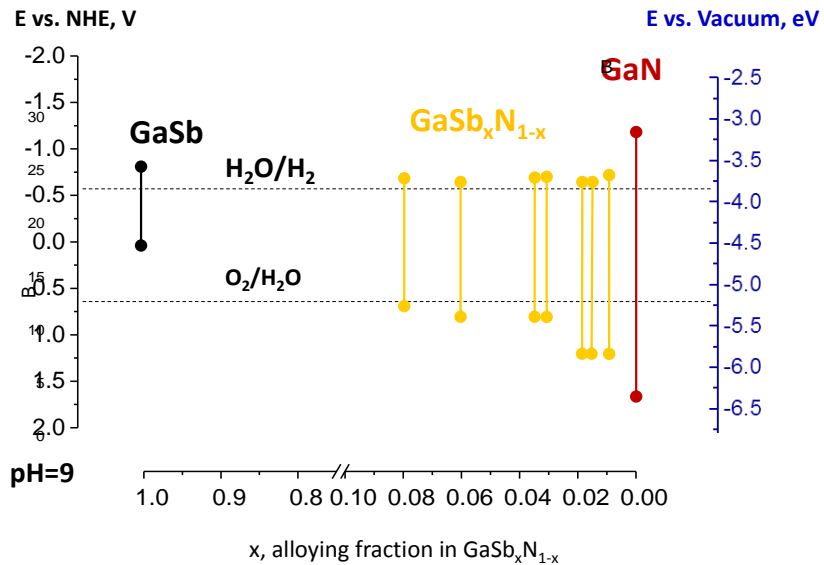


Figure 4.10 Energy diagram showing the band edge positions for various $\text{GaSb}_x\text{N}_{1-x}$ alloy samples. The band edge positions of GaSb and GaN are added for reference.

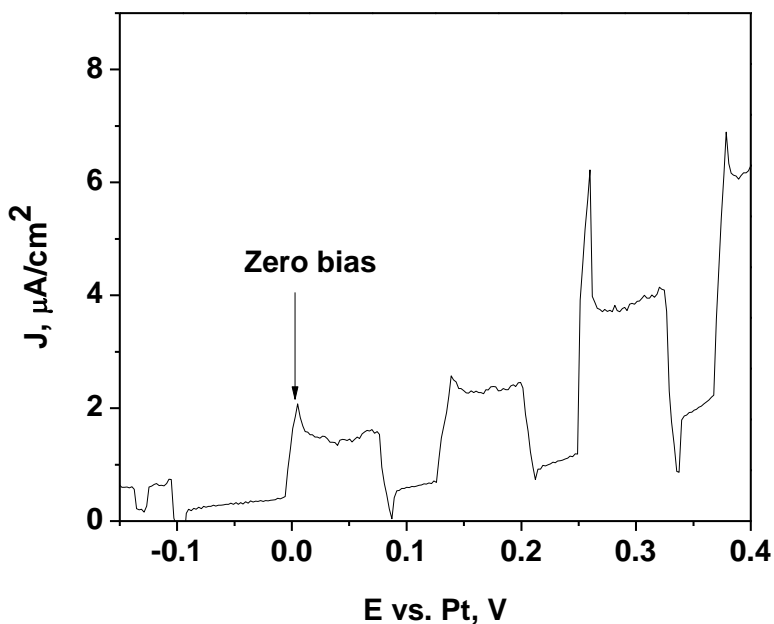


Figure 4.11 Two electrode chopped light linear sweep voltammogram for a $\text{GaSb}_x\text{N}_{1-x}$ sample in a 0.5 M Na_2SO_4 at pH = 9.

4.4.2 Illuminated Open Circuit Potential

Open circuit potential measurements were performed on $\text{GaSb}_x\text{N}_{1-x}$ layers to determine the conductivity type of the samples using a three electrode setup as explained in chapter 3. Light was chopped manually onto the working electrode which is $\text{GaSb}_x\text{N}_{1-x}$ samples and voltage was measured between working electrode and reference electrode using potentiostat. Ag/AgCl was used as reference electrode. Open circuit potential measured w.r.t time is shown in Figure 4.12 which was done for 25 minutes. From the plot, it is observed that the direction of the potential shift is positive which shows that material is n-type.

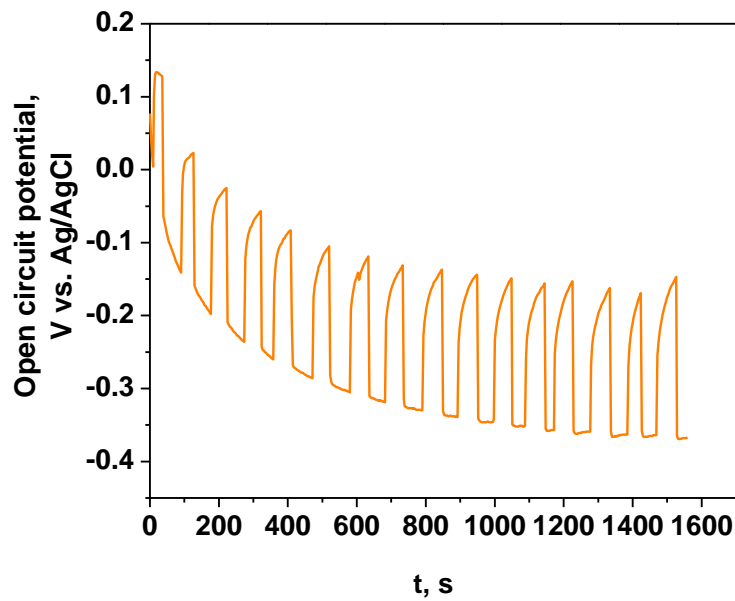


Figure 4.12 Chopped open circuit potential vs time for a $\text{GaSb}_x\text{N}_{1-x}$ sample.

4.4.3 Photocurrent Measurements

Photo-electrochemical measurements of polycrystalline $\text{Ga}(\text{Sb}_x)\text{N}_{1-x}$ films (200-300 nm) with small grain sizes (11nm) showed that they are photoactive as shown in Figure 4.13 b). The photo-electrochemical characterization was performed on polycrystalline $\text{GaSb}_x\text{N}_{1-x}$ thin films. Figure 4.13 a) shows a linear sweep voltammogram of a polycrystalline film ($x = 6\%$) under prepared on a fluorinated tin oxide coated (FTO) glass substrate. An ohmic contact was established with the FTO substrate using a silver epoxy. A chopped light of 1 Sun intensity ($100 \text{ mW}/\text{cm}^2$) from a Xenon lamp equipped with an AM 1.5 filter was used.

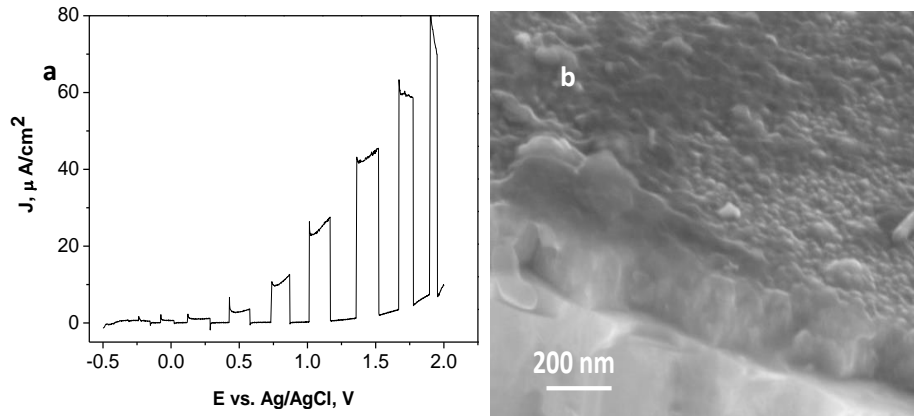


Figure 4.13 (a) Linear sweep voltammogram for a polycrystalline $\text{GaSb}_x\text{N}_{1-x}$ thin film sample ($x=6\%$) under chopped AM 1.5 illumination at 1 Sun (b) Cross-section scanning electron microscopy image of thin film sample.

A $0.5 \text{ M Na}_2\text{SO}_4$ solution adjusted to $\text{pH}=9$ (using a 1 M NaOH solution) was used as the electrolyte. The characterization was performed using a 3-electrode setup comprising of Ag/AgCl reference electrode, Pt mesh counter electrode and $\text{GaSb}_x\text{N}_{1-x}$ working electrode. These thin film samples ($\sim 200 \text{ nm}$) showed no loss in photocurrents in short

term stability test performed for 10 min. A bias of 0.9 V vs. Ag/AgCl was applied and the sample was exposed to chopped AM 1.5 light at 1Sun intensity. The photocurrent magnitude is limited by the shorter carrier diffusion lengths due to the small grain sizes, limited film thickness for the light absorption and the accumulation of charge carriers at the semiconductor-water interface. The grain size was calculated from full width half maxima of the XRD peak of $\text{GaSb}_x\text{N}_{1-x}$ thin film shown in Figure 4.14 using the Scherrer equation $B \times 2\theta = (k\lambda)/l \cos \theta$ which came about 11nm which is very low. This clearly states that thin film samples have very small grain sizes which act as grain boundaries where recombination occurs. Even though the material is efficiently generating carriers upon light absorption due to this recombination the photocurrents turning out to be very low.

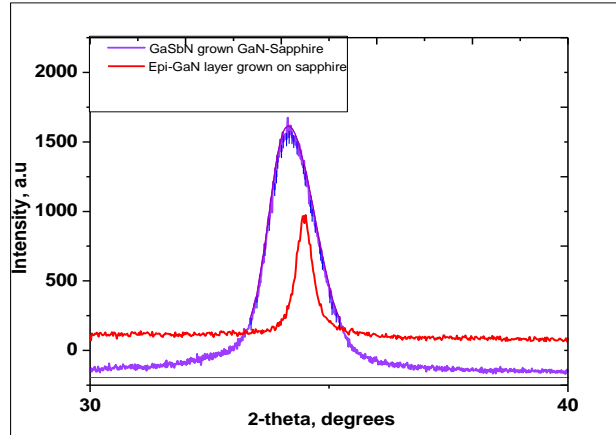


Figure 4.14 XRD patterns for a $\text{GaSb}_x\text{N}_{1-x}$ sample and GaN showing peak at 34.5 °.

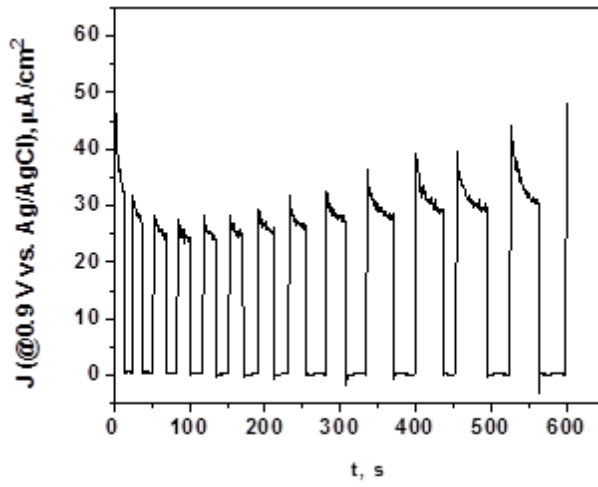


Figure 4.15 Chopped photocurrent density versus time for a $\text{GaSb}_x\text{N}_{1-x}$ sample at an applied bias of 0.9 V vs Ag/AgCl using AM 1.5 illumination at 1 sun.

The current density at high light intensity ($\sim 700 \mu\text{A}/\text{cm}^2$ at 5 Sun and 0.9 V vs. Ag/AgCl) shows that material hold great promise for solar water splitting. Increase in current density with light intensity and transient decay associated with current density (Figure 4.17) indicate the low light absorption in thin films (< 1 micron) and interfacial charge accumulation as important factors limiting the photocurrents for the polycrystalline samples. These phenomena also contribute to the more positive photocurrent onset potential seen than that would be expected from the Mott-Schottky determined flatband potential. Further, the high overpotential associated with oxygen evolution due to no surface catalyst, recombination at low bending could lead to more positive flat band potential values observed from photocurrent onsets.¹²² All the above preliminary PEC characterization results suggest an excellent suitability and high promise for using $\text{Ga}(\text{Sb}_x)\text{N}_{1-x}$ towards solar water splitting. There is a large parametric space available

with the MOCVD technique necessary to obtain highly textured films and epitaxial growth on nanowire array substrates for improved photoactivity.

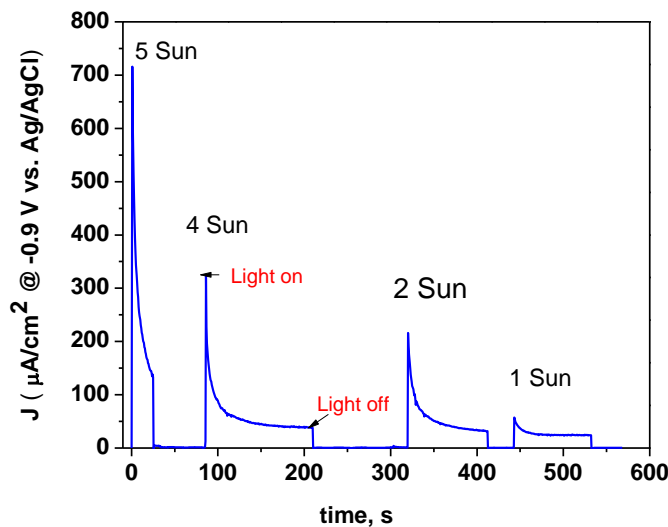


Figure 4.16 Photocurrent density vs light intensity for a $\text{GaSb}_x\text{N}_{1-x}$ sample at 0.9 V vs Ag/AgCl.

In summary, the synthesis of crystalline $\text{Ga}(\text{Sb}_x)\text{N}_{1-x}$ alloys is reported for first time and the optical properties demonstrate significant reduction of the band gap for GaN from 3.45 eV to 2 eV when alloyed with small amounts of antimonide (about 2%). Most importantly, the band edges for $\text{Ga}(\text{Sb}_x)\text{N}_{1-x}$ alloys (with x from 1.5% to 8%) straddle water splitting reactions for a range of band gap values from ~ 2 eV to 1.54 eV. The alloys with Sb levels beyond 7% showed indirect band gap values. The corresponding photo-electrochemical data on activity and stability suggest that these alloys are highly suitable for solar water splitting. Even though, the MOCVD is conducted at much lower temperatures of around 575 $^\circ\text{C}$ for $\text{Ga}(\text{Sb}_x)\text{N}_{1-x}$ alloys, the growth on GaN nanowire substrates allowed for epitaxial growth over entire lengths suggesting faster adatom diffusion.

CHAPTER 5

VAPOR-LIQUID-SOLID (VLS) GROWTH OF $\text{GaSb}_x\text{N}_{1-x}$ NANOWIRES

5.1 Introduction

In this chapter, the experimental investigation of $\text{GaSb}_x\text{N}_{1-x}$ nanowire growth via MOCVD using copper as a catalyst has been studied in detail. The resulting nanowires were characterized for antimony incorporation and also for their optical and photoelectrochemical properties.

5.2 Rationale/Motivation

The rationale for using vapor-liquid-solid growth is to see the possibility of increasing antimony incorporation and improve quality through VLS growth for $\text{GaSb}_x\text{N}_{1-x}$ Nanowires. Single crystalline films and/or single crystal nanowire arrays are ideal for efficient photocurrent generation as they have high mobility and ideal optical absorption and diffusion length scales. It is typically difficult to synthesize single crystalline films and requires special lattice matching substrates. In the case of $\text{GaSb}_x\text{N}_{1-x}$ alloys, it is even more difficult because of the synthesis temperature that is too high for allowing antimony incorporation. Polycrystalline thin films possess several grain boundaries where annihilation of generated carriers occurs in the recombination process, thus acting as trap sites. The carrier recombination process destroys the current resulting in near zero response despite efficient generation of carriers upon light absorption. Therefore,

polycrystalline films are not reliable to show efficient photoresponse. Instead, it is easier to obtain single crystal quality 1-D materials using vapor-liquid-solid method. In addition to quality, nanowire arrays also offer another advantage, i.e., provide the necessary length scales for absorption depth while reducing the length scale for minority carrier diffusion to semiconductor-electrolyte interface.¹²³ This in turn drives the electrochemical reactions in nanowires resulting in efficient light absorption and charge transport, hence making them reliable materials for solar water splitting.

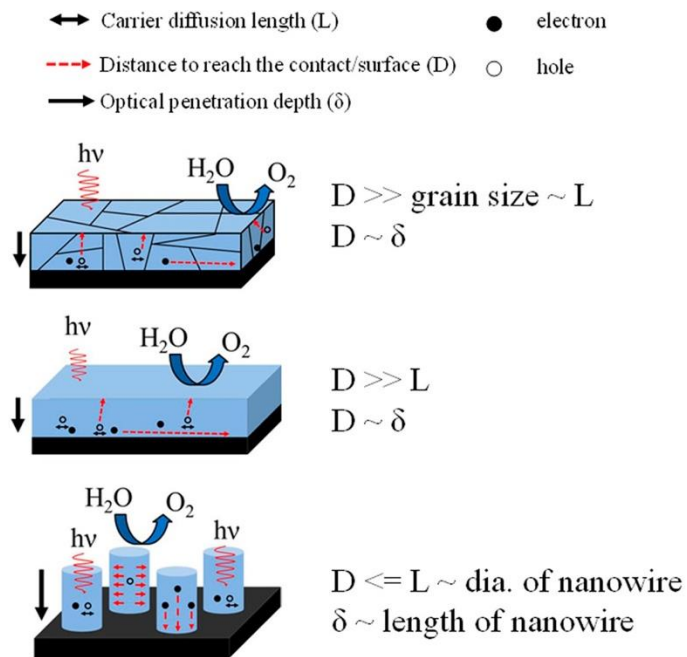


Figure 5.1 Schematics illustrating differences with carrier diffusion and absorption length scales involved with polycrystalline film vs single crystalline films vs nanowire array samples when used for photoelectrochemical water splitting.⁶⁰

There is a significant interest in growing nanowire arrays of III-V materials for improving the charge transport and light absorption toward solar energy conversion to fuels. Understanding the growth mechanism of III-V ternary alloy nanowires is crucial

for minimizing the defects. Unlike elemental and binary compounds, the growth of ternary alloy nanowires is not straight forward and fewer studies have reported ternary alloy nanowires particularly for III-V alloys. Despite the advantages of ternary alloy nanowires, they often undergo the complications like lattice mismatch, composition inhomogeneity, defects due to their complex thermodynamics and growth kinetics. In addition, understanding the growth mechanism of ternary alloys is not straight forward as it is for binary compound nanowires as binary and ternary alloys have different competing mechanisms for incorporation and diffusion of different species during growth. In addition, the differences with solubility in to catalyst metal and precipitation kinetics can also impact non-homogeneity of the composition along the nanowire.

Recently, a few attempts have been made to grow ternary alloy nanowires. For example in the case of $\text{Al}_x\text{Ga}_{1-x}\text{As}$ nanowires by Lim et al,¹²⁴ and $\text{In}_x\text{G}_{1-x}\text{As}$ nanowires by Guo et al,¹²⁵ composition inhomogeneity was observed, having high Al content in the AlGaAs whereas indium rich content near the InGaAs nanowire tip. Low diffusion lengths of Al and In that of compared to Ga were the reasons for this inhomogeneity. Tambe et al attempted to address this problem by growing AlGaAs nanowires at higher temperatures in capped morphology with GaAs nanowires.¹²⁴ Several other studies that were reported on ternary alloy nanowires showed the role of growth temperature in achieving uniform and defect free nanowires.¹²⁶⁻¹²⁹ Most of the III-V ternary alloy nanowires were synthesized on single crystalline substrates like GaAs which are very expensive. The synthesis was done using gold as a catalyst, which can introduce defects and is also very expensive.¹²⁴

Hence, there is a need to investigate the growth of ternary alloys nanowires on different substrates and using non-precious metals such as copper as catalysts. Especially, dilute ternary alloy nanowires could be very interesting as they have the potential to overcome phase segregation and composition inhomogeneity seen in the prior attempts. In a catalyst assisted VLS growth, the vapor phase species react on the catalyst surface supported on the substrate. Advantage of the catalyst is that it enhances the selectivity of vapor phase reactions on the surface. In VLS growth single nanowire is produced by single catalyst cluster so the diameter of the nanowire greatly depends on catalyst droplet. Hence, the selection of the catalyst in VLS growth is of utmost importance. In this study, among several metal catalysts like gallium, gold, tin and copper, copper was selected as a catalyst for the growth of $\text{GaSb}_x\text{N}_{1-x}$ nanowires. One reason for selecting copper was it is an inexpensive catalyst compared to all other metal catalysts available. Another reason was that it can be easily removed after deposition. Also our prior work showed that copper can form eutectic alloy with gallium at low temperatures around 550 °C and allow for vertical nanowire arrays.¹²³ Moreover from the phase diagram of Cu-Ga and Cu-Sb it was observed that formation of Cu-Sb eutectic alloy leads to bulk nucleation and growth due to low solubility eutectic of gallium species in the droplet. In the case of Cu-Sb, the composition of antimony in copper is very high which form micron size droplet favoring tip led growth. Moreover, the solubility of antimony in copper increases with increase in temperature that allows for more antimony incorporation at high temperatures which was very difficult while growing thin films. Therefore, our approach of using VLS growth will lead a path for antimony incorporation at high temperatures thereby achieving good crystalline quality nanowires.

5.3 Experimental Details

5.3.1 Catalyst deposition

Thermal evaporation method was used for the deposition of copper onto the substrates. The thermal evaporator used was a typical vertical bell jar with supply for heating, gas flow, pressure measurement and pumping. Inside the bell jar contains tungsten crucible where desired source material is placed. Prior to the evaporation, substrates were cleaned in 1M hydrochloric acid followed by rinsing with ethanol and DI water. Firstly copper pieces were placed in the crucible. Once the chamber reaches desired vacuum the crucible was heated to a desired temperature based on the melting point of the material that was evaporated. After the melting point was reached, material evaporated onto the substrates that were placed above the crucible. The time of the reaction was based on the desired thickness of the material. Reaction was done at 10^{-8} torr for two minutes.

5.3.2 MOCVD growth

In our MOCVD system, group III element Ga and group V element Sb were supplied as vapor phase organometallic precursor species: trimethylgallium ($\text{Ga}(\text{CH}_3)_3$, TMGa, trimethylantimony ($\text{Sb}(\text{CH}_3)_3$, TMSb) respectively. Also group V element N was supplied as vapor phase hydride ammonia. These reactants were carried into the reactor by carrier gas N_2 . Precursors pyrolyse to release group III and group V elements during the growth. A number of reports describe precursor pyrolysis in detail.^{81, 130}

For the experiments, several substrates were used for nanowire growth like GaN, highly doped n-type silicon, quartz where GaN was the mostly used substrate. Typically,

nanowires were grown on substrates of the same material, for instance GaAs nanowires were grown on GaAs substrates. Before growth, copper (Cu) nanoparticles were deposited on the substrate surface, as described in Section 5.3.1. The prepared substrate with deposited Cu nanoparticles was placed into the reactor on an AlN susceptor. The substrate was heated to 950 °C and annealed for 10 min to desorb surface contaminants, including the surface oxide. Annealing was performed under group V overpressure to prevent decomposition of the substrate. After annealing, the substrate was cooled to growth temperature, typically between 700-900 °C. The group V flow rate was adjusted for the growth. Then group III precursors were fed to the reaction chamber to initiate growth. The precursor flow rates used for the experiment were 0.2 μmol/min of trimethyl gallium and trimethyl antimonide was varied to achieve different compositions and ammonia with flow rate of 1 lpm. Growth times were generally between 30 minutes to 120 minutes, chosen according to the growth rate and the desired nanowire length. Upon completion of the growth, the samples were cooled under group V overpressure. All samples were grown with a reactor pressure of 70-80 torr range

5.3.3 Characterization

The synthesized nanowires were characterized by X-ray diffraction (XRD) in a Bruker Discovery D8 system utilizing Cu K α radiation (0.154 nm), Energy Dispersive X-ray Spectroscopy (EDS) in JEOL JSM-5310 scanning electron microscope (SEM) operating at 20 keV for elemental composition analysis, FEI Tecnai F20 field emission transmission electron microscope (TEM). TEM-based EDS measurements were conducted on these samples to further confirm the Sb concentration in the samples. High-resolution TEM (HRTEM) imaging of selected samples was used to characterize the

crystalline quality of the nanowires. All samples were optically characterized using a Perkin Elmer Lambda 950 UV-Vis spectrometer, with a 60 mm integrating sphere. The Kubelka-Mulk absorbance, estimated from the reflectance was used in the Tauc plot analysis. The thickness of the samples was measured using scanning electron microscopy and was used for the calculation of the absorption coefficient.

5.4 Results & Discussion

Firstly, the growth of $\text{GaSb}_x\text{N}_{1-x}$ nanowires was attempted in MOCVD using different catalysts Gallium (Ga), Copper (Cu), Tin (Sn) and antimony (Sb). Figure 5.2 shows SEM images of $\text{GaSb}_x\text{N}_{1-x}$ nanowires growth using different catalysts.

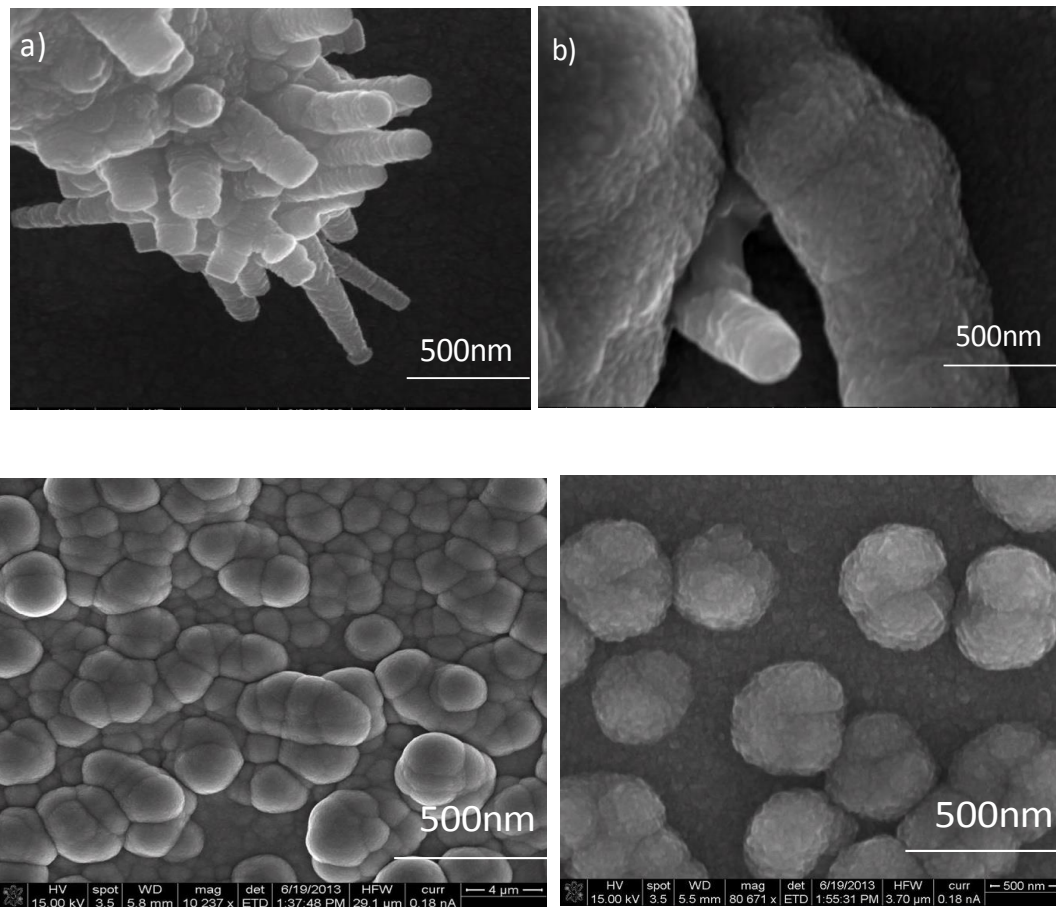


Figure 5.2 SEM images of $\text{GaSb}_x\text{N}_{1-x}$ nanowires grown using a) copper b) Gallium c) Tin d) antimony

Tin d) Antimony.

In Figure 6.2, image a) shows the growth of nanowires using copper as a catalyst. Images b, c & d show the growth using Ga, Sn and Sb droplets as catalysts. And from the images it was observed that the nanowire growth was occurred with copper whereas with other catalysts there was no nanowire formation. In order to understand this, phase diagrams of these catalysts with gallium and antimony were analyzed. From the phase diagrams of Ga-Sb, Cu-Ga, Cu-Sb, Sn-Ga and Sn-Sb, it was observed that at the growth temperatures used, copper and antimony form eutectic alloy. Figure 5.3 shows the phase diagram of the Cu-Sb system, which can be referred to the growth of 1D $\text{GaSb}_x\text{N}_{1-x}$ structures with copper. The phase diagram also indicates that the composition of the Cu-Sb alloy above the eutectic point will follow the liquidus line (solid lie) that denotes equilibrium between the solid and liquid phase. Therefore, the composition of the liquid alloy can be found at the liquidus line at a given temperature. The phase diagram of copper and antimony indicates that, with increase in the temperature, solubility of antimony in copper increases

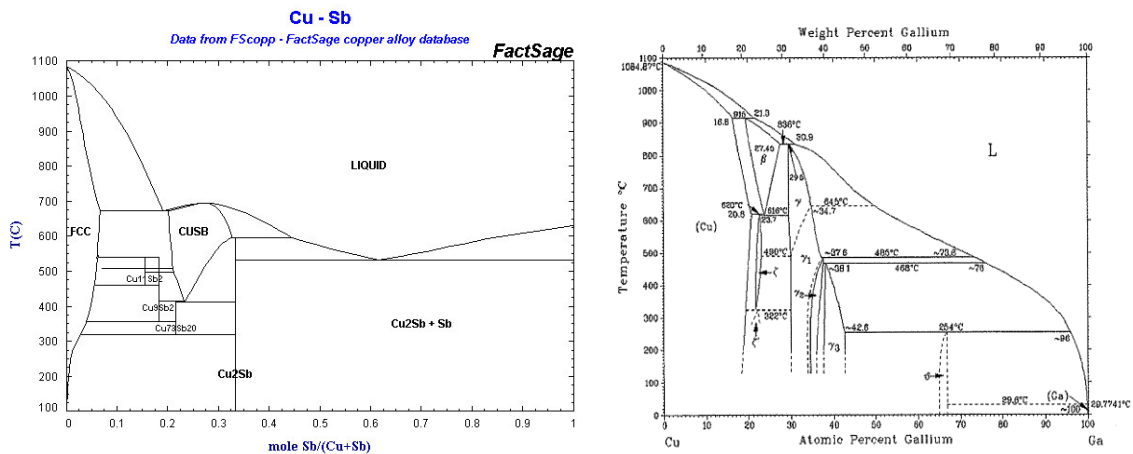


Figure 5.3 Phase diagrams of Copper- Antimony(ref:

<http://factsage.cn/fact/documentation/FScopp/Cu-Sb.jpg>) and Copper- Gallium

(<http://www.himikatus.ru/art/phase-diagr1/Cu-Ga.php>)

. Experiments were conducted using evaporated and sprayed copper particles on various substrates such as stainless steel, quartz and GaN on sapphire. In the Figure 5.4 a) SEM images show that nanowire growth was not uniform, this was because the copper catalyst was deposited using spray coating. In the subsequent experiments, Copper was deposited using thermal evaporation technique. Figure 5.4 shows SEM images of $\text{GaSb}_x\text{N}_{1-x}$ nanowires with copper as a catalyst which was deposited using thermal evaporation. The samples showed vertically inclined growth of nanowires with respect to the substrate which were uniform all over the sample. They were observed to be 2 microns long and 50-100nm diameters and densities of $0.4\text{--}0.5 \mu\text{m}^{-2}$. Nanowires were shown to have tapered morphology with reduced diameters from base of the NW to its tip. From literature, three main reasons were reported for tapering which were, increase in the contact angle of the tip of NW,^{131, 132} surface diffusion of excess adatoms to base of NW¹³³, instability of a catalyst tip.¹³⁴ All of the mentioned reasons show that they occurred due to change in the catalyst tip.

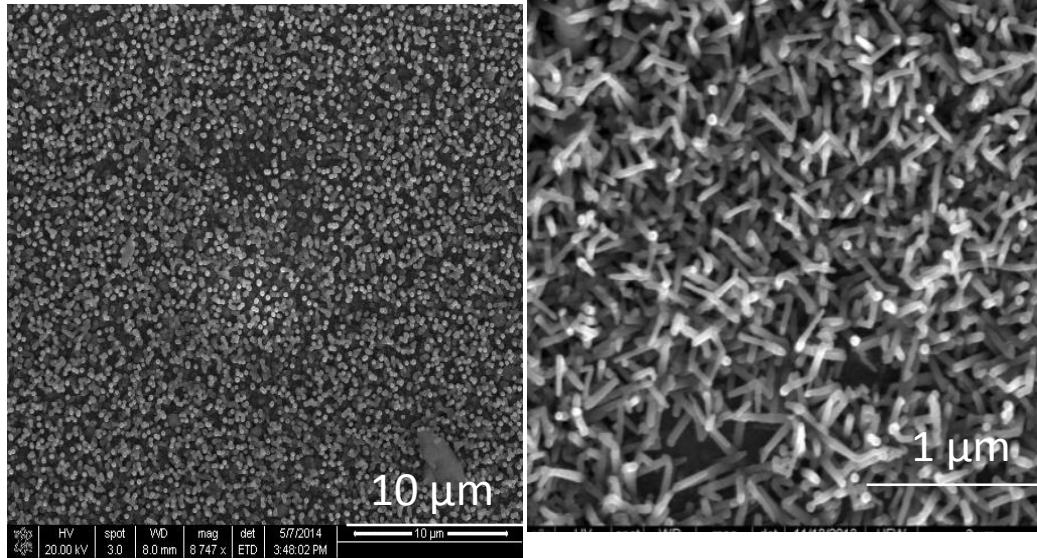


Figure 5.4 SEM image of $\text{GaSb}_x\text{N}_{1-x}$ nanowire array sample synthesized at 700 °C using copper as catalyst.

From the SEM images, spherical particles were observed at the nanowire top ends. In order to analyze and understand the tips of the nanowire, TEM analysis was performed. TEM investigations were performed on over a dozen nanowires from each sample to understand their structural and chemical characteristics. Firstly, TEM-EDS analysis was performed on the nanowires from base to the tip. Figure 5.5 shows TEM-EDS spectra obtained at different locations along the nanowires. From the EDS results on $\text{GaSb}_x\text{N}_{1-x}$ nanowire samples, the nanowire ends consist of antimony and copper, without Ga or N. Additionally, for each nanowire the EDS spectra comparison indicates that the Sb concentration in the nanowire tip was higher than that in the nanowire base. Figure 5.5 shows the composition analysis especially on the tip of the nanowire. The first profile in the figure shows the overall composition of the tip and rest of the profiles are showing for

individual elemental analysis. From these profiles, it was observed that the composition of antimony increased from neck of the nanowire to the tip.

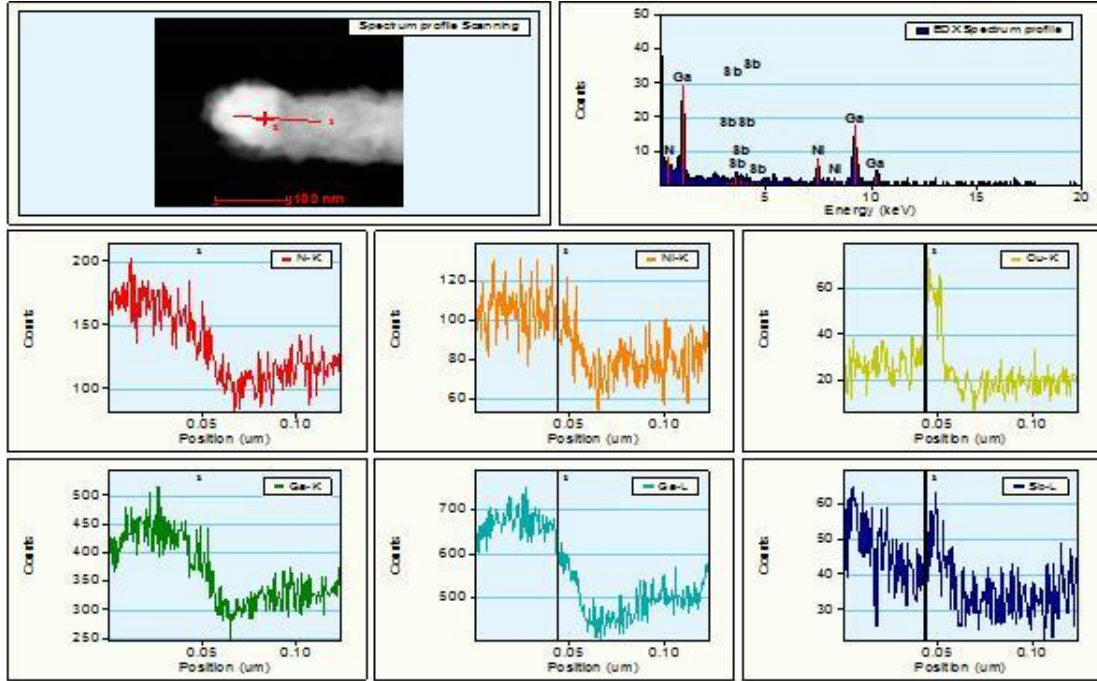


Figure 5.5 TEM-EDS line-scan compositional profile across a $\text{GaSb}_x\text{N}_{1-x}$ nanowire.

All the samples that were analyzed by TEM-EDS showed copper and antimony alloy on the nanowire tips thereby confirming our analysis from the phase diagram. The nanowire diameters were controlled using different thicknesses for the evaporated copper film. For example, evaporated copper films at 2 nm and 5 nm thicknesses resulted in $\text{GaSb}_x\text{N}_{1-x}$ nanowires with diameters of 50-70 nm and 80-100 nm respectively as shown in Figure 5.6 a) and b) respectively. As the size of the particle size increased from 5 nm film to 1 nm film, diameter of the nanowires was increased. Typically, III-V nanowire growth is limited by the nucleation rate at the three-phase boundary, which is related to the supersaturation of antimony in the seed particle and the surface energies of the vapor-

seed, vapor–solid, and seed–solid interfaces. Also, the EDS analysis on different samples revealed different antimony compositions, which corresponded with the optical data obtained from UV-Vis. The change in the antimony composition in the nanowires was due to the change in the antimony precursor flow rate.

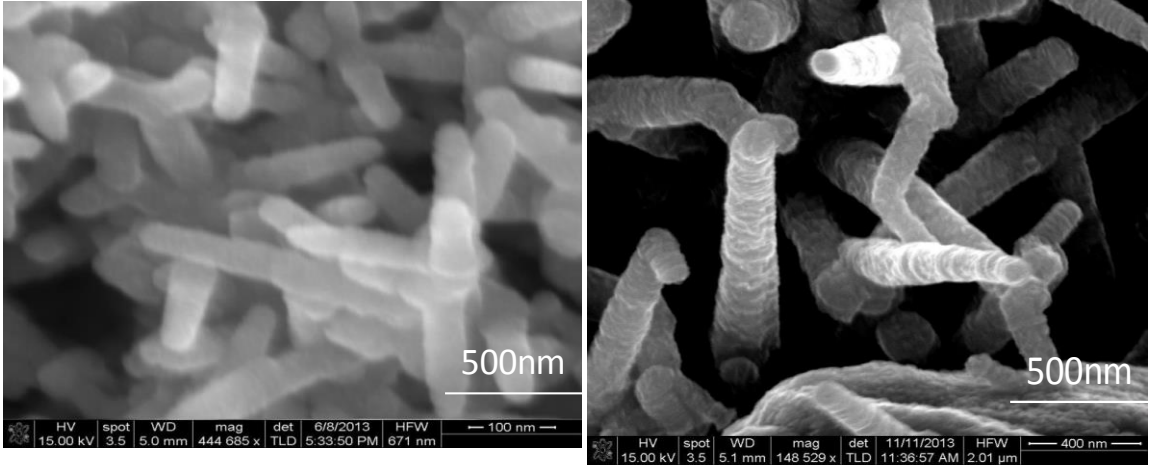


Figure 5.6 SEM images of $\text{GaSb}_x\text{N}_{1-x}$ nanowire growth using different catalyst thicknesses a) 2nm film b) 4nm film.

The optical properties of the nanowires grown at 700 °C were analyzed by UV-Vis spectroscopy and the Tauc plot showed a band gap value of 2eV with Sb composition of 2% that was calculated from SEM-EDS as shown in the Tauc plot in the Figure 5.7. Also X-ray diffraction pattern analysis of as synthesized $\text{GaSb}_x\text{N}_{1-x}$ alloy nanowires showed that peaks were similar to those we got from the previous work of $\text{GaSb}_x\text{N}_{1-x}$ thin films indicating the peak shift to lower angles with antimonide concentration. The d-spacing values were calculated using equations

$$\text{Hexagonal: } \frac{1}{d^2} = \frac{4}{3} * \left(\frac{h^2 + hk + k^2}{a^2} \right) + l^2 / c^2 \quad 5.1$$

$$\sin^2 \theta = \frac{\lambda^2}{4d^2}$$

5.2

$$\sin^2 \theta = \left(\frac{\lambda^2}{4} \right) = \left[\frac{4}{3} \left(\frac{h^2 + hk + k^2}{a^2} \right) + \frac{l^2}{c^2} \right]$$

5.3

The d-spacing value calculated for GaSb_xN_{1-x} nanowires grown at 700 C with 2 % Sb incorporation was found to be 2.6 Å which was also matched with the value determined from HRTEM analysis. This clearly confirmed that the antimony was incorporated into the nanowire. Figure 5.8 shows the TEM image of GaSb_xN_{1-x} nanowire where it shows the periodic narrowing and broadening along the nanowire. This could be due to the change in the geometry of the facets and shape of the droplet at liquid-vapor-solid interface where nucleation occurs. The geometry changes as the surface energy of the crystal changes while surface reconstructs for different precursor flow rates. This affects the geometry. Also HRTEM imaging was done on the samples which can be used to analyze crystal quality and d-spacing of the nanowires. From HRTEM analysis it was found that GaSb_xN_{1-x} nanowires have c-plane orientation and these wires were shown to be single crystalline with the presence of stacking faults. The defects usually form when there is a phase change from HCP to FCC, resulting in stacking faults. In the VLS growth, phase change is caused mainly due to change in chemical potential of liquid-solid interface (controlling the crystal precipitation) which is affected by the change in the molten alloy catalyst composition with changes occurring at vapor-liquid interface.¹²³ The stable phase for GaN is wurtzite phase but when the nucleation rate is fast, a nucleus

in the HCP orientation can grow into more energetically favorable FCC orientation. Also from the studies it was found that stacking faults will be prevalent at lower temperatures as FCC & HCP orientations were strongly favorable for smallest nucleus whereas at higher temperatures with larger nucleus only HCP orientation was favorable.¹²⁷

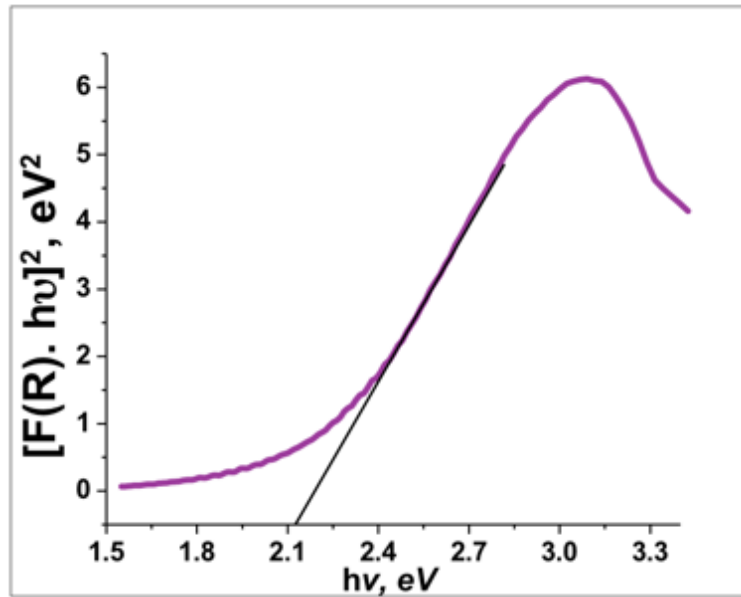


Figure 5.7 A Tauc plot obtained for a $\text{GaSb}_x\text{N}_{1-x}$ nanowire array sample grown on GaN substrate at 700°C .

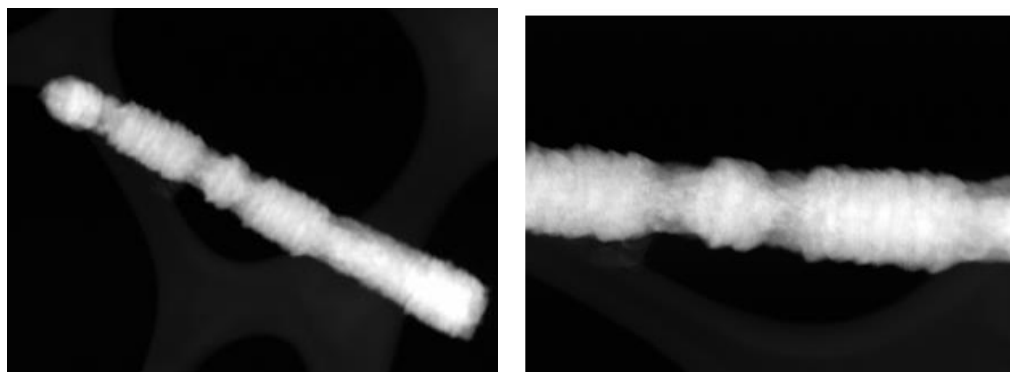


Figure 5.8 HRTEM images of $\text{GaSb}_x\text{N}_{1-x}$ nanowires on GaN substrate.

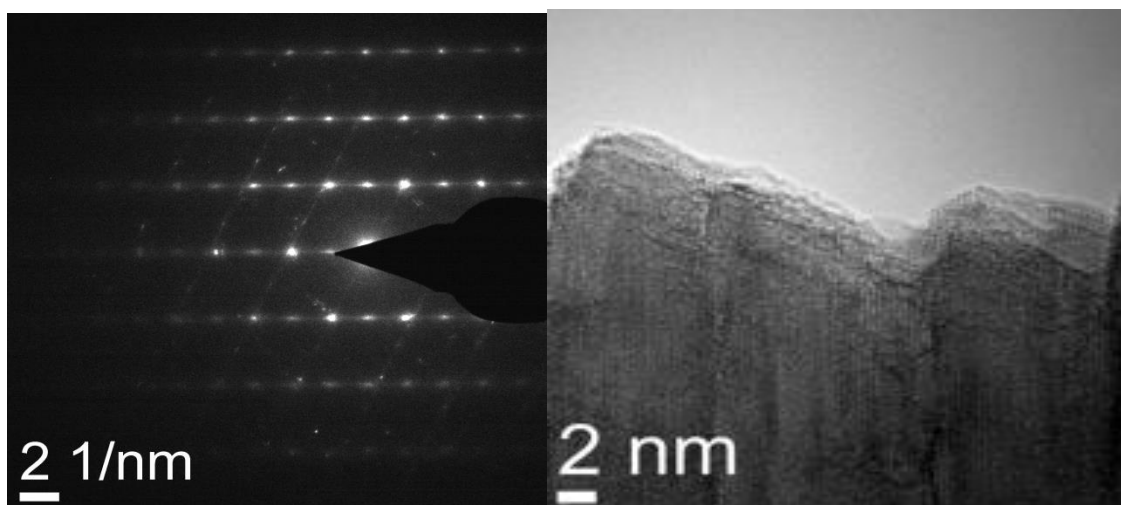


Figure 5.9 HRTEM image and SAED pattern of $\text{GaSb}_x\text{N}_{1-x}$ nanowire.

In order to improve the crystallinity, high temperature growth is of utmost importance. Literature studies have shown that the stacking fault density has been reduced with increase in the temperature.¹²⁷ Also, the thin films showed the improvement in crystallinity and increase in the grain size when grown at higher temperatures but antimony incorporation into the nanowires was not an easy task. This is further explained in detail in chapter 6. Figure 5.10 shows the SEM images and Tauc plots for $\text{GaSb}_x\text{N}_{1-x}$ nanowires at different temperatures. TEM-EDS analysis on the nanowires at different temperatures was performed and showed Sb incorporation into nanowires with slight increase in antimony with increase in temperature. Antimony composition was plotted at different temperatures as shown in Figure 5.11 and clearly showed the trend where antimony incorporation increased with increase in temperature. Also antimony composition in nanowires was corroborated with the band gap values measured using UV-Vis spectroscopy at different temperatures which also revealed tiny reduction in band gap with increase in temperature. This showed that the incorporation of antimony into

nanowires was easier when compared to thin films, which was explained by Cu-Sb phase diagram. From HRTEM analysis, it was clearly observed that $\text{GaSb}_x\text{N}_{1-x}$ nanowires have a Cu-Sb tip which led to the nanowire growth.

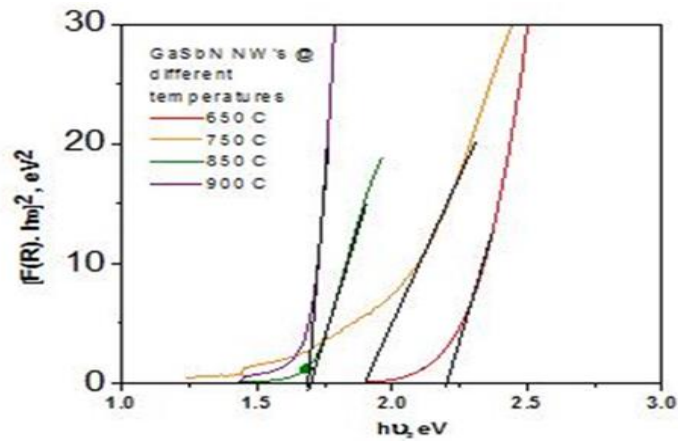
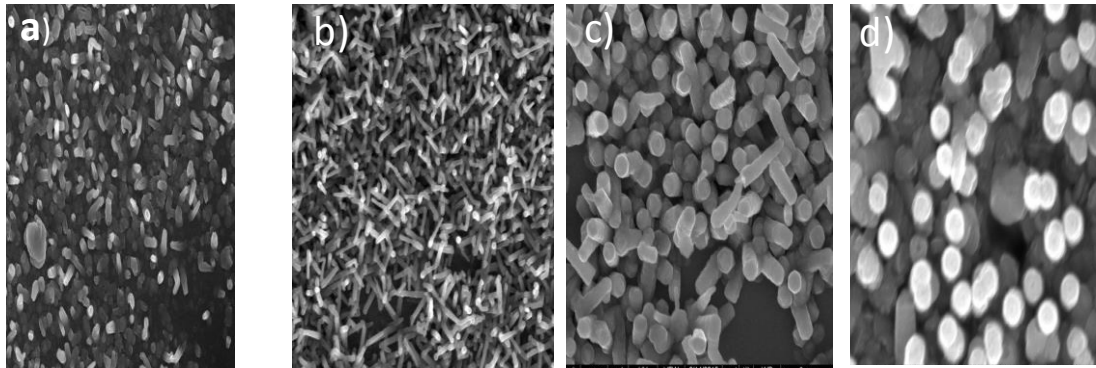


Figure 5.10 SEM images and Tauc plots of $\text{GaSb}_x\text{N}_{1-x}$ nanowires at different temperatures. The experimental conditions for the SEM images were a) 650 °C, Sb%- 2%, b) 700 °C Sb%- 2%, c) 800 °C Sb%- 3%, d) 900 °C Sb%- 4 %. Antimony composition was determined from TEM-EDS

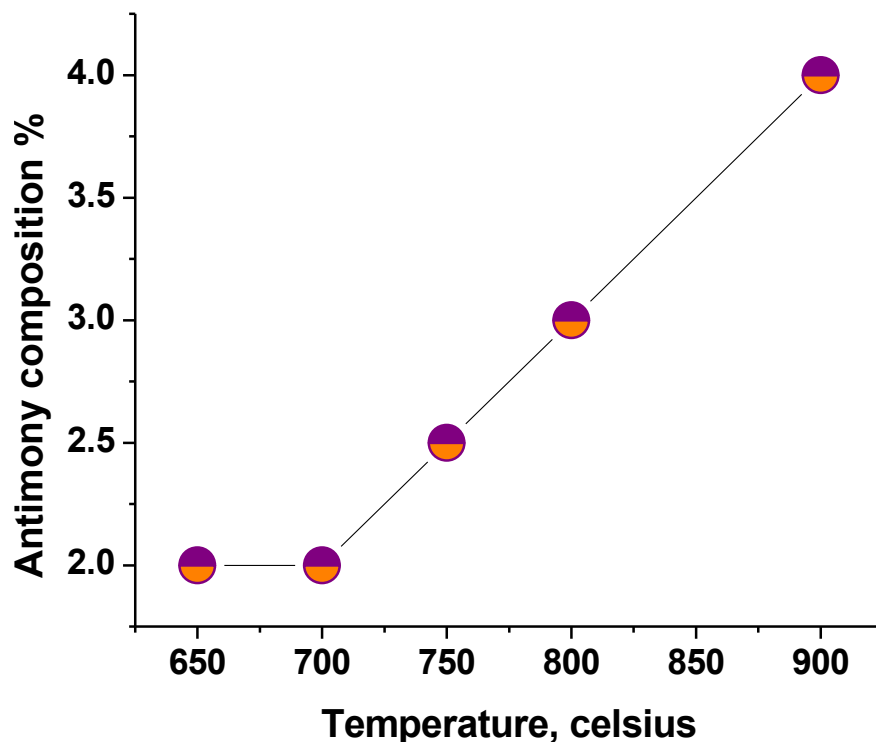


Figure 5.11 Plot of antimony composition as a function of synthesis temperature used for growing $\text{GaSb}_x\text{N}_{1-x}$ nanowires.

Figure 5.12 shows SEM images of $\text{GaSb}_x\text{N}_{1-x}$ nanowires at different temperatures. It was observed that morphology of the nanowires has been changed with temperature. At higher temperatures, nanowires were short and more perpendicular to the substrate. This typically occurs because of the increase in the rate of precursor decomposition and the adatom diffusion length, with the increase in the temperature. Also the diameters of the nanowires at high temperatures were slightly increased compared to that of low temperatures. This could be due to more adatoms diffusing from the substrate and along nanowire sidewalls. Tapering of the nanowires was also reduced at high temperatures which shows that growing nanowires has not only the advantage of high antimony incorporation and less defects but also less tapering which is very essential for many

device applications.

The growth of $\text{GaSb}_x\text{N}_{1-x}$ nanowires and all of the observations could be explained with principles involved with simple VLS mechanism as shown in Figure 6.11. The first step involves copper deposition followed by MOCVD growth. During MOCVD growth, as explained from the phase diagram, copper and antimony formed a eutectic alloy at around 650 °C and dissolution of Ga, Sb and N led to supersaturation which precipitates as $\text{GaSb}_x\text{N}_{1-x}$ nanowire. The catalyst was used to enhance the selectivity of the dissolution kinetics and diameter and growth direction of these nanowires were affected by the nucleation from the supersaturated metal droplet. Another interesting and important observation found from the phase diagram was that the solubility of antimony in copper increased with increase in temperature. Contrary to thin film growth, antimony dissolution into molten metals increased with temperature. This led to the higher antimony incorporation and better crystal quality of nanowires at higher temperatures. Taking advantage of this observation, a mechanism is proposed in this study to explain the growth of $\text{GaSb}_x\text{N}_{1-x}$ nanowires in the low antimonide region using VLS mechanism.

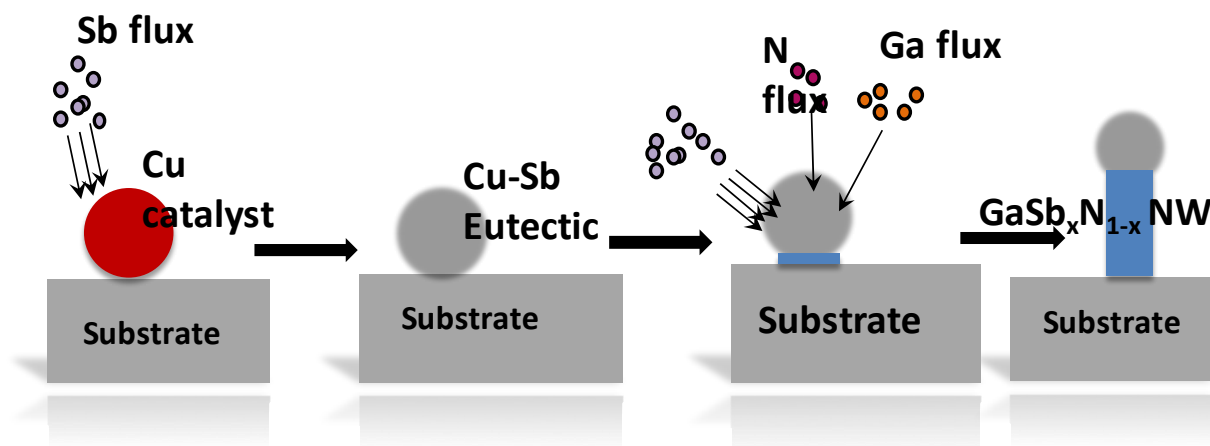


Figure 5.12 A schematic illustrating various stages of proposed growth mechanism for $\text{GaSb}_x\text{N}_{1-x}$ nanowires.

Several $\text{GaSb}_x\text{N}_{1-x}$ alloy nanowire array samples were characterized using photoelectrochemical and electrochemical techniques for their photoactivity. Linear sweep voltammetry was performed under chopped AM 1.5 illumination for the measurement of photoactivity of the $\text{GaSb}_x\text{N}_{1-x}$ nanowires. The photocurrent gradually increased with potential and attained a steady state value, indicating diffusion limited photocurrent at high potentials. A photocurrent of 0.35 mA/cm^2 was observed at potential of 1.5 V vs. RHE and was significantly higher than reported for polycrystalline $\text{GaSb}_x\text{N}_{1-x}$ thin films (\sim few tens of $\mu\text{A/cm}^2$). Figure 5.13 shows the chopped I-V measurement for $\text{GaSb}_x\text{N}_{1-x}$ nanowires grown at 700°C with 2% Sb incorporation. The observed onset potential of -0.2 V vs. RHE and the 2 eV band gap of the samples indicate that the material straddles the water redox potentials and hence does not require an external bias to split water unlike other III-V semiconductors that typically require a huge external bias to drive the water redox reactions because of their unfavorable band edge locations for water splitting. Although two orders of magnitude increase in photoactivity

has been observed in nanowires when compared to thin films, the photoactivity was still smaller than the theoretically expected value for a semiconductor with a 2eV bandgap. The reason behind the limitation could be due to several reasons like recombination of majority and minority carriers, slow catalysis at the semiconductor-liquid interface. The recombination in the nanowires occur mainly due to the presence of stacking faults which act as recombination centers.

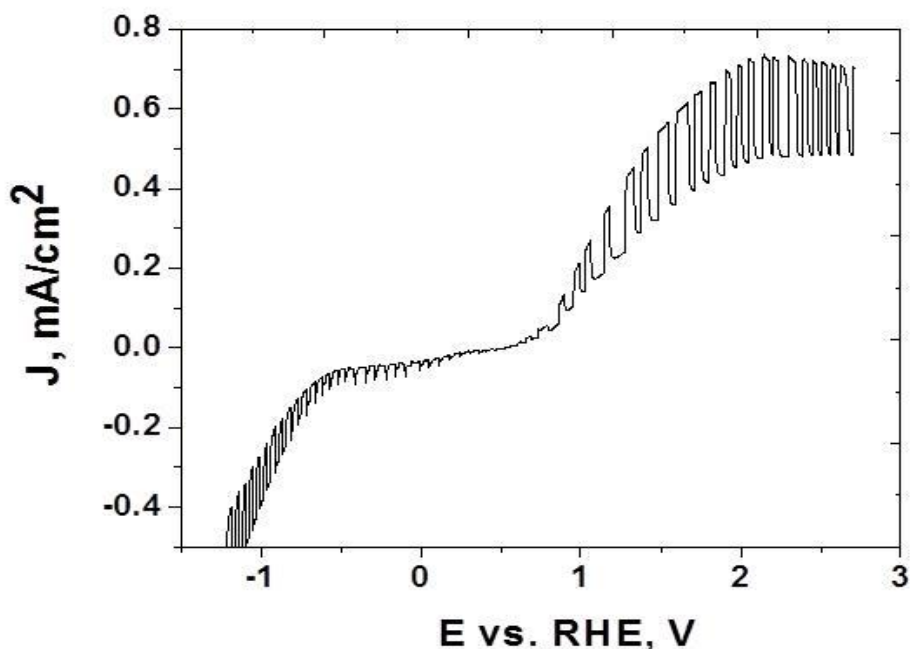


Figure 5.13 Chopped photocurrent density – voltage plot of $\text{GaSb}_x\text{N}_{1-x}$ NW array sample under AM 1.5 illumination.

The photoactivity in the negative potential region indicates that $\text{GaSb}_x\text{N}_{1-x}$ electrodes exhibited p-type behavior in addition to the observed n-type region. However, the photocurrents in the p-type regions were observed to be smaller when compared to the photocurrents in the n-type region. The copper catalyst on the tips of the nanowires could

be oxidized and the resultant oxide could explain the observed p-type behavior. The p-type behavior was not observed after the oxide was etched using HCl. Further, there was a significant reduction in the dark currents after acid etching.

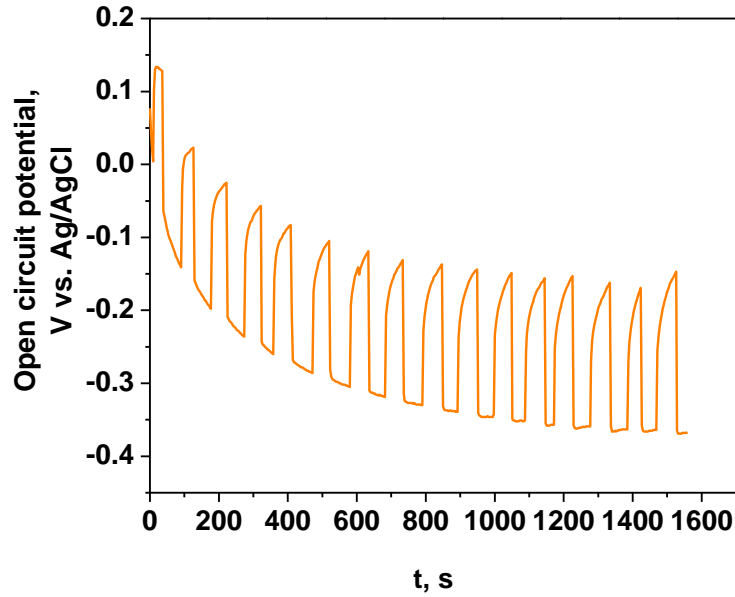


Figure 5.14 Chopped open circuit potential of $\text{GaSb}_x\text{N}_{1-x}$ nanowire array sample under AM 1.5 illumination.

Open circuit potential measurements were performed on $\text{GaSb}_x\text{N}_{1-x}$ nanowires to determine the conductivity type of the samples with a three electrode setup as explained in chapter 3. Open circuit potential measured w.r.t time is shown in Figure 5.14 which was done for 5 minutes. From the plot, it is observed that the direction of the potential shift was positive which showed that material is n-type similar to the observed result from $\text{GaSb}_x\text{N}_{1-x}$ films.

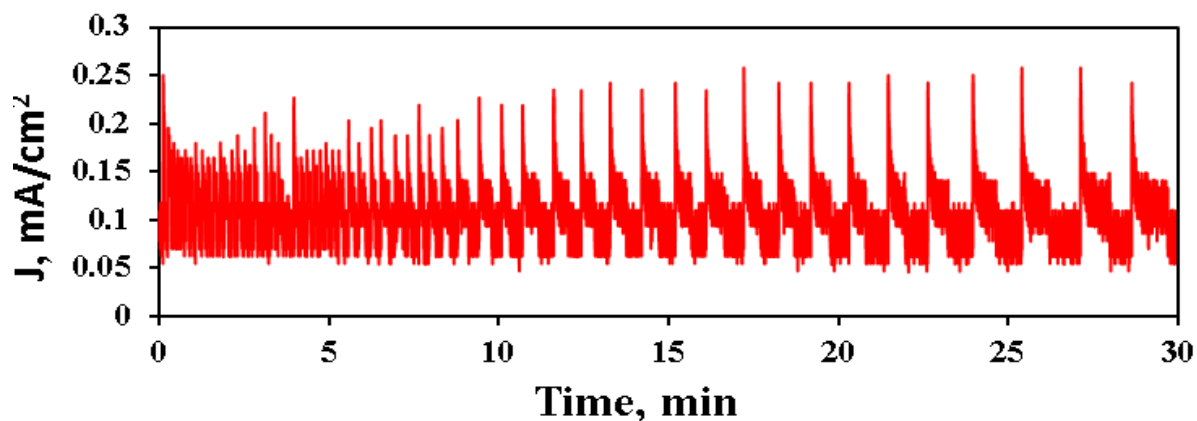


Figure 5.15 Chopped photocurrent vs time plot of $\text{GaSb}_x\text{N}_{1-x}$ electrodes under AM 1.5 illumination at a potential of -0.6 V.

Figure 5.15 shows the time evolution of photocurrents of $\text{GaSb}_x\text{N}_{1-x}$ nanowires, when a potential of -0.6 V vs. Ag/AgCl was applied to the electrode under 5 Sun illumination. The $\text{GaSb}_x\text{N}_{1-x}$ nanowires showed no loss in photocurrents for 30 minutes indicating promising aqueous stability. Photoactivity measurements were performed on samples grown at different temperatures. Figure 5.16 shows I-V measurement for $\text{GaSb}_x\text{N}_{1-x}$ nanowires at 700 °C and 850 °C. From the plot it clearly showed that the photocurrents have been increased for the nanowires at 850 °C when compared to 700 °C. This could be due to the improvement in the crystallinity of nanowires at high temperatures.

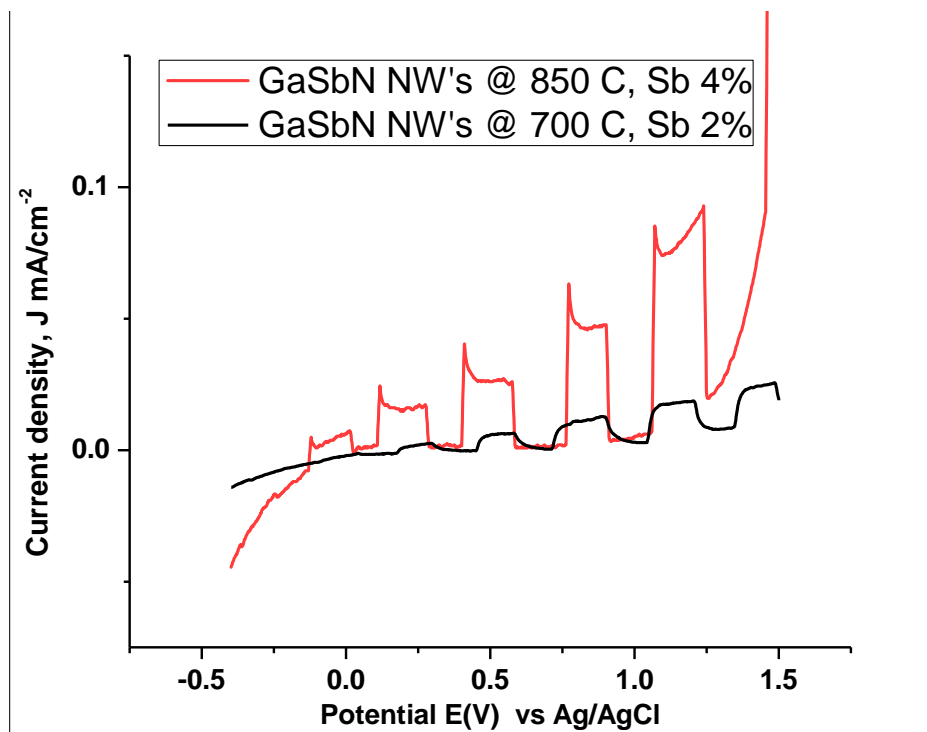


Figure 5.16 Photocurrent densities of $\text{GaSb}_x\text{N}_{1-x}$ nanowires comparing at 700°C and 800°C .

5.5 Summary

In summary $\text{GaSb}_x\text{N}_{1-x}$ nanowires have been synthesized by MOCVD through VLS approach using copper as a catalyst. Copper-antimony alloy has been observed at the tip of the nanowire which led to the formation of $\text{GaSb}_x\text{N}_{1-x}$ nanowire. Antimony incorporation in $\text{GaSb}_x\text{N}_{1-x}$ nanowire has been observed to increase with increase in temperature due to the increase in solubility of Sb in copper at higher temperatures. This showed that incorporation of antimony was easier for nanowires compared to thin films at high temperatures. The photoactivity of $\text{GaSb}_x\text{N}_{1-x}$ nanowires has been improved when compared with $\text{GaSb}_x\text{N}_{1-x}$ thin films.

CHAPTER 6

HIGHLY TEXTURED Ga(Sb)_xN_{1-x} FILMS

6.1 Introduction

In this chapter, experiments were conducted to improve the quality of GaSb_xN_{1-x} growth via metalorganic chemical vapor deposition (MOCVD) is studied in detail. Effect of process parameters like growth temperature, precursor flow rate on the nucleation layers of GaSb_xN_{1-x} and their structural properties are investigated. The resulting films were also tested for their optical and photoelectrochemical properties.

6.2 Rationale

The photoelectrochemical properties of highly polycrystalline GaSb_xN_{1-x} films are limited due to short distances for carrier diffusion before recombination at trap states. Polycrystalline thin films contain grain boundaries which act as recombination centers for charge carriers. The quality of the thin film growth can be tuned by process parameters such as pressure, precursor composition and substrate temperature. However, there are many challenges with synthesis of GaSb_xN_{1-x} alloys at high temperatures. Antimony does not incorporate into GaN phase at 900° C or higher. So, it is important to understand on how to improve the quality of the resulting films within the context of improving the photoelectrochemical properties. In the absence of complete epitaxial growth using the necessary temperatures of 900°C or higher, two concepts are investigated: One concept is

to obtain highly textured films with grains being larger than few microns and film thicknesses around 2 microns and the second concept is to grow highly oriented and textured films using liquid-phase epitaxy through a catalyst layer.

In order to understand the growth of highly textured films, it is important to understand the factors that control the nucleation of new crystals and individual crystal growth. As shown in Figure 6.1, high density of nucleation in the initial stages followed by crystal growth will lead to thickening of individual crystals and alignment of facets at certain thickness. The texture of the resulting film only depends upon the process conditions and the fastest growth direction associated with the process conditions used. Therefore, a set of experiments are conducted to understand the relationship between the morphology of resulting films as a function of the growth conditions.

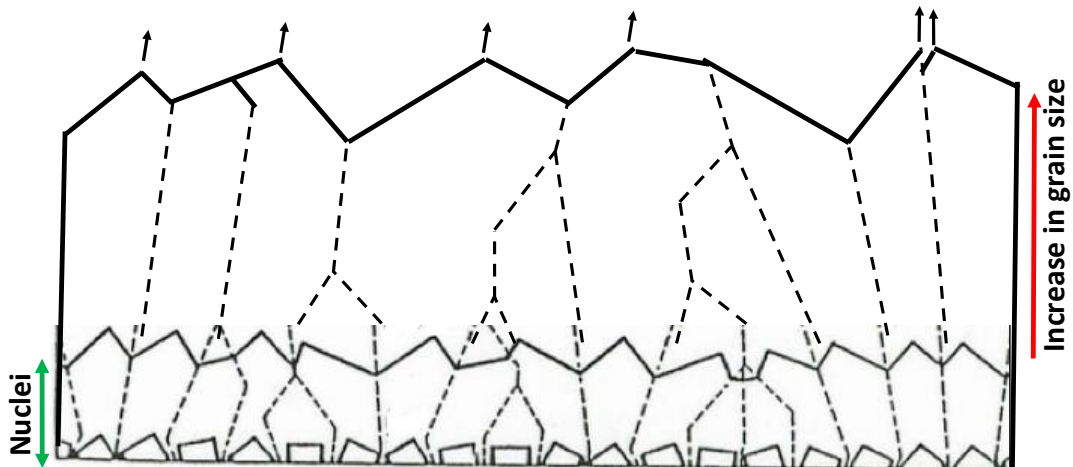


Figure 6.1 A schematic illustrating cross-sectional view for textured thin film growth.

In the second approach, it is important to understand the growth of highly oriented films through a concept called imperfect epitaxy where the thin film is partially oriented to the

substrate



Figure 6.2 A schematic illustrating cross-sectional view for highly oriented film growth.

In an ideal scenario, at high enough temperatures, it is possible to obtain perfect epitaxy film which is completely oriented to the substrate parallel and perpendicularly. It occurs as layer by layer in which new layer is nucleated only after completion of the layer below and this growth is the ideal case for achieving single crystal.



Figure 6.3 A schematic illustrating cross-sectional view for epitaxial growth.

The growth mode and the resulting film morphology are mainly influenced by the growth temperature and precursor flow rates. Therefore, these parameters were used to tune the growth modes.

6.3 Experimental Section

GaSb_xN_{1-x} layers investigated in this study were grown on epi GaN-sapphire and highly doped n-type silicon substrates using MOCVD. Prior to the deposition, substrates were cleaned in HF:HCl:CH₃CH₂OH:DIwater (equal proportions) by sonicating for 20 minutes and after drying the samples in nitrogen, samples were loaded into the MOCVD chamber for deposition. Firstly, all the substrates were annealed under ammonia at 950° C for 30 minutes to remove any native oxide layers from the substrates. After annealing step, temperature was cooled down to the desired growth temperature window and then precursors were supplied to the chamber using nitrogen as a carrier gas. Hydrogen was replaced in place of Nitrogen as carrier gas to study the effect of compensation in the material. Ammonia flow rate used for all the experiments was 1000 sccm. The samples were grown at different TMG: TMSb ratios and substrate temperatures ranging from 450° to 600 °C.

Their morphology was examined by JEOL-NOVA SEM where the thickness of the films and quality of the crystal growth was examined. UV-Vis spectroscopy was used to measure the band gap of all the samples. PL was performed on GaSb_xN_{1-x} layers at room temperature and cold temperature using 325 nm laser excitation source. Crystallinity and lattice parameters were determined using X-ray diffraction analysis.

6.4 Results & Discussion

Growth of GaSb_xN_{1-x} films at low temperatures resulted in polycrystalline films with small grains all over the surface which created lot of grain boundaries. The grain boundaries act as recombination centers limiting the photoactivity. Therefore, increasing

the grain size and reducing the defects will overcome this issue. To achieve that, growth of the films has been done at high temperatures and huge improvement in the crystal quality has been observed at high temperatures but there was no antimony incorporation as shown in the Figure 6.4

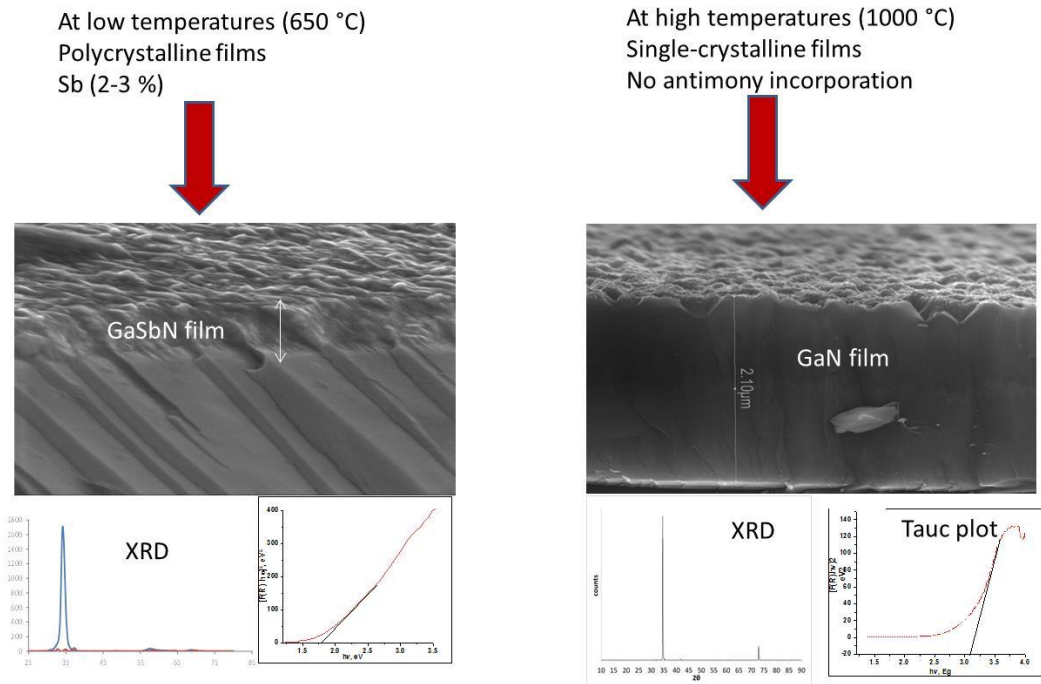


Figure 6.4 Comparison of crystal quality and antimony incorporation at low and high temperatures

The grain size was calculated from FWHM of the XRD peak and it turned out to be 11 nm which clearly showed that grains were very small with lot of grain boundaries. Ga: Sb ratio was 1:5 with an antimony incorporation of 2-4 %.

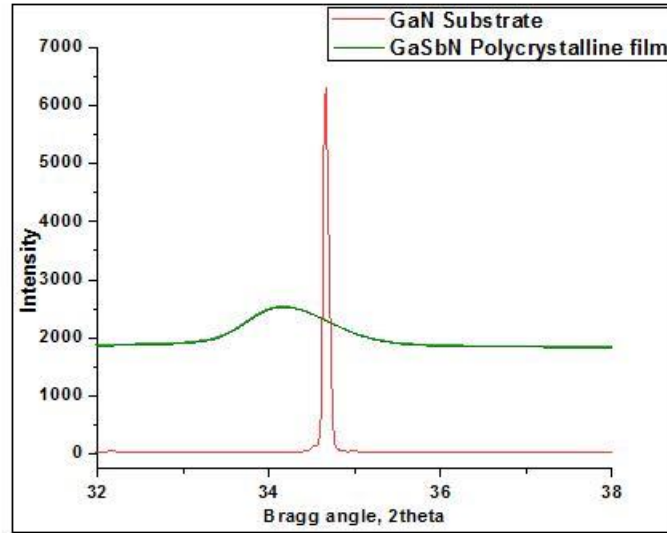


Figure 6.5 Comparison of XRD peak for $\text{GaSb}_x\text{N}_{1-x}$ polycrystalline film vs GaN substrate.

The reason for no antimony incorporation at high temperatures was due to the high rate of desorption at high temperatures due to the high vapor pressures of ammonia. Figure 6.6 showing the schematic of desorption of antimony and gallium intermediate species at high temperatures.

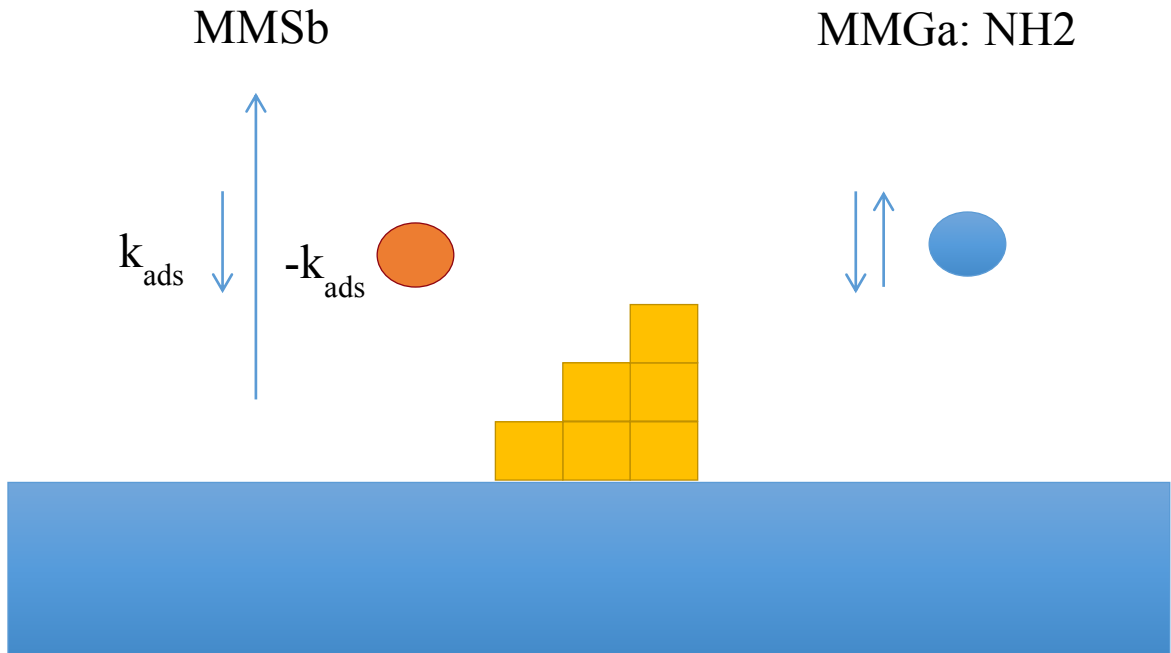


Figure 6.6 Adsorption processes of MOCVD precursors on substrate at elevated temperatures

Possible growth mechanism of antimony incorporation into GaN or $\text{GaSb}_x\text{N}_{1-x}$ ternary alloy formation in MOCVD synthesis is discussed in this section. Several studies on GaN growth chemistry in MOCVD have shown that there are two pathways for GaN formation: (i) formation via adduct pathway and (ii) pyrolysis of precursor (Trimethyl Gallium). Formation of GaN through an adduct pathway occurs when trimethyl gallium reacts with ammonia on entering into the chamber, upon reaction they form several intermediate species called adducts which plays major role in the formation of GaN. Another route is pyrolysis of precursor where trimethylgallium decompose into dimethyl gallium and then monomethyl gallium. Also mass spectroscopy studies on decomposition of trimethyl antimony (TMSb) show that it yields monomethyl antimony (MMSb) and methyl radicals. Further kinetic studies on decomposition of TMSb under different

incorporation when we change parameters like flux and temperature as it affects the rate of adsorption or desorption.

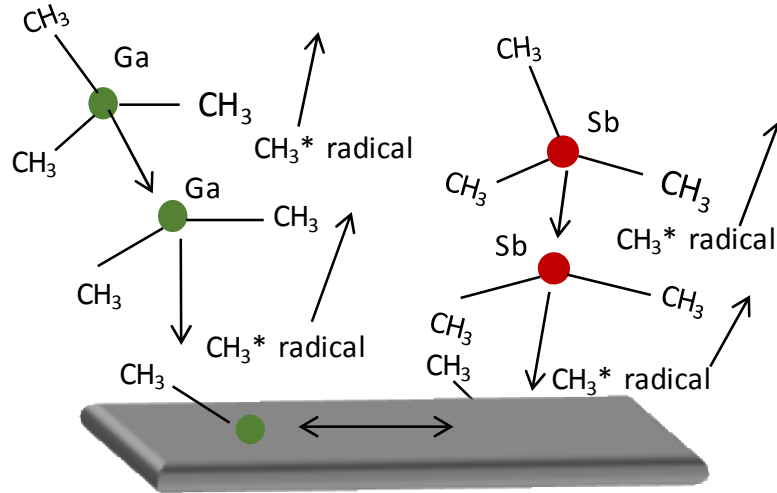


Figure 6.7 (b) Chemical reaction pathway for formation of GaSb during metal organic chemical vapor deposition.

The heteroepitaxial growth of especially group III nitrides is a strenuous task as several factors play a major role in hindering the epitaxial growth. The first one is the selection of the substrate that does not have any lattice mismatch. In our case GaN substrate is the ideal substrate for epitaxial growth as the lattice mismatch between $\text{GaSb}_x\text{N}_{1-x}$ and GaN is very small. Other disadvantages are poor cracking efficiency of ammonia and large dissociation pressure of N_2 from the nitrides at commonly used growth temperatures. To achieve the high quality epitaxial films a combination of buffer layers, high growth temperatures ($\sim 700\text{-}1400\text{ }^\circ\text{C}$), activated N_2 species, large nitrogen source overpressures and separated gas inlet technology have been used to overcome these difficulties and obtain device quality films.¹³⁵ Growth of group III nitrides by MOCVD requires a

minimum deposition temperature to provide sufficient mobility of surface species during growth to obtain epitaxial, single-crystalline growth of the group III nitrides. For example, in the case of GaN growth, the commonly used precursor that is TMG starts pyrolyzing at 475 °C and polycrystalline GaN films can be deposited at 475 °C using TMG and ammonia. However, in order to form a single crystalline high quality GaN films on sapphire the temperatures should be above 800 °C. It was reported that the GaN films with the best electrical and optical properties were grown at 1050 °C. At substrate temperatures exceeding 1100 °C the dissociation of GaN and desorption of species over the substrate dominate in the growth layer.¹³⁶ But in the case of GaSb, epitaxial growth can occur below 600 °C with a V/III ratio close to 1.¹³⁷⁻¹³⁹ It was reported that the optimized V/III ratio for the high-quality GaSb growth depends largely on the reactor design, growth conditions, and sources used.¹³⁷ The most commonly used precursors for GaSb growth are TMG and TMSb. Taking the growth conditions of GaN and GaSb into consideration, the parameters were optimized for obtaining high quality GaSb_xN_{1-x} layers.

6.4.1 Process Optimization for Textured and Oriented Film Growth

Growth of GaSb was found to be strongly dependent on precursor flow rates.

$$R = \frac{k_{GaSb} K_{Ga} K_{MMSb} P_{TMGa} P_{TMSb}}{(1 + K_{Ga} P_{TMGa})(1 + K_{MMSb} P_{TMSb})}$$

In Nakamura's papers of 1992 the growth of single crystalline InGaN was achieved at 800 °C by flowing a 24:1 molar ratio of TMI: TMG.¹⁴⁰ Even in case of InGaN growth it is very difficult to incorporate Indium into GaN at high temperatures as desorption rate of

In-adducts is also very rapid at high temperatures, but they increased the Indium concentration in the gas phase by a whole lot to achieve the desired incorporation level. Considering this fact, different experimental conditions of temperature and flow rates were investigated in our study until the high quality crystal with antimony incorporation was achieved. Figure 6.8 shows the evolution of highly textured GaSb_xN_{1-x} films by increasing the flow rates and temperature.

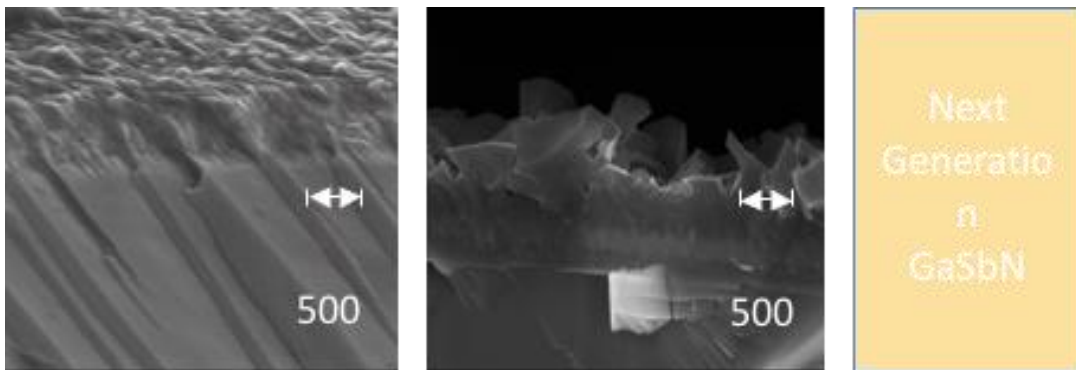
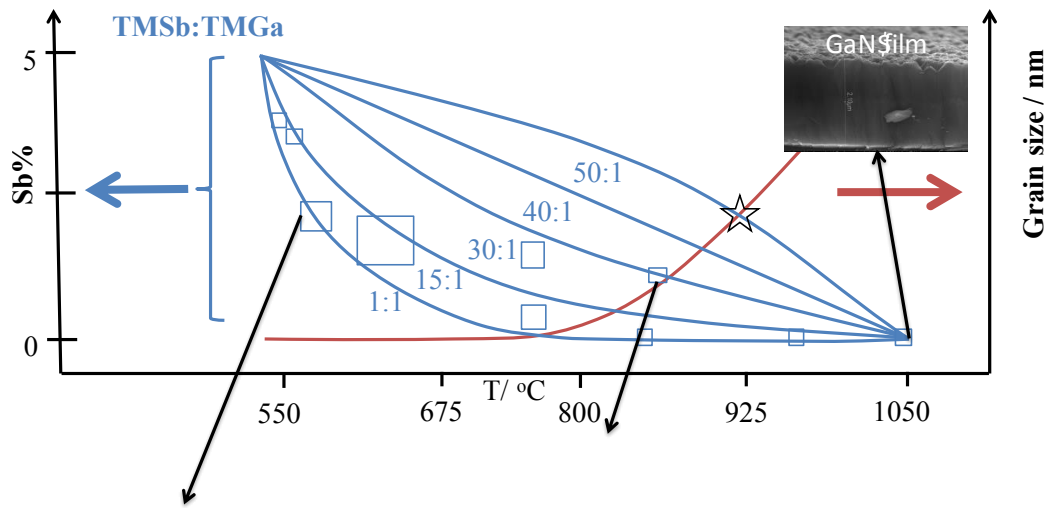


Figure 6.8 Evolution of epitaxial GaSb_xN_{1-x} films by changing the growth temperature and TMSb: TMG flux ratio.

In the figure, red curve is showing the increase in grain size as temperature goes high. Blue curve showing the change in the incorporation of antimony at different TMSb:TMGa ratios. The improvement in the crystal quality of $\text{GaSb}_x\text{N}_{1-x}$ layers at different temperatures was analyzed by examining the morphology of these layers using SEM. Figure 6.9 shows SEM images of $\text{GaSb}_x\text{N}_{1-x}$ films at different temperatures. The improvement in the crystal quality with increase in the temperature was clearly observed. SEM images in Figure 6.9 are showing the interface between GaN and $\text{GaSb}_x\text{N}_{1-x}$. At low temperatures, the resulting films were completely polycrystalline with random orientation. The grain size increased with temperature. Several experiments were performed in the temperature range 700- 900 °C to investigate the evolution of epitaxial $\text{GaSb}_x\text{N}_{1-x}$ films. The orientation of crystals also improved when the temperature increased beyond 900 °C or more.

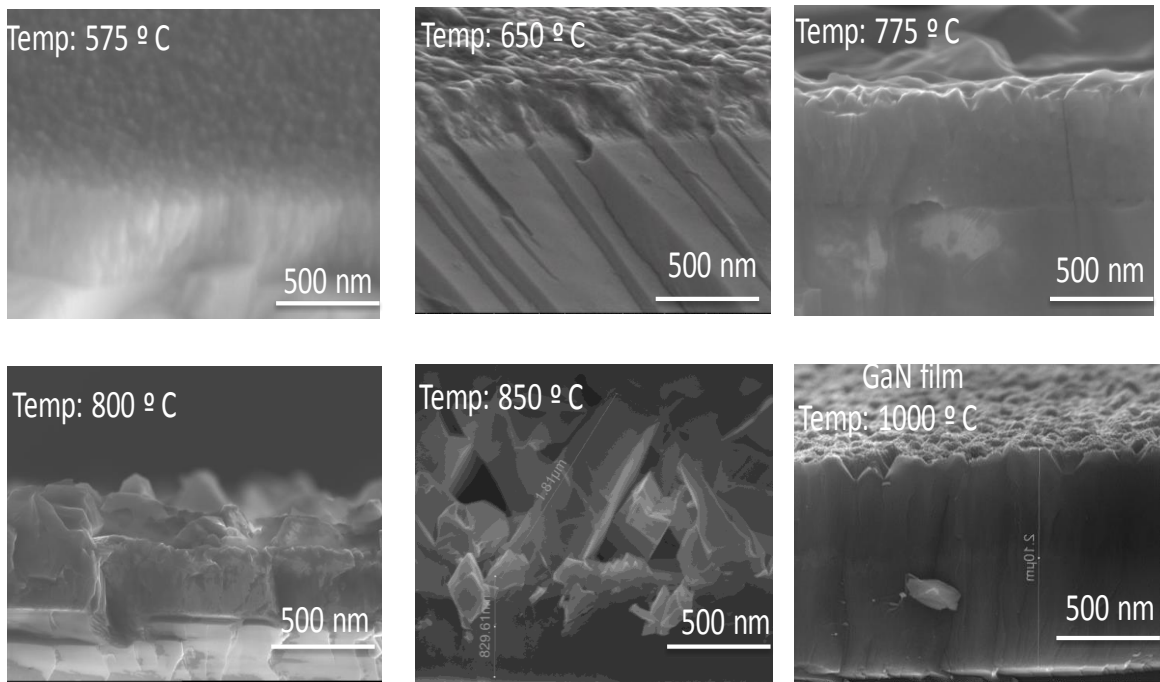


Figure 6.9 SEM images of $\text{GaSb}_x\text{N}_{1-x}$ layers grown at different temperatures on GaN

substrates.

From the Figure 6.8 it can be observed that by using TMSb: TMGa = 40: 1, antimony incorporation was achieved at high temperature 800 °C with a huge improvement in the crystal quality. As the temperature increased, antimony incorporation has been reduced and growth rates were observed to be increased resulting in thicker films at high temperatures.

In order to understand the crystallinity, XRD analysis has been performed on these samples at different temperatures. Figure 6.10 comparing the XRD of GaSb_xN_{1-x} layers for low temperatures and high temperature and GaN substrate is shown for comparison. The difference in Full Width Half Maxima (FWHM) of the peak has been clearly observed. The narrow and intense GaN 0002 and 0004 peaks were observed at approximately 34.6° and 72.8° respectively for GaN substrate indicating that the GaN film was a single phase with a wurzite crystal structure. For GaSb_xN_{1-x} films, peaks were observed around same angles with a shift to lower angles for different samples. Samples that were grown at different temperatures were compared for full width at half-maximum FWHM values of the XRD to determine the epitaxial quality of the layers. For sample that was grown at low temperature the FWHM was very broad with a value of 1440 arcsecs whereas for the sample grown at high temperature (800 °C) the FWHM was 540 arcsecs which indicates that GaSb_xN_{1-x} film was of highly quality and the shift of the peak to lower angles from GaN substrate clearly imply increase in lattice spacing thereby antimony incorporation.

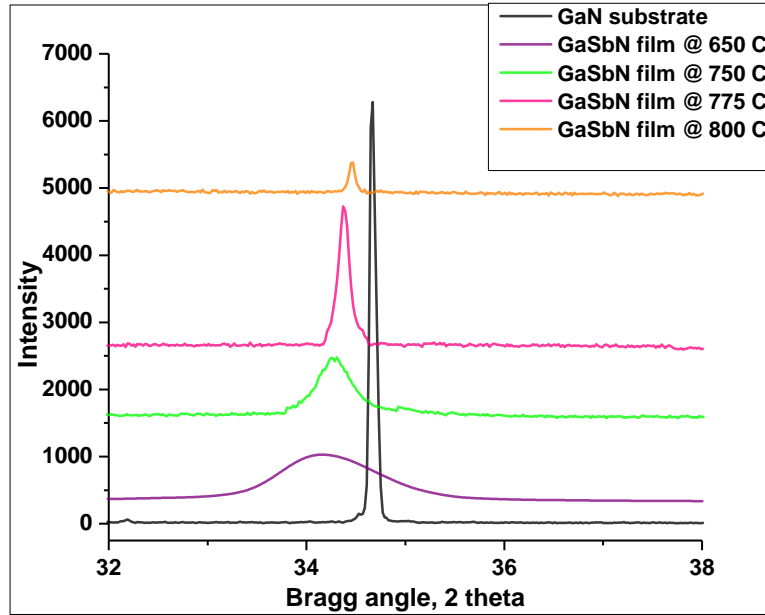


Figure 6.10 Comparison of XRD peaks for $\text{GaSb}_x\text{N}_{1-x}$ layers grown at different temperatures.

The Optical properties of these $\text{GaSb}_x\text{N}_{1-x}$ layers were measured using UV-Vis spectroscopy and PL. From diffuse reflectance measurement by UV-Vis spectroscopy the Tauc plots were obtained for the samples at different temperatures as shown in the Figure 6.11. The band gaps of 1.7 eV and 2.1 eV were obtained for $\text{GaSb}_x\text{N}_{1-x}$ layers at temperatures 775 °C to 800 °C. These values were corroborated

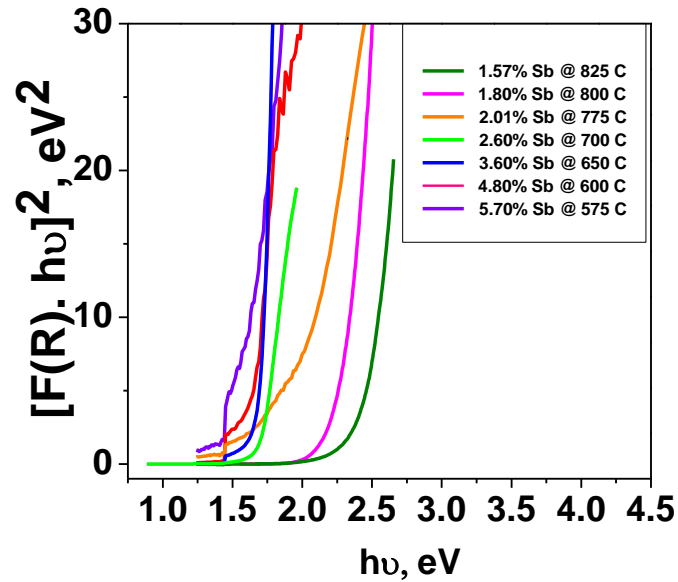


Figure 6.11 Tauc plots obtained for $\text{GaSb}_x\text{N}_{1-x}$ layers grown at different temperatures.

with the peak shift obtained from the XRD and antimony composition from SEM-EDS analysis. Nitrogen was replaced with hydrogen as a carrier gas to passivate the defects in the crystal. Figure 6.12 shows the XRD of $\text{GaSb}_x\text{N}_{1-x}$ layers comparing between hydrogen and nitrogen as a carrier gas. From the plot, it was clearly observed that for the layers grown using hydrogen as carrier gas, the XRD peaks were very sharp with small FWHM. This indicated that hydrogen improved the crystal quality. Also PL analysis has been performed on $\text{GaSb}_x\text{N}_{1-x}$ layers at different temperatures at room temperature. Interesting observation was that there was no PL signal for $\text{GaSb}_x\text{N}_{1-x}$ polycrystalline films at room temperature. But for the films synthesized at high temperatures and using hydrogen as a carrier gas, a sharp PL signal was obtained at 1.8 eV and 2.1 eV for 775° C and 800 °C respectively. This is another way to tell that defects have been reduced and crystal quality has been improved.

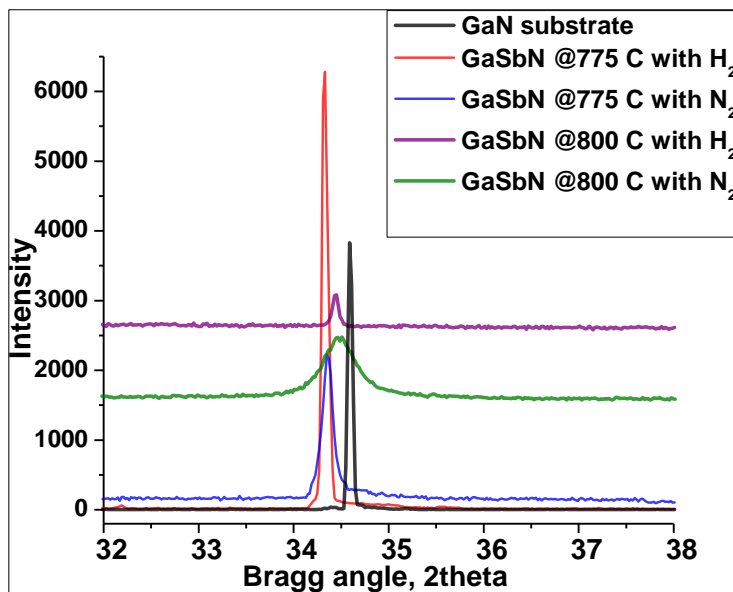


Figure 6.12 Comparison of XRD peaks for GaSb_xN_{1-x} layers grown using H₂ and N₂ as carrier gas for metal organic precursors.

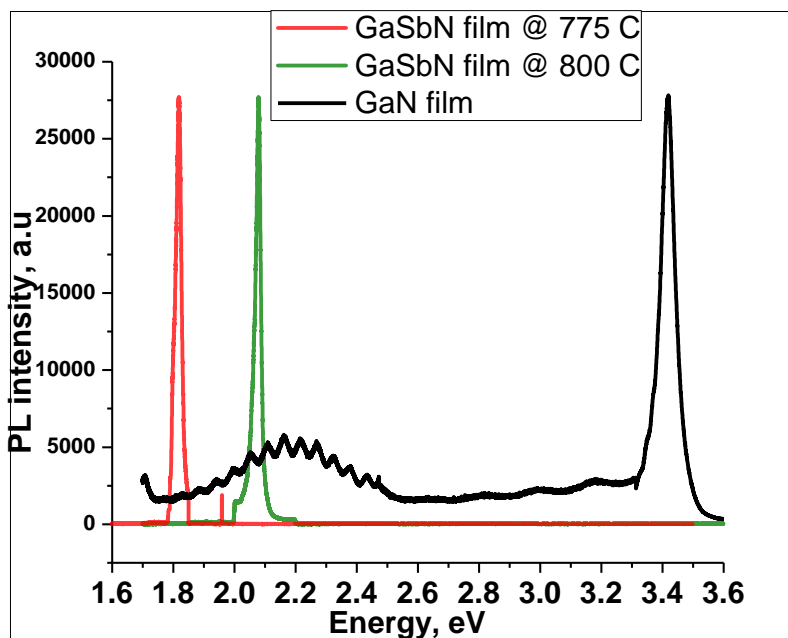


Figure 6.13 Photoluminescence of GaSb_xN_{1-x} layers at 775 C and 800 C using H₂ as

carrier gas.

Even though the high textured growth has been achieved, the single crystal growth would be ideal for efficient photoresponse. Also high TMSb: TMG flux ratios are required to incorporate antimony at higher temperatures.

A VLS approach in making single crystal quality films has been demonstrated using copper as a catalyst layer. The growth mechanism of this approach is similar to the VLS growth of $\text{GaSb}_x\text{N}_{1-x}$ nanowires explained in chapter 5. However, in this growth, copper catalyst has been deposited by sonication of copper nanoparticles in ethanol and drop casting them on the substrates. After that, they have been reduced in hydrogen using microwave plasma reactor for 30 minutes at 900 W and 40 torr. After the reduction in hydrogen, substrates have been transferred to MOCVD chamber and pretreatment step has been performed at 900 °C for 30 minutes under ammonia. The deposition was carried out at 700 °C with a ratio of TMG: TMSb = 1:5 for 40 minutes at 80 torr. The growth started with the formation of $\text{GaSb}_x\text{N}_{1-x}$ nanowires via VLS and coalesced into a compact epitaxy films with antimony incorporation. Figure 6.14 shows the schematic of formation of $\text{GaSb}_x\text{N}_{1-x}$ epitaxy films via VLS approach. In the figure, the first step is the copper nanoparticle deposition on the substrate. The second step is the MOCVD growth where copper forms eutectic with antimony and the dissolution of precursor species into the molten alloy precipitates as nanowire. These nanowires coalesce into epitaxy film leaving a copper-antimony melt on the top layer.

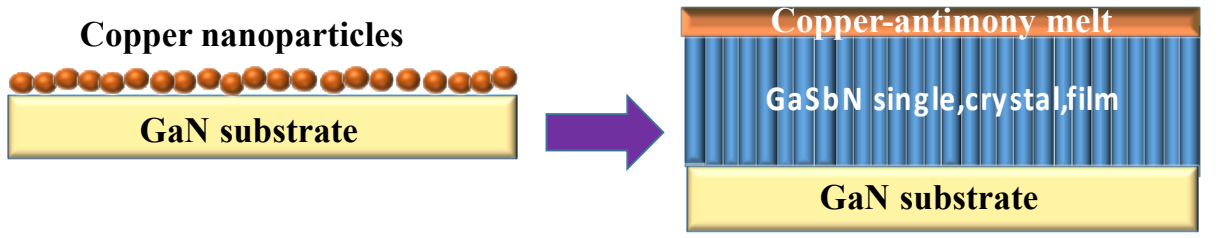


Figure 6.14 A schematic of formation of $\text{GaSb}_x\text{N}_{1-x}$ film using copper as catalyst.

Figure 6.15 shows the SEM images of epitaxial films synthesized using a catalyst layer. Figures 6.15 a) and b) shows the top view of the films before and after etching in KOH. It can be observed from the images that morphology has changed after etching in KOH leading to ordered facets on the top layer. By etching in KOH, the metallic layer copper-antimony or copper has been removed and sharp pyramids have been revealed.

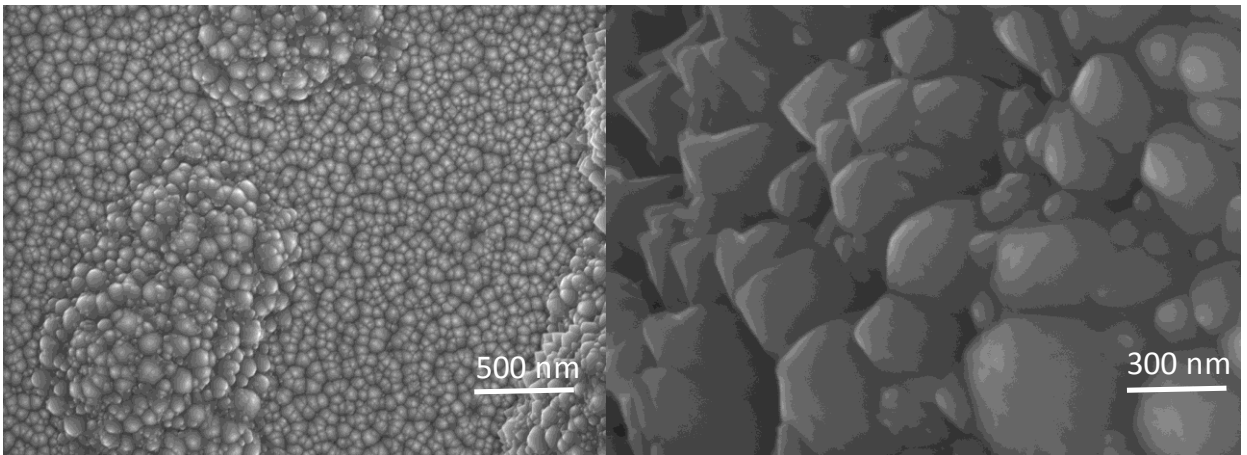


Figure 6.15 a) SEM images showing top view of $\text{GaSb}_x\text{N}_{1-x}$ epitaxial films grown at 700 C using catalyst layer (before etching)

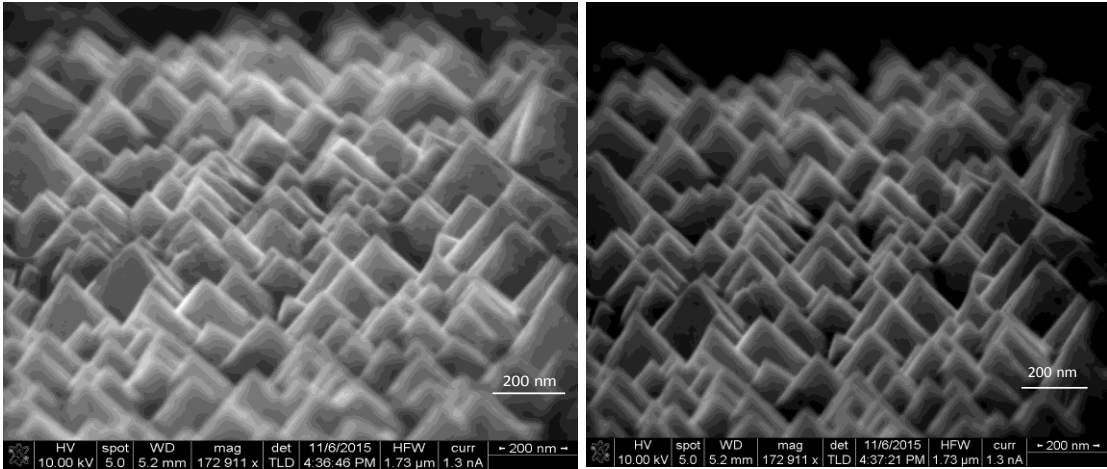


Figure 6.15 b) Top view of $\text{GaSb}_x\text{N}_{1-x}$ epitaxial film via VLS growth using copper as catalyst (after etching in KOH)

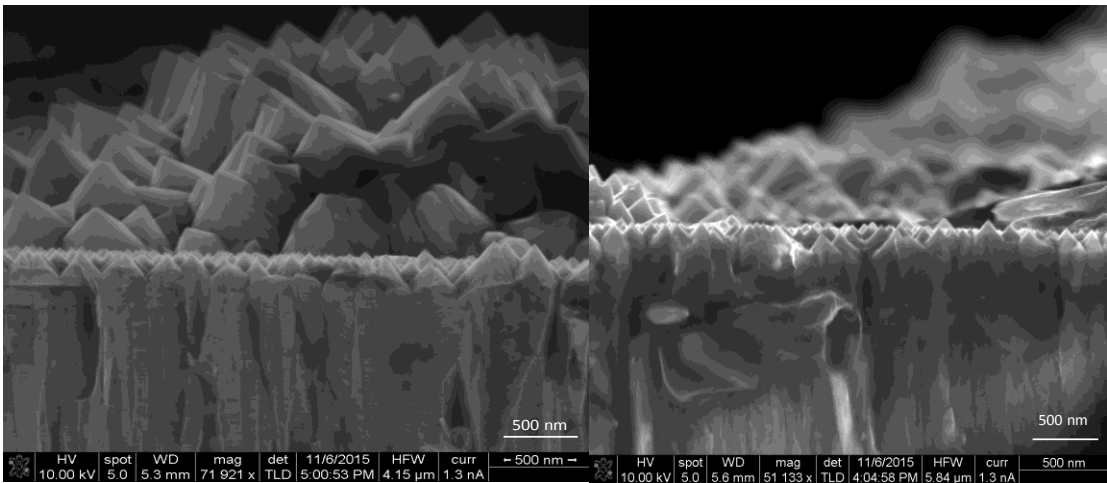


Figure 6.15 c) Cross view showing $\text{GaSb}_x\text{N}_{1-x}$ coalesced into an epitaxial film (after etching in KOH)

6.3.2 Photoelectrochemical Characterization

GaSb_xN_{1-x} layers synthesized at different temperatures were tested for photoactivity measurements. Firstly, chopped I-V measurement has been done using 450 nm filter which blocked all of the UV absorption and part of violet light. This fundamental analysis is important to understand if the resulting photocurrent densities were coming from the deposited GaSb_xN_{1-x} due to band gap reduction or from the GaN substrate. The underlying substrate was GaN with a band gap of 3.4 eV which cannot absorb any light with 450 nm filter. Figure 6.16 is showing the chopped I-V of GaSb_xN_{1-x} film with and without filter comparing for GaSb_xN_{1-x} and GaN substrate. From the figure it can be inferred that GaN substrate with filter did not show any photoresponse whereas with filter there was little photoactivity. This indicates that GaN only showed UV response. Therefore, the photocurrents that were observed for GaSb_xN_{1-x} sample exhibited only from GaSb_xN_{1-x} visible response suggesting photocurrents were from actual band gap reduction from 3.4 eV to visible region in GaSb_xN_{1-x}. However, the interesting observation was photoactivity from GaSb_xN_{1-x} was higher without filter than with filter. This could be due to UV + Visible absorption. Even though GaN does not contribute to photocurrents in heterojunction, it might be helping in charge separation.

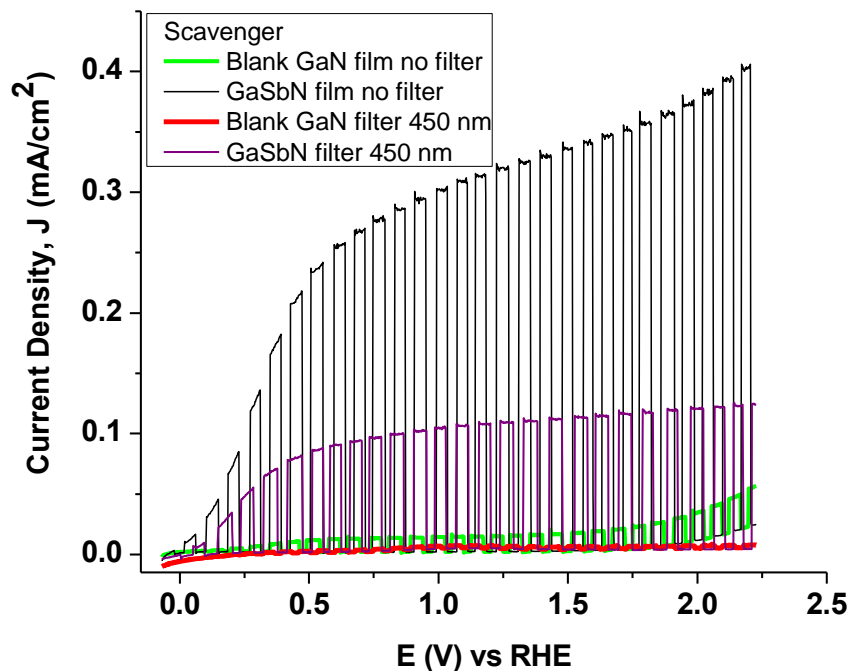


Figure 6.16 Chopped I-V measurement of $\text{GaSb}_x\text{N}_{1-x}$ film comparing photoactivity with and without using 450 nm filter for AM1.5 illumination.

Figure 6.17 shows the chopped I-V measurement comparing for $\text{GaSb}_x\text{N}_{1-x}$ polycrystalline thin film vs textured thick film. From the I-V measurement, it clearly suggests that photoactivity has been increased for thick and good quality film when compared to polycrystalline film. This could be due to two reasons one is because of increase in the thickness which allows for more absorption of photons. The optical absorption depth calculated for $\text{GaSb}_x\text{N}_{1-x}$ layers from transmission spectroscopy was around 2 microns which suggests that the thickness of the film needs to be 2 microns. Another one is due to the increase in quality of the crystal which has tremendously fewer defects when compared to polycrystalline films which reduce the recombination of charge carriers.

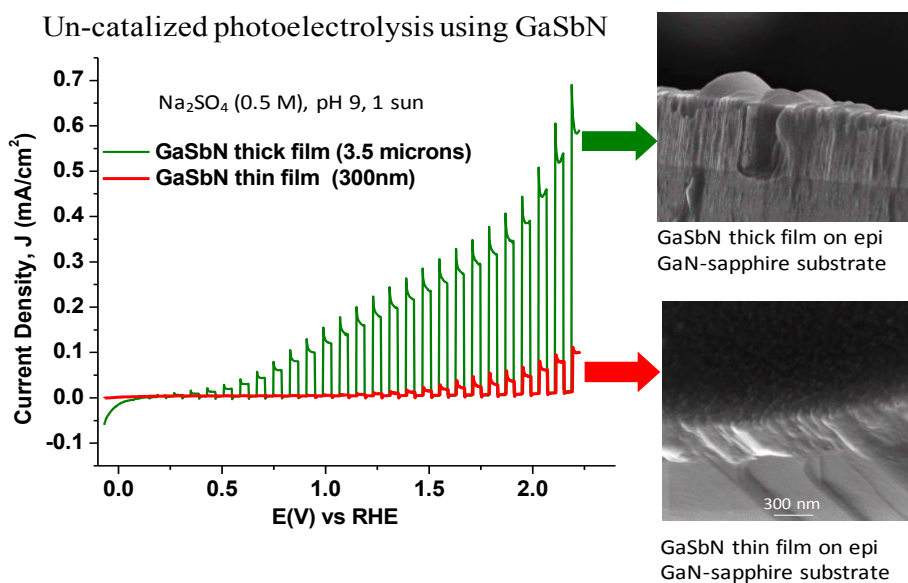
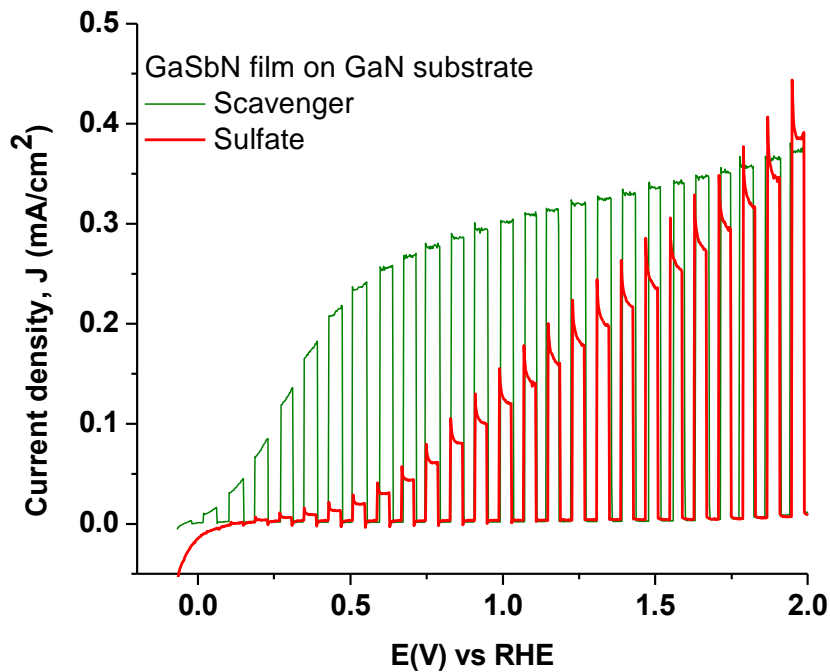
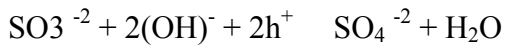


Figure 6.17 Comparison of chopped I-V curves obtained for $\text{GaSb}_x\text{N}_{1-x}$ polycrystalline thin film and textured thick film using AM 1.5 illumination.

In order to have a better understanding of what is limiting the photocurrent densities fundamental photoelectrochemical characterization has been performed on $\text{GaSb}_x\text{N}_{1-x}$ layers. One main reason would be electron-hole recombination and accumulation of photogenerated holes at the interface which slower the process of water oxidation. This was also evident from the magnitude of slow transient decay phase from the I-V measurement under illumination. Therefore, a hole scavenger was used as an electrolyte that was sodium sulfite to promote the photocatalytic activity and enhance the visible light response. The experiment was conducted using similar conditions except that sodium sulfite was replaced in place of sodium sulfate. Figure 6.18 showing the chopped I-V measurement of $\text{GaSb}_x\text{N}_{1-x}$ layers under illumination with sulfate and sulfite. The

interesting observations found from the measurement were more cathodic onset potential with hole scavenger, better fill factor and magnitude of the transient decay reduced indicating less hole accumulation at liquid junction and less capacitive behavior. Also the important one to be observed from the plot was increase in the photocurrent densities. Hole scavenger acts as electron donor which react irreversibly with the photogenerated holes and enhance the charge separation resulting in better photoresponse. The reaction of hole scavenger at the interface is given below



□

Figure 6.18 Chopped I-V curves obtained for GaSb_xN_{1-x} films under illumination using sodium sulfite and sodium sulfate in electrolyte solution.

Moreover, by adding a hole scavenger, the kinetic barrier for the hole transfer that is overpotential required to drive the oxygen evolution reaction will be reduced. Therefore, this analysis suggested that $\text{GaSb}_x\text{N}_{1-x}$ alloys were undergoing kinetic limitation and hole accumulation at the interface which created rapid recombination.

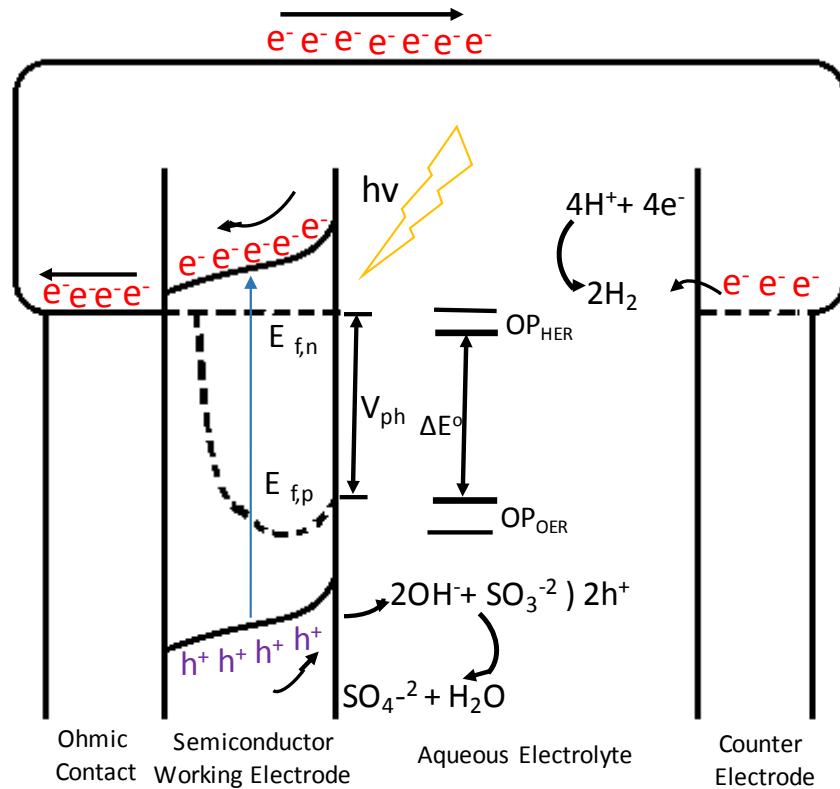


Figure 6.19 Band edge diagram showing the energetic requirements associated with the minimum thermodynamic energy to drive HER and OER reactions, catalytic overpotentials and photovoltage.

Films that were synthesized at high temperatures with a high textured growth and the single crystal films grown via VLS exhibited very low photoactivity. Moreover, the films grown using catalyst layer exhibited p-type behavior. Same type of behavior has been

observed for $\text{GaSb}_x\text{N}_{1-x}$ nanowires grown using copper as a catalyst. This indicates that p-type behavior was coming from copper-antimony alloy on top of the films.

6.5 Summary

In summary two concepts were proposed to improve the quality of $\text{GaSb}_x\text{N}_{1-x}$ films, one to increase the grain size by growing at high temperatures and another one to grow single crystal layers through liquid phase epitaxy with a catalyst layer. The growth of highly textured $\text{GaSb}_x\text{N}_{1-x}$ films was achieved at high temperatures including antimony incorporation by increasing the TMG:TMSb ratio from 1:5 to 1:40. The quality of the films and grain size has tremendously improved when compared to the films synthesized at low temperatures. The FWHM of XRD peak reduced with increase in temperature indicating the increase in grain size. Moreover FWHM of XRD and PL peaks has been reduced when nitrogen was replaced with hydrogen as a carrier gas. Fundamental photoelectrochemical characterization using 450 nm filter revealed that photoresponse exhibited from the $\text{GaSb}_x\text{N}_{1-x}$ films were only from visible photoresponse due to the band gap reduction from GaN to $\text{GaSb}_x\text{N}_{1-x}$. Additionally using hole scavenger improved the photocurrents and fill factor indicating the hole accumulation at the interface. In addition, single crystal layers have been synthesized by VLS approach with copper as a catalyst layer in the temperatures range between 700 °C to 850 °C. Although the quality of the films improved, the photoresponse dropped down which could be due to the doped impurities.

CHAPTER 7

CONCLUSIONS

This project revealed a new visible light absorbing material suitable for photoelectrochemical (PEC) water splitting using sunlight. In this dissertation, large band gap bowing of GaN alloys in the low antimonide region has been investigated. This was the first successful attempt on the experimental synthesis of crystalline GaN based alloy in the low antimonide regime and PEC data on activity, band edge energetics and stability that showed high suitability for direct solar water splitting. Fundamental PEC characterization on these alloys that will be helpful to understand the important photoelectrochemical properties has been performed. Deep insight into improving the crystal quality of the films has been investigated in order to improve the photoactivity. Also, new approach of making ternary alloy single crystal films using VLS mechanism has been demonstrated. Fundamental growth mechanisms and structural properties of the ternary alloy nanowires have been studied which can be extended to other ternary alloy materials of interest. A remarkable feature of this work is the striking qualitative and quantitative agreement between experiment and theory with main aspects about the material. The above material with a combination of properties suitable for PEC water splitting can play a significant role in other applications such as photocatalysts, tandem solar cells.

Novel alloy $\text{GaSb}_x\text{N}_{1-x}$ has been synthesized on various semiconductor (GaN and highly

doped n-type silicon), metal (stainless steel) and amorphous insulator (fused silica). The band gap of the $\text{GaSb}_x\text{N}_{1-x}$ ternary alloys exhibited around 2eV to 1.5 eV direct transitions with Sb levels ranging from about 2 at% to 8 at%. This dilute amount of antimony incorporation into GaN can lead to efficient visible light absorption. Also the alloys with more than 7% antimony incorporation exhibited indirect band gap transition. The band edges of $\text{GaSb}_x\text{N}_{1-x}$ straddle the water oxidation and reduction reactions for all of the above band gap values. The agreements have been consistent in terms of lattice expansion, band gap transition from direct to indirect with Sb levels >7 at% and large band gap reduction just with 2 at% Sb inclusion. Specifically, all the experimental observation matched with theoretical DFT + U predictions. Moreover, crystal quality of these alloys was polycrystalline with small grains all over the surface with a grain size of around 11nm. As synthesized $\text{GaSb}_x\text{N}_{1-x}$ alloys were able to drive the water splitting reaction without any external bias but exhibited low photocurrent densities of 10-20 micro amperes. In order to improve the performance single crystalline nanowires, highly textured film growth and epitaxial growth via VLS have been demonstrated.

Single crystalline $\text{GaSb}_x\text{N}_{1-x}$ nanowires were synthesized by MOCVD using VLS growth with copper as a catalyst. The antimony incorporation into GaN has shown to increase with increase in temperature. This was due to the high solubility of antimony in copper at high temperatures. Incorporation of antimony in GaN at high temperatures was done with TMGa : TMSb ratio of 1: 5 whereas for films high TMSb:TMGa ratio was used. The photoactivity of $\text{GaSb}_x\text{N}_{1-x}$ nanowires has been increased at two orders of magnitude when compared with thin polycrystalline films.

At low growth temperatures, $\text{GaSb}_x\text{N}_{1-x}$ layers resulted in polycrystalline films with lot of

grain boundaries which limited the photoactivity. To improve the crystal quality, alloys were synthesized at high temperatures but found no antimony incorporation with TMGa:TMSb = 1:5. For TMGa:TMSb = 1:40, the antimony was incorporated into GaN even at high temperatures. By employing pretreatment step, crystal quality has been improved tremendously starting at temperature 750 °C. The FWHM of the highly textured films was observed to be 500 arcsecs which reduced drastically when compared with films grown at low temperatures without pretreatment step. This indicates that crystal quality has been improved. PL analysis at room temperature exhibited band gap values of 1.8 eV and 2.1 eV at 775 and 800 C respectively. The band gap values corroborated with the values determined from UV-Vis and antimony composition. The antimony composition obtained from SEM-EDS for the films at high temperatures matched with XRD peak shift and lattice expansion. The samples with good crystal quality have shown improvement in photoactivity of around $1\text{mA}/\text{cm}^2$ when compared to polycrystalline films but still low when compared with the theoretical photocurrent densities the material can exhibit. The photoactivity observed from the samples was proven to be exhibited from $\text{GaSb}_x\text{N}_{1-x}$ due to band gap reduction from 3.4 eV to 1.8 – 2 eV. This was done with the use of 450nm filter which blocked the UV absorption from GaN substrate. GaN substrate showed no photoactivity with filter and indicated that the extra currents exhibited from $\text{GaSb}_x\text{N}_{1-x}$ films were actually coming from the visible response due to the bandgap reduction. By using hole scavenger as an electrolyte the photoactivity has been increased tremendously and also the magnitude of the transient decay has been reduced. This clearly indicated that there was a huge accumulation of photogenerated holes at the semiconductor- electrolyte interface thereby slowing the

oxygen evolution process. In addition, new approach of growing epitaxy $\text{GaSb}_x\text{N}_{1-x}$ films using catalyst layer has been demonstrated. $\text{GaSb}_x\text{N}_{1-x}$ growth started as nanowires and coalesced into a compact epitaxy film through VLS mechanism by using copper as a catalyst. Single crystal quality has been observed even at low temperatures of 700 C which is usually difficult to achieve through vapor phase deposition. Moreover, the band gap of the samples was observed to be 1.7-1.8 eV.

CHAPTER 8

FUTURE RECOMMENDATIONS

8.1 Growing quality GaSb_xN_{1-x} films

The synthesized GaSb_xN_{1-x} layers helped in understanding fundamental properties of the material. But the photoactivity of the material still needs to be improved. Growing a complete single crystal GaSb_xN_{1-x} film with band gap of 1.8 eV to 2 eV would be ideal for achieving high solar to hydrogen efficiencies. Also defect free single crystalline nanowires would be useful in improving light absorption and thereby better PEC performance. In order to achieve uniform epitaxial growth of GaSb_xN_{1-x} films, employing a rotation of the substrate is recommended. Growing epitaxy films without catalyst layers using plasma excitation allowing for antimony incorporation is recommended and growing them on inexpensive substrates like stainless steel needs to be studied. Studying the role of different catalysts that allows for VLS growth would be useful in understanding the doping in the films. Moreover, studying the properties of films with >7% Sb incorporation is recommended.

8.2 Photoelectrochemical Properties:

Although the material has all the requirements to efficiently split water, the photoactivity was limited due to several factors like surface defects, poor kinetics at semiconductor-

liquid interface, accumulation of photogenerated charge carriers at the interface. To overcome these issues, it is recommended to investigate the surface passivation of these layers to passivate the surface defects. Gallium oxide is one material that can be studied for surface passivation. To address the problem with slow kinetics, study of different electrocatalysts on these layers would be helpful. The high quality films obtained using catalyst layer exhibited p-type behavior with very low photoactivity due to the compensation effect developing p and n-type impurities. The reason for this contamination in the films needs to be studied. Clean epitaxy films without any compensation needs to be synthesized for high PEC efficiencies. Also the role of hydrogen in passivating the defects in the material needs to be studied. Synthesis of graded band gap nanowire architectures, comprising of ternary alloy layers with a gradual decrease in band gap from core-shell is recommended. By creating a graded semiconductor, all the carriers are swept in the steep internal electric field and charge separation is boosted. Most importantly, the composition gradient also results in layers of different band gaps, which results in improved light harvesting of the solar spectrum. Figure 13 shows the charge carrier in graded band gap semiconductor and a conventional n-type electrode. The gradient in the composition allows light of several different wavelengths to be absorbed. In contrast, in the conventional n-type electrode, only a single wavelength is absorbed.

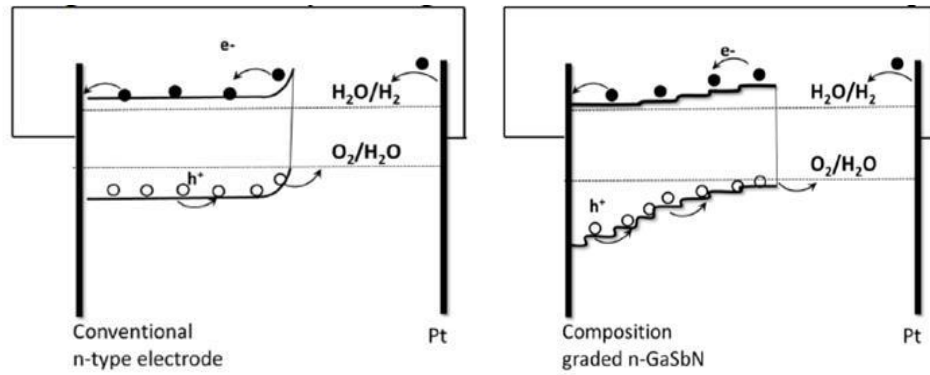


Figure 8 A schematic illustrating the charge carrier transport in compositionally graded $\text{GaSb}_x\text{N}_{1-x}$ and conventional n-type electrode.

Developing a two absorber based PEC cell using n-type $\text{GaSb}_x\text{N}_{1-x}$ with a band gap of 1.8 -2.0 eV as the photoanode and p-type GaSbP with a band gap of 1.0 – 1.3 eV as the photocathode would be ideal for high efficiencies.

8.3 Electrical Properties:

Studying the minority carrier diffusion lengths and lifetimes, mobilities would give better understanding on why the photoactivity is limiting even though the quality has been improved. These properties will give an idea on charge accumulation and subsequent recombination at the semiconductor-electrolyte interface. $\text{GaSb}_x\text{N}_{1-x}$ has huge potential towards efficient solar water splitting so by growing high quality and performing the above recommended studies would definitely pave the way for high solar to hydrogen efficiencies.

REFERENCES

1. Lewis, N. S.; Nocera, D. G. Powering the planet: Chemical challenges in solar energy utilization. *Proceedings of the National Academy of Sciences* 2006, 103, 15729-15735.
2. Lewis, N. S.; Crabtree, G. Basic research needs for solar energy utilization: report of the basic energy sciences workshop on solar energy utilization, April 18-21, 2005. 2005.
3. Van de Krol, R.; Grätzel, M.; Grätzel, M.; Grätzel, M. *Photoelectrochemical hydrogen production*. Springer: 2012.
4. Turner, J. A. Sustainable hydrogen production. *Science* 2004, 305, 972-974.
5. Turner, J.; Sverdrup, G.; Mann, M. K.; Maness, P. C.; Kroposki, B.; Ghirardi, M.; Evans, R. J.; Blake, D. Renewable hydrogen production. *International Journal of Energy Research* 2008, 32, 379-407.
6. Koval, C.; Sutin, N.; Turner, J. *Solar hydrogen production*; National Renewable Energy Lab., Golden, CO (United States): 1996.
7. Khaselev, O.; Turner, J. A. A monolithic photovoltaic-photoelectrochemical device for hydrogen production via water splitting. *Science* 1998, 280, 425-427.
8. Chen, G.; Gallo, E. M.; Burger, J.; Nabet, B.; Cola, A.; Prete, P.; Lovergine, N.; Spanier, J. E. On direct-writing methods for electrically contacting GaAs and Ge nanowire devices. *Applied Physics Letters* 2010, 96, 223107.
9. Walter, M. G.; Warren, E. L.; McKone, J. R.; Boettcher, S. W.; Mi, Q.; Santori, E. A.; Lewis, N. S. Solar water splitting cells. *Chemical reviews* 2010, 110, 6446-6473.
10. van de Krol, R.; Liang, Y.; Schoonman, J. Solar hydrogen production with nanostructured metal oxides. *Journal of Materials Chemistry* 2008, 18, 2311-2320.
11. Currao, A. Photoelectrochemical water splitting. *CHIMIA International Journal for Chemistry* 2007, 61, 815-819.
12. Van de Walle, C. G.; Neugebauer, J. Universal alignment of hydrogen levels in semiconductors, insulators and solutions. *Nature* 2003, 423, 626-628.
13. Sheetz, R. M.; Richter, E.; Andriotis, A. N.; Lisenkov, S.; Pendyala, C.; Sunkara, M. K.; Menon, M. Visible-light absorption and large band-gap bowing of GaN 1- x Sb x from first principles. *Physical Review B* 2011, 84, 075304.
14. Bard, A. J.; Fox, M. A. Artificial photosynthesis: solar splitting of water to hydrogen and oxygen. *Accounts of Chemical Research* 1995, 28, 141-145.
15. Mavroides, J.; Kafalas, J.; Kolesar, D. Photoelectrolysis of water in cells with SrTiO₃ anodes. *applied physics letters* 1976, 28, 241-243.
16. Schoppel, H.; H, G. CATHODIC REDUCTION OF CU-I OXIDE ELECTRODES AS EXAMPLE FOR REDUCTION MECHANISM OF SEMICONDUCTOR CRYSTAL. *BERICHTE DER BUNSEN-GESELLSCHAFT FUR PHYSIKALISCHE CHEMIE* 1971, 75, 1237-&.
17. Nagasubramanian, G.; Gioda, A. S.; Bard, A. J. Semiconductor Electrodes XXXVII. Photoelectrochemical Behavior of p-Type in Acetonitrile Solutions. *Journal of the Electrochemical Society* 1981, 128, 2158-2164.

18. Sun, K.; McDowell, M. T.; Saadi, F. H.; Zhou, X.; Lewis, N. S. Solar & Alternative Energy Protection of small-bandgap semiconductors for solar-fuel production.
19. Y. Xu, M. A. A. S. a. A. M. 2000, 85, 3-4.
20. Haxel, G. B.; Hedrick, J. B.; Orris, G. J.; Stauffer, P. H.; Hendley II, J. W. *Rare earth elements: critical resources for high technology*; 2327-6932; 2002.
21. Katz, J. E.; Gingrich, T. R.; Santori, E. A.; Lewis, N. S. Combinatorial synthesis and high-throughput photopotential and photocurrent screening of mixed-metal oxides for photoelectrochemical water splitting. *Energy & Environmental Science* 2009, 2, 103-112.
22. Kanan, M. W.; Nocera, D. G. In situ formation of an oxygen-evolving catalyst in neutral water containing phosphate and Co^{2+} . *Science* 2008, 321, 1072-1075.
23. Esswein, A. J.; Nocera, D. G. Hydrogen production by molecular photocatalysis. *Chemical reviews* 2007, 107, 4022-4047.
24. Wang, R.; Hashimoto, K.; Fujishima, A.; Chikuni, M.; Kojima, E.; Kitamura, A.; Shimohigoshi, M.; Watanabe, T. Light-induced amphiphilic surfaces. *Nature* 1997, 388, 431-432.
25. Warren, S. C.; Voitchovsky, K.; Dotan, H.; Leroy, C. M.; Cornuz, M.; Stellacci, F.; Hébert, C.; Rothschild, A.; Grätzel, M. Identifying champion nanostructures for solar water-splitting. *Nature materials* 2013, 12, 842-849.
26. Chernomordik, B. D.; Russell, H. B.; Cvelbar, U.; Jasinski, J. B.; Kumar, V.; Deutsch, T.; Sunkara, M. K. Photoelectrochemical activity of as-grown, α - Fe_2O_3 nanowire array electrodes for water splitting. *Nanotechnology* 2012, 23, 194009.
27. Su, J.; Guo, L.; Bao, N.; Grimes, C. A. Nanostructured $\text{WO}_3/\text{BiVO}_4$ heterojunction films for efficient photoelectrochemical water splitting. *Nano letters* 2011, 11, 1928-1933.
28. Paracchino, A.; Laporte, V.; Sivula, K.; Grätzel, M.; Thimsen, E. Highly active oxide photocathode for photoelectrochemical water reduction. *Nature materials* 2011, 10, 456-461.
29. Martínez-García, A.; Vendra, V. K.; Sunkara, S.; Haldankar, P.; Jasinski, J.; Sunkara, M. K. Tungsten oxide-coated copper oxide nanowire arrays for enhanced activity and durability with photoelectrochemical water splitting. *Journal of Materials Chemistry A* 2013, 1, 15235-15241.
30. Sunkara, S.; Vendra, V. K.; Kim, J. H.; Druffel, T.; Sunkara, M. K. Scalable synthesis and photoelectrochemical properties of copper oxide nanowire arrays and films. *Catalysis Today* 2013, 199, 27-35.
31. Kim, T. W.; Choi, K.-S. Nanoporous BiVO_4 photoanodes with dual-layer oxygen evolution catalysts for solar water splitting. *Science* 2014, 343, 990-994.
32. Solarska, R.; Królikowska, A.; Augustyński, J. Silver nanoparticle induced photocurrent enhancement at WO_3 photoanodes. *Angewandte Chemie International Edition* 2010, 49, 7980-7983.
33. Wang, H.; Turner, J. A. Characterization of hematite thin films for photoelectrochemical water splitting in a dual photoelectrode device. *Journal of The Electrochemical Society* 2010, 157, F173-F178.
34. Sivula, K.; Formal, F. L.; Grätzel, M. WO_3 - Fe_2O_3 photoanodes for water splitting: A host scaffold, guest absorber approach. *Chemistry of Materials* 2009, 21, 2862-2867.
35. Miller, E.; Rocheleau, R.; Deng, X. Design considerations for a hybrid amorphous silicon/photoelectrochemical multijunction cell for hydrogen production. *International Journal of Hydrogen Energy* 2003, 28, 615-623.
36. Brillet, J.; Grätzel, M.; Sivula, K. Decoupling feature size and functionality in solution-processed, porous hematite electrodes for solar water splitting. *Nano letters* 2010, 10, 4155-4160.

37. Tributsch, H.; Bennett, J. Electrochemistry and photochemistry of MoS₂ layer crystals. I. *Journal of Electroanalytical Chemistry and Interfacial Electrochemistry* 1977, 81, 97-111.
38. Jaramillo, T. F.; Jørgensen, K. P.; Bonde, J.; Nielsen, J. H.; Horch, S.; Chorkendorff, I. Identification of active edge sites for electrochemical H₂ evolution from MoS₂ nanocatalysts. *science* 2007, 317, 100-102.
39. Hu, S.; Shaner, M. R.; Beardslee, J. A.; Lichterman, M.; Brunschwig, B. S.; Lewis, N. S. Amorphous TiO₂ coatings stabilize Si, GaAs, and GaP photoanodes for efficient water oxidation. *Science* 2014, 344, 1005-1009.
40. Hisatomi, T.; Kubota, J.; Domen, K. Recent advances in semiconductors for photocatalytic and photoelectrochemical water splitting. *Chemical Society Reviews* 2014, 43, 7520-7535.
41. Beach, J.; Collins, R.; Turner, J. Band-edge Potentials of n-type and p-type GaN. *Journal of The Electrochemical Society* 2003, 150, A899-A904.
42. Gil, B.; Briot, O.; Aulombard, R.-L. Valence-band physics and the optical properties of GaN epilayers grown onto sapphire with wurtzite symmetry. *Physical Review B* 1995, 52, R17028.
43. Pendyala, C.; Jasinski, J. B.; Kim, J. H.; Vendra, V. K.; Lisenkov, S.; Menon, M.; Sunkara, M. K. Nanowires as semi-rigid substrates for growth of thick, In_xGa_{1-x}N (x > 0.4) epi-layers without phase segregation for photoelectrochemical water splitting. *Nanoscale* 2012, 4, 6269-6275.
44. Lin, Y.-G.; Hsu, Y.-K.; Basilio, A. M.; Chen, Y.-T.; Chen, K.-H.; Chen, L.-C. Photoelectrochemical activity on Ga-polar and N-polar GaN surfaces for energy conversion. *Optics express* 2014, 22, A21-A27.
45. Bornoz, P.; Abdi, F. F.; Tilley, S. D.; Dam, B.; Van De Krol, R.; Graetzel, M.; Sivula, K. A bismuth vanadate–cuprous oxide tandem cell for overall solar water splitting. *The Journal of Physical Chemistry C* 2014, 118, 16959-16966.
46. Wang, Z.; Yang, C.; Lin, T.; Yin, H.; Chen, P.; Wan, D.; Xu, F.; Huang, F.; Lin, J.; Xie, X. Visible-light photocatalytic, solar thermal and photoelectrochemical properties of aluminium-reduced black titania. *Energy & Environmental Science* 2013, 6, 3007-3014.
47. Kelly, J.; Memming, R. The Influence of Surface Recombination and Trapping on the Cathodic Photocurrent at p-Type III-V Electrodes. *Journal of the Electrochemical Society* 1982, 129, 730-738.
48. Reiss, P.; Protiere, M.; Li, L. Core/shell semiconductor nanocrystals. *small* 2009, 5, 154-168.
49. Maeda, K.; Teramura, K.; Takata, T.; Hara, M.; Saito, N.; Toda, K.; Inoue, Y.; Kobayashi, H.; Domen, K. Overall Water Splitting on (Ga_{1-x}Zn_x)(N_{1-x}O_x) Solid Solution Photocatalyst: Relationship between Physical Properties and Photocatalytic Activity. *The Journal of Physical Chemistry B* 2005, 109, 20504-20510.
50. Maeda, K.; Teramura, K.; Masuda, H.; Takata, T.; Saito, N.; Inoue, Y.; Domen, K. Efficient Overall Water Splitting under Visible-Light Irradiation on (Ga_{1-x}Zn_x)(N_{1-x}O_x) Dispersed with Rh-Cr Mixed-Oxide Nanoparticles: Effect of Reaction Conditions on Photocatalytic Activity. *The Journal of Physical Chemistry B* 2006, 110, 13107-13112.
51. Aryal, K.; Pantha, B.; Li, J.; Lin, J.; Jiang, H. Hydrogen generation by solar water splitting using p-InGaN photoelectrochemical cells. *GaN* 2010, 15, 2.1.
52. Li, J.; Lin, J.; Jiang, H. Direct hydrogen gas generation by using InGaN epilayers as working electrodes. *Applied Physics Letters* 2008, 93, 162107.

53. Kibria, M. G.; Nguyen, H. P.; Cui, K.; Zhao, S.; Liu, D.; Guo, H.; Trudeau, M. L.; Paradis, S.; Hakima, A.-R.; Mi, Z. One-step overall water splitting under visible light using multiband InGaN/GaN nanowire heterostructures. *ACS nano* 2013, 7, 7886-7893.
54. Deutsch, T. G.; Koval, C. A.; Turner, J. A. III-V nitride epilayers for photoelectrochemical water splitting: GaPN and GaAsPN. *The Journal of Physical Chemistry B* 2006, 110, 25297-25307.
55. Novikov, S. Molecular beam epitaxy of GaNAs alloys with high As content for potential photoanode applications in hydrogen production. *Lawrence Berkeley National Laboratory* 2011.
56. Levander, A. X.; Novikov, S. V.; Liliental-Weber, Z.; Dos Reis, R.; Denlinger, J. D.; Wu, J.; Dubon, O. D.; Foxon, C.; Yu, K. M.; Walukiewicz, W. Growth and transport properties of p-type GaN_{1-x}Bi_x alloys. *Journal of Materials Research* 2011, 26, 2887-2894.
57. Nunna, K.; Iyer, S.; Wu, L.; Li, J.; Bharatan, S.; Wei, X.; Senger, R.; Bajaj, K. Nitrogen incorporation and optical studies of GaAsSbN/GaAs single quantum well heterostructures. *Journal of Applied Physics* 2007, 102, 053106.
58. Veal, T. D.; Piper, L.; Jollands, S.; Bennett, B.; Jefferson, P. H.; Thomas, P. A.; McConville, C. F.; Murdin, B.; Buckle, L.; Smith, G. Band gap reduction in GaNSb alloys due to the anion mismatch. *Applied Physics Letters* 2005, 87, 132101.
59. Belabbes, A.; Ferhata, M.; Zaouib, A. Giant and composition-dependent optical band gap bowing in dilute GaSb N_x alloys. *Applied physics letters* 2006, 88, 152109.
60. Sunkara, M. K.; Pendyala, C. Searching for new solar-hydrogen materials using nanowires.
61. Hodes, G.; Cahen, D.; Manassen, J. Tungsten trioxide as a photoanode for a photoelectrochemical cell (PEC). *Nature* 1976, 260, 312-313.
62. Chakrapani, V.; Thangala, J.; Sunkara, M. K. WO₃ and W₂N nanowire arrays for photoelectrochemical hydrogen production. *international journal of hydrogen energy* 2009, 34, 9050-9059.
63. Hardee, K. L.; Bard, A. J. Semiconductor electrodes V. The application of chemically vapor deposited iron oxide films to photosensitized electrolysis. *Journal of the Electrochemical Society* 1976, 123, 1024-1026.
64. Kennedy, J. H.; Frese, K. W. Photooxidation of Water at α -Fe₂O₃ Electrodes. *Journal of the Electrochemical Society* 1978, 125, 709-714.
65. Hahn, N. T.; Ye, H.; Flaherty, D. W.; Bard, A. J.; Mullins, C. B. Reactive ballistic deposition of α -Fe₂O₃ thin films for photoelectrochemical water oxidation. *ACS nano* 2010, 4, 1977-1986.
66. Osterloh, F. E. Inorganic nanostructures for photoelectrochemical and photocatalytic water splitting. *Chemical Society Reviews* 2013, 42, 2294-2320.
67. Vayssieres, L.; Sathe, C.; Butorin, S. M.; Shuh, D. K.; Nordgren, J.; Guo, J. One-dimensional quantum-confinement effect in α -Fe₂O₃ ultrafine nanorod arrays. *Adv. Mater* 2005, 17, 2320-2323.
68. Wagner, R.; Ellis, W. Vapor-liquid-solid mechanism of single crystal growth. *Applied Physics Letters* 1964, 89-90.
69. Meyyappan, M.; Sunkara, M. K. *Inorganic nanowires: applications, properties, and characterization*. CRC Press: 2009.
70. Choi, H.-J.; Lee, J.-G. Continuous synthesis of silicon carbide whiskers. *Journal of materials science* 1995, 30, 1982-1986.
71. Wu, Y.; Yang, P. Direct observation of vapor-liquid-solid nanowire growth. *Journal of the American Chemical Society* 2001, 123, 3165-3166.
72. Trentler, T. J.; Hickman, K. M.; Goel, S. C.; Viano, A. M.; Gibbons, P. C.; Buhro, W. E. Solution-liquid-solid growth of crystalline III-V semiconductors: an analogy to vapor-liquid-solid growth. *Science* 1995, 270, 1791-1794.

73. Chockla, A. M.; Korgel, B. A. Seeded germanium nanowire synthesis in solution. *Journal of Materials Chemistry* 2009, 19, 996-1001.
74. Hanrath, T.; Korgel, B. A. Nucleation and growth of germanium nanowires seeded by organic monolayer-coated gold nanocrystals. *Journal of the American Chemical Society* 2002, 124, 1424-1429.
75. Hanrath, T.; Korgel, B. A. Supercritical fluid–liquid–solid (SFLS) synthesis of Si and Ge nanowires seeded by colloidal metal nanocrystals. *Advanced Materials* 2003, 15, 437-440.
76. Sarkar, J.; Khan, G. G.; Basumallick, A. Nanowires: properties, applications and synthesis via porous anodic aluminium oxide template. *Bulletin of Materials Science* 2007, 30, 271-290.
77. Thurn-Albrecht, T.; Schotter, J.; Kästle, G.; Emley, N.; Shibauchi, T.; Krusin-Elbaum, L.; Guarini, K.; Black, C.; Tuominen, M.; Russell, T. Ultrahigh-density nanowire arrays grown in self-assembled diblock copolymer templates. *Science* 2000, 290, 2126-2129.
78. Bunsen, R. *Ann. Pharm. (Justus Leibigs Ann. Chem.)* 1839, 31.
79. Manasevit, H. M. *Applied Physics Letters* 1968, 12.
80. Nakamura, S. GaN growth using GaN buffer layer. *Japanese Journal of Applied Physics* 1991, 30, L1705.
81. Moscatelli, D.; Cavallotti, C. A Kinetic Study of the MOCVD of GaN.
82. Safvi, S.; Redwing, J.; Tischler, M.; Kuech, T. GaN growth by metallorganic vapor phase epitaxy a comparison of modeling and experimental measurements. *Journal of The Electrochemical Society* 1997, 144, 1789-1796.
83. Dauelsberg, M.; Martin, C.; Protzmann, H.; Boyd, A.; Thrush, E.; Käppeler, J.; Heuken, M.; Talalaev, R.; Yakovlev, E.; Kondratyev, A. Modeling and process design of III-nitride MOVPE at near-atmospheric pressure in close coupled showerhead and planetary reactors. *Journal of crystal growth* 2007, 298, 418-424.
84. Hui, L. Mass transport analysis of a showerhead MOCVD reactor. *Journal of Semiconductors* 2011, 32, 033006.
85. Yuan, C.; Salagaj, T.; Gurary, A.; Zawadzki, P.; Chern, C.; Kroll, W.; Stall, R.; Li, Y.; Schurman, M.; Hwang, C. Y. High Quality P-Type GaN Deposition on c-Sapphire Substrates in a Multiwafer Rotating-Disk Reactor. *Journal of The Electrochemical Society* 1995, 142, L163-L165.
86. Nakamura, F.; Hashimoto, S.; Hara, M.; Imanaga, S.; Ikeda, M.; Kawai, H. AlN and AlGaIn growth using low-pressure metalorganic chemical vapor deposition. *Journal of crystal growth* 1998, 195, 280-285.
87. Han, J.; Baca, A.; Shul, R.; Willison, C.; Zhang, L.; Ren, F.; Zhang, A.; Dang, G.; Donovan, S.; Cao, X. Growth and fabrication of GaN/AlGaIn heterojunction bipolar transistor. *Applied physics letters* 1999, 74, 2702-2704.
88. Mihopoulos, T. G.; Gupta, V.; Jensen, K. F. A reaction-transport model for AlGaIn MOVPE growth. *Journal of Crystal Growth* 1998, 195, 733-739.
89. Mo, C.; Fang, W.; Pu, Y.; Liu, H.; Jiang, F. Growth and characterization of InGaIn blue LED structure on Si (111) by MOCVD. *Journal of crystal growth* 2005, 285, 312-317.
90. Matsuoka, T.; Yoshimoto, N.; Sasaki, T.; Katsui, A. Wide-gap semiconductor InGaIn and InGaAlN grown by MOVPE. *Journal of electronic materials* 1992, 21, 157-163.
91. Ougazzaden, A.; Le Bellego, Y.; Rao, E.; Juhel, M.; Leprince, L.; Patriarche, G. Metal organic vapor phase epitaxy growth of GaAsN on GaAs using dimethylhydrazine and tertiarybutylarsine. *Applied physics letters* 1997, 70, 2861-2863.
92. Keller, S.; Keller, B.; Kopolnek, D.; Abare, A.; Masui, H.; Coldren, L.; Mishra, U.; Den Baars, S. Growth and characterization of bulk InGaIn films and quantum wells. *Applied physics letters* 1996, 68, 3147-3149.

93. Lobanova, A.; Mazaev, K.; Talalaev, R.; Leys, M.; Boeykens, S.; Cheng, K.; Degroote, S. Effect of V/III ratio in AlN and AlGa_N MOVPE. *Journal of crystal growth* 2006, 287, 601-604.
94. Tessarek, C.; Yamaguchi, T.; Figge, S.; Hommel, D. Improved capping layer growth towards increased stability of InGa_N quantum dots. *physica status solidi (c)* 2009, 6, S561-S564.
95. Piner, E.; Behbehani, M.; El-Masry, N.; McIntosh, F.; Roberts, J.; Boutros, K.; Bedair, S. Effect of hydrogen on the indium incorporation in InGa_N epitaxial films. *Applied physics letters* 1997, 70, 461-463.
96. Dupuis, R. Epitaxial growth of III-V nitride semiconductors by metalorganic chemical vapor deposition. *Journal of crystal growth* 1997, 178, 56-73.
97. Mondal, A.; Das, T.; Halder, N.; Dhar, S.; Kumar, J. Growth of dilute GaSbN layers by liquid-phase epitaxy. *Journal of crystal growth* 2006, 297, 4-6.
98. Alberi, K.; Dubon, O.; Walukiewicz, W.; Yu, K.; Bertulis, K.; Krotkus, A. Valence band anticrossing in GaBixAs1-x. *Applied Physics Letters* 2007, 91, 051909.
99. Kudrawiec, R.; Kopaczek, J.; Sitarek, P.; Misiewicz, J.; Henini, M.; Novikov, S. Unusual broadening of E₀ and E₀+ ΔSO transitions in GaAsBi studied by electromodulation spectroscopy. *Journal of Applied Physics* 2012, 111, 066103.
100. Yu, K.; Sarney, W.; Novikov, S.; Detert, D.; Zhao, R.; Denlinger, J.; Svensson, S.; Dubon, O.; Walukiewicz, W.; Foxon, C. Highly mismatched N-rich GaN_{1-x}Sbx films grown by low temperature molecular beam epitaxy. *Applied Physics Letters* 2013, 102, 102104.
101. Warren, B. E. *X-ray Diffraction*. Courier Corporation: 1969.
102. Edwards, A. HP Klug and LE Alexander, x-ray diffraction procedures for polycrystalline and amorphous materials: Wiley-Interscience, New York, 2nd edn., 1974, xxv+ 966 pp. price£ 18.55. Elsevier: 1975.
103. Williams, D. B.; Carter, C. B. *Transmission Electron Microscopy* Plenum. New York, NY 1996.
104. Chattopadhyay, K. *Introduction To Nanoscience And Nanotechnology*. PHI Learning Pvt. Ltd.: 2009.
105. Leenheer, A. J. Light to electrons to bonds: imaging water splitting and collecting photoexcited electrons. California Institute of Technology, 2013.
106. Miyajima, T.; Ozawa, M.; Asatsuma, T.; Kawai, H.; Ikeda, M. Minority carrier diffusion length in GaN and ZnSe. *Journal of crystal growth* 1998, 189, 768-772.
107. Chernyak, L.; Osinsky, A.; Fuflyigin, V.; Schubert, E. Electron beam-induced increase of electron diffusion length in p-type GaN and AlGa_N/GaN superlattices. *Applied Physics Letters* 2000, 77, 875-877.
108. Bandić, Z.; Bridger, P.; Piquette, E.; McGill, T. Electron diffusion length and lifetime in p-type GaN. *Applied physics letters* 1998, 73, 3276-3278.
109. Perdew, J.; Burke, K.; Ernzerhof, M. Phys Rev Lett 77: 3865. *Errata:(1997) Phys Rev Lett* 1996, 78, 1396.
110. Kresse, G.; Joubert, D. From ultrasoft pseudopotentials to the projector augmented-wave method. *Physical Review B* 1999, 59, 1758.
111. Perdew, J. P.; Wang, Y. Pair-distribution function and its coupling-constant average for the spin-polarized electron gas. *Physical Review B* 1992, 46, 12947.
112. Perdew, J. P.; Burke, K.; Ernzerhof, M. Generalized gradient approximation made simple. *Physical review letters* 1996, 77, 3865.
113. Segall, M.; Lindan, P. J.; Probert, M. a.; Pickard, C.; Hasnip, P.; Clark, S.; Payne, M. First-principles simulation: ideas, illustrations and the CASTEP code. *Journal of Physics: Condensed Matter* 2002, 14, 2717.

114. Walsh, A.; Da Silva, J. L.; Wei, S.-H. Origins of band-gap renormalization in degenerately doped semiconductors. *Physical Review B* 2008, 78, 075211.
115. Andriotis, A. N.; Mpourmpakis, G.; Lisenkov, S.; Sheetz, R. M.; Menon, M. U-calculation of the LSDA+ U functional using the hybrid B3LYP and HSE functionals. *physica status solidi (b)* 2013, 250, 356-363.
116. Vurgaftman, I.; Meyer, J. Band parameters for nitrogen-containing semiconductors. *Journal of Applied Physics* 2003, 94, 3675-3696.
117. DeWinter, J.; Pollack, M.; Srivastava, A.; Zyskind, J. Liquid phase epitaxial Ga_{1-x}In_xAs_ySb_{1-y} lattice-matched to (100) GaSb over the 1.71 to 2.33 μm wavelength range. *Journal of electronic materials* 1985, 14, 729-747.
118. Perdew, J. P.; Wang, Y. Erratum: pair-distribution function and its coupling-constant average for the spin-polarized electron gas [Phys. Rev. B 46, 12 947 (1992)]. *Physical Review B* 1997, 56, 7018.
119. Siegle, H.; Kaczmarczyk, G.; Filippidis, L.; Litvinchuk, A.; Hoffmann, A.; Thomsen, C. Zone-boundary phonons in hexagonal and cubic GaN. *Physical Review B* 1997, 55, 7000.
120. Reshchikov, M. A.; Morkoc, H. Luminescence properties of defects in GaN. *Journal of applied physics* 2005, 97, 061301.
121. Park, I.-K.; Kwon, M.-K.; Baek, S.-H.; Ok, Y.-W.; Seong, T.-Y.; Park, S.-J.; Kim, Y.-S.; Moon, Y.-T.; Kim, D.-J. Enhancement of phase separation in the InGaN layer for self-assembled In-rich quantum dots. *Applied Physics Letters* 2005, 87, 061906.
122. Deutsch, T. G.; Head, J. L.; Turner, J. A. Photoelectrochemical characterization and durability analysis of GaInPN epilayers. *Journal of the Electrochemical Society* 2008, 155, B903-B907.
123. Sunkara, M. K.; Pendyala, C.; Cummins, D.; Meduri, P.; Jasinski, J.; Kumar, V.; Russell, H.; Clark, E.; Kim, J. Inorganic nanowires: a perspective about their role in energy conversion and storage applications. *Journal of Physics D: Applied Physics* 2011, 44, 174032.
124. Lim, S. K.; Tambe, M. J.; Brewster, M. M.; Gradecak, S. Controlled growth of ternary alloy nanowires using metalorganic chemical vapor deposition. *Nano letters* 2008, 8, 1386-1392.
125. Guo, Y.-N.; Xu, H.-Y.; Auchterlonie, G. J.; Burgess, T.; Joyce, H. J.; Gao, Q.; Tan, H. H.; Jagadish, C.; Shu, H.-B.; Chen, X.-S. Phase separation induced by Au catalysts in ternary InGaAs nanowires. *Nano letters* 2013, 13, 643-650.
126. Tateno, K.; Zhang, G.; Nakano, H. Growth of GaInAs/AlInAs heterostructure nanowires for long-wavelength photon emission. *Nano letters* 2008, 8, 3645-3650.
127. Shapiro, J. N.; Lin, A.; Ratsch, C.; Huffaker, D. Temperature dependence of stacking faults in catalyst-free GaAs nanopillars. *Nanotechnology* 2013, 24, 475601.
128. Zhou, H.; Pozuelo, M.; Hicks, R. F.; Kodambaka, S. Self-catalyzed vapor-liquid-solid growth of InP_{1-x}Sb_x nanostructures. *Journal of Crystal Growth* 2011, 319, 25-30.
129. Kodambaka, S.; Tersoff, J.; Reuter, M.; Ross, F. Germanium nanowire growth below the eutectic temperature. *Science* 2007, 316, 729-732.
130. Fu, K. Growth Dynamics of Semiconductor Nanostructures by MOCVD. 2009.
131. Kar, A.; Low, K.-B.; Oye, M.; Strocio, M. A.; Dutta, M.; Nicholls, A.; Meyyappan, M. Investigation of nucleation mechanism and tapering observed in ZnO nanowire growth by carbothermal reduction technique. *Nanoscale Res Lett* 2011, 6.
132. Koblmüller, G.; Abstreiter, G. Growth and properties of InGaAs nanowires on silicon. *physica status solidi (RRL)-Rapid Research Letters* 2014, 8, 11-30.
133. Hannon, J.; Kodambaka, S.; Ross, F.; Tromp, R. The influence of the surface migration of gold on the growth of silicon nanowires. *Nature* 2006, 440, 69-71.

134. Givargizov, E. Fundamental aspects of VLS growth. *Journal of Crystal Growth* 1975, 31, 20-30.
135. Neumayer, D. A.; Ekerdt, J. G. Growth of group III nitrides. A review of precursors and techniques. *Chemistry of materials* 1996, 8, 9-25.
136. Niebuhr, R.; Bachem, K.; Dombrowski, K.; Maier, M.; Pletschen, W.; Kaufmann, U. Basic studies of gallium nitride growth on sapphire by metalorganic chemical vapor deposition and optical properties of deposited layers. *Journal of electronic materials* 1995, 24, 1531-1534.
137. Haywood, S.; Mason, N.; Walker, P. Growth of GaSb by MOVPE; Optimization of electrical quality with respect to growth rate, pressure, temperature and IIIIV ratio. *Journal of Crystal Growth* 1988, 93, 56-61.
138. Haywood, S.; Henriques, A.; Mason, N.; Nicholas, R.; Walker, P. Growth of GaSb by MOVPE. *Semiconductor Science and Technology* 1988, 3, 315.
139. Chidley, E.; Haywood, S.; Mallard, R.; Mason, N.; Nicholas, R.; Walker, P.; Warburton, R. GaSb heterostructures grown by MOVPE. *Journal of Crystal Growth* 1988, 93, 70-78.
140. Nakamura, S.; Senoh, M.; Mukai, T. High-power InGaN/GaN double-heterostructure violet light emitting diodes. *Applied Physics Letters* 1993, 62, 2390-2392.

APPENDIX

Scalable synthesis and photoelectrochemical properties of copper oxide nanowire arrays and films

Swathi Sunkara^a, Venkat Kalyan Vendra^a, Jeong Hoon Kim^b, Mahendra K. Sunkara*^{a, b}

^aDepartment of Chemical Engineering, University of Louisville, Louisville, KY 40292.

^bConn Center for Renewable Energy Research, University of Louisville, Louisville, KY 40292.

* Corresponding author email: mahendra@louisville.edu

Abstract

Here, we present a scalable method based on both atmospheric plasma and wet chemical oxidation methods to synthesize thin films and nanowire arrays of both cupric and cuprous oxides. In terms of nanowire arrays, the wet chemical oxidation is shown to produce copper hydroxide nanowire arrays on copper foils using hydrogen peroxide as the oxidant similar to ammonium persulfate. Experiments using different concentrations of hydrogen peroxide at constant pH resulted in higher nucleation density and smaller diameter of copper hydroxide nanowires. A scheme involving short period wet chemical

oxidation followed by plasma annealing resulted in high density of Cu_2O nanowire arrays. The overall process is rapid on the order of 1 minute reaction time scale. Photoelectrochemical characterization of titania coated copper oxide nanowire and thin film electrodes showed that the nanowire array electrodes showed significantly higher photoactivity than the thin film electrodes. The performance of resulting Cu_2O NW array electrodes can be optimized further with other protective coatings.

Keywords: copper oxide nanowires, atmospheric plasma, solar water splitting, atomic layer deposition, photoelectrochemical characterization

Introduction

Photoelectrochemical water splitting for solar hydrogen production represents one of the grand challenges towards carbon free energy generation. However, there are no known semiconductor materials with the appropriate band gap, band edge positions and aqueous stability required for solar water splitting.^{1,2} Cuprous oxide (Cu_2O) is an attractive material because of the non-toxicity, earth abundance of its constituent elements and has a band gap of approximately 2.2 eV, with its band edges straddling the water reduction and oxidation potential.³⁻⁵ As-synthesized, Cu_2O is a p-type semiconductor due to the acceptor states resulting from copper vacancies located at 0.4 eV above the valence band.⁶ Cuprous oxide can act as efficient photocathode for hydrogen evolution. However, the valence band position is just below the oxygen evolution potential and this would imply less driving force for oxygen evolution.

One of the main challenges with cuprous oxide is its inherent instability in aqueous solutions.⁷ The photostability challenge posed by the Cu_2O electrodes has been

addressed by depositing thin films of titania on cuprous oxide by atomic layer deposition.⁸ The resulting hetero-junction is not only expected to improve stability but also reduces recombination by enhancing the electron transport due to the inbuilt electric-field at the hetero-junction. Gratzel and co-workers modified the cuprous oxide photocathode by coating it with a layer of titania followed by aluminum doped zinc oxide and then electrodepositing platinum nanoparticles to improve the stability and performance of the Cu₂O electrodes.⁹ It was found that the titania coated cuprous oxide photocathodes had poor stability in aqueous solutions and exhibited no photoactivity after 20 min. Pin holes formed during the ALD of titania have been found to result in instability in aqueous solutions. Additional layers of zinc oxide and alumina improved the photostability (78 % of the short-circuit current density retained after 20 min) and also play an important role in enhancing the charge separation and mitigating the electron-hole recombination in Cu₂O.

The poor electrical conductivity of Cu₂O has been a limiting factor in achieving high efficiency for Cu₂O based solar cells and is also a major concern for solar water splitting cells.¹⁰ The absorption depth corresponding to the band gap of Cu₂O has been reported to be 10 μm.¹¹ However, the diffusion length of carriers in electrodeposited copper oxide (Cu₂O) has been found to be on the order of 20-100 nm.¹² In view of this, 1-D single crystal architectures in the form of nanowire arrays could offer the thickness necessary for optical absorption and short length scales for diffusion of minority carriers to semiconductor-electrolyte interface to drive the water splitting reaction. The single crystal nature of one-dimensional structures should allow direct conduction pathways for faster charge transport.^{13,14} However, the performance and stability of single crystal

copper oxide nanowires coated with titania for solar hydrogen production has not been investigated.

The synthesis of polycrystalline cuprous oxide films has been accomplished with a number of techniques such as electrodeposition, photochemical deposition, RF magnetron sputtering, chemical bath deposition, anodic oxidation and thermal oxidation methods.^{9,15-19} However, the synthesis of cuprous oxide nanowire arrays has been achieved using a limited number of techniques. Synthesis using template and surfactant assisted methods has mostly yielded polycrystalline cuprous oxide nanowires with the exception of a few reports describing the growth of single crystal cuprous oxide nanowires.²⁰⁻²³ Wu and co-workers reported the synthesis of linearly aligned complex chains of metal cations which could be reduced by glucose to form single crystal cuprous oxide nanowires with a diameter of 20 nm and lengths of several microns.²⁴ Li et al. demonstrated the liquid phase synthesis of Cu₂O NW (diameter ~ 20 nm) by the reduction of cupric acetate using reducing agents with methoxy group.²⁵ Ajayan and co-workers reported a simple electrochemical method utilizing only Cu foil and DI water to synthesize cuprous oxide nanowires.²⁶ To the best of our knowledge there have not been any reports describing the growth of single crystalline cuprous oxide nanowires arrays directly on conducting substrates by thermal or plasma oxidation. Several reports suggest thermal oxidation of copper foils at temperatures between 400-700 °C over several hours resulted in bicrystalline CuO nanowire arrays.²⁷⁻³¹ To synthesize Cu₂O nanowire arrays, a two-step process has been primarily developed: In the first step, copper is subjected to wet chemical oxidation using ammonium persulfate in sodium hydroxide solutions to produce copper hydroxide nanowire arrays; and in the second step, the copper hydroxide

nanowire arrays are thermally annealed at temperatures around 450 °C to convert them to Cu₂O nanowire arrays.³²

All the synthesis techniques discussed above require several hours of oxidation or annealing time scales to produce few microns long Cu₂O nanowire arrays on copper foils. In addition, the resulting nanowires had diameters in excess of 100 nm and it is not clear as to what factors control the diameters and the number density of the resulting nanowire arrays. Here, we present a scalable approach for producing Cu₂O nanowire arrays on copper foils and on other substrates such as quartz, fluorinated tin oxide (FTO) substrates and other metallic foils. Specifically, we investigated the use of atmospheric plasma combined with wet chemical oxidation to produce cuprous oxide nanowire arrays. Also, we performed a series of experiments to understand nucleation and growth of copper hydroxide and copper oxide nanowires using both wet chemical oxidation and plasma oxidation processes. Most importantly, the photoelectrochemical performance of films and nanowire arrays coated with thin layers of titania are investigated and compared.

Experimental

Atmospheric plasma exposure experiments are conducted using a microwave plasma discharge whose details are described elsewhere.³³ Various experiments were conducted using atmospheric plasma discharge at powers ranging from 500-900W and air flow rates ranging from 5-10 lpm. Wet chemical oxidation experiments were conducted by immersing copper foils in sodium hydroxide solutions at pH values ranging from 7-14 containing different amounts of oxidizers such as ammonium persulfate ((NH₄)₂S₂O₈) and hydrogen peroxide. Atomic layer deposition of titania films on the copper oxide thin films and nanowire arrays was carried out using a Savannah 100 ALD system

(Cambridge Nanotech). The deposition was carried out at a pressure of 600 mTorr and a temperature of 250 °C using water and titanium isopropoxide as the precursors. The deposition process was carried out for 650 cycles to form a 20 nm titania coating on the electrodes. The synthesized samples were analyzed using X-ray diffraction (Bruker Instruments) and Scanning electron microscopy (Nova FEI SEM). The optical band gap of the films was determined using diffuse reflectance obtained with a UV-VIS spectrophotometer (Perkin Elmer, Lambda 900).

For photoelectrochemical characterization, the resulting copper oxide film and nanowire arrays samples are made into electrodes using the following procedure. The copper foils are connected to an electrical wire at the back using conductive silver epoxy and then the entire non-active area was covered with Hysol epoxy (Loctite 9464). The electrodes were cured for 110 °C for 1h. A Hysol E120HP, which has excellent chemical resistance, was applied over the previously cured epoxy coating and was allowed to dry at room temperature for 12 h.

All the photoelectrochemical measurements were performed in photoelectrochemical cell equipped with a quartz window. A three electrode configuration comprising of copper oxide working electrode, Ag/AgCl reference electrode and a platinum mesh counter electrode was used for the characterization. A solution sodium sulfate (1 M), buffered to pH 4.9 using a sodium phosphate solution (0.1 M) was used as the electrolyte. For analyzing current-potential (J-E) curves, the potentials measured w.r.t. Ag/AgCl electrode was converted to potential w.r.t reference hydrogen electrode (RHE). The data were not corrected for any other extrinsic losses such as the iR losses. The photoresponse of electrodes was measured under chopped AM

1.5 radiation from a 200 W Xe lamp (Newport Instruments). The light intensity was adjusted to 100 mW/cm^2 (1 Sun illumination) using a calibrated Si photodiode. The typical active area of the electrodes was 0.68 cm^2 . For the linear sweep voltammetry experiments (J-E curves), a scan rate of 5 mV/s was used. All the electrochemical measurements were recorded using an EG&G Princeton Applied Research 273 A potentiostat. The Mott-Schottky analysis was done under 1 sun illumination and a frequency of 10 Hz was used. Platinum loading onto the nanowire arrays was performed using a three electrode setup using copper oxide as the working electrode, Ag/AgCl as the reference and a Pt mesh as the counter electrode. An aqueous solution of 1 mM chloroplatinic acid was used as the electrolyte and a potential of -0.1 V vs. Ag/AgCl was applied for 10 minutes. Copper electroplating on the gold sputtered fluorinated tin oxide (FTO) glass slides was performed using a two electrode configuration where FTO glass was used as the counter electrode, a copper foil was used as the working electrode. An aqueous solution of 1 M copper sulfate and 0.5 M sulfuric acid was used the electrolyte and a current density of -10 mA/cm^2 was applied for 10 minutes.

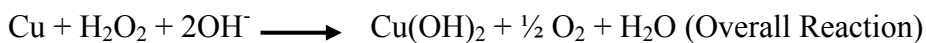
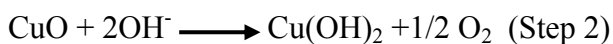
Results and discussion

Several researchers have shown that wet chemical oxidation using ammonium persulfate in sodium hydroxide solutions. The experiments performed at pH values >10 resulted in copper hydroxide ($\text{Cu}(\text{OH})_2$) nanowire arrays on copper foil.³⁴ Similarly, such wet chemical oxidation method has been shown to work with several other metals in producing their respective hydroxide nanowire arrays.^{35,36,37} However, it is not clear about the underlying reasons for producing one-dimensional structures and the role of ammonium or sodium persulfate. Here, a set of experiments are conducted to gain insight

in to wet chemical oxidation procedure. Firstly, experiments are performed at different pH values using sodium hydroxide and potassium hydroxide. The results showed that copper hydroxide nanowire arrays resulted at pH >10 and no differences were seen between experiments involving sodium hydroxide and potassium hydroxide. In order to understand the role of oxidizer, experiments are performed using hydrogen peroxide instead of ammonium persulfate. The experiments resulted in copper hydroxide nanowire arrays similar to those obtained using ammonium persulfate. In the case of ammonium persulfate as oxidizer, the growth of copper hydroxide nanowires proceeds by an oxidation process according to the reaction.



The above overall reaction can be understood better with the use of hydrogen peroxide as the oxidizer. The oxidation of copper foils with hydrogen peroxide is expected to follow two steps:



The above proposed two-step reaction suggests that the oxidation proceeds in forming copper oxide first and then hydrolyzing to form hydroxide. The copper hydroxide, copper oxide phases are not stable when the pH of the solution is less than 10 as indicated by the Pourbaix diagram (Figure 1) and this explains why no nanowire formation was observed in the experiments carried with pH < 10.

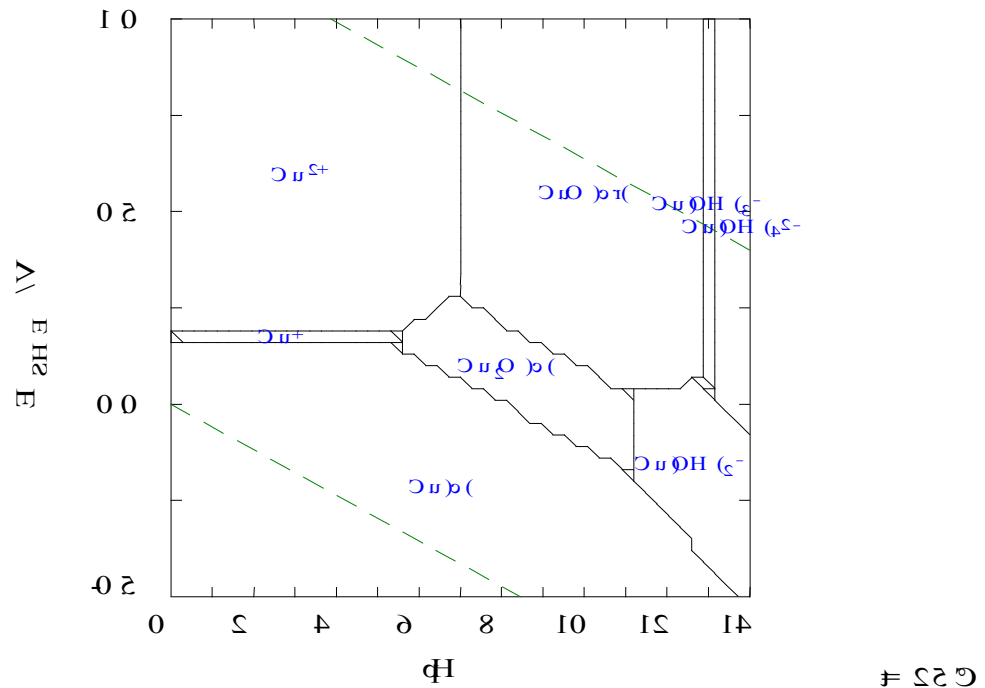


Figure 1 Pourbaix diagram of copper-water system at 25 °C generated using Medusa software. $[Cu^{2+}]$ concentration of 1 μ M was used. The green dotted lines show the hydrogen and oxygen evolution potential.

Experiments using different concentrations of hydrogen peroxide at constant pH of 12 showed that the number density of nanowire arrays increased and diameter of resulting nanowires decreased with increasing concentration of hydrogen peroxide as depicted in Figure 2. It is important to note that pH of the solution would change with time as sodium hydroxide is being consumed in the reaction and hence it is essential to maintain constant pH to ensure proper growth of the nanowires. As the reactions proceeds it was observed color of the solution changed to dark blue suggesting the presence of a copper ions in the solution phase. These copper ions in the solution could cause deviations in nanowire growth when pH is not maintained.

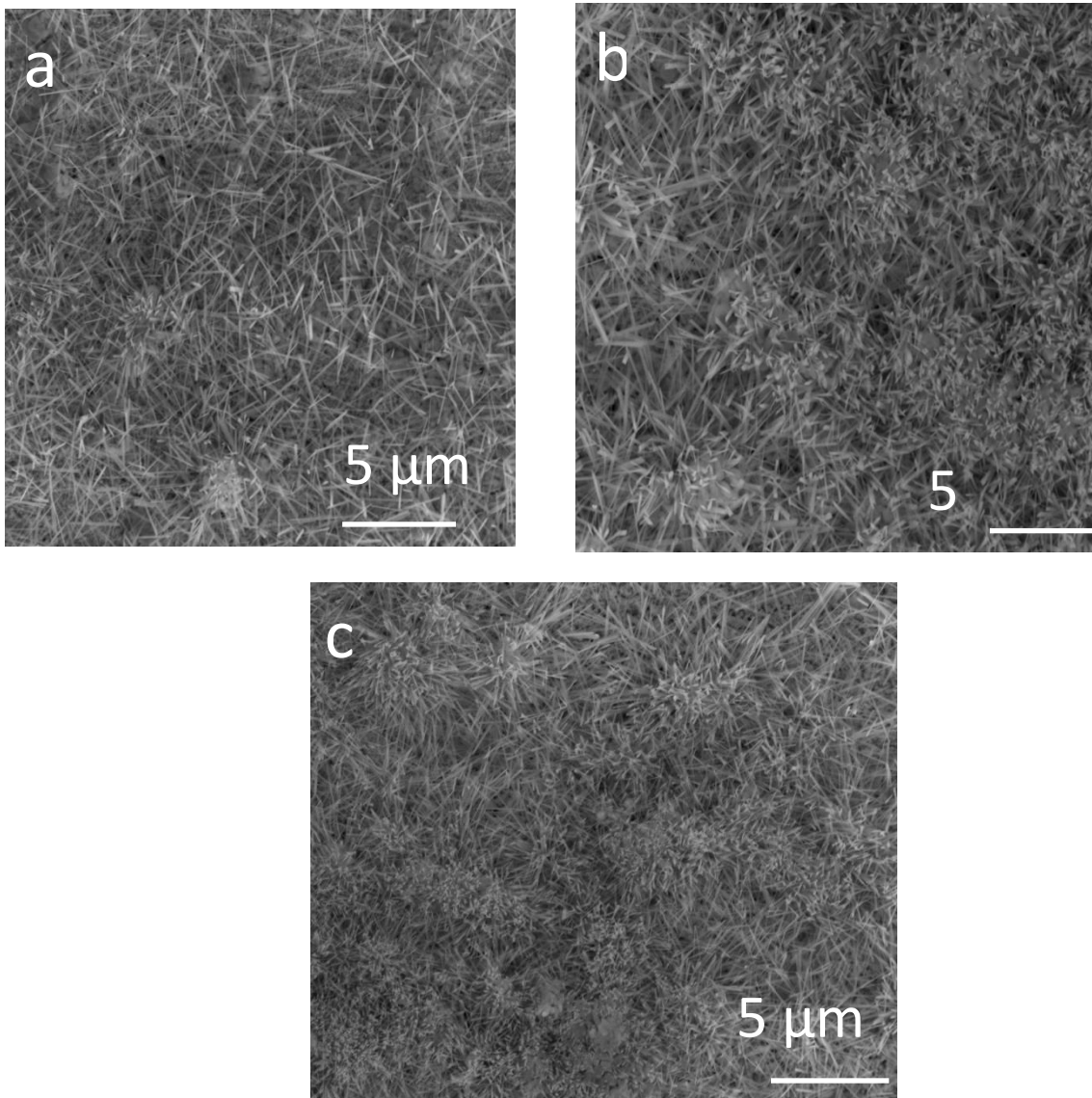
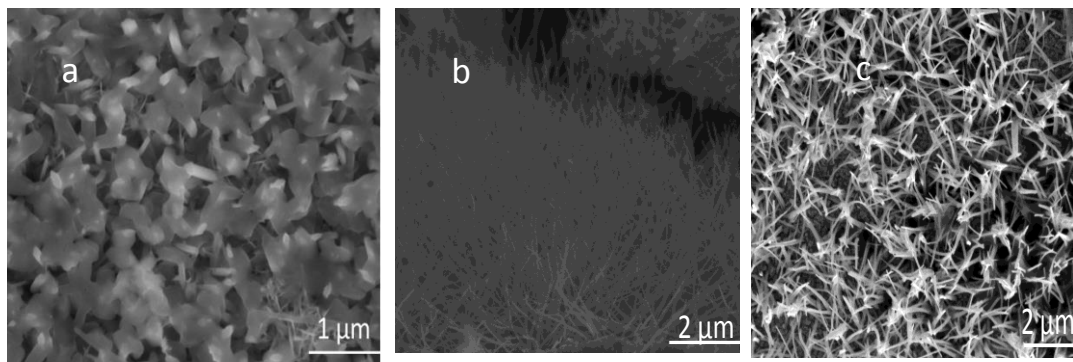


Figure 2 Scanning electron microscopy images showing increase in nanowire density with increase in H_2O_2 concentration: (a) 0.5 M (b) 1 M (c) 1.5 M



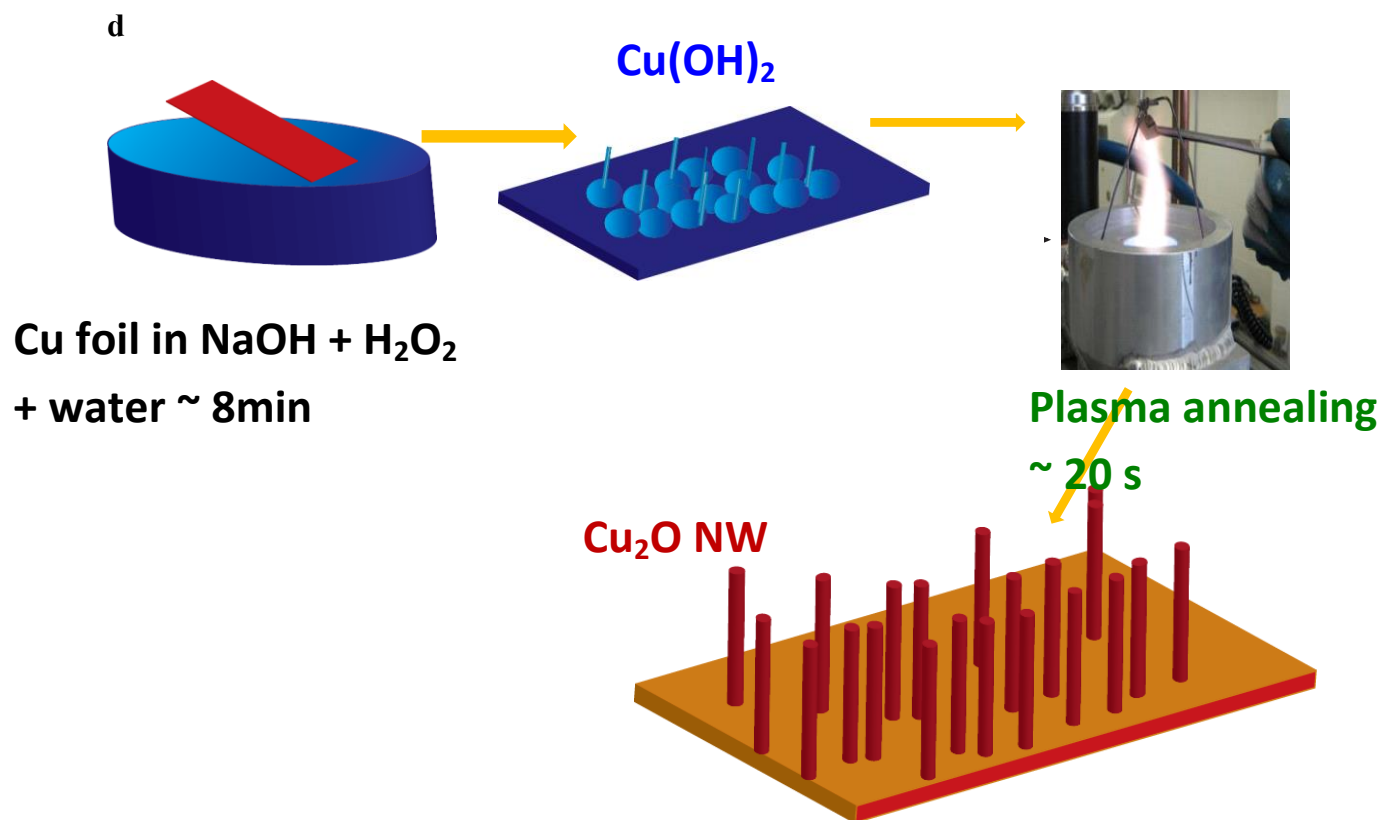


Figure 3 (a) SEM image showing the nucleation of NW by wet chemical oxidation and their growth by (b) thermal oxidation for 10 min and (c) plasma oxidation for 20 s. (d) Schematic illustrating growth of wires through plasma oxidation

The length of the copper hydroxide nanowires increased with increased oxidation times. As wet oxidation time increased, the length of the nanowires was found to increase from 500 nm (30s immersion time) to 3 microns (1-2 minutes immersion time) as shown in Figure S2 (refer Supplementary Information). There was no significant change in the nanowire length at longer immersion times of 30 minutes. These observations support the argument that nanowire formation mechanism is through basal growth at nanowire/substrate interface. To further validate the growth mechanism, short copper hydroxide nanowires (~500 nm in length) were grown by wet chemical oxidation and

then exposed to plasma oxidation for 20 s or thermal oxidation for 10 minutes. The increase in length of the nanowires after the oxidation step shows that nanowires nucleated by the wet oxidation method grow longer by preferential oxidation at the nanowire/oxide film interface. Hence, the nucleation and growth mechanism of copper hydroxide nanowires can be thought to proceed in similar to the plasma oxidation of metal foils to form metal oxide nanowires. See schematic in Figure 4. The only difference is that high pH conditions result in the formation of metal hydroxide nanowires, where as in plasma oxidation metal oxide nanowires are formed.

Direct plasma oxidation of copper foils resulted in thin films of Cu_2O and CuO with different exposure conditions. Cu_2O thin films resulted when exposed to

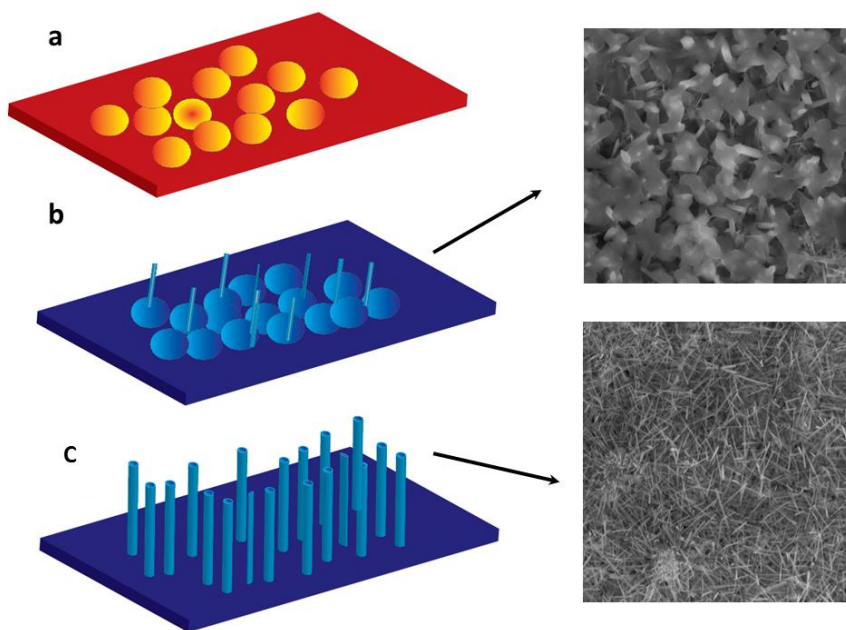


Figure 4 Schematic explaining the mechanism for the formation of copper hydroxide nanowires: (a) Cu foil reacts with the oxidizer to form copper oxide and subsequent nucleation (b) copper oxide is converted to copper hydroxide and nucleation of copper hydroxide (d) basal growth of nanowires

atmospheric plasma flame that resulted in higher temperatures $< 500\text{ }^{\circ}\text{C}$ for the copper foils. CuO films resulted with exposures that resulted in temperatures $> 500\text{ }^{\circ}\text{C}$ for the copper foils. The resulting films were about 2-3 μm thickness with only about exposure over 2-3 minutes unlike thermal oxidation or other methods that require processing over several tens of minutes. Figure S3 shows the SEM images of the copper oxide thin films produced by plasma oxidation. A few of the thin film samples prepared by the plasma oxidation technique also showed a low density of nanowires as shown in Figure S2 in supplementary information document. Prior work on the growth of hematite nanowire arrays on iron foil showed that the plasma overheating or the initial temperature rise before the substrate reaches an equilibrium temperature is a critical factor controlling the nucleation density.^{38,39} Also, earlier reports have shown that the thermal oxidation of copper foils over 4 hours at atmospheric pressure results in cupric oxide (CuO) nanowire arrays in temperature window of 400-700 $^{\circ}\text{C}$ for 4 h.²⁷ These findings suggest that temperature control of the copper will play a key role in determining the number density of the nanowires on copper foil.

The synthesis of copper oxide nanowires was carried out using a two-step approach: In the first step, copper hydroxide nanowires were formed by a wet oxidation using hydrogen peroxide and in the second step, the copper hydroxide nanowires were annealed in the atmospheric air plasma for few seconds to convert the copper hydroxide nanowires to copper oxide nanowires. Figure 3 illustrates the synthesis scheme for making copper oxide nanowires. The XRD spectrum of the copper oxide thin films and nanowires are shown in Figure 5. Analysis of the peak positions showed that a small fraction of CuO phase was present in the Cu_2O nanowire samples. In addition, the

synthesis of nanowire arrays was also carried out on glass slides coated with fluorinated tin oxide (FTO). Copper was electrodeposited on gold sputtered FTO slides which were then immersed into a solution of hydrogen peroxide and sodium hydroxide for a very short period of time ~ 2 minutes. Unlike Cu foils, the electrodeposited Cu formed a film of copper hydroxide nanoparticles. Interestingly, copper oxide nanowires were observed

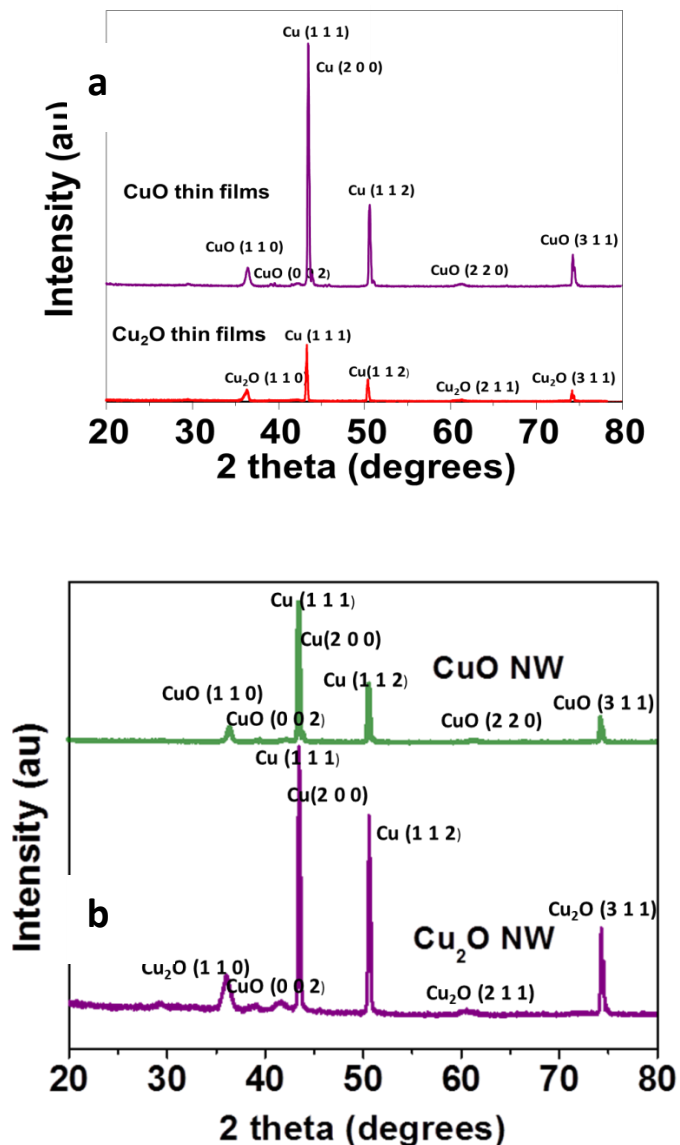


Figure 5 (a) XRD spectrum of the Cu₂O and CuO thin films and (b) NW arrays synthesized on copper foils

when these copper hydroxide nanoparticles were annealed using plasma oxidation. Even though copper hydroxide nanowires are not formed in the wet oxidation procedure, the copper hydroxide nanoparticles could act as nucleation sites for the growth of copper oxide nanowires during the plasma oxidation step.

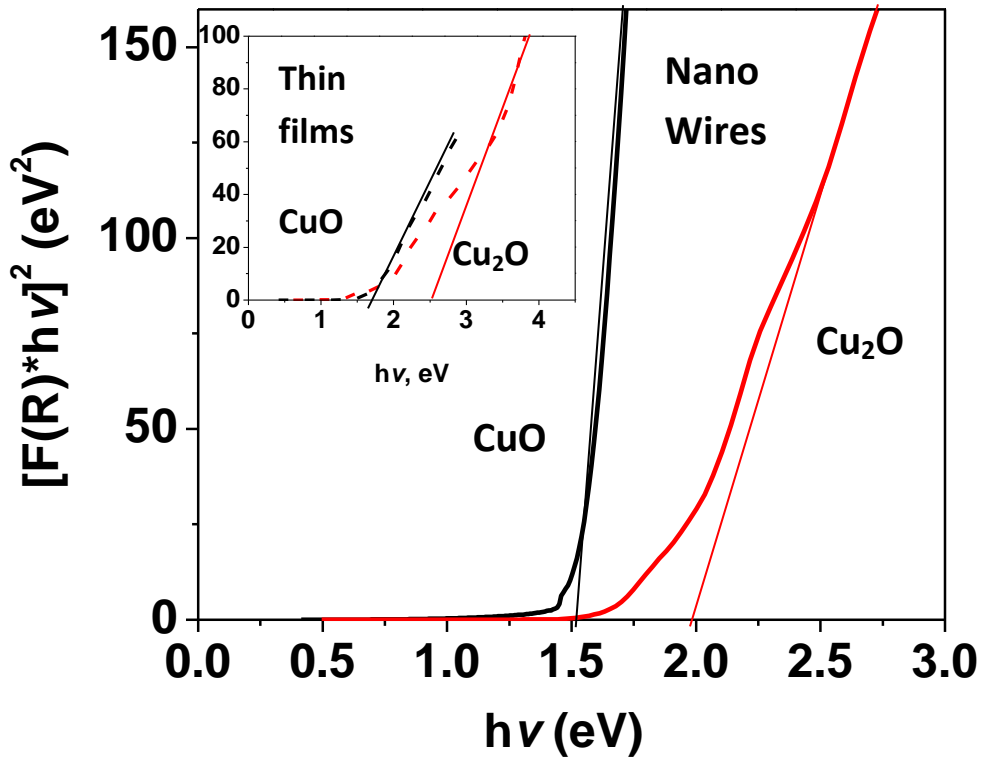


Figure 6 Tauc plots for CuO (black) and Cu₂O NW (red) for determining the band gap. The inset shows the Tauc plots for CuO (black) and Cu₂O thin films. Both Cu₂O thin films and nanowire arrays samples show the presence of CuO, which is most likely to be present as an oxide layer beneath the nanowires

The optical band gap of the resulting samples is determined using diffuse reflectance data as shown in Figure 6. The band gap values are found to be about 1.5 eV for CuO and 2.1 for Cu₂O, NW respectively. The band gap for the CuO thin films was

found to be 1.5 eV and 2.4 eV for Cu₂O. The difference in the band of Cu₂O thin films and nanowire arrays might originate due to difference in the crystalline grain sizes. Analysis of the Tauc plot for Cu₂O NW samples evidence for some CuO present in the Cu₂O NW samples and this is also in agreement with the XRD results.. The phase purity of Cu₂O NW arrays has also been shown to be challenge with the nanowire annealed by thermal oxidation.^{31,32} The CuO in the Cu₂O nanowire array sample is most likely to be present as a polycrystalline layer beneath the Cu₂O NW arrays.

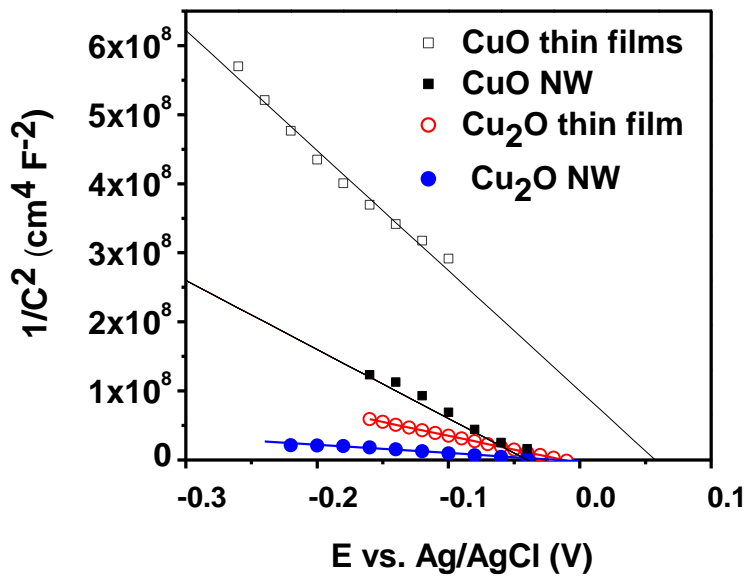


Figure 7 Mott-Schottky plot for Cu₂O NW and thin films obtained at 1 sun illumination (100 mW/cm²) and 10 Hz frequency.

The Mott-Schottky of the Cu₂O NW and thin film electrodes are represented in Figure 7. The intercept of the Mott-Schottky plot gives the value $V_{fb} + kT/q$, where V_{fb} is the flat band potential, k is Boltzmann constant, q is the electron charge. The flat band potential

for the Cu₂O NW arrays and the thin films was estimated to be 0.012 V vs. Ag/AgCl or -4.05 eV vs. vacuum. The CuO NW had a flat band potential of 0.01 V vs. Ag/AgCl while CuO thin films had a flat band potential of 0.06 V vs. Ag/AgCl. The negative slope in the Mott-Schottky curves indicates that Cu₂O and CuO electrodes show p-type behavior.

The hole concentration can be estimated using the equation.

$$N = \frac{2}{q\epsilon_0\epsilon_r \frac{d}{dV} \left(\frac{1}{C^2} \right)}$$

where N is the carrier density, $\epsilon_0 = (8.854 \times 10^{-12} \text{ F/m})$ is permittivity of free space, ϵ_r is the dielectric constant, and $\frac{d}{dV} \left(\frac{1}{C^2} \right)$ is the slope of the Mott-Schottky curve. A dielectric constant of 6.3 for cuprous oxide and 10.26 for cupric oxide was used for the calculations.^{40,41} Basing on the slopes obtained from the Mott-Schottky plots the carrier densities are calculated as $5.6 \times 10^{22} \text{ cm}^{-3}$ for the Cu₂O thin films and $1.9 \times 10^{23} \text{ cm}^{-3}$ for the Cu₂O nanowires. The carrier density is estimated to be $5 \times 10^{21} \text{ cm}^{-3}$ for CuO thin films and $1.37 \times 10^{22} \text{ cm}^{-3}$ for CuO NW respectively. The open-circuit potential data as shown in Figure 8 indicate slightly negative values for nanowire arrays compared to films. This difference is similar to that observed with flat band potential values using Mott-Schottky technique.

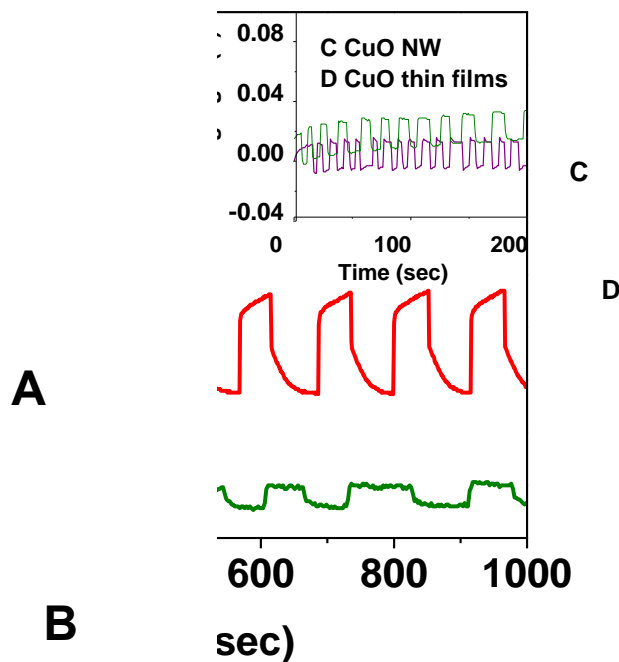


Figure 8 Photovoltage transients for the Cu_2O and CuO thin films and nanowires under open circuit condition. The electrodes were illuminated with a chopped AM 1.5 light (100 mW/cm^2).

The J-E curves measured under chopped AM 1.5 illumination for Cu_2O thin films and nanowires are shown in Figure 9. The chopped illumination method has the advantage of monitoring the light and dark current simultaneously. Cu_2O NW array electrodes showed significantly higher photocurrent than the thin film electrodes. At a potential of 0V w.r.t. reference hydrogen electrode the photocurrent density ($J_{\text{light}} - J_{\text{dark}}$) was found to be 0.06 mA/cm^2 and 0.26 mA/cm^2 for the thin film and Cu_2O NW array electrodes respectively. Thin films of CuO and nanowire arrays of CuO showed very low photocurrents.

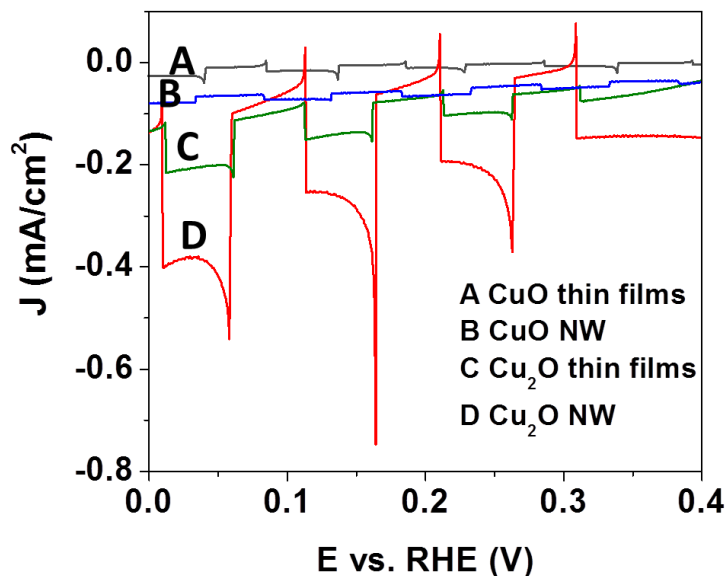


Figure 9 Current density vs. Potential characteristics for the Cu_2O , CuO thin films and nanowire arrays measured under chopped AM 1.5 illumination (100 mW/cm^2).

The work function of copper (4.65 eV)⁴² is less than that of copper oxide ($4.8\text{-}5.2 \text{ eV}$)⁴³, causing the bands bending downwards at the copper oxide-copper interface after the Fermi levels equilibrate. This results in the formation of a Schottky barrier for the holes at the copper oxide-copper interface.⁴⁴ The experimentally measured barrier heights range from $0.74\text{-}0.84 \text{ eV}$.⁴⁵ For a p-type semiconductor the holes have to move through the bulk of the semiconductor to counter electrode to participate in water oxidation reaction, while the electrons are transferred from the surface of the semiconductor to electrolyte for the hydrogen evolution reaction. The Schottky-barrier for the holes at the copper-oxide/copper interface would result in slower transport of holes across the interface. This would increase the recombination of the holes with electrons thereby lowering the current density. To eliminate this Schottky barrier, the synthesis was carried

out with FTO slides, sputtered with gold and subsequently coated with copper by electrodeposition. The SEM images of cuprous oxide nanowires grown on FTO are shown in Figure 10. Interestingly, the nanowires grown on FTO also showed similar performance as that of nanowires grown on Cu foil, suggesting the minimal role of the Schottky barrier affecting the performance (Figure S6, Supplementary information). The low photocurrents seen with nanowire electrodes could be due to recombination arising at the polycrystalline copper oxide film present beneath the nanowire arrays (Figure S7, Supplementary information). Also the presence of Ti^{+3} trap states in titania could hinder the transport of electrons at the semiconductor-electrolyte interface and lower the observed photocurrents.⁴⁶ Another possibility is the sluggish kinetics of H_2 reduction at the titania interface and a suitable catalyst like platinum could help overcome this problem. Preliminary experiments involving loading platinum particles onto the titania coated nanowire arrays showed no significant improvement in photoactivity. Also, it was found that the photocurrent density saturates when the light intensity is increased beyond 1 Sun (Figure S8, Supplementary Information). These results clearly point out the detrimental role of the interfacial oxide which limits the performance of the copper oxide nanowire arrays. The interfacial oxide layer not acts as transport barrier for the charge carrier but also increases the recombination losses and has to be eliminated to achieve higher photocurrents from the nanowire arrays.

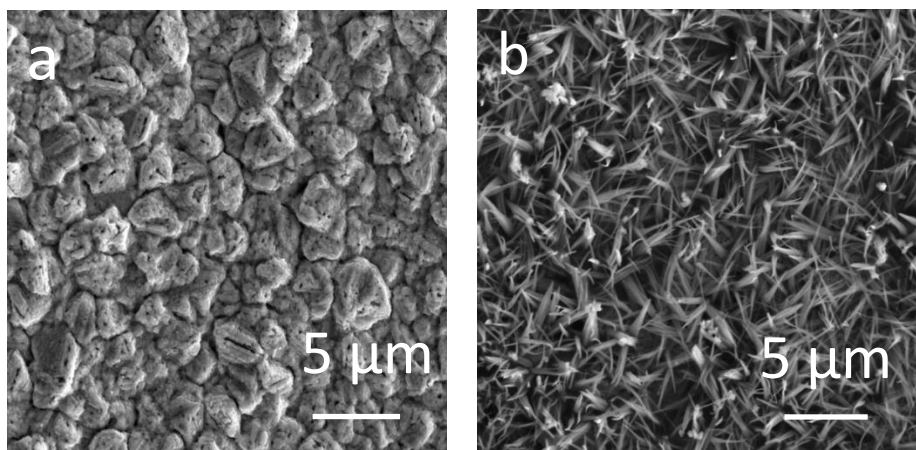


Figure 10 Scanning electron microscopy images of (a) copper hydroxide film formed on the FTO slides after the wet chemical oxidation and (b) growth of Cu₂O NW arrays after plasma annealing for 2 minutes.

The stability of the electrodes was tested by monitoring the open circuit voltage under 1 chopped AM 1.5 conditions. The open circuit voltage vs. time plots is shown in Figure 8 and it can be seen that both the nanowire and thin film electrodes are stable for at least 1000 seconds. A significant loss of photoactivity was seen after long exposure times (>2000 seconds). The loss in photoactivity was found to be more rapid when a potential was applied. The loss in photoactivity could be due to the pin holes in the titania coated Cu₂O electrodes and after 300s no photoactivity was observed with cuprous oxide nanowire electrodes when a potential of -0.55V vs. Ag/AgCl was applied. Similar observations on the stability of titania coated Cu₂O electrodes, were made by Gratzel and co-workers who found that a black layer, corresponding to formation of copper, was found on the illuminated region of the Cu₂O photocathodes. The CuO thin film and NW electrodes were only stable for few minutes and showed no photocatalytic activity after 5 mins.

The fabrication of a thick mesoporous cuprous oxide nanowire electrode without any interfacial oxide layer would be the ideal architecture. This would provide the necessary thickness for light absorption, provide more intimate contact between the nanowires and electrolyte for better charge transport at the semiconductor-electrolyte interface, solve the issue of phase purity and would eliminate recombination losses due to the polycrystalline oxide layer. Our ongoing research efforts include the fabrication of these mesoporous electrodes and investigation of alternative protective layers for improving the stability and performance of the cuprous oxide nanowires.

Conclusions

A generic and scalable synthesis technique for growing cuprous oxide nanowire arrays on different substrates is presented. The synthesis of nanowire arrays was carried out on copper foils, glass slides coated with fluorinated tin oxide, other metallic foils and could be extended to other substrates. Experiments using hydrogen peroxide for wet chemical oxidation suggest that the nucleation and growth of copper hydroxide nanowires proceed in similar fashion to that of plasma oxidation. Also, the combination of wet chemical and plasma oxidation can be interesting for reducing the time scales for a variety of other materials systems. Photoelectrochemical characterization of the copper oxide film and nanowire arrays showed that the nanowires show a significant enhancement in photocurrents. Cuprous oxide nanowires grown on gold sputtered FTO slides showed similar performance as that of the nanowires grown on copper foils suggesting that the presence of Schottky barrier is not limiting the performance. The presence of an oxide layer beneath the nanowire arrays limits the high photocurrents that can be achieved with

nanowire arrays. The performance of the thick, mesoporous copper oxide nanowire electrodes without any interfacial oxide layers is currently under investigation.

Supporting information

Figure S1 shows the effect of wet chemical oxidation times on the nanowire length. The nanowires are about 500 nm in length for 30 s oxidation time and increase in length to about 3-4 μm at 30 minutes. The increase in length with time suggests that nanowire formation occurs nucleation followed by basal growth.

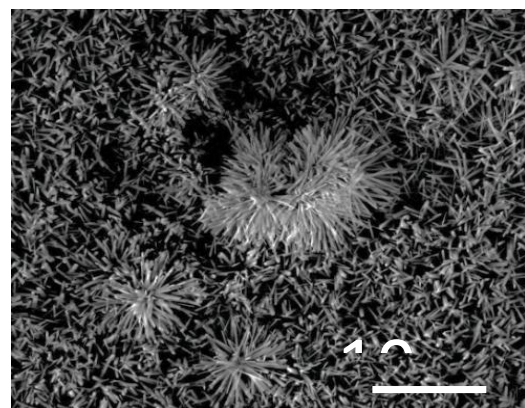
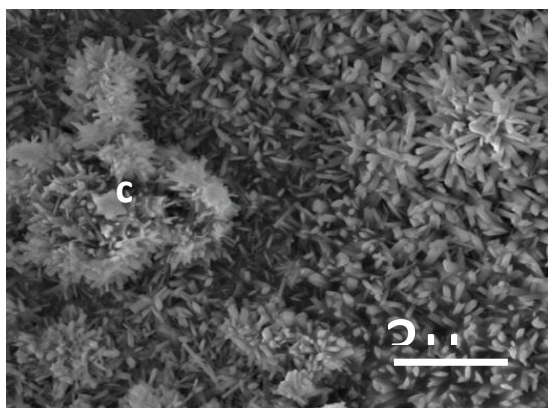
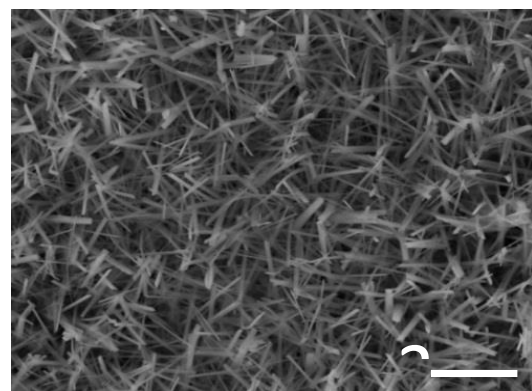
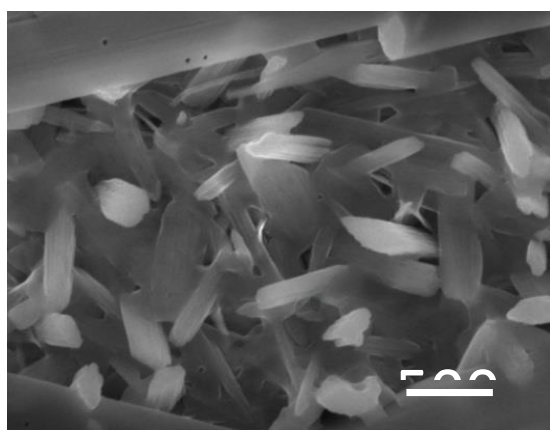


Figure S1 SEM images of copper hydroxide nanowires with different immersion times (a) 30 s (b) 1 min (c) 10 min (d) 30 min

Figure S2 shows the scanning electron microscopy images for copper oxide thin films produced by direct plasma oxidation. A few of the thin film samples showed a low density of nanowires. Temperature control of the copper foil is critical for achieving nucleation density and is tough achieve in direct plasma oxidation techniques. A wet chemical oxidation followed by plasma annealing is more attractive synthesis route for achieving high density of nanowires.

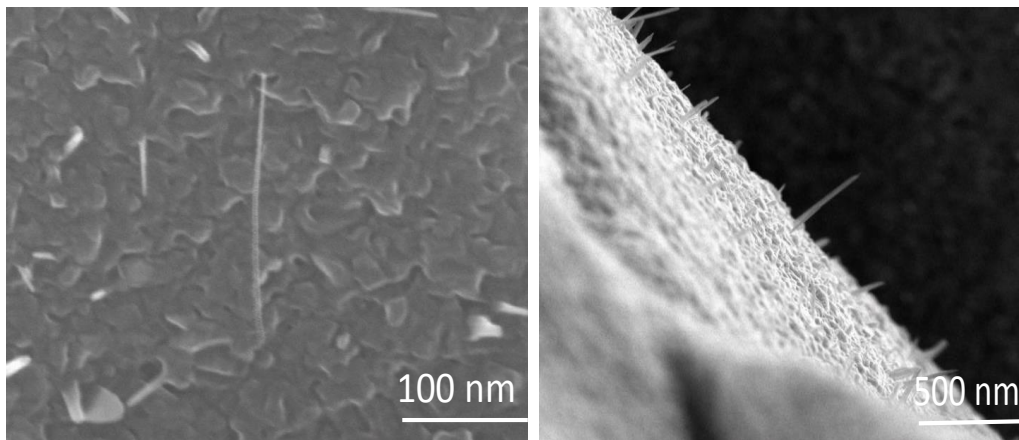


Figure S2 Scanning electron microscopy images of copper oxide nanowires formed by direct oxidation of copper foils in atmospheric air plasma. (a) top view (b) cross-section view.

Figure S3 shows the copper oxide thin films produced by direct plasma oxidation. Films of 2-3 μm thickness could be produced in a very short time scales on the order of a

minute. Figure S4 shows the Cu_2O and CuO nanowires that were synthesized by plasma annealing the $\text{Cu}(\text{OH})_2$ nanowires.

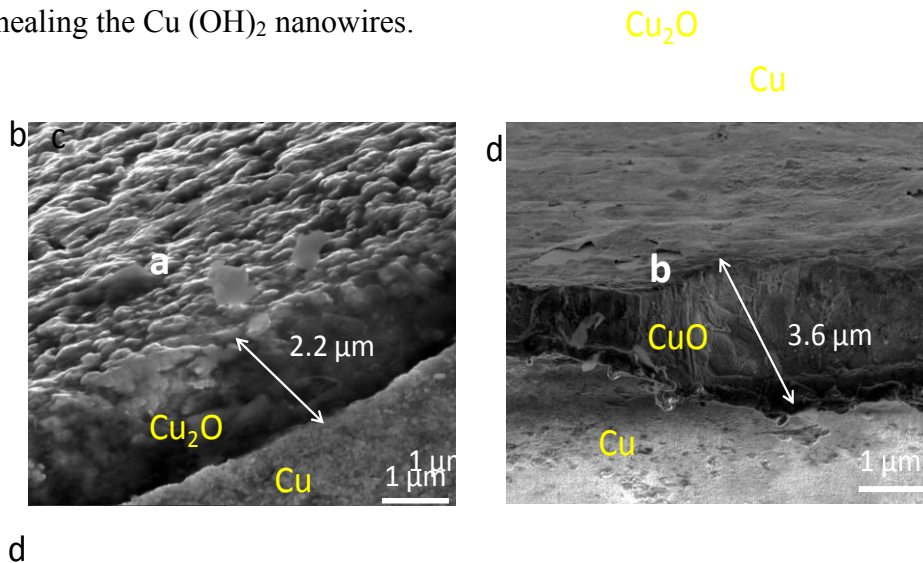


Figure S3. SEM images of Cu_2O and CuO thin films synthesized through plasma oxidation.

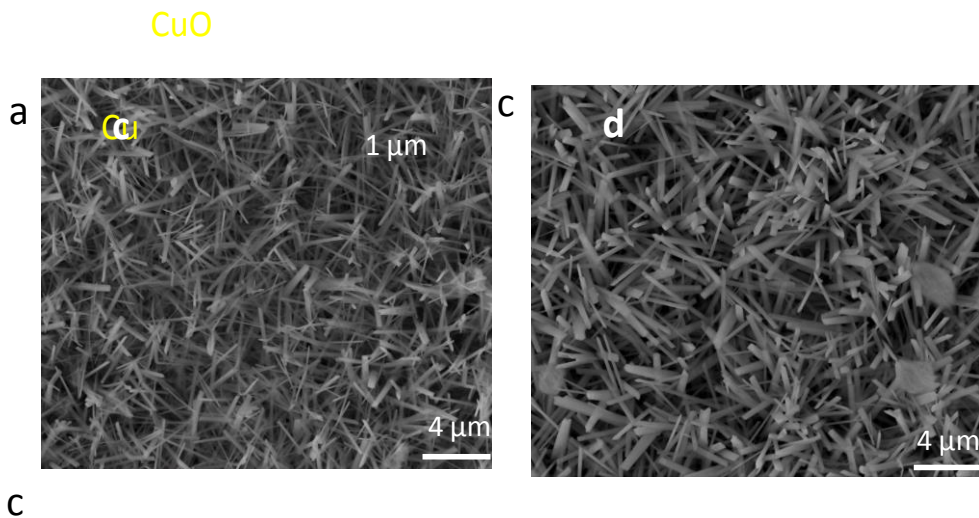


Figure S4 SEM images of Cu_2O and CuO nanowires formed after the plasma annealing the copper hydroxide nanowires.

Figure S4 shows the photocurrent transients for copper oxide thin films and nanowires obtained at 0 V vs. Ag/AgCl . The nanowires and thin films showed no loss in photocurrent for at least 200s when no bias (w.r.t. Ag/AgCl) was applied. The spikes seen

in the photocurrent transients and also in the J-E curves could be arising from the accumulation of charge carriers at the semiconductor-electrolyte interface . The decay in current density to a steady state value might be due to recombination of these accumulated carriers.

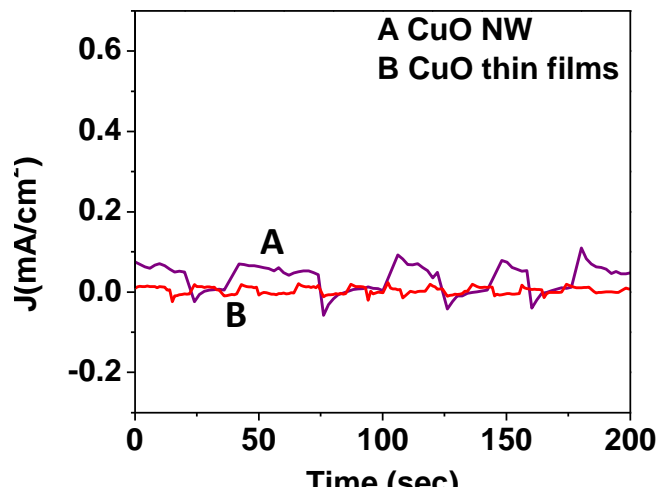
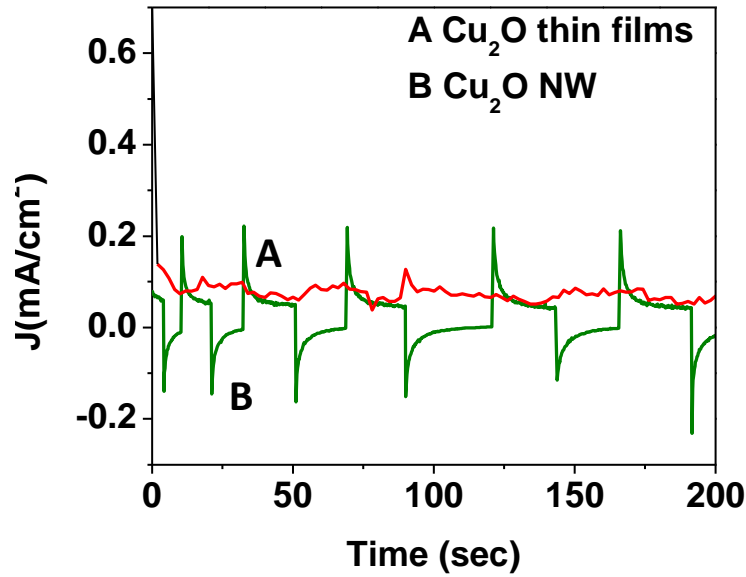


Figure S4 Photocurrent transients for the copper oxide thin films and nanowires under short circuit condition. The electrodes were illuminated with a chopped AM 1.5 light (100 mW/cm²).

Figure S5 shows the energy diagram depicting with the band edge positions of Cu₂O and TiO₂. The fermi level of copper, Cu₂O and Au are also shown. The work function of Cu is less than that of Cu₂O resulting in a Schottky barrier at the Cu₂O/Cu interface.

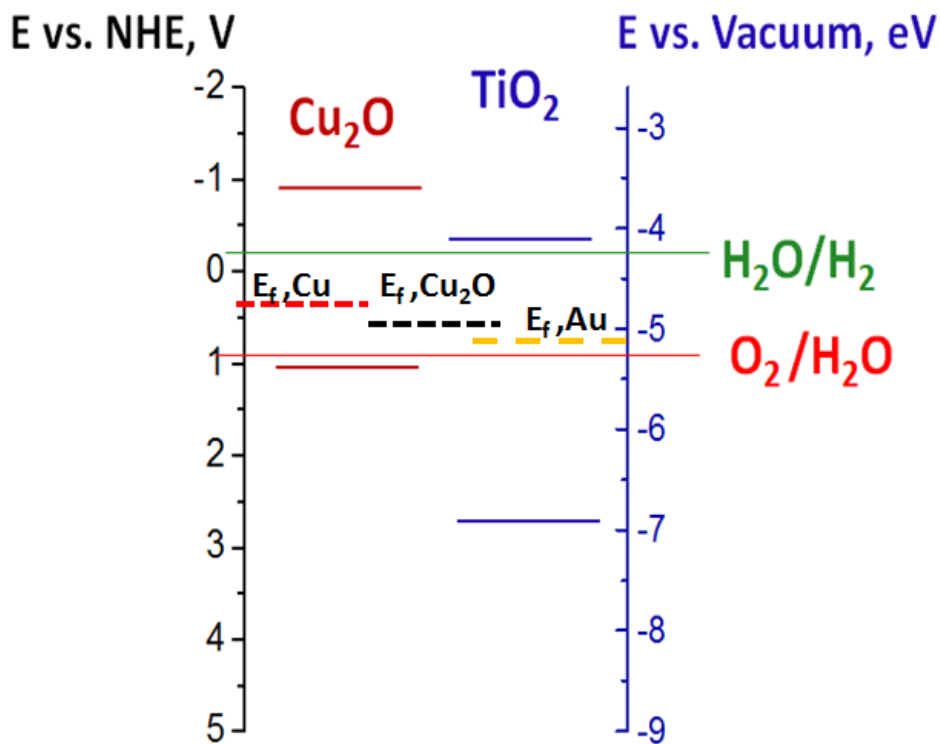


Figure S5 Energy band diagram showing the locations of the band edges of Cu₂O, TiO₂, hydrogen and oxygen evolution potential at pH = 4.9. The Fermi level of Cu, Cu₂O and Au are also indicated.

In order to remove the Schottky barrier present at the $\text{Cu}_2\text{O}/\text{Cu}$ interface, a layer of gold was sputtered on an FTO glass slide followed by the electrodeposition of copper. Cuprous oxide nanowires were synthesized on these FTO glass slides and the electrochemical performance was evaluated. Figure S6 shows the J-E curves for the Cu_2O wires grown on gold sputtered FTO slides. At 0 V vs. RHE a photocurrent density of $0.15 \text{ mA}/\text{cm}^2$ was obtained. The unexpected lower value of the photocurrent density could be due to the presence of an oxide layer beneath the wires that could result in the recombination of charge carriers.

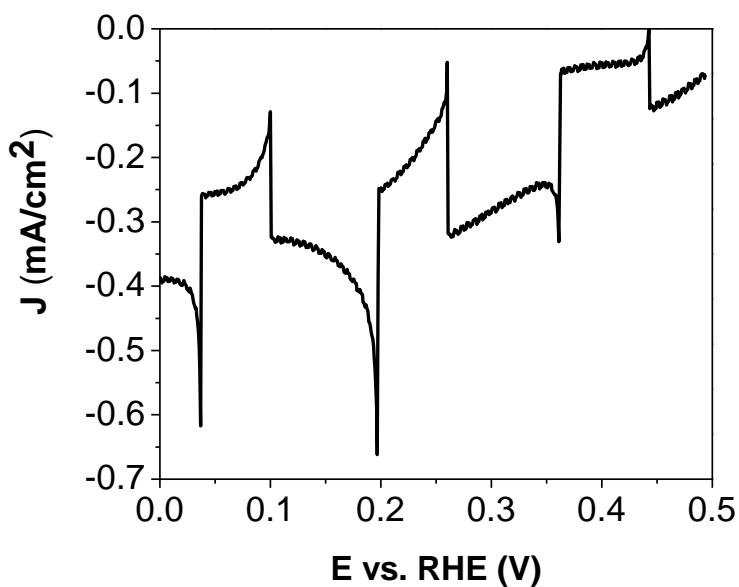


Figure S6 J-E plots of Cu_2O NW synthesized on gold sputtered FTO glass slides under chopped AM 1.5 illumination.

Figure S7 shows the cross-sectional SEM image of copper oxide nanowire array sample synthesized on a copper foil. Recombination of charge of carriers this polycrystalline

oxide layer leads to a significant loss in the observed photocurrent densities for nanowire arrays samples.

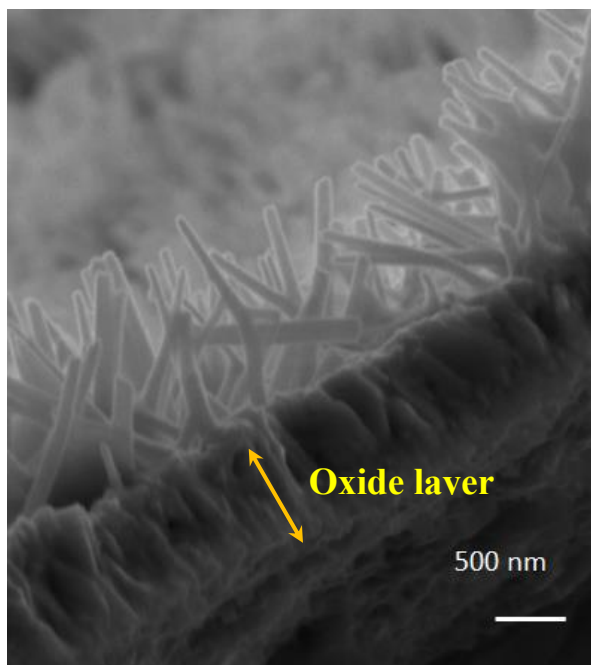


Figure S7 Scanning electron microscopy sample showing the presence of an oxide layer beneath the copper oxide nanowire arrays.

Acknowledgements

The authors acknowledge support from DOE toward infrastructure support to Conn Center for Renewable Energy Research at University of Louisville (DE-EE0003206), Kentucky Department of Energy Development and Independence (KY DEDI) and personnel, infrastructure support from the Conn Center.

References

- (1) Walter, M. G.; Warren, E. L.; McKone, J. R.; Boettcher, S. W.; Mi, Q. X.; Santori, E. A.; Lewis, N. S.: Solar Water Splitting Cells. *Chemical Reviews* **2010**, *110*, 6446-6473.
- (2) Chen, Z. B.; Jaramillo, T. F.; Deutsch, T. G.; Kleiman-Shwarscstein, A.; Forman, A. J.; Gaillard, N.; Garland, R.; Takanabe, K.; Heske, C.; Sunkara, M.; McFarland, E. W.; Domen, K.; Miller, E. L.; Turner, J. A.; Dinh, H. N.: Accelerating materials development for photoelectrochemical hydrogen production: Standards for methods, definitions, and reporting protocols. *J. Mater. Res.* **2010**, *25*, 3-16.
- (3) Musa, A. O.; Akomolafe, T.; Carter, M. J.: Production of cuprous oxide, a solar cell material, by thermal oxidation and a study of its physical and electrical properties. *Sol. Energy Mater. Sol. Cells* **1998**, *51*, 305-316.
- (4) Rakhshani, A. E.: PREPARATION, CHARACTERISTICS AND PHOTOVOLTAIC PROPERTIES OF CUPROUS-OXIDE - A REVIEW. *Solid-State Electronics* **1986**, *29*, 7-17.
- (5) Chatterjee, A. P.; Mukhopadhyay, A. K.; Chakraborty, A. K.; Sasmal, R. N.; Lahiri, S. K.: ELECTRODEPOSITION AND CHARACTERIZATION OF CUPROUS-OXIDE FILMS. *Materials Letters* **1991**, *11*, 358-362.
- (6) Pollack, G. P.; Trivich, D.: PHOTOELECTRIC PROPERTIES OF CUPROUS-OXIDE. *Journal of Applied Physics* **1975**, *46*, 163-172.
- (7) Gerischer, H.: STABILITY OF SEMICONDUCTOR ELECTRODES AGAINST PHOTODECOMPOSITION. *Journal of Electroanalytical Chemistry* **1977**, *82*, 133-143.
- (8) Siripala, W.; Ivanovskaya, A.; Jaramillo, T. F.; Baeck, S. H.; McFarland, E. W.: A CU₂O/TiO₂ heterojunction thin film cathode for photoelectrocatalysis. *Sol. Energy Mater. Sol. Cells* **2003**, *77*, 229-237.
- (9) Paracchino, A.; Laporte, V.; Sivula, K.; Gratzel, M.; Thimsen, E.: Highly active oxide photocathode for photoelectrochemical water reduction. *Nature Materials* **2011**, *10*, 456-461.
- (10) Rai, B. P.: CU₂O SOLAR-CELLS - A REVIEW. *Solar Cells* **1988**, *25*, 265-272.
- (11) Engel, C. J.; Polson, T. A.; Spado, J. R.; Bell, J. M.; Fillinger, A.: Photoelectrochemistry of porous p-Cu₂O films. *Journal of the Electrochemical Society* **2008**, *155*, F37-F42.
- (12) de Jongh, P. E.; Vanmaekelbergh, D.; Kelly, J. J.: Photoelectrochemistry of electrodeposited Cu₂O. *Journal of the Electrochemical Society* **2000**, *147*, 486-489.
- (13) Sunkara, M. K.; Pendyala, C.; Cummins, D.; Meduri, P.; Jasinski, J.; Kumar, V.; Russell, H. B.; Clark, E. L.; Kim, J. H.: Inorganic nanowires: a perspective about their role in energy conversion and storage applications. *Journal of Physics D-Applied Physics* **2011**, *44*.
- (14) Chakrapani, V.; Thangala, J.; Sunkara, M. K.: WO₃ and W₂N nanowire arrays for photoelectrochemical hydrogen production. *International Journal of Hydrogen Energy* **2009**, *34*, 9050-9059.
- (15) Izaki, M.; Mizuno, K.-t.; Shinagawa, T.; Inaba, M.; Tasaka, A.: Photochemical construction of photovoltaic device composed of p-copper(I) oxide and n-zinc oxide. *Journal of the Electrochemical Society* **2006**, *153*, C668-C672.
- (16) Yin, Z. G.; Zhang, H. T.; Goodner, D. M.; Bedzyk, M. J.; Chang, R. P. H.; Sun, Y.; Ketterson, J. B.: Two-dimensional growth of continuous Cu₂O thin films by magnetron sputtering. *Applied Physics Letters* **2005**, *86*.
- (17) E. Fortin, D. M.: Photovoltaic effects in Cu₂O/Cu solar cells grown by anodic oxidation. *Solid-State Electronics* **1982**, *24*, 281-283.

- (18) Xiang, C. X.; Kimball, G. M.; Grimm, R. L.; Brunschwig, B. S.; Atwater, H. A.; Lewis, N. S.: 820 mV open-circuit voltages from Cu₂O/CH₃CN junctions. *Energy & Environmental Science* **2011**, *4*, 1311-1318.
- (19) Ristov, M.; Sinadinovski, G.; Grozdanov, I.: CHEMICAL-DEPOSITION OF CU₂O THIN-FILMS. *Thin Solid Films* **1985**, *123*, 63-67.
- (20) Wang, W. Z.; Wang, G. H.; Wang, X. S.; Zhan, Y. J.; Liu, Y. K.; Zheng, C. L.: Synthesis and characterization of Cu₂O nanowires by a novel reduction route. *Advanced Materials* **2002**, *14*, 67-69.
- (21) Orel, Z. C.; Anzlovar, A.; Drazic, G.; Zigon, M.: Cuprous oxide nanowires prepared by an additive-free polyol process. *Crystal Growth & Design* **2007**, *7*, 453-458.
- (22) Walton, A. S.; Gorzny, M. L.; Bramble, J. P.; Evans, S. D.: Photoelectric Properties of Electrodeposited Copper(I) Oxide Nanowires. *Journal of the Electrochemical Society* **2009**, *156*, K191-K195.
- (23) Shin, H. S.; Song, J. Y.; Yu, J.: Template-assisted electrochemical synthesis of cuprous oxide nanowires. *Materials Letters* **2009**, *63*, 397-399.
- (24) Xiong, Y. J.; Li, Z. Q.; Zhang, R.; Xie, Y.; Yang, J.; Wu, C. Z.: From complex chains to 1D metal oxides: A novel strategy to Cu₂O nanowires. *Journal of Physical Chemistry B* **2003**, *107*, 3697-3702.
- (25) Tan, Y. W.; Xue, X. Y.; Peng, Q.; Zhao, H.; Wang, T. H.; Li, Y. D.: Controllable fabrication and electrical performance of single crystalline Cu₂O nanowires with high aspect ratios. *Nano Letters* **2007**, *7*, 3723-3728.
- (26) Sahoo, S.; Husale, S.; Colwill, B.; Lu, T. M.; Nayak, S.; Ajayan, P. M.: Electric Field Directed Self-Assembly of Cuprous Oxide Nanostructures for Photon Sensing. *Acs Nano* **2009**, *3*, 3935-3944.
- (27) Jiang, X. C.; Herricks, T.; Xia, Y. N.: CuO nanowires can be synthesized by heating copper substrates in air. *Nano Letters* **2002**, *2*, 1333-1338.
- (28) Xu, C. H.; Woo, C. H.; Shi, S. Q.: Formation of CuO nanowires on Cu foil. *Chemical Physics Letters* **2004**, *399*, 62-66.
- (29) Wang, Y.; Shen, R. Q.; Jin, X. Y.; Zhu, P.; Ye, Y. H.; Hu, Y.: Formation of CuO nanowires by thermal annealing copper film deposited on Ti/Si substrate. *Applied Surface Science* **2011**, *258*, 201-206.
- (30) Kaur, M.; Muthe, K. P.; Deshpande, S. K.; Choudhury, S.; Singh, J. B.; Verma, N.; Gupta, S. K.; Yakhmi, J. V.: Growth and branching of CuO nanowires by thermal oxidation of copper. *Journal of Crystal Growth* **2006**, *289*, 670-675.
- (31) Jin-Woo Han, A. L., Nobuhiko P. Kobayashi, M. Meyyappan: Evolutional Transformation of Copper Oxide Nanowires to Copper Nanowires by a Reduction Technique. *Materials Express* **2011**, *1*, 176-180.
- (32) Qian, F.; Wang, G. M.; Li, Y.: Solar-Driven Microbial Photoelectrochemical Cells with a Nanowire Photocathode. *Nano Letters* **2010**, *10*, 4686-4691.
- (33) Kumar, V.; Kim, J. H.; Jasinski, J. B.; Clark, E. L.; Sunkara, M. K.: Alkali-Assisted, Atmospheric Plasma Production of Titania Nanowire Powders and Arrays. *Crystal Growth & Design* **2011**, *11*, 2913-2919.
- (34) Zhang, W. X.; Wen, X. G.; Yang, S. H.; Berta, Y.; Wang, Z. L.: Single-crystalline scroll-type nanotube arrays of copper hydroxide synthesized at room temperature. *Advanced Materials* **2003**, *15*, 822-+.
- (35) Chaudhari, N. K.; Fang, B.; Bae, T. S.; Yu, J. S.: Low Temperature Synthesis of Single Crystalline Iron Hydroxide and Oxide Nanorods in Aqueous Media. *Journal of Nanoscience and Nanotechnology* **2011**, *11*, 4457-4462.

- (36) Jia, C. J.; Sun, L. D.; Yan, Z. G.; You, L. P.; Luo, F.; Han, X. D.; Pang, Y. C.; Zhang, Z.; Yan, C. H.: Iron oxide nanotubes - Single-crystalline iron oxide nanotubes. *Angewandte Chemie-International Edition* **2005**, *44*, 4328-4333.
- (37) Hongwei Hou, Y. X., Qing Yang, Qixun Guo, Chenrong Tan: Preparation and characterization of γ -AlOOH nanotubes and nanorods. *Nanotechnology* **2005**, *6*.
- (38) Cvelbar, U.; Chen, Z. Q.; Sunkara, M. K.; Mozetic, M.: Spontaneous Growth of Superstructure α -Fe₂O₃ Nanowire and Nanobelt Arrays in Reactive Oxygen Plasma. *Small* **2008**, *4*, 1610-1614.
- (39) Cvelbar, U.; Ostrikov, K.; Levchenko, I.; Mozetic, M.; Sunkara, M. K.: Control of morphology and nucleation density of iron oxide nanostructures by electric conditions on iron surfaces exposed to reactive oxygen plasmas. *Applied Physics Letters* **2009**, *94*.
- (40) Wang, L. C.; Tao, M.: Fabrication and characterization of p-n homojunctions in cuprous oxide by electrochemical deposition. *Electrochemical and Solid State Letters* **2007**, *10*, H248-H250.
- (41) Nakaoka, K.; Ueyama, J.; Ogura, K.: Photoelectrochemical behavior of electrodeposited CuO and Cu₂O thin films on conducting substrates. *Journal of the Electrochemical Society* **2004**, *151*, C661-C665.
- (42) Mao, Z.; Song, W.; Chen, L.; Ji, W.; Xue, X. X.; Ruan, W. D.; Li, Z. S.; Mao, H. J.; Ma, S.; Lombardi, J. R.; Zhao, B.: Metal-Semiconductor Contacts Induce the Charge-Transfer Mechanism of Surface-Enhanced Raman Scattering. *J. Phys. Chem. C* **2011**, *115*, 18378-18383.
- (43) Kevin, M.; Ong, W. L.; Lee, G. H.; Ho, G. W.: Formation of hybrid structures: copper oxide nanocrystals templated on ultralong copper nanowires for open network sensing at room temperature. *Nanotechnology* **2011**, *22*.
- (44) Olsen, L. C.; Addis, F. W.; Miller, W.: EXPERIMENTAL AND THEORETICAL-STUDIES OF CU₂O SOLAR-CELLS. *Solar Cells* **1982**, *7*, 247-279.
- (45) Olsen, L. C.; Bohara, R. C.; Urie, M. W.: EXPLANATION FOR LOW-EFFICIENCY CU₂O SCHOTTKY-BARRIER SOLAR-CELLS. *Applied Physics Letters* **1979**, *34*, 47-49.
- (46) Richter, C.; Schmuttenmaer, C. A.: Exciton-like trap states limit electron mobility in TiO₂(2) nanotubes. *Nature Nanotechnology* **2010**, *5*, 769-772.

CURRICULUM VITAE

Swathi Sunkara
swathi.sunkara@louisville.edu
(502)- 572-7369
789 Eastern Parkway, apt 1
Louisville, KY 40217

Objective

Seeking a process/materials engineer position at semiconductor/materials/energy industry to utilize my chemical vapor deposition experience and contribute to the organization's growth

Education

PhD in Chemical Engineering Expected Dec 2015
University of Louisville- Louisville, Kentucky
Advisor: Dr. Mahendra Sunkara, GPA: 3.67/4.0

Bachelor of Technology in Chemical Engineering March 2010
Jawaharlal Nehru Technological University, GPA: 70% (Top 10 in the class)

Research Accomplishments

- Rebuilt a MOCVD reactor that led to more productivity and safety
- Developed the experimental synthesis of GaN based alloy in the low antimonide regime for the first time
- Developed a method for increasing antimony incorporation in GaN nanowires for improved crystallinity and photoelectrochemical performance which can extend to other III-V alloys
- Developed a systematic fundamental photoelectrochemical characterization of III-V alloys
- Investigated a epitaxial $\text{GaSb}_x\text{N}_{1-x}$ films on free standing GaN wafers for improved photoactivity
- Developed a step by step process and characterization to understand the nanowire growth mechanism
- Developed a new $\text{GaSb}_x\text{N}_{1-x}$ nanowire architecture that will reduce recombination and improve photoactivity
- Developed a highly scalable process for growth of copper oxide nanowires using a combination of wet chemical and atmospheric plasma methods. The process can be very easily integrated into modern manufacturing techniques such as roll to roll

Research skills and expertise

- Metal Organic Chemical Vapor Deposition (MOCVD) synthesis of III-V nitride alloys for photo-electrochemical water splitting, Atomic Layer Deposition
- Extensive Materials Characterization using techniques like Scanning Electron Microscopy, X-Ray Diffraction, Raman Spectroscopy, Photoluminescence, UV- Vis Spectroscopy.
- Hands on experience in troubleshooting issues with CVD reactors
- Regular maintenance of the MOCVD reactor
- Hot wire CVD
- Photoelectrochemical Characterization of semiconductors

Peer reviewed Publications

- Sunkara, S., Vendra, V.K., Kim, J.H., Druffel, T., Sunkara, M.K., Scalable synthesis of copper oxide nanowires and their photoelectrochemical properties, *Catalysis Today* 2013, 199, 27-35.
- Sunkara, S., Vendra, V.K., Jasinski, J., Deutsch, T., Andriotis, A.N., Menon, M., Sunkara, M.K., New Visible Light Absorbing Materials for Solar Fuels, Ga(Sb_x)N_{1-x} Alloys. *Advanced Materials*. (2014)
- Martinez, A., Vendra, V.K., Jasinski, J., Sunkara, S., Haldankar, P., Sunkara, M.K., Copper tungsten oxide coated copper oxide nanowire arrays as highly photoactive cathode for solar water splitting, *Journal of Materials chemistry A*, 1 (48), 15235 - 15241, (2013)
- Sunkara, S., Martinez, A., Jaramillo, D., Jasinski, J., Menon, M., Sunkara, M.K., Vapor Liquid Solid (VLS) growth of Ga(Sb_x)N_{1-x} nanowires, (manuscript under preparation)
- Martinez, A., Sunkara, S., Jasinski, J., Sunkara, M.K., MOCVD of highly textured Ga(Sb_x)N_{1-x} films, (manuscript under preparation)
- Sunkara, S., Jasinski, J., Sunkara, M.K., Formation of stacking faults in nanowires- A Review (manuscript under preparation)

Patents

Sunkara, M.K., Menon, M., Sheetz, M., Jasinski, J., Pendyala, C., Sunkara, S., Photoelectrochemical Cell Including Ga(Sb_x)N_{1-x} semiconductor, US Patent Application Number 13630875.

Conference Presentations

- Sunkara, S., Jasinski, J., Menon, M., Sunkara, M.K., Metal organic chemical vapor deposition of band edge engineered GaSb_xN_{1-x} ternary alloys for solar water splitting and carbon dioxide reduction, Materials Research Society Fall meeting, Boston, MA (2012).
- Sunkara, S., Jasinski, J., Menon, M., Sunkara, M, k., Synthesis of novel ternary GaSb_xN_{1-x} alloys and it's application in Photo-electrochemical water splitting for hydrogen production., 23rd North American Meeting, North American Catalysis Society, Louisville, KY (2013)
- Sunkara, S., Jasinski, J., Menon, M., Sunkara, M, k., Metal Organic Chemical Vapor Deposition of Ga(Sb_x)N_{1-x}: Experimental Verification of Anomalous Band Gap Reduction with Sb Incorporation, RE3 workshop, Louisville, KY (2013)

- Sunkara, S., Jasinski, J., Vendra, V., Sunkara, M, K., Solar Fuels: Photoelectrochemical Water Splitting and Carbon dioxide Reduction, KY EPSCOR, Lexington, KY (2012)
- Sunkara, S., Kim, J., Jasinski, J., Sunkara, M,K., Photoelectrochemical Water Splitting and Carbon dioxide Reduction, Kentucky State Wide Workshop, Louisville, KY (2010)
- Sunkara, S., Jasinski, J., Menon, M., Sunkara, M.K., Metal organic chemical vapor deposition of band edge engineered GaSb_xN_{1-x} ternary alloys for solar water splitting and carbon dioxide reduction, ECS meeting, San Francisco , CA (2013)
- Sunkara, S., Jasinski, J., Menon, M., Sunkara, M, k., Synthesis of novel ternary GaSb_xN_{1-x} alloys and it's application in Photo-electrochemical water splitting for hydrogen production., ECS meeting, Toronto, Canada (2013)

Awards

- Electrochemical society (ECS) student travel grant award, 225th ECS meeting, Orlando, FL (2014)
- Second Prize for Poster presentation at RE3 workshop for Renewable Energy, Louisville, KY (2013)
- Participation Award for Science as Art Competition at Materials Research Society (MRS) Fall, Boston, MA (2012)
- Second Prize for Talk at Indian Institute of Technology, Kharagpur, WB, India (2008)

Coursework

- Chemical Vapor Deposition, Physical Electronics, Materials Characterization, Electroanalytical Chemistry, Energy and Environmental Science,
- Trained on photoelectrochemical characterization of semiconductors at Joint Center for Artificial Photosynthesis winter school, CALTECH, Pasadena , CA
- Trained on making electrical contacts for materials to be tested for solar water splitting at NREL, Colorado

Professional membership

- Materials Research Society
- Electrochemical Society
- Vice President of Chemical Engineering Graduate Student Association, University of Louisville
- Indian Institute of Chemical Engineers

Mentoring Experience

- Teaching assistant for chemical vapor deposition
- Teaching assistant for transport phenomena
- Mentored two high school students
- Conducted labs in summer research camps